HAL
open science

Modélisation, conception et intégration de nouvelles architectures différentielles pour des capteurs M/NEMS résonants

Pierre Prache

To cite this version:

Pierre Prache. Modélisation, conception et intégration de nouvelles architectures différentielles pour des capteurs M/NEMS résonants. Autre. Université Paris Saclay (COmUE); Universitat autònoma de Barcelona, 2017. Français. NNT : 2017SACLC054 . tel-01682483

HAL Id: tel-01682483

https://theses.hal.science/tel-01682483v1

Submitted on 12 Jan 2018

HAL is a multi-disciplinary open access archive for the deposit and dissemination of scientific research documents, whether they are published or not. The documents may come from teaching and research institutions in France or abroad, or from public or private research centers.

L'archive ouverte pluridisciplinaire **HAL**, est destinée au dépôt et à la diffusion de documents scientifiques de niveau recherche, publiés ou non, émanant des établissements d'enseignement et de recherche français ou étrangers, des laboratoires publics ou privés.

université PARIS-SACLAY

NNT : 2017SACLC054

CentraleSupélec

UAB Universitat Autònoma de Barcelona

Modelling, design and integration of new differential architectures for M/NEMS resonant sensors

Thèse de doctorat de l'Universitat Autonoma de Barcelona et de l'Université Paris-Saclay, préparée à CentraleSupelec

École doctorale n°575 EOBE Electrical, optical, bio-physics and engineering (Physique et ingénierie : Electrons, Photons, Sciences du vivant)
Spécialité du doctorat : électronique et optoélectronique, nano- et microtechnologies

Thèse présentée et soutenue à Gif-sur-Yvette, le 9 novembre 2017 par

Pierre Prache

Composition du Jury :

Hélène Tap Professeur, LAAS	Président
Michael Kraft Professeur, ULG	Rapporteur
Pascal Nouet Professeur, LIRMM	Rapporteur
Sébastien Hentz Ingénieur de recherche, CEA	Examinateur
Hervé Matthias Maître de conférence, C2N	Examinateur
Joan Bausells Professeur, IMB-CNM	Examinateur
Jérôme Juillard Professeur, Centralesupelec	Directeur de thèse
Núria Barniol Professeur, UAB	Co-Directeur de thèse

Thèse de doctorat

C’est pas faux.

Perceval, Kaamelott

Remerciements

L'écriture des remerciements arrive comme la cavalerie, à la fin, lorsque tout s'est finalement calmé. Et ces quelques phrases qui semblaient simples à écrire, symbolisant l'aboutissement du manuscrit et d'un peu plus de trois années de travail sont en fait plus difficiles à trouver, afin de décrire avec simplicité les sentiments qui m'ont habité durant cet épisode de ma vie.

A tout seigneur tout honneur, j'aimerai commencer par remercier Jérôme Juillard, mon directeur de thèse « principal », mais aussi professeur, compagnon de voyage de virées nocturnes dans les rues de Barcelone ou de Shanghai. Merci d'avoir su trouver l'équilibre entre mon besoin d'autonomie, le travail en collaboration et parfois la guidance nécessaire lorsque j'étais un peu égaré. Merci pour les découvertes musicales lors des longues séances de mesure, pour les discussions philosophiques lors des trajets en voiture, pour les petits délires du quotidien qui rendent le travail agréable. Merci enfin pour les interminables heures passées à corriger mes écrits divers, et désolé de ne pas m'opposer frontalement, mais que veux-tu, ainsi suis-je ! J'aimerai ensuite remercier Nuria Barniol, ma co-directrice à Barcelone pour avoir rendu tout cela possible matériellement. Même si nous avons eu moins de proximité, nos échanges m'ont beaucoup apporté scientifiquement. Merci d'avoir accepté cette cotutelle qui fut riche pour les deux partis, et a permis d'aboutir à ce beau travail.

J'aimerai remercier tout particulièrement Michael Kraft et Pascal Nouet, rapporteurs de ce manuscrit, qui m'ont beaucoup apporté grâce à la rigueur de leur rapport, leurs questions et interrogations qui permettent de remettre en cause ce que l'on prenait – à tort – pour acquis. J'aimerai également remercier Hélène Tap, Hervé Mathias, Sebastien Hentz et Joan Bausells pour avoir pris le temps d'étudier mon travail, et de venir à la soutenance pour apporter leurs connaissances et expertises afin de les partager.

J'aimerai ensuite remercier les soutiens techniques, logistiques et administratifs de Supélec et de l'UAB, avec en premier lieu Alexandra puis Sophie, toujours au poste prêtes à donner des coups de main niveau paperasse (domaine dans lequel j'excelle…). Merci à Philippe Dessante et Anne Batalie pour leur patience dans la gestion de mon dossier au niveau de l'école doctorale et de Supelec malgré mes retards, manque d'organisation et de rigueur. Merci à Arantxa Uranga pour les coups de mains dans la relation avec l'école doctorale de l'UAB. Pour le soutien matériel, merci à Luc et Julien à Supelec et Javier Hellin à l'UAB.

Merci aux compagnons du 4ème étage, que ça soit pour les pauses cafés, bons délires (malgré mon absence au tarot), Morgan, Laurent, et les doctorants Pierre, Juliette, Ludwig, et évidement mon compagnon de bureau au début : Alexis, qui m'a aussi bien aidé au début de la thèse afin de comprendre la vie au labo et comment Jérôme fonctionne ! Merci à Pietro pour les avis techniques, et aux autres permanents pour les petits conseils, Caroline, Philippe, Francis et Anthony. Merci aux compagnons du troisième, Gisela, Antoine, Gilles, Arthur, Arnaud, et ceux du département énergie au second, Mickael, Eléonore, Olivier, Simon, Marine, Paul, Bogdan, Davi, et les autres, pour les pauses déjeuner, les bonnes discussions et quelques soirées bien sympas.

Merci aux doctorants de Barcelone pour m'avoir fait découvrir ce pays et cette ville, malgré l'époque troublé que traverse la Catalogne en ce moment. Merci à Martin pour les doigts de fées, merci à Guillermo pour les bons délire (et dota2) ainsi que pour les conseils en électronique. Merci à Oscar, Marcus, Carlos, et toute la bande pour les déjeuners et cafés à l'UAB, et Pau, Ferran, Paris, Bonache & co pour les restos du vendredi !

Enfin, merci à mes amis, ma famille et tous ceux qui ont été là au long de ces trois ans, qui n'ont jamais bien compris ce que je faisais, même après cinq explications et après avoir assisté à la soutenance ! Merci tout particulièrement à mes parents, qui me soutiennent et me conseillent depuis le

début, depuis le choix du sujet de thèse à vrai dire ! Merci à mes frères et sœurs qui me connaissent si bien et sont toujours là pour se faire des bons repas et partager les joies comme les moments difficiles. Merci aux cousins pour les énormes soutiens, les grosses soirées sans mesure, les vacances organisées aux petits soins. Merci à Vincent pour les kebabs (merci à Serge, de Plein Sud à Orsay pour les meilleurs kebabs du sud de l'île de France !), merci aux Castors pour le soutien psychologique sans faille, aux marques constantes d'amitié, qui font chaud au cœur lorsque l'on est un peu perdu dans le projet. Merci à Marie Estelle pour les longues discussions et (trop rares) séances d'escalade pour se changer les idées ! Merci à Katia de m'avoir accompagné en cette fin de thèse, qui n'est pas le moment le plus facile. Enfin, merci aux potes de Normale, John, Chaps, Ron, Manon, et tous les autres pour les grosses soirées, les apéros à la butte aux cailles et les pétanques du vendredi soir.

Summary

Summary 1

Résumé long en français 4

Notations 15

List of tables 18

List of figures 20

Introduction 25

Chapter 1 From resonance to MEMS differential resonant sensor 29

1.1 Resonance 29

1.2 MEMS resonators 31

1.2.1 What is a MEMS resonator? 31

1.2.2 MEMS resonators, yesterday and today 32

1.2.3 CMOS-MEMS integration 35

1.2.4 CMOS-MEMS monolithic integration using AMS 0.35 µm. 36

1.2.5 VIA structures 41

1.3 Modelling of capacitive MEMS beams 47

1.3.1 Framework and objectives of this section 47

1.3.2 Reduced-order model of a three-port beam with electrostatic actuation 49

1.3.3 Butterworth-Van Dyke model of electrostatically-actuated resonator with capacitive detection 55

1.3.4 Illustration 57

1.4 Differential architectures for temperature drift cancellation 62

1.4.1 Effect of temperature 62

1.4.2 MEMS-based oscillating loop 65

1.4.3 Temperature sensors in Integrated Circuits technology 67

1.4.4 Differential measurement and temperature compensation for clocking and sensing applications 68

1.4.5 Mode localization of coupled MEMS resonators 72

1.4.6 Synchronization of oscillators 75

Chapter 2 Design and integration of a monolithic CMOS/MEMS Mutually Injection-Locked Oscillator 79

2.1 Design guidelines for MILOs 79

2.2 CMOS-MEMS readout design 86

2.3 Integration of the NOT QUADDRO coupler 91

2.3.1 Digital mixer principle 91
2.3.2 Comparator and bias tee design 94
2.3.3 Digital mixer and buffer design 97
2.4 Miscellaneous design issues 99
2.4.1 Decoupling capacitances and low-resistance access matrix 99
2.4.2 Potentiometer bridge 100
2.5 Final chip layout and extracted simulation 103
2.6 Electronics' dependence on the temperature 107
Chapter 3 Experimental results 110
3.1 Open-loop characterization of the MILO. 110
3.1.1 Open-loop characterization of the CMOS-MEMS resonators 110
3.1.2 Open-loop characterization of the entire circuitry 122
3.2 Characterization of two co-integrated CMOS-MEMS resonators 124
3.2.1 Matching of resonance frequencies 124
3.2.2 Matching of quality factors 126
3.2.3 Consequences for the MILO 128
3.3 Closed-loop characterization 130
3.3.1 Closed-loop waveforms 130
3.3.2 Amplitude, saturation and hysteresis 132
3.4 Phase difference sensitivity to mismatch 135
3.4.1 Sensitivity to mismatch of CFB MILO 137
3.4.2 Sensitivity to mismatch of CCB MILO 140
3.5 Locking range 144
3.6 Common-mode rejection 146
3.6.1 Common-mode rejection of CFB MILOs 147
3.6.2 Common-mode rejection of CCB MILOs 151
3.7 Frequency noise, phase difference noise and resolution 153
3.7.1 Noise and resolution of CCB MILOs 153
3.7.2 Noise and resolution of CFB MILOs 161
3.8 Electrometer application 162
Chapter 4 Conclusion and perspectives 165
4.1 Conclusion 165
4.2 Device improvements 166
4.3 Future work 168
4.3.1 Investigation on the concept 168

4.3.2 Locking-range extension 169
4.3.3 Resonant accelerometer 170
Layout AMS C35B4C3 173
Annex 1: Analysis of Mutually Injection-Locked Oscillators for Differential Resonant Sensing [130] 174
Annex 2: Code for the characteristics of a MILO 187
Annex 3: Periodogram and Allan deviation 191
References 193

Résumé long en français

I- Introduction

Les microsystèmes électro mécaniques (MEMS) sont des systèmes ayant au moins un degré de liberté mécanique, dont au moins l'une des dimensions est micrométrique, et dont l'actionnement et la détection du mouvement est réalisé par transduction électronique. Ces transductions peuvent se faire en exploitant différents phénomènes physiques (piézoelectricité, piézorésistivité, transduction électrostatique, électrothermique ou optique…).

a. Résonateurs MEMS, principe et applications

Les MEMS ont permis l'émergence de capteurs (inertiels, de masse, de température, de pression…) d'horloges, d'actionneurs de taille microscopique et basse consommation. Par ailleurs, étant issus des technologies de fabrications de circuits intégrés, ils peuvent être fabriqués en grande quantité, à bas coût. Comme tout systèmes mécaniques, ils possèdent un jeu de fréquences spécifiques, dites fréquences de résonance, auxquelles l'amplitude de mouvement est particulièrement élevée. Certains de ces systèmes sont fabriqués pour travailler à ces fréquences, en général à la première d'entre elle, appelée fréquence propre, pour deux raisons principales. La première est que l'amplitude du mouvement est telle que le dispositif d'amplification du signal peut être réduit, donc moins bruyant, tout en sortant un signal exploitable par la suite. Placé dans une boucle de rétroaction électronique, qui injecte suffisamment d'énergie à chaque cycle pour compenser les pertes, un tel dispositif permet la génération d'une fréquence de manière stable. Pour de telles applications, les MEMS sont utiles car ils peuvent présenter un facteur de qualité (Q) élevé si encapsulé dans le vide, c'est-à-dire de faibles pertes par cycle, donc à la fois un besoin d'amplification réduit et une stabilité fréquentielle élevée.

La seconde raison pour laquelle les résonateurs sont utilisés vient du fait que la valeur de la fréquence de résonance est hautement liée aux caractéristiques physiques du résonateur (représentées par sa masse et sa raideur). Une modification de la masse ou de la raideur résulte en une modification de la fréquence de résonance. Grâce à une conception particulière, on peut relier une quantité physique à mesurer (le mesurande) à la masse ou la raideur du résonateur, et ainsi réaliser un capteur dit « résonant ». Le résonateur est alors généralement placé dans une boucle de rétroaction, formant un oscillateur dont la fréquence d'oscillation est liée au mesurande. L'intérêt de tels dispositifs par rapport à des capteurs « statiques » dont la grandeur de sortie est une amplitude est que la fréquence peut être directement injectée dans une chaine de commande numérique sans conversion analogique numérique. En effet, cette étape entraine nécessairement une perte de résolution et de rapidité ainsi qu'une complexité supplémentaire. Le facteur de qualité potentiellement important des MEMS est utile pour de tels capteurs car il entraine une meilleure stabilité fréquentielle, donc une résolution accrue.

b. Effet des dérives environnementales et mesure différentielle

Dans les deux applications (capteurs et base de temps) la technologie MEMS est limitée par sa sensibilité aux dérives environnementales, notamment la dérive en température. En effet, la raideur des résonateurs est systématiquement liée à la température, ce qui entraîne une modification de la fréquence propre. Plusieurs solutions ont été développées pour palier à cette dérive. L'une d'elle est de placer le résonateur dans une atmosphère dont la température est

contrôlée par un micro-four, grâce à un capteur de température. Outre le désavantage en termes de consommation et d'espace, cette solution est limitée par la précision du capteur de température. Pour les MEMS utilisés en tant que capteurs résonants, une autre solution est d'utiliser deux résonateurs identiques montés tel que le mesurande à un effet différent sur les deux (par exemple une accélération augmente la fréquence de l'un et diminue celle de l'autre), et tel que les dérives affectent identiquement les deux résonateurs. En concevant deux boucles oscillantes séparées, la différence des fréquences d'oscillation est théoriquement insensible aux dérives. Cette solution, outre sa redondance électronique (besoin de deux boucles oscillantes et d'un moyen de comparer des fréquences) est limitée par le fait que si les deux résonateurs sont placés proches l'un de l'autre, afin de rejeter correctement les dérives, ils sont nécessairement couplés par différents processus (couplage mécanique ou électrique à travers le substrat par exemple) ce qui peut donner lieu à un verrouillage en fréquence entre les deux résonateurs si leurs fréquences propres sont proches. Ce verrouillage annule le fonctionnement du dispositif, qui est basé sur la différence de fréquence.

c. Couplage actif ou passif de résonateurs

A l'inverse, ce couplage peut être renforcé soit passivement soit activement, comme schématiquement représenté *Figure 1*.

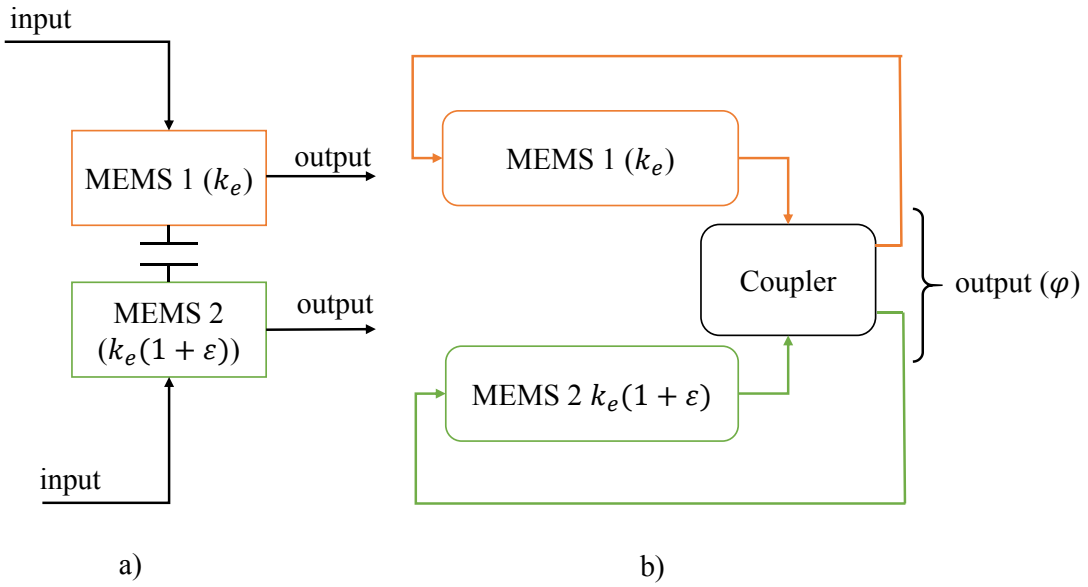

Figure 1 : couplage de résonateurs pour la mesure de différence de raideur mécanique : a) couplage passif, b) couplage actif.

Dans le cas passif, un élément mécanique ou électrostatique est placé entre les deux résonateurs, ce qui permet un transfert d'énergie entre les deux résonateurs et donne lieu à l'apparition de deux modes de résonance. Plusieurs grandeurs de sortie sont possibles, comme l'écart de fréquence entre les deux modes, ou le rapport de leurs amplitudes. Ces grandeurs sont hautement lié au rapport des raideurs (et des masses) des deux résonateurs, mais ne sont pas affectées si ce rapport reste inchangé. L'avantage de cette technique est que la sensibilité de la différence de fréquence des deux modes peut être augmentée par rapport à la lecture de fréquence (qui est la sortie d'un capteur résonant « classique »). Le coefficient d'augmentation est lié au rapport entre la force de couplage et la force de rappel des résonateurs qui peut être arbitrairement choisi lors de la conception, donc potentiellement très élevé, même si la limite haute est le facteur de qualité des résonateurs. Cela veut dire que la sensibilité du dispositif à

une variation de raideur, par exemple, est de l'ordre de Q fois plus importante que dans le cas d'un capteur résonant classique, tout en étant insensible aux variations affectant identiquement les deux résonateurs. L'inconvénient réside dans le caractère « boucle ouverte » du dispositif, c'est-à-dire qu'il faut effectuer un balayage en fréquence afin de localiser les deux modes, ce qui est potentiellement long. Certaines techniques en boucle fermée ont été suggérées, sans preuve expérimentale pour le moment.

Dans le cas du couplage actif, les deux résonateurs sont placés dans une seule boucle oscillante, à l'intérieur de laquelle leurs signaux d'excitation sont issus d'un mélange entre les deux signaux de sortie des résonateurs. Pour certaines conditions dans la composition du mélange, et si les fréquences propres des résonateurs sont suffisamment proches, les deux résonateurs se synchronisent et l'oscillation démarre. Ils oscillent à la même fréquence. La grandeur de sortie est la différence de phase entre les deux résonateurs : elle est liée au rapport entre les fréquences propres, mais ne varie pas si les deux fréquences propres varient simultanément. L'avantage de cette technique est son caractère intrinsèquement « boucle fermée » donc adaptée aux chaines de commandes numériques. L'augmentation de sensibilité entre la différence de phase et la fréquence est dans ce cas fixée par le mélangeur, et peut potentiellement dépasser le facteur de qualité des résonateurs. L'inconvénient est la réduction de la plage de verrouillage, qui est d'autant plus petite que la sensibilité est grande.

d. Cadre général de la thèse, présentation des objectifs et plan

Dans cette thèse, nous nous intéressons à la méthode de synchronisation car c'est un sujet très nouveau et ayant des applications potentielles en tant que capteur de grande précision, travaillant en conditions difficiles. Le couplage se faisant électroniquement, cette technique est également compatible avec l'intégration à grande échelle car elle demande un ajout de complexité assez réduit comparé aux autres techniques de mesure différentielle. La synchronisation de résonateurs a été extensivement étudiée dans le cadre de résonateurs LC pour la génération d'horloges multiphases, mais c'est la première fois qu'elle est étudiée dans le cadre de capteurs MEMS résonants. Cette thèse a été précédée par des travaux théoriques sur la synchronisation pour la mesure, effectués au sein du laboratoire, ainsi qu'une première preuve expérimentale effectuée avec une électronique discrète. L'objectif est de réaliser un démonstrateur entièrement co-intégré (c'est-à-dire que l'intégralité de ces composants sont fabriqués en une seule étape) afin de valider les prédictions théoriques et les simulations, ainsi que de prouver la faisabilité à grande échelle de ce genre d'architecture. La co-intégration du dispositif est également requise car la synchronisation ne s'effectue que si les résonateurs sont suffisamment identiques, et cette condition est aussi requise pour le rejet du mode commun. Or, étant donné la variabilité du processus de fabrication, ce besoin de similarité implique de fabriquer les deux résonateurs sur une seule puce, le plus proche possible. Si un désaccord subsiste, il peut être comblé en ajustant les fréquences propres grâce à leur tension de polarisation. Dans un premier temps, les résultats théoriques sont analysés afin d'en déduire un jeu de paramètres du mélangeur qui assure théoriquement un fonctionnement optimal du dispositif. Ensuite, la conception électronique de la puce est réalisée dans l'objectif de respecter ces paramètres. La technologie choisie est AMS 0.35 µm car elle est très bien maitrisée par l'équipe ECAS à l'UAB (Espagne) pour la fabrication de circuits CMOS-MEMS (c'est-à-dire co-intégrant sur une même puce les circuits électroniques et les MEMS), et que cette thèse est réalisée en collaboration avec ce groupe. Enfin, le circuit est fabriqué dans la fonderie AMS, puis caractérisée expérimentalement d'abord bloc par bloc en boucle ouverte afin de s'assurer

de la correspondance entre les simulations bas-niveau et les mesures, puis en boucle fermée afin d'en estimer les performances expérimentales, et leurs correspondances avec la théorie.

II- Modélisation de l'oscillateur et conception électronique

a. Mélangeur électronique numérique

La première partie de ce travail consiste à la simplification du cadre théorique complet de la synchronisation par injection mutuelle, en utilisant le phaseur plutôt que la résolution de systèmes d'équations gouvernant la dynamique des résonateurs. En effet, ces systèmes donnent des résultats relativement complexes à exploiter. Le mélangeur générique est composé de deux comparateurs, d'un étage d'adaptation de gain γ puis d'une opération + et d'une opération -, ainsi que de blocs de déphasage comme schématiquement représenté *Figure 2*.

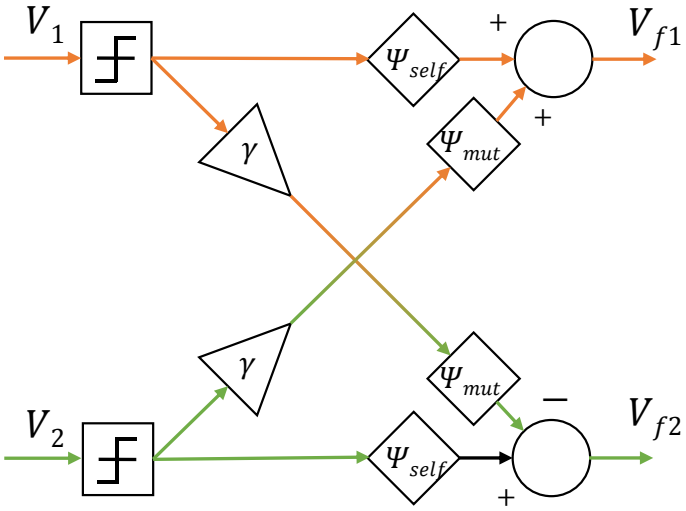

Figure 2 : Schéma haut niveau d'un mélangeur générique

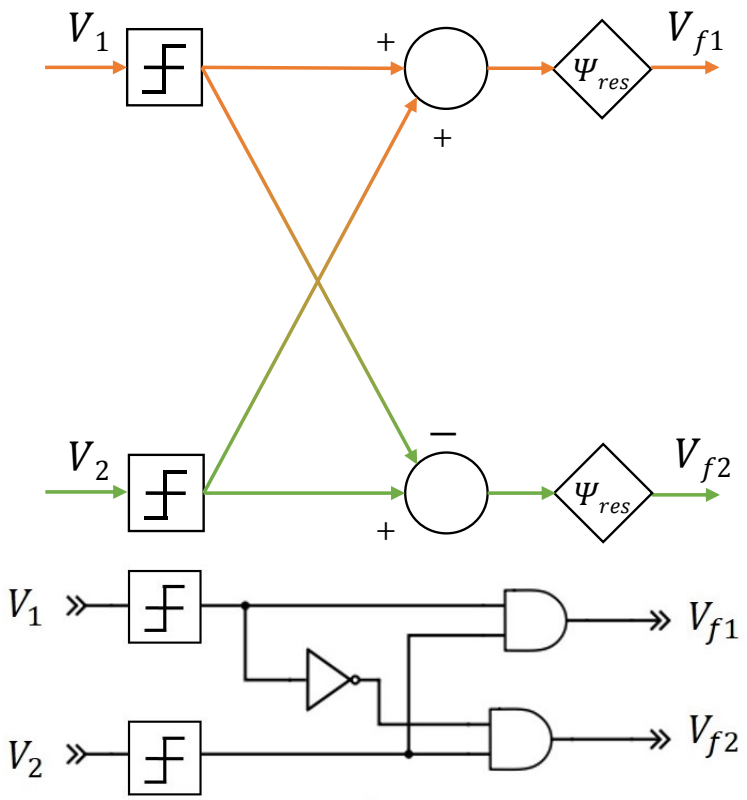

Figure 3 : Haut : Schéma haut niveau simplifié du mélangeur. Bas : proposition d'implémentation électronique numérique.

Plusieurs choix sont effectués à cette étape de la conception du dispositif. Dans le cadre du développement d'une solution intégrable à grande échelle, l'utilisation d'un mélangeur numérique (c'est-à-dire utilisant des portes logiques AND et NOT effectuant les opérations logiques « somme » et « différence », comme indiqué *Figure 3*) plutôt qu'analogique (avec des sommateurs et soustracteurs analogiques) est pertinent dans un souci de réduction de consommation et de complexité. Cependant, cela supprime un degré de liberté dans le mélangeur, qui était le rapport des amplitudes γ des signaux. En effet, en logique seuls les niveaux 0 et 1 (correspondant à 0 V et 3.3 V en AMS 0.35 µm) sont disponibles, sans modulation d'amplitude possible. Le degré de liberté restant est la phase dans les deux branches du mélangeur (un côté par résonateur). La notation en phaseur permet de dégager une équation liant le déphasage dans les résonateurs CMOS-MEMS (association du résonateur MEMS et d'un amplificateur CMOS permettant la génération de signaux « exploitables », d'amplitude supérieure à la centaine de mV) et le déphasage dans les branches du mélangeur afin d'assurer un fonctionnement optimal, soit en se plaçant le plus proche possible de la résonance des deux résonateurs. On peut alors considérer le mélangeur comme étant composé d'éléments parfaits réalisant les opérations + et -, et d'éléments de déphasage regroupant les délais de différents blocs, comme représenté *Figure 3*. L'équation donne un lien entre ces éléments de déphasage et le déphasage dans le résonateur CMOS-MEMS.

a. Résonateurs CMOS-MEMS

Le déphasage dans les résonateurs CMOS-MEMS est fixé par l'amplificateur. Dans ce travail, un amplificateur conçu en 2013 par le groupe ECAS est réutilisé, car il fournit

suffisamment de gain, et est déjà extensivement caractérisé en phase. A ce niveau, le déphasage que doit fournir le mélangeur, en plus de l'opération logique, est donc connu. Deux types de résonateurs sont fabriqués, tous deux basés sur la couche VIA 3 du processus de fabrication, donc en tungstène : des poutres encastré-libre de 10 µm de long (pour 1.3 µm d'épaisseur et 0.5 µm de large) ainsi que des ponts encastré-encastré de 30 µm de long (même épaisseur et largeur), voir *Figure 4*. Les résonateurs sont modélisés par des circuits RLC donc les valeurs sont obtenus par l'application des équations de la mécanique classique des poutres. Ces modèles seront injectés dans le simulateur de Cadence pour représenter les résonateurs MEMS. Ils sont valides tant que les résonateurs fonctionnent en régime linéaire. Les limites de linéarité sont obtenues en estimant et simulant les non-linéarités électrostatiques et de Duffing, puis en trouvant les valeurs de tension de polarisation et d'actionnement à partir desquelles ces non-linéarités ont suffisamment d'effet pour générer des phénomènes comme la conversion amplitude-fréquence.

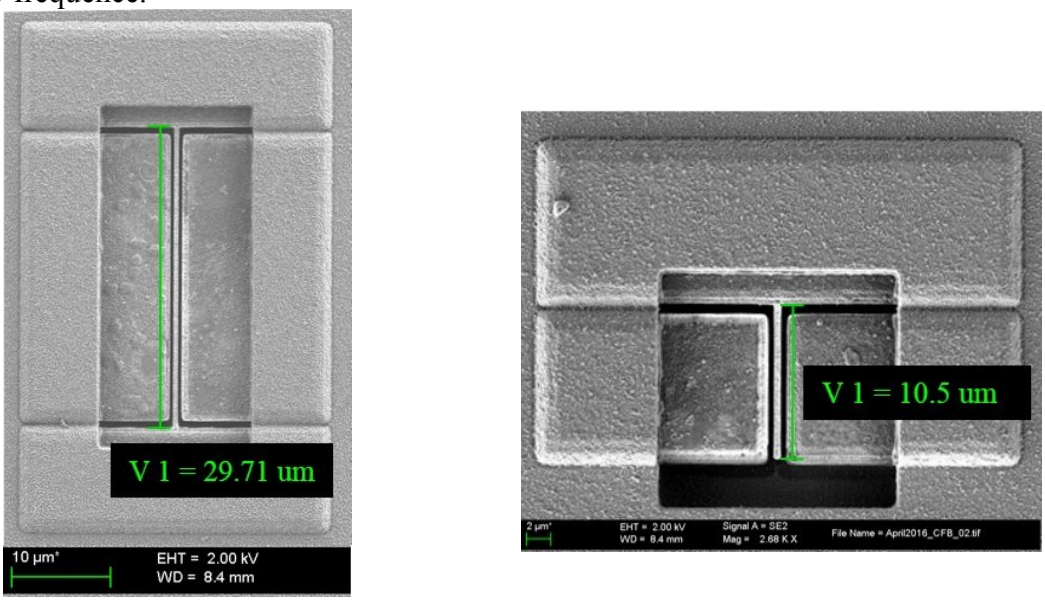

Figure 4 : Photographie SEM des résonateurs MEMS : gauche : pont encastré-encastré de 30 µm de long. Droite : poutre encastrée-libre de 10 µm de long

Plusieurs difficultés sont toutefois présentes. Tout d'abord, la sortie du mélangeur est une alternance de niveaux entre 0 V et 3.3 V ce qui est une amplitude trop importante pour rester dans la zone de linéarité des résonateurs. Il faut donc abaisser cette tension, et le choix a été fait de ne pas co-intégrer le réducteur de tension. Il en résulte un déphasage à priori difficile à estimer dans le pont diviseur de tension, car ce pont doit être connecté à la puce par des câbles coaxiaux, eux-mêmes représentants des capacités à charger donc des phases. Une certaine marge d'erreur lors de la conception est inévitable pour un premier essai. Enfin, Si la fréquence propre des poutres est bien connue à l'avance selon la théorie mécanique, celle des ponts dépend de la contrainte résiduelle issue du processus de fabrication, qui est inconnue à l'avance. Or la phase de l'amplificateur dépend de la fréquence, et les délais dans les portes logiques correspondent à des phases qui dépendent également de la fréquence. L'architecture peut donc être optimale pour une fréquence, mais ne le saura pas si la contrainte résiduelle éloigne trop la fréquence propre des ponts de la valeur « non-contrainte ».

b. Conception électronique de la puce et fabrication

Le choix a donc été fait d'optimiser l'architecture pour une fréquence de travail autour de 3 MHz, qui correspond à la fréquence propre théorique des poutres. Celle des ponts est, sans contrainte, de 2.6 MHz. Les éléments qui constituent le mélangeur sont issus des différentes bibliothèques disponibles (Analog CELLS pour les comparateurs, Corelib Digital pour les portes logiques). Un buffer numérique est également placé en sortie du mélangeur en prévision des capacités à charger pour connecter le pont diviseur à la puce. Enfin, une matrice de capacités de découplage est également placée sur la puce entre chaque bloc afin de limiter l'impact des transitions logiques sur la partie analogique (les amplificateurs). Une vue schématique du dispositif complet est donnée *Figure 5*. Le placement de chacun des blocs est fait de sorte que les liaisons les plus critiques soient les plus courtes, soit celles entre les MEMS et l'amplificateur respectif, puis l'amplificateur et le comparateur, car ce sont des liaisons analogiques donc susceptibles d'être perturbées. Ce choix impose une liaison assez longue entre les comparateurs et les portes logiques (1 mm). Afin de réduire la capacité parasite avec le substrat, la largeur de cette piste est réduite, ce qui la rend assez sensible à d'éventuelles surcharges de courant, ou usure de la piste par électro migration, même si le courant qui la traverse est théoriquement très faible. Les simulations bas-niveau sous Cadence prévoient qu'à 3 MHz, la condition trouvée plus haut est respectée.

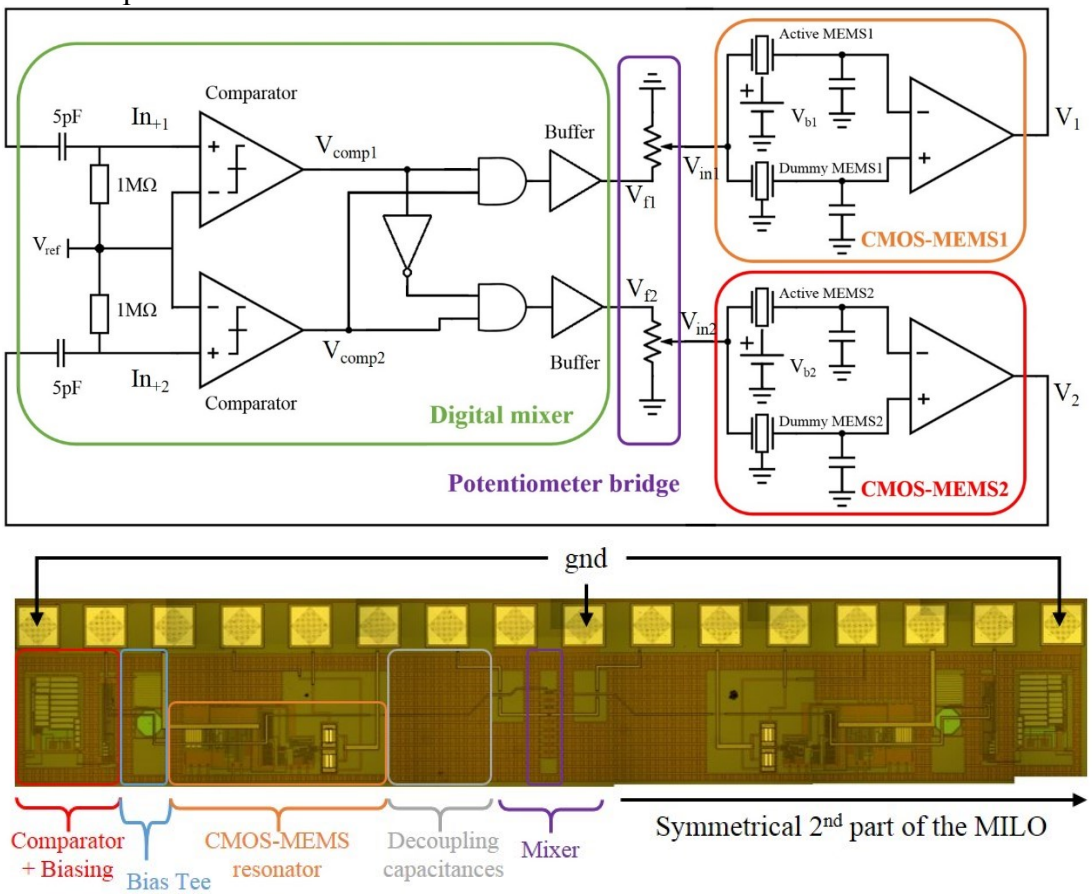

Figure 5 : Dispositif complet : haut : vue schématique ; bas : photographie microscopique

42 exemplaires de la puce sont fabriqués, chacun intégrant un dispositif ayant pour résonateurs des ponts et un dispositif des poutres. Les résonateurs sont libérés de l'oxyde de silicium par attaque humide à l'acide fluorhydrique dans la salle blanche de l'UAB selon un protocole expérimental établi. Certains sont caractérisés au microscope électronique à balayage

car le processus de fabrication n'est pas dédié aux MEMS, et les dimensions spécifiées ne sont pas garanties. Les puces libérées sont ensuite caractérisées grossièrement grâce à une station sous pointe et un connecteur fabriqué pour l'occasion, afin de vérifier la libération des résonateurs. Si l'un des résonateurs n'est pas bien libéré, ou que leurs fréquences propres sont trop éloignées, un second essai de libération est effectué, sinon la puce est placée sur une plaque en or et micro soudé au PCB. La puce est alors caractérisée plus soigneusement : les résonateurs sont d'abord caractérisés en boucle ouverte, puis le circuit complet (résonateurs et mélangeur) est étudié en boucle ouverte également afin de vérifier la correspondance entre les déphasages simulés et expérimentaux. Si l'équation assurant l'optimalité de l'architecture est vérifiée, le cadre théorique simple donnant les performances trouvé dans ce travail est suffisant, mais sinon une référence au cadre théorique complet est nécessaire. Enfin, la boucle est fermée, et les performances des circuits sont extraites.

III- Résultats expérimentaux

a. Caractérisation en boucle ouverte des résonateurs et du système complet

Lors de la libération des résonateurs, les poutres affichent une fréquence de résonance moyenne autour de 3 MHz, comme prévue par la théorie, mais les ponts sont en moyenne autour de 4 MHz, ce qui les place en dehors de l'optimalité de l'architecture. Cependant, c'est l'occasion de vérifier l'effet de la non-optimalité sur les performances du dispositif. Comme prévu, la co-intégration réduit l'écart entre les fréquences propres de deux résonateurs d'un facteur 3 en moyenne, dans notre cas. Ce facteur peut sans doute être augmenté en plaçant les résonateurs plus proches sur la puce. La caractérisation en boucle ouverte des résonateurs puis de la puce entière permet de vérifier la validité des simulations en bas niveau, et d'obtenir les valeurs expérimentales des phases dans l'amplificateur et dans le mélangeur. Les valeurs expérimentales des phases sont en accord avec les simulations pour les deux fréquences de travail (3 MHz et 4 MHz), dont un exemple est donné *Figure 6*.

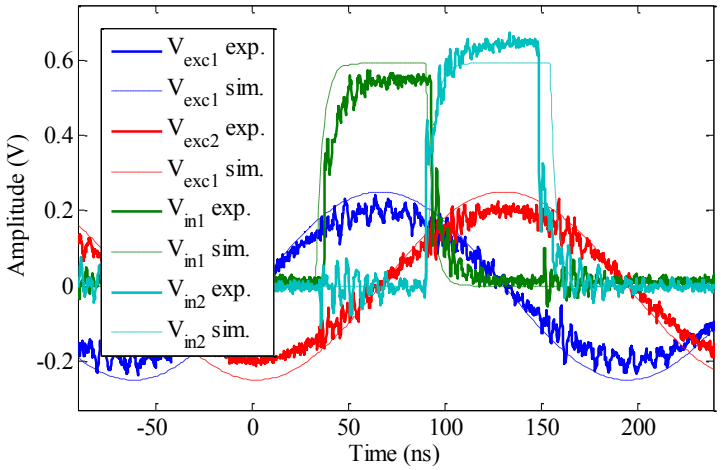

Figure 6 : Simulation et mesures d'une caractérisation en boucle ouverte du système entier : en rouge et bleu les signaux d'excitation des résonateurs MEMS (ici des ponts ajustés pour résonner à 3.884 MHz), et en vert et cyan les signaux de sortie du mélangeur.

b. Caractérisation en boucle fermée : sensibilité au mode différentielle et rejet du mode commun

Enfin, la boucle est fermée et les dispositifs sont caractérisés. D'abord, la sensibilité de la différence de phase à un désaccord de fréquence propre est analysée. Ce désaccord est obtenu

en modifiant légèrement la tension de polarisation d'un des résonateurs autour de la valeur pour laquelle l'architecture est équilibrée (c'est-à-dire les fréquences propres des deux résonateurs sont égales). Durant cette expérience, la fréquence de l'oscillateur et la différence de phase sont enregistrées. Les résultats sont en accord avec la théorie : pour les poutres, la relation entre désaccord de fréquence et phase est linéaire, et le coefficient directeur est le même que celui prévu par la théorie. Sa valeur dépend du facteur de qualité des résonateurs. Dans le cas des ponts, la courbe est légèrement saturée, ce qui est prévu par la théorie complète (voir *Figure 7*. Ceci est du déphasage supplémentaire dans le mélangeur, qui place un des résonateurs loin de sa résonance, donc à l'endroit où la relation entre phase et fréquence est très non-linéaire. Il est intéressant de noter que malgré un déphasage loin de l'optimal (40 % d'écart), la sensibilité n'est dégradé que de 8 %, ce qui montre la robustesse de l'architecture aux aléas du processus de fabrication. La plage de verrouillage expérimentale est légèrement inférieure à celle prévue.

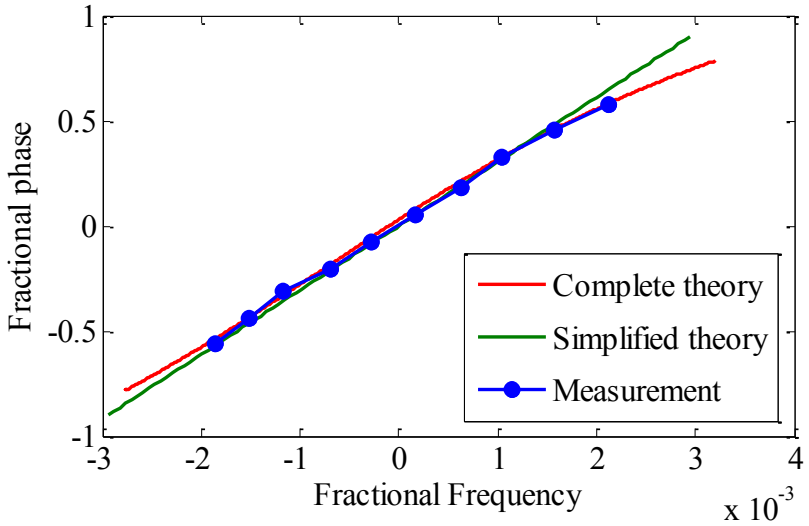

Figure 7 : phase réduite selon la fréquence réduite pour un balayage de tension de polarisation d'un dispositif avec des ponts à 4 MHz, montrant le très bon accord avec la théorie complète, et un léger désaccord avec la théorie simplifiée.

Le rejet de la dérive thermique est obtenu par chauffage de la puce sur une plaque chauffante, entre 30 °C et 100 °C. Durant le chauffage, qui est effectué par paliers de 10 °C, la fréquence d'oscillation et la différence de phase sont enregistrés (voir *Figure 8*. A chaque palier, un balayage de la plage de verrouillage est également effectué afin de vérifier que la qualité du dispositif en tant que capteur différentielle n'est pas affectée par la température. Il résulte de ces expériences qu'une légère dérive de la différence de phase avec la température est systématiquement observée.

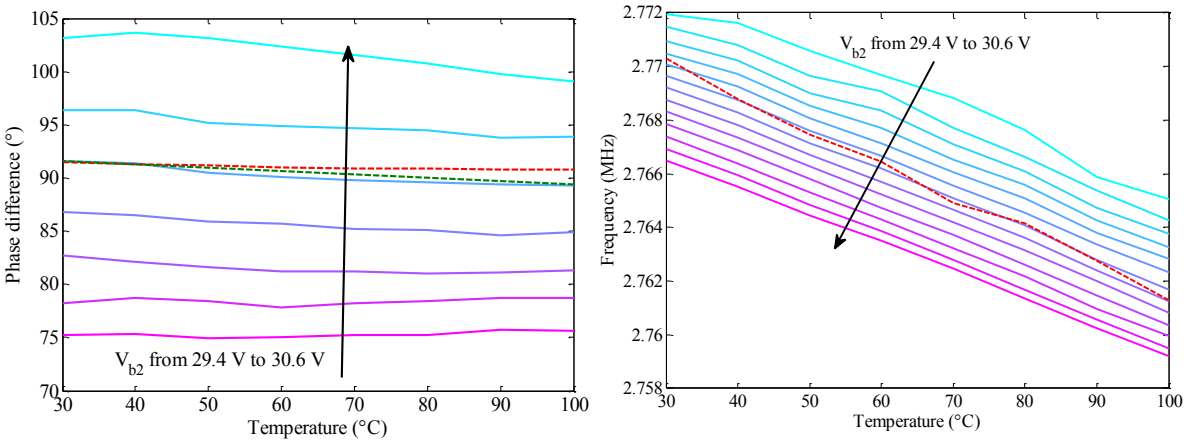

Figure 8 : Différence de phase et variation de fréquence en fonction de la température, montrant le rejet du mode commun

Cet effet est bien expliqué par le fait que, lorsqu'on accorde manuellement la fréquence de résonance des deux résonateurs à travers leur tension de polarisation, c'est afin de palier un désaccord de raideur mécanique. Or, lorsque la température augmente, la variation de leur fréquence propre n'est pas la même, puisque leur raideur mécanique n'est pas identique. Cet effet est inhérent à la variabilité du processus de fabrication. On pourra essayer plus tard de le réduire en fabricant les résonateurs encore plus proche. Cependant, on peut noter que dans le cas d'une application de capteur, si l'on compare l'effet de la dérive thermique sur la fréquence d'oscillation (capteur classique) et sur la différence de phase (capteur différentiel), le rejet de la dérive est de l'ordre de 200 malgré tout.

Finalement, pour déterminer la résolution du capteur, le bruit sur la fréquence et sur la différence de phase sont mesurés. Il ressort de cette caractérisation que le bruit sur la différence de phase est très largement plus important que le bruit sur la fréquence d'oscillation. En fait, le rapport entre les deux est égal au gain de sensibilité entre la fréquence et la phase, trouvé plus haut. Cela veut dire que les sources de bruits qui dominent ne sont pas corrélées entre les deux résonateurs, puisqu'elles ne sont pas filtrées par l'architecture différentielle. Nous avons également observé que le rapport signal à bruit diminuait lorsque les tensions d'actionnement ou de polarisation augmentait, ce qui aurait tendance à indiquer un bruit additif plutôt que paramétrique. Ce bruit n'est pas lié aux fluctuations de tension de polarisation car exactement les mêmes figures sont obtenues si l'on polarise les deux résonateurs grâce au même générateur de tension. A ce stade, l'hypothèse qui domine est la transformation de fluctuation d'amplitude en fluctuation de fréquence et de phase à cause de l'hystérésis de 17 mV dans les comparateurs. Ces figures montrent que dans l'état actuel, l'augmentation de sensibilité de l'architecture n'entraîne pas d'augmentation de résolution du capteur, parce que les fluctuations internes génèrent un bruit beaucoup plus important sur la différence de phase que sur la fréquence, ce qui limite la quantité minimale détectable grâce à la mesure de différence de phase.

IV- Conclusion et perspectives

En conclusion, ce travail a prouvé la faisabilité de la technique de synchronisation dans l'objectif du rejet de la dérive thermique. Un travail complet a été mené, depuis la modélisation mathématique jusqu'à la réalisation d'un démonstrateur et sa caractérisation expérimentale. La puce se comporte comme prévu, grâce au soin qui a été mis dans sa conception, afin d'en optimiser les performances. Plusieurs pistes peuvent être explorées dans la continuité de ce travail. D'abord, penser différemment le placement des blocs afin de pouvoir rapprocher les

deux résonateurs, et ainsi essayer d'augmenter encore leur similarité géométrique. Ensuite, co-intégrer le diviseur de tension, afin de maîtriser plus proprement les déphasages, éventuellement se passer du buffer qui engendre une consommation de courant par pics, qui ont tendance à perturber le fonctionnement du système. On peut également penser à concevoir une seconde boucle de rétroaction qui contrôle la tension de polarisation d'un des résonateurs afin d'assurer l'équilibre permanent de l'oscillateur, même lors de l'application du mesurande. Cela permet d'augmenter la plage de verrouillage dans les limites physiques des résonateurs (le régime linéaire pour les hautes tensions de polarisation, et une amplitude suffisante pour déclencher les comparateurs pour les basses tensions de polarisation). Cependant, la grandeur de sortie du système devient alors la tension de polarisation, puisque le déphasage est théoriquement fixé, et la relation entre tension de polarisation et fréquence naturelle est non-linéaire, ce qui est une difficulté dans l'exploitation du dispositif dans une chaîne de commande. Une autre idée est de modifier légèrement l'amplificateur en y ajoutant un étage supplémentaire à faible gain (3 dB par exemple), afin de pouvoir abaisser légèrement les tensions d'actionnement, donc la saturation de l'amplificateur, sans perte d'amplitude. Enfin, une dernière piste est l'implémentation d'un capteur « réel », par exemple un accéléromètre résonant, basé sur la technique de résonateurs synchronisés.

Notations

L	Beam's length
h	Beam's width
b	Beam's thickness
G_0	Actuation and detection gap
a	position of beam's midpoint for a CCB, of beam's extremity for a CFB, normalized with respect to G_0
$\dot{a}$	First temporal derivative of a
$\ddot{a}$	Second temporal derivative of a
ε_0	Vacuum permittivity
ρ	Tungsten's density
E	Tungsten's Young Modulus
k_e	Resonator's effective stiffness considering the first resonating mode
m_e	Resonator's effective mass considering the first resonating mode
ω_{σ_s,V_b}	Resonator's resonance pulsation considering a stress σ_s and a bias voltage V_b
Q	Quality factor of the resonator
γ_D	Cubic non-linearity coefficient (Duffing coefficient)
σ_s	Residual stress inside the beam
σ_{crit}	Critical value of the residual stress
η	Electromechanical coefficient
V_{bi}	i^{th} resonator's bias voltage
V_{ini}	i^{th} resonator's actuation voltage
V_i	Readout's output voltage of the ith resonator
V_{out}	Output electrode's bias voltage coming from the readout auto bias voltage
C_{in}	Input capacitance between the actuation electrode and the beam
C_{out}	Output capacitance between the beam and the sense electrode
$C_{electrode}$	Parasitic capacitance between the substrate and the sense electrode
C_{amp}	Readout input transistor parasitic capacitance

C_{probe}	Parasitic capacitance of an oscillator's probe
$N(a)$	Dependence of the electrostatic forces on the deflection of the resonator
$\Gamma(a)$	Dependence of the input and output capacitances on the deflection of the resonator
λ	Air's mean free path at atmospheric pressure
μ	Air's viscosity
i_{deti}	Output current at the sense electrode of the ith resonator
i_{mot}	Motional contribution of the output current
i_{mot}	Parasitic contribution of the output current
R_m	Motional resistance
L_m	Motional inductance
C_m	Motional capacitance
TCE	Thermal coefficient of the Young Modulus
TCd	Thermal coefficient of the dimension d
$TC\sigma_s$	Thermal coefficient of the residual stress
k_1 & k_2	Geometry-dependent coefficients
ε	Normalized stiffness mismatch between two resonators
X	Normalized movement of resonator 1 in the mode localization theory
Y	Normalized movement of resonator 2 in the mode localization theory
κ	Coupling restoring force coefficient in the mode localization theory
u_i	Eigenvector of the ith mode in the mode localization theory
φ	Phase difference between two synchronized resonators
m	Coupling factor in the mutual injection theory
θ_{res}	Readout phase at the resonator's resonance
K	Readout transimpedance gain at the resonator's resonance
V_f	Coupler's output voltage
K'	Voltage divider ratio
Ψ_{self}	Phase of the self contribution on the actuation voltage
Ψ_{mut}	Phase of the mutual contribution on the actuation voltage
γ	Cross-coupling gain
ε_{lock}	Locking range in term of normalized stiffness mismatch

Ψ_{res}	Phase of the coupler at the resonator's resonance
S_{φ}	Sensitivity of the phase difference to ε
S_{ω}	Sensitivity of the pulsation difference to ε
S_{MILO}	Ratio between the phase sensitivity and the pulsation sensitivity to ε
DC_i	Coupler's ith output's duty cycle
C_{CP}	Parasitic capacitance of the connection between the coupler and the potentiometer
C_{PM}	Parasitic capacitance of the connection between the potentiometer and the MEMS
R_S and R_G	Potentiometer's bridge resistances
V_{dd}	Supply voltage
V_{comp}	Comparator's output voltage
In_{+}	Comparator's input voltage
V_{exc}	Resonator's input voltage
T	Temperature
$\Delta f(\varepsilon)$	MILO's oscillation frequency variation induced by ε
S_{ϕ}	Power Spectral Density of the relative phase difference
S_f	Power Spectral Density of the relative frequency

List of tables

Table 1.1 Typical dimensions and materials available in AMS C35b4c3 technology. 37
Table 1.2 Dimensions for the considered geometries. 46
Table 1.3: Effective mass and stiffness of the first resonant mode of the resonating structures for the first vibrating mode, calculated for the considered structures presented in paragraph 1.2.5 50
Table 1.4: Geometry-dependent functions N and Γ for the considered geometries. 51
Table 1.5: Resonance frequency for the CCB and CFB for 20 V of bias voltage. 52
Table 1.6: Values of Vb to put the resonators to instability for the two considered geometries. 53
Table 1.7: Young's modulus and experimental residual stress of various materials used for MEMS resonators. Note that in this work, it is derived from the modelling. 54
Table 1.8: Values of the electrical equivalent components of the Butterworth-Van Dyke model of cantilever beam and bridge resonator given its dimension and material properties. 57
Table 1.9: Numerical applications for our geometries, for $Q = 100$, $\sigma s = 475\ MPa$ and $Vb = 20\ V$ 57
Table 1.10 Values of constants $k1$ and $k2$ for our geometries. 64
Table 1.11: Values of the temperature coefficients found in the literature. 64
Table 1.12: Theoretical thermal drift only taking into account the Young's modulus shift and the thermal expansion, and experimental results of the thermal drift. 65
Table 1.13: Advantages and drawbacks of three techniques for drift-free resonant sensing 77
Table 2.1: Electrode's parasitic capacitance, transimpedance gain and phase of the amplifier at the resonance frequency of the MEMS. 90
Table 2.2: Measured duty cycle from the three cases of Figure 2.13 and calculated φ according to (35). 94
Table 2.3: Size of the transistors from the digital buffer. 98
Table 2.4: Simulated delays and current spikes at each coupler's transition, and extracted added phase by the association mixer + buffer for various capacitive loads. 99
Table 2.5: Capacitances to load and theoretical phase delay added by the potentiometer's bridge connection for the two set-ups. 102
Table 2.6: Phase delays in the different blocks for the complete extracted model of the chip. 106
Table 2.7: Phase delays in the blocks for two temperatures extracted from transient simulations of the device at 3 MHz. 108
Table 2.8: Phase delays in the blocks for two temperatures extracted from transient simulations of the device at 3.9 MHz. 108
Table 3.1: Measured θres for the two geometries, with the estimated contribution of the experimental set-up, an extrapolation of the actual θres, and the evaluation of θres with the simulated phase of the amplifier alone made in Table 2.1. 121
Table 3.2: Summarized measured phase delays across the loop and comparison with the optimal value according to Equation (29). 124
Table 3.3: Matching improvement in term of resonance frequency due to co-integration 126
Table 3.4: Calculated phase difference φ based on duty cycles measurements for different levels of amplitudes of the outputs of the amplifiers. 134
Table 3.5: Extracted dependence of the frequency and phase difference with the temperature for the CFB MILO (sample 1) for various values of $\Delta Vb2$. 150
Table 3.6: Effect of the temperature on the measurement of $\Delta Vb2$ with a CFB MILO if the output signal is the f or φ, and ratio between these two. 150
Table 3.7: Extracted dependence of the frequency and phase difference with the temperature for the CCB MILO (sample 16) for various values of $\Delta Vb2$. 153
Table 3.8: Effect of the temperature on the measurement of $\Delta Vb2$ with a CCB MILO if the output signal is the f or φ, and ratio between these two. 153

Table 3.9: Table characterizing a CFB MILO-based electrometer. 163
Table 3.10: Table characterizing a CCB MILO-based electrometer. 163

List of figures

Figure 1.1: Cross section of a resonant pressure sensor [39]: one of the anchor of the resonator is placed over the membrane which deflects under pressure. The deflection modifies the stress in the beam, shifting its resonance frequency. 33
Figure 1.2: Resonant strain sensor [40]: a) schematic of the operating principle and b) SEM of the device. 33
Figure 1.3: Motorola MMAA1220D z-axis accelerometer [41]: a) schematic of the operating principle and b) SEM of the device. 34
Figure 1.4 Cross section of all layers available in the AMS C35b4c3. 37
Figure 1.5 AMS 0.35 inter-metal layers deposition process for the different geometries. 38
Figure 1.6: SEM image of a VIA3 beam close to a MET3-VIA3-MET4 [62] showing the different layers and the fact that a VIA3 beam alone is thicker than when it connects two metal layers. 38
Figure 1.7 SEM image of a MET3-VIA3-MET4 stack, showing the different layers including the TiN. 39
Figure 1.8 Cross section of a tungsten beam between two electrodes illustrating the effect of the isotropic wet etching: the electrodes can fall off. 40
Figure 1.9 SEM image of two under-etched electrodes (MET-VIA-MET stack). The beam is not in the section of the FIB cut. 41
Figure 1.10 a) Layout of a resonant accelerometer: VIA3 Stack MET3-MET4 b) zoom with the layout dimensions. 42
Figure 1.11 SEM image of the structure whose layout is presented in Figure 1.10. The spring of 500nm width and 1.5µm gap is well fabricated, but the resonator with 350nm is not. The seismic mass which is only made of VIA without any metal has only been fabricated on its edges. 43
Figure 1.12: a) layout of a 30µm*0.5µm clamped-clamped VIA3 beam (CCB) b) SEM image of this structure. 44
Figure 1.13: a) layout of a 10µm*0.5µm clamped-free VIA3 beam (CFB) b) SEM image of this structure. 45
Figure 1.14 SEM image of a clamped-clamped beam close to the anchor, with a designed 450nm gap. 45
Figure 1.15 SEM image of a clamped-free beam away from the anchor, with a designed 450nm gap. 46
Figure 1.16 Schematic of the capacitive CFB with the different geometrical and electrical notations used in this work. 46
Figure 1.17: Electrostatic CFB in the three-port configuration. 48
Figure 1.18: In-plane motion of the CFB 48
Figure 1.19: Resonance frequencies of the CCB for $Vb = 20V$. Each dot represents a CCB, and 2 active CCB are fabricated on each sample. 54
Figure 1.20: Resonance frequency of every CFB for $Vb = 20V$. Each dot represents a CCB, and 2 active CFB are fabricated on each sample. 55
Figure 1.21 Butterwort-Van Dyke model of the capacitive MEMS resonator. 56
Figure 1.22: Simulated Bode diagram (input: Vin, output: $imot$) of the CCB at $Q = 100$, $\sigma s = 475\ MPa$ for Vbvarying from 20V to 30V. 58
Figure 1.23: Simulated Bode diagram (input: Vin, output: $imot$) of the CFB at $Q = 100$ for Vbvarying from 20V to 30V. 59
Figure 1.24: Measured electrostatic softening effect on a CFB, with simulated predictions. 59
Figure 1.25: Measured electrostatic softening effect on a CCB, with simulated predictions. 60
Figure 1.26: Simulated Bode diagram (input: Vin, output: $idet$) of the CFB at $Vb = 20V$ and $Q = 100$ for Cft varying from 0 to 0.5fF. 60

Figure 1.27: Fully nonlinear model of the CCB for different actuation voltage, at $Vb = 20\ V$, $Q = 100$ (scale in Volt). 61
Figure 1.28: Fully nonlinear model of the CFB for different actuation voltage, at $Vb = 20\ V, Q = 100$ (scale in Volt). 62
Figure 1.29: Experimental temperature dependence of the resonance frequency of one CCB. 63
Figure 1.30 Experimental temperature dependence of the resonance frequency of one CFB. 63
Figure 1.31 Structure of a MEMS oscillator based on a control feedback. 66
Figure 1.32 Frequency-temperature characteristics for a variety of common quartz resonator cuts [95] 67
Figure 1.33 Block diagram of temperature compensation system using two MEMS resonators with different temperature dependence [101]. 69
Figure 1.34 Dual MEMS temperature compensation by post-processing scheme [104]. 70
Figure 1.35: Concept of the differential resonant accelerometer of Trusov [105]. Red and orange arrows show axes of sensitivity to external acceleration and temperature (i.e. the resonators have the same temperature dependence but opposite acceleration dependence). 71
Figure 1.36 Experimental results of Trusov [105]: Differential frequency split is invariant to temperature 71
Figure 1.37 (a): mechanical coupling two resonators through an overhang [110]. (b): coupling three resonators by placing them very close one to the other [112]. 72
Figure 1.38 Lumped model of two coupled MEMS resonators (without the dampers). Ke is the mechanical stiffness of the resonators, κ is the constant corresponding to the coupling restoring force and ε a mechanical stiffness change corresponding to the measurand. 73
Figure 1.39 Simulated amplitude responses for varying pulsation, when $Q = 1000, \kappa = 5.10 - 3,\ \varepsilon = 0$ (full curves) or $\varepsilon = 10 - 3$ (dotted curves) [116]. 74
Figure 1.40 a): block diagram of two passively coupled MEMS resonators (mode localization technique) for the sensing of a mechanical stiffness mismatch ε. b): block diagram of two actively coupled MEMS resonators through their actuation for the sensing of a stiffness mismatch ε. 75
Figure 2.1: High-level schematic of our proposition for the synchronization of two resonators by injection-locking. 80
Figure 2.2: Low-level schematic of the architecture of a generic coupler. 81
Figure 2.3: Low-level schematic of the coupler implemented in this work 84
Figure 2.4: Schematic of the MILO. Only the potentiometer bridge is not co-integrated. 85
Figure 2.5: Capacitive current sensing scheme. 86
Figure 2.6: Transistor-level circuit scheme of the differential sustaining circuit based on a cascode voltage amplifier [131]. 87
Figure 2.7: block-level schematic of the feedthrough compensation scheme 88
Figure 2.8: Entire amplifier: up) microphotograph, down) layout 89
Figure 2.9: Transimpedance gain of the amplifier: extracted simulation + added $Celectrode$ capacitance corresponding to the resonator's geometry for the two cases. 90
Figure 2.10: Phase of the amplifier: extracted simulation, which is not affected by $Celectrode$. 90
Figure 2.11: High-level Simulink simulation. Top: mixer's inputs $V1$ and $V2$. Middle: output voltages of the digital mixer of Figure 2.12 with $\Psi res = 0$. Down: output voltages of the analog mixer of Figure 2.3 with $\Psi res = 0$. 92
Figure 2.12: Two possible implementations for the QUADDRO coupler phase and gain conditions: a) is implemented in [128] and [130], while b) is studied in [133] and implemented in this work. 92
Figure 2.13: High-level Simulink simulation of $V1$ (blue), $V2$ (green), $Vf1$ (red) and $Vf2$ (teal). Top: $\varphi = 60\ °$; middle: $\varphi = 90\ °$; bottom: $\varphi = 120\ °$. 94
Figure 2.14: Transistor-level schematic of the A_CELLS comparator. 95
Figure 2.15: Transient schematic simulation to illustration the hysteresis and the input biasing requirement: a) 0V bias, b) 1V bias. 96

Figure 2.16: Schematic of the bias tee routing. 96
Figure 2.17: Transient schematic simulation of the A_CELLS comparator for various capacitive loads at 3 MHz: a) positive threshold, b) negative threshold (2ns added delay corresponding to the 17mV hysteresis). 97
Figure 2.18: Transient schematic simulation of the complete coupler at 3MHz: a) for various loads, b) current consumption at the transitions for a load of 20pF. 98
Figure 2.19: Design and routing of the decoupling capacitance. 100
Figure 2.20: Two experimental set-ups. 101
Figure 2.21: Connection of the potentiometer's bridge. 101
Figure 2.22: Transient closed-loop simulation of the MILO at 3.9 MHz for the two set-ups, taking into account the RLC equivalent of the wire which supplies V_{dd} (10 nH, 80 pF, 0.3 Ω) 102
Figure 2.23: Microscopic image of a co-integrated CMOS-CCB MILO (dimensions: 2.4 mm × 375 µm). 105
Figure 2.24: Open loop transient simulation of the entire chip. The amplitudes are reduced for better readability. Top: CCB (3.9 MHz). Bottom: CFB (3 MHz) 106
Figure 2.25: Extracted simulation of the phase of the amplifier for different temperatures. 108
Figure 3.1: Microscopic images of the two CMOS-MEMS resonators: a) CFB b) CCB. 112
Figure 3.2: Experimental set-up for the CMOS-MEMS resonators characterization: entire set-up (left), and zoom on the Wedge7 probe card (right). 112
Figure 3.3: Experimental set-up for the extraction of CMOS-MEMS frequency responses. 113
Figure 3.4: Experimental frequency responses of the CMOS-CFB 1 and 2 for $Vb1 = 40\ V$ and $Vb2 = 40\ V$ (both are excited simultaneously, excitation level: -20 dBm = 63 mVrms). 113
Figure 3.5: Experimental frequency responses of the CMOS-CFB 1 and 2 for $Vb1 = 20\ V$ and $Vb2 = 0\ V$ (both are excited simultaneously, excitation level: -20 dBm = 63 mVrms). 114
Figure 3.6: Schematic of the wedge probe card experimental set-up. Illustration of the capacitive coupling between the lines. The black arrows represent the probes. 116
Figure 3.7: Experimental test-bench for the measurement of the coupling capacitances between the lines of the wedge probe card and the connector. 116
Figure 3.8: Measured coupling capacitance between line 1 and lines from 2 to 9 of the wedge probe card and the connector. 116
Figure 3.9: Simulated frequency responses of the extracted model of the amplifier + BVD model of the CCB ($Vb1 = 11\ V, Vb2 = 30\ V$) + coupling capacitances between the lines. 117
Figure 3.10: Experimental open-loop oscillogram extracted with the wedge probe card set-up: chip 2, $Vb1 = 30\ V$, $Vb2 = 48\ V$, $Vexc = 200\ mVrms$ @ 3.05 MHz. 118
Figure 3.11: a) image of the chip wire-bonded on a PCB, b) details on the aluminum wire bondings. 119
Figure 3.12: Experimental frequency response (full lines) and model (dashed lines, dimensions L=29.6 µm, b=1.3 µm, h=0.5 µm, G_0 :370 nm, Q=120) of a CCB for Vb from 15 V to 25 V in 2 V steps, input power of -20 dBm. 120
Figure 3.13: Experimental frequency response (full lines) and model (dashed lines, dimensions L=10.57 µm, b=1.3 µm, h=0.45 µm, G_0 :330 nm, Q=100) of a CFB for $Vb = 30\ V$, input power of -20 dBm. 121
Figure 3.14: Experimental frequency response of a wire-bonded CFB MILO where the CMOS-CFB 1 and 2 are simultaneously excited at -20 dBm, with $Vb1 = 20\ V$ and $Vb2 = 0\ V$. 122
Figure 3.15: open loop waveform of a CFB (chip 12) with the following adjustment: $Vb1 = 28\ V$, $Vb2 = 30\ V$, excitation voltage: 170 mVrms, 3.0059 MHz, and comparison with the transient extracted simulations 123
Figure 3.16: open loop waveform of a CCB (chip 17) with the following adjustment: $Vb1 = 28\ V$, $Vb2 = 29.2\ V$, excitation voltage: 200 mVrms, 3.854 MHz, and comparison with the transient extracted simulations 124

Figure 3.17: Resonance frequency at $Vb = 20\,V$ of the different resonators released in this work. 126
Figure 3.18: Quality factor in air of the different CMOS-MEMS resonators released in this work. 128
Figure 3.19: CFB MILO: sample 12, $Vb1 = 30\,V$, $Vb2 = 28\,V$ CMOS-MEMS frequency response and closed-loop waveforms (simulated and measured)..... 131
Figure 3.20: CCB MILO: sample 16, $Vb1 = 20\,V$, $Vb2 = 22.3\,V$: CMOS-MEMS frequency response and closed-loop waveforms (simulated and measured)..... 132
Figure 3.21: Closed loop experimental oscillogram of CFB MILO (sample 12, $Vb1 = 30\,V$, $Vb2 = 28\,V$) obtained with setup a) and setup b)..... 132
Figure 3.22: Transient simulation of a CCB MILO with two different input amplitudes. The dashed blue waveform is not saturated, showing the true zero crossing, while the purple full waveform is highly saturated, showing a 5 ns shift from the true zero crossing, leading to a reduction of the duty cycle. 133
Figure 3.23: Experimental oscillograms of a CCB MILO (sample 16) for different biasing voltages. $Vb1$ and $Vb2$ are respectively: a) 20 V and 22.3 V; b) 25 V and 25.3 V; c) 30 V and 32.3 V; d) 35 and 37.3 V. 134
Figure 3.24: Simulink high-level simulation of the coupler, illustrating a potential drawback of the hysteresis. 135
Figure 3.25: Differential resonant sensing scheme of the MILO. 137
Figure 3.26: Measured oscillation frequency (Top) and duty cycles (Bottom) for different values of $\Delta Vb2$. 139
Figure 3.27: a) calculated φ VS calculated ε; b) measured f VS calculated ε. 140
Figure 3.28: Fractional phase VS fractional frequency for the CFB MILO, measurement and theoretical predictions. 140
Figure 3.29: Measured oscillation frequency of the CCB MILO for different values of $\Delta Vb2$..... 141
Figure 3.30: Measured duty cycles of $Vin1$ and $Vin2$ for different values of $\Delta Vb2$. 142
Figure 3.31: a) Measured φ VS measured ε; b) measured f VS calculated ε. 142
Figure 3.32: Fractional phase VS fractional frequency: measurements, simplified theory from Equation (34) and complete theory from [129], with the extracted linear slopes. 144
Figure 3.33: Measurements, predictions from the simplified theory and the complete theory: a) Phase difference vs. epsilon; b) Frequency vs. epsilon, each time..... 144
Figure 3.34: Measurements and predictions of the fractional phase vs. fractional frequency. 145
Figure 3.35: Simulated fractional phase vs. fractional frequency according to [129] for a balanced architecture (blue line) and two imbalanced architectures (red and green lines). 146
Figure 3.36: Experimental set-up for the drift rejection measurements. 147
Figure 3.37: Experimental spectra of the CMOS-CFB resonators (sample 1) with $Vb1 = 23\,V$, $Vb2 = 30\,V$. 147
Figure 3.38: Experimental oscillation frequency of the CFB MILO of sample 1 for various temperature and $Vb2$. In red dotted lines, Cadence transient simulations, both setups (different BVD and same BVD) shows same results. 149
Figure 3.39: Experimental phase difference for the CFB MILO of sample 1 for various temperature and $Vb2$. In red dotted lines, Cadence transient simulations for two similar BVD models which change equally with the temperature. In green dotted line, Cadence transient simulations for two different BVD models. 149
Figure 3.40: Full lines: experimental oscillation frequency of the CCB MILO of sample 16, for various temperature and $Vb2$. Red dotted line: simulated phase difference (both simulations show the same frequency variation) 152
Figure 3.41: Full lines: experimental phase difference for the CCB MILO of sample 16, for various temperature and $Vb2$. Red dotted line: simulated phase difference with same BVD models. Green dotted line: simulated phase difference with different BVD models. 152

Figure 3.42: Extracted periods and duty cycles for 150000 periods of the CCB MILO of sample 18. 155
Figure 3.43: Frequency noise Sf and phase difference noise $S\phi$ measured using the Periodogram (single acquisition) or DPOJET (averaged on 5 acquisitions) algorithm, and theoretical floor noise. 156
Figure 3.44: Sf, $S\phi$ and calculated $S\phi/SMILO$. 157
Figure 3.45: Phase difference PSD for $Vb1 = Vb2 = 44.6\ V$, using one or two voltage generators for the bias voltages. 158
Figure 3.46: $S\phi$ (a) and Sf (b) measured with the DPOJET algorithm for several bias voltage pairs, for $Vin = 500\ mV$ 159
Figure 3.47: $S\phi$ (a) and Sf (b) measured with the DPOJET algorithm for $Vb1 = 28\ V$, $Vb2 = 28.6\ V$, and two values of Vin. 159
Figure 3.48: Allan deviation of the period and duty cycles. 160
Figure 3.49: Sf, $S\phi$, calculated $S\phi/SMILO$, and calculated floor noise according to Equation (51) for the CFB MILO (sample 12). 161
Figure 3.50: Allan deviation of the period and duty cycles for the CFB MILO (sample 12). 162
Figure 4.1: effect of an ESD on the input transistor's gate of the transistor. 167
Figure 4.2: attacked MET4 connection between the comparator and the mixer 167
Figure 4.3: High-level schematic of a second feedback loop proposition, details on the analog extraction of φ. 170
Figure 4.4: Resonant accelerometer (seismic mass and resonant beam electrostatically coupled) and the CMOS readout. Left: SEM image; right: microscopic image. 171
Figure 4.5: MILO-based resonant accelerometer principle. 171
Figure 4.6: SEM image of a seismic mass which anchor broke out due to the residual stress. 172
Figure 4.7: Layout of the two CMOS-MEMS MILO. 173

Introduction

Over the past decades, the need for sensors has grown drastically. On the one hand, everyday objects are increasingly autonomous and complex (autonomous cars, smartphones, smart watches, home-automation equipment, etc.). These objects are "so-called" smart first and foremost because they integrate various sensors and a microprocessor to compute the important amount of data collected. Size, consumption and cost are the important criteria. On the other hand, high-end systems (satellites, civil and military planes, missiles, drones) are more and more common, requiring precise sensors, able to work in harsh environments with very good reliability.

A derivation from Integrated Circuits (IC) fabrication process, adding a sacrificial layer and a release fabrication step led to the emergence of Micro Electro-Mechanical Systems (MEMS). These systems are in general composed of a moving part, a transduction from the electrical domain to the mechanical domain to actuate the moving part, and another transduction back to the electrical domain to sense the motion. Used as sensors (i.e. the quantity to be sensed is related to the movement of the moving part) they take advantage of their size, consumption, with good performance, and potential for applications in the two categories described in the last paragraph. Moreover, since they are based on IC fabrication process, they benefit from batch fabrication techniques, so good repeatability, and very low cost if fabricated on a large scale level. They are used as accelerometers [1], gyroscopes [2], pressure sensors [3], and temperature sensors [4] for instance.

Some of these systems will be designed in order to show very little damping, high mechanical stiffness and intrinsically low mass. They can be used as resonant sensors: excited at their resonance frequency, which is determined by their mass and stiffness, their motion's amplitude is very high compared to the motion at other frequencies. If the measurand is related to their stiffness or mass, it will affect the resonance frequency, which is tracked in open-loop configuration (i.e. the input signal's frequency is swept and the resonance frequency is estimated thanks to the high amplitude of motion) or closed-loop configuration (i.e. the resonator is placed in an electronic feedback loop to maintain the oscillation, and if the loop is carefully built, it naturally oscillates at the resonance frequency). The MEMS resonators are generally

smaller than static MEMS in order to be light, thus having high resonance frequencies and low response time. They are especially suited to be embedded into digital chains since they output a frequency, or a pulse count, which can be directly fed into microprocessors without requiring analog-to-digital converters.

However, the effect of environmental parameters like temperature or humidity, or even the aging of the moving part can modify the resonator's mass and stiffness, leading to resonance frequency change uncorrelated to the measurand. Concerning the thermal drift, several solutions were developed to ensure the thermal stability of the resonator using temperature sensor and ovenized atmosphere, or to compensate for the drift in a microprocessor. Another approach is to track the difference between two resonators fabricated such as the drifts affect equally both resonance frequencies, and the measurand affect them differently. The differential solution takes advantage from the cancellation of every drift affecting both resonators (not only the thermal one), and potentially amplification of the difference between the resonators, thus sensitivity enhancement. The existing techniques for differential resonant sensing can be split in three main categories. First, the frequency difference technique tracks the difference between two oscillating loops. Then, the exploitation of mode localization phenomenon, in which the resonators are passively coupled, leads to the apparition of two resonance modes and several output metrics theoretically drift-free and sensitive to stiffness mismatch between the resonators. Finally the synchronization, in which the resonators are actively coupled, oscillating at the same frequency, enables the tracking of the phase difference between the resonators, which is as well theoretically drift-free, potentially very sensitive to mass or stiffness mismatches between the resonators.

In this thesis, a synchronized architecture co-integrating two MEMS resonators and the coupler enabling their synchronization is developed. In the first chapter, the physical phenomenon of resonance is presented, and the reason why MEMS are good candidates for sensing applications. The monolithical CMOS-MEMS co-integration, which is the fabrication technique used in this work, and the fabricated resonators are presented and modelled in order to obtain an electrical equivalent circuit. The effect of temperature on these resonators is analysed theoretically and experimentally, and the different solutions for drift cancellation are presented. In chapter 2, the

synchronization of two resonators by mutual injection is modelled under simplifying assumptions, and several guidelines are derived for the implementation of VLSI-compatible synchronized architectures, leading to the choice of one architecture in particular. This architecture's implementation is then described block-by-block, simulated using the model developed in the first chapter to ensure the respect of the above-mentioned design guidelines, and fabricated. The experimental characterization of the fabricated device is performed in chapter 3, and the figures are compared to the simulation and the theoretical model. Finally, the work is concluded in chapter 4, and perspectives are given to improve the existing device and extend the idea of synchronized resonators for differential resonant sensing.

Hereafter follows a list of the contributions made during this thesis. A copy of the TCAS paper can be found in Annex 1.

- P. Prache, J. Juillard, N. Barniol, "Une nouvelle architecture pour les capteurs M/NEMS résonants." *Journées Nationales du Réseau Doctoral en Micro-nanoélectronique (JNRDM 2015)*.
- P. Prache, P. M. Ferreira, N. Barniol, J. Juillard, "Couplage for de capteurs M/NEMS résonants : rejet de la dérive thermique, " *Journées Nationales du Réseau Doctoral en Micro-nanoélectronique (JNRDM 2016).*
- P. Prache, A. Uranga, N. Barniol, J. Juillard, "Temperature-drift rejection and sensitivity to mismatch of synchronized strongly-coupled M/NEMS resonators," *29th IEEE International Conference on Micro Electro Mechanical Systems (MEMS 2016).*
- P. Prache, P. M. Ferreira, N. Barniol, J. Juillard, "Monolithic integration of mutually injection-locked CMOS-MEMS oscillators for differential resonant sensing applications," *23rd IEEE International Conference on Electronics, Circuits and Systems (ICECS)*.
- J. Juillard, P. Prache, N. Barniol, "Analysis of Mutually Injection-Locked Oscillators for Differential Resonant Sensing," *Circuits and Systems I: Regular Papers, IEEE Transactions on*, IEEE, 2016, 63 (7), pp.1055 - 1066.

- J. Juillard, P. Prache, P. Maris Ferreira and N. Barniol, “Impact of output metric on the resolution of mode-localized MEMS resonant sensors,” *2017 IEEE International Frequency Control Symposium (IFCS),* 2017.
- P. Prache, J. Juillard, P. M. Ferreira, N. Barniol, M. Riverola, “Design and characterization of a monolithic CMOS-MEMS mutually injection-locked oscillator for differential resonant sensing”, *Sensors & Actuators A: Physical (Submitted).*

Chapter 1 From resonance to MEMS differential resonant sensor

This chapter gives an introduction to the work presented in this thesis. It aims to properly define the problematic, and give the tools in term of ideas, concepts and models which are used throughout this work. It starts with some physical generalities about the resonance, and why and how one can take advantage of the resonance to make sensors and clocks. The resonators used in this work are then presented, and modelled in order to obtain a functional linear model of the resonators that is used in the next chapter. The effect of temperature variation on such devices is presented as well as the different solutions that were developed to tackle this issue. Our solution is outlined with its advantages and drawbacks, compared to the others.

1.1 Resonance

In physics, resonance is the property of a system to oscillate at greater amplitude for specific frequencies. It results from the ability of the system to store and transfer energy between two or more different storage modes, and can occur with all types of vibration and waves. Resonance may be observed in nature at very different scales: for example, such impressive phenomena as the tidal range's height of the Bay of Fundy or the gaps in the rings of Saturn, are explained by tidal resonance [5] or orbital resonance [6]. Systems can also be put at resonance on purpose, in order to enable interesting properties: nuclear magnetic resonance [7] is used for imaging, optical resonance [8] is used for the creation of coherent light. Sometimes, it can occur unwantedly, destroying the system which was not built to withstand such amplitudes, as illustrated by the famous example of the bridge of Tacoma [9]. The design of accurate timekeeping devices is usually based on a physical resonance phenomenon, e.g. mechanical resonance in balance-wheel or quartz crystal clocks [10]. The accuracy of such a device depends on whether its resonance frequency fluctuates with time: the main design challenges is then to make sure that the resonance is very "sharp", to avoid

short-term frequency fluctuations, and that the system is as invariant as possible, to avoid long-term fluctuations.

In a mechanical resonator, energy is supplied as work done by an outside periodic force, and stored in the resonator as kinetic and potential (elastic) energy. The efficiency of this transfer of energy is frequency-dependent, and it is optimal at a discrete set of frequencies, called resonance frequencies. In this manuscript, the case of a single resonance frequency f_0, also called *natural* resonance frequency, is considered. Frequency f_0 depends on the physical characteristics of the system, such as its geometry, its material properties or those of the medium in which it is placed. The other representative quantity of a resonant system is its quality factor Q. It measures the ratio of the energy stored in the system to the energy dissipated per cycle. The larger Q is, the less energy is dissipated each cycle, and the less energy must be supplied to the resonator to sustain its oscillation. Moreover, in the frequency domain, a larger Q also means a narrower bandwidth of the system relative to its natural frequency, i.e. a sharper resonance peak. For accurate timekeeping systems, high quality factors are preferable because less dissipation entails less fluctuations, according to the fluctuation-dissipation theorem [11], [12]. Moreover, the physical properties of the system which determine f_0 must be as stable as possible through time. Consequently, in order to avoid environmental drift (such as temperature, pressure or humidity variations, leading to slow fluctuations of f_0), the resonators in high-accuracy timekeeping applications are generally encapsulated in a controlled atmosphere, and the effect of temperature must be compensated [13].

While timekeeping devices aim for the most stable resonant frequency, resonant sensors exploit the dependence of the natural frequency of a device to a particular physical quantity called the measurand (e.g. external acceleration or rotation [14], added mass [15], ambient pressure [16]), while trying to reduce its dependence to other environmental changes. Thus, by comparing the natural frequency of the device to that of a fixed frequency reference, it is possible to monitor the variations of the measurand. High Q (of both the resonator used for sensing, and the one used as reference) is also required in such applications in order to have a good frequency stability and thus be able to detect minute variations of the measurand. In fact, assuming perfectly stable frequencies, “quasi-digital” period or frequency measurements (typically, pulse

counts) can be performed with arbitrarily small resolution [17] at the cost of sensor response time. Thus, the limitation of a resonant sensor is essentially intrinsic to the resonator itself: high values of Q and f_0 ensure a good resolution and a good bandwidth. This is as opposed to "analog" sensors, in which an amplitude is measured: the resolution of such sensors not only depends on the intrinsic noise of the sensor, but also on the resolution of the analog-digital conversion stage, which often becomes a bottleneck in applications where high accuracy is required [18], entailing tradeoffs between accuracy and consumption. 20 bits ADCs are readily available (e.g. Analog Devices LTC2378-20) but at the cost of an increased power consumption (21 mW in this case).

Several embedded sensing or clocking applications require high accuracy, repeatability, low cost and low power consumption. Micro-Electro-Mechanical Systems (MEMS) resonators are well-suited for such applications, as described in the next section. The outline of this section is the following. Section 1.2 contains a brief review of MEMS resonators. Then basic modelling tools used in this work are given in section 1.3. Finally, temperature drift and its compensation is addressed in section 1.4.

1.2 MEMS resonators

This section gives an overview of MEMS resonators, starting with a definition, followed by a short history of the topic, their main applications, and a focus on CMOS-MEMS resonators.

1.2.1 What is a MEMS resonator?

A MEMS (resp. NEMS) device is a microfabricated mechanical structure with at least one micrometric (resp. nanometric) dimension, with a moving part whose motion can be excited and/or sensed electrically. A MEMS resonator is a structure designed to exhibit mechanical resonance at a specific frequency; energy is supplied from the electrical domain to the mechanical domain through actuators, e.g. electrostatic [19], piezoelectric [20], electro-thermal [21] or electromagnetic [22] transducers, which may also be used to detect the motion of the structure, and convert

it into an electrical signal. The most common type of transduction, the electrostatic method, is described in section 1.3.1. A description of the other methods can be found in [23]. M/NEMS resonators can reach quality factors of one million if properly sealed in vacuum [24] and exhibit a wide range of natural frequencies (from 10 Hz [25] to 1 GHz [26]).

1.2.2 MEMS resonators, yesterday and today

In 1967 the first article about a MEMS resonator was published by Nathanson [27]. The device was a field effect transistor whose metal gate had been suspended over the channel. This gate could be actuated electrostatically and vibrate, with a resonance at 5 kHz and a quality factor of 500. By moving up and down, it would modulate the conductance of the channel, enabling high-Q filtering in integrated circuit technology. After that proof of concept, some inertial and pressure sensors were developed [28] but the first breakthrough happened in the mid 80's at the research level when Howe and Muller adapted Nathanson's idea, coating a suspended cantilever with a polymer capable of adsorbing particular molecules, putting it to resonance through capacitive actuation and detection, and thus creating the first micromechanical device for chemical vapour detection [19]. New geometries began to appear, for example the comb-drive structure [29], and as the fabrication techniques got more and more domesticated, thinner and smaller structures were built, with higher frequencies and quality factor. Resonant sensors for force, pressure, rotation, acceleration began to appear at the industrial level in the early 90's (see [30] and [31] for a review), and RF MEMS resonators with GHz frequencies in the early 00's [26], [32].

Nowadays, the industrial field of applications of MEMS resonators is centered on timing, sensing and filtering, especially for highly integrated systems [33]. For timing applications, they are of a special interest for serial communication protocols (USB for instance) where short term frequency stability is not a determining factor, but a reduced cost and size is [34]. For very high quality frequency synthesizers, where the spectral purity of the wireless standards is too high for MEMS resonators, quartz crystals with their higher Q (up to a billion [35]) are still dominant.

For sensing applications, a huge variety of sensors with very different coupling techniques between the measurand and the natural frequency exists. The gas sensing technique for chemical sensors described earlier is appearing at the industry level [36], and is a topic of extensive investigation [37], [38]. An example of a resonant pressure sensors is given in Figure 1.1

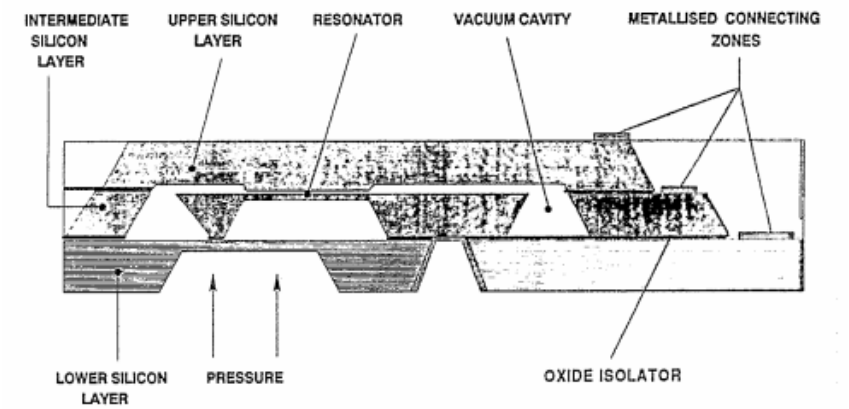

Figure 1.1: Cross section of a resonant pressure sensor [39]: one of the anchor of the resonator is placed over the membrane which deflects under pressure. The deflection modifies the stress in the beam, shifting its resonance frequency.

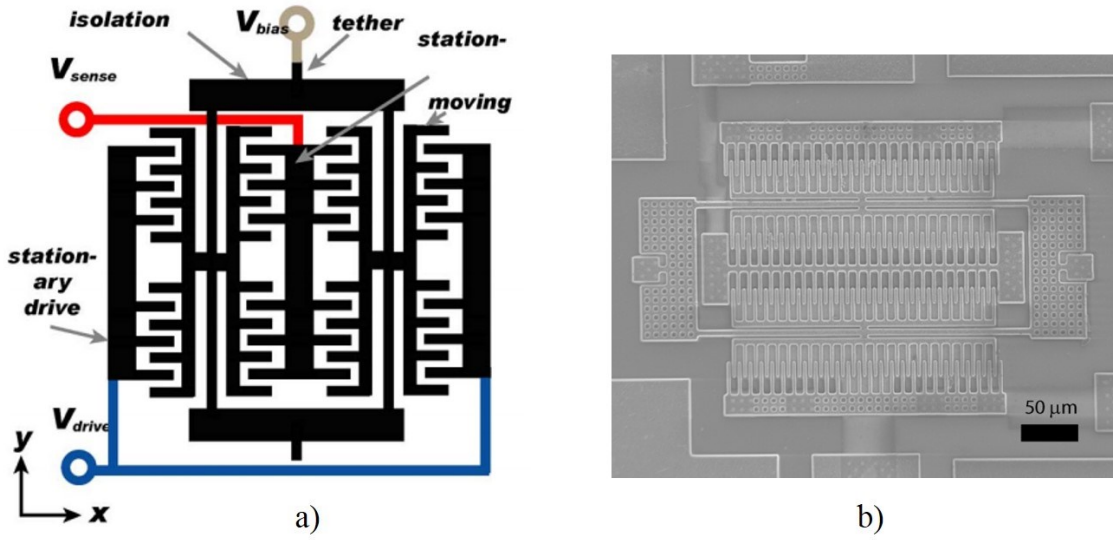

Figure 1.2: Resonant strain sensor [40]: a) schematic of the operating principle and b) SEM of the device.

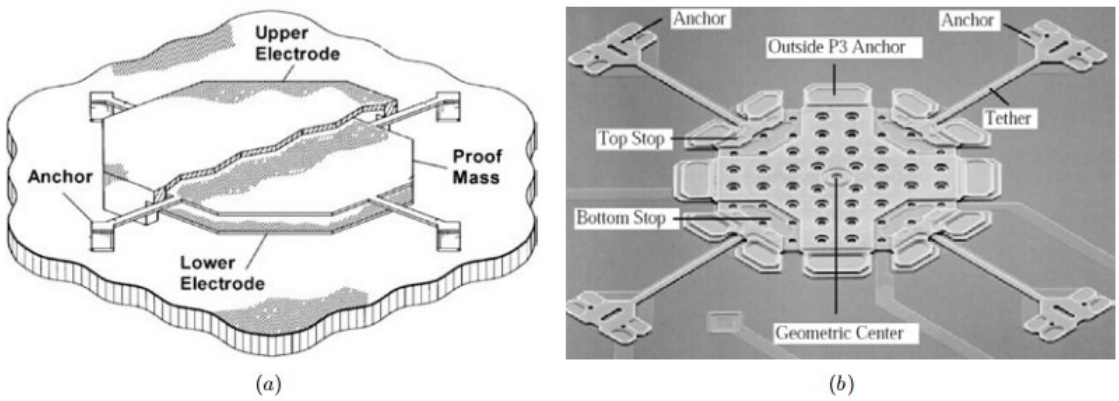

Figure 1.3: Motorola MMAA1220D z-axis accelerometer [41]: a) schematic of the operating principle and b) SEM of the device.

Strain sensors [42] and magnetic field sensors [43] are also used due to their high resolution. The former use the fact that mechanical strain modifies the resonance frequency of a beam. The design is critical in order to transfer the strain between two structures to the beams, leading to complex structures [40], see Figure 1.2 for an illustration. They are used in civil engineering, automotive applications, and robotic applications. The latter take advantage of the Lorentz force, acting like an additional equivalent spring on a piezoelectric cantilever beam in presence of a magnetic field, and modifying its resonance frequency [44]. They are used in medical and biomedical applications as well as compass for positioning [45]. Resonant inertial sensors (accelerometers and gyroscopes), achieving very high resolution but at the cost of slow response time can be used for special high-end applications (military for instance) [41], see Figure 1.3 for an illustration. Various techniques for the coupling between the movement of a seismic mass and the resonance of a beam exist. One is the electrostatic softening variation, explained in section 1.3: the distance between the mass and the resonating beam, if a DC voltage is applied between them, affects the resonance frequency [46]. Another one is to anchor the beam on the seismic mass: its movement modifies the strain of the beam, thus changing its resonance frequency [47].

In RF applications, MEMS resonators can be placed in transceiver chains as frequency synthesizers, filters or mixers. They benefit from their high quality factor (Q over 30,000 at 2.97 GHz [48]) compared to LC-tank (20 at 1.16GHz in [49] or 110 at 915MHz in [50]), but suffer from various other drawbacks (insertion losses, drift and variability [51]).

Finally, MEMS energy harvesters with low resonance frequencies are also a subject of research, in order to scavenge vibratory energy from the ambient environment and power autonomous systems [33], [52]. These resonators must have natural frequencies of the same order of magnitude as the vibrations from which they seek to harvest energy. These are typically very low (e.g. <100Hz), leading to "large" MEMS structures (of the order of mm^2, see [53] for a review).

1.2.3 CMOS-MEMS integration

Because of their size, MEMS resonators output small electric signals that need to be amplified, thanks to an electronic readout, to be usable in a control chain. This readout may be fabricated in the same technological process as the MEMS resonator: this "monolithic co-integration" results in the resonator and the readout being on the same chip. Alternatively the mechanical resonator and its electronic readout may be fabricated with two separate technological processes, each on its own chip, which can then be connected using various techniques: this is called "hybrid co-integration".

Hybrid co-integration benefits from the dedication of each fabrication step. Since the MEMS and the circuitry are fabricated on different chips, the process can be optimized for each. A review of interconnection techniques can be found in [54]. The most commonly-used are wire bonding and flip-chip. The flip-chip technique consists in fabricating the two chips with a symmetrical pad distribution [55]. One chip is then flipped over so that its top side faces down; it is then aligned and soldered to the other one. It benefits from contact resistance of the order of mΩ. It brings possible design constraints resulting from pad alignment, and disables any easy replacement in case of malfunction of one of the chips. The wire bonding technique consists in soldering a wire (aluminum, copper, silver or gold) to connect the two chips. It exhibits low contact resistance as well, between 10 mΩ and 100 mΩ depending on the effective contact area [56]) but suffers from parasitic capacitances and mutual inductances with the other wires which depends on the length of the wire and its proximity to the other ones [57], [57], [58]. The technique benefits from a larger freedom on pad disposition, at the cost of an increased area compared to the flip-chip technique.

In monolithic co-integration, since the MEMS and its readout are fabricated using the same technological process, interconnection distances can be reduced to their minimum, meaning smaller parasitic capacitances (of the order of 5fF if optimized, as is mentioned in section 2.2), mutual inductances and contact resistance. It also means a reduced size which can be an asset for VLSI applications. The main drawback is that there exists no standard process for co-fabricating MEMS devices and their associated readouts [59], [60]. If a standard CMOS process is used as a basis for the monolithic CMOS-MEMS device, this leaves a limited choice of resonator shapes and materials open. For example, in the AMS technological process (described in subsection 1.2.4) used in this work, silicon, polysilicon, aluminum, tungsten, and silicon oxide layers with specific thicknesses are available. Other technological CMOS nodes enable the use of other materials. Moreover, a post-processing step for the release of the mechanical structure must be performed, which can be a cause of failure and add geometrical variability to the one of the fabrication process.

This project has been conducted in collaboration with the research group ECAS, at the UAB, Spain. This group has been working for 15 years on the monolithic integration of CMOS-MEMS resonators, using almost every available layer in the AMS CMOS technology: polysilicon [61], aluminum [62], and tungsten [63].

1.2.4 CMOS-MEMS monolithic integration using AMS 0.35 µm.

At the UAB, CMOS-MEMS monolithic integration is mostly performed using the AMS 0.35um technology [64] with a post-processing step of wet etching using hydrofluoric acid. The fabrication and post-processing are well described in [63]; an overview of this technique is given here.

The AMS 0.35um fabrication process relies on the deposition of various layers of materials one above the other, above a P-doped silicon substrate. In the case of the C35b4c3 technology, used in this work, 4 layers of metal are available. A Poly-Poly capacitor module is also available, which can be useful for the fabrication of low gap polysilicon resonator [65]. In Figure 1.4 we present a cross section of the different metal layers, and in Table 1.1 the typical dimensions. Note that the MIM capacitor module and Thick Metal module are not available in C35b4c3, they are in C34b4M3.

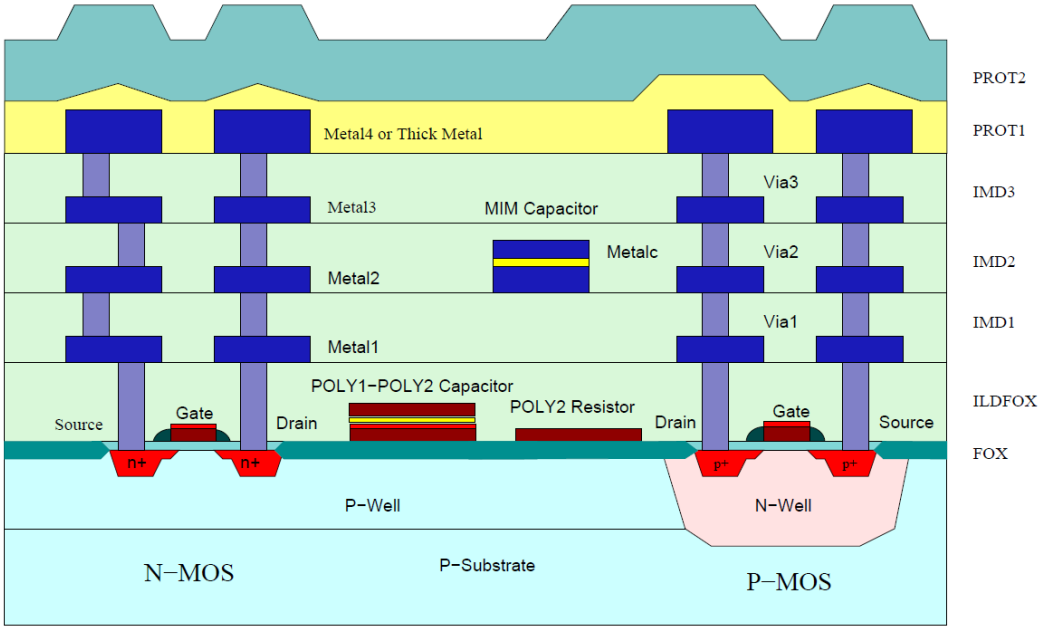

Figure 1.4 Cross section of all layers available in the AMS C35b4c3.

Parameter	Symbol	Typical dimension	Material
Field oxide thickness	FOX	290nm	$Si0_2$
Poly1 thickness	POLY1	282nm	Polysilicon
Metal1-poly oxide thickness	ILDFOX	1600nm	$Si0_2$
Metal1 thickness	MET1	600nm	Al
Metal2-Metal1 thickness	IMD1	1600nm	$Si0_2$
Metal2 thickness	MET2	600nm	Al
Metal3-Metal2 thickness	IMD2	1000nm	$Si0_2$
Metal3 thickness	MET3	600nm	Al
Metal4-Metal3 thickness	IMD3	1000nm	$Si0_2$
Metal4 thickness	MET4	925nm	Al
Passivation thickness 1	PROT1	1030nm	Si_3N_4
Passivation thickness 2	PROT2	1000nm	Si_3N_4

Table 1.1 Typical dimensions and materials available in AMS C35b4c3 technology.

The way inter-metal (IMD) layers' thickness works is presented in Figure 1.5 and described here. If no metal is defined, a 1600 nm layer of SiO_2 is deposited. If a metal connection is defined with or without metal on top, a 600 nm layer of aluminum is deposited. If there is nothing on top, a layer of SiO_2 of 1000 nm is deposited. If there

is metal on top, the 1000 nm layer is made of tungsten to connect both metals. If only a VIA layer is defined with metal on top (for example to make contact between MET1 and MET3), a 1200 nm tungsten layer is deposited. Finally, if the design rules are broken and a VIA layer is defined with nothing above or below, an approximately 1300 nm tungsten layer is deposited, as illustrated in Figure 1.5. It should be noted that each time a VIA or MET layer is fabricated, a 100nm titanium nitride layer (TiN) is deposited above and below to protect its walls from the deposition of SiO_2. Figure 1.7 presents a SEM image of the case of a MET-VIA-MET stack which illustrate the MET-VIA-MET case.

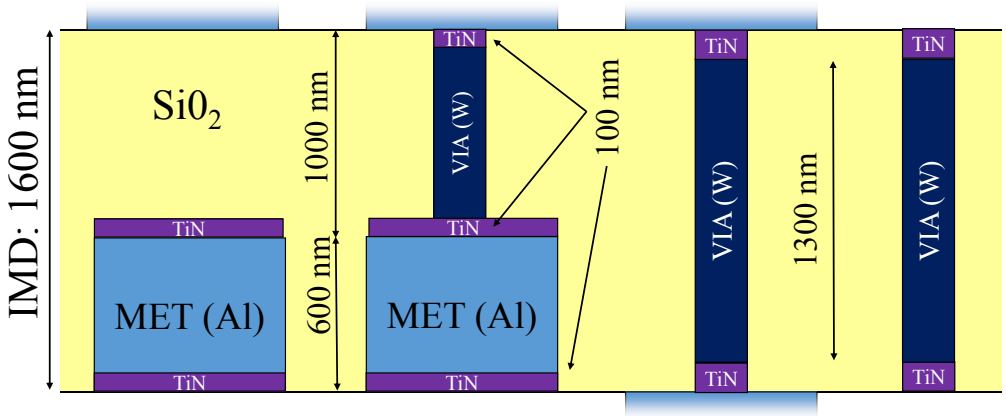

Figure 1.5 AMS 0.35 inter-metal layers deposition process for the different geometries.

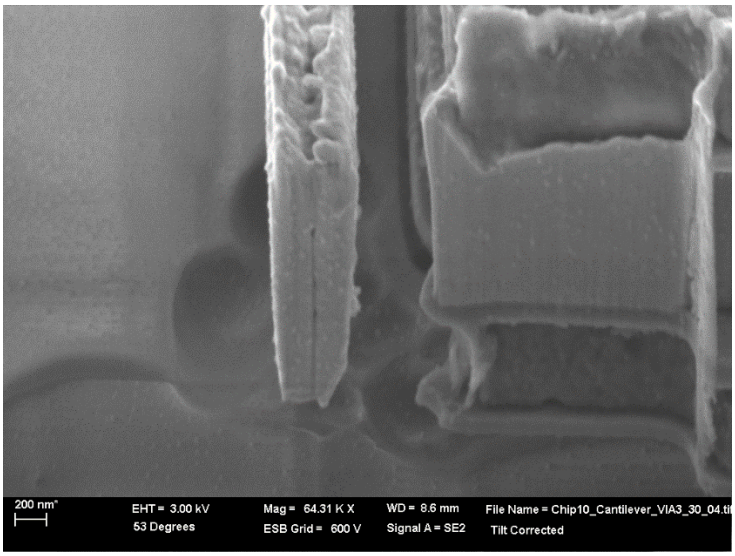

Figure 1.6: SEM image of a VIA3 beam close to a MET3-VIA3-MET4 [63] showing the different layers and the fact that a VIA3 beam alone is thicker than when it connects two metal layers.

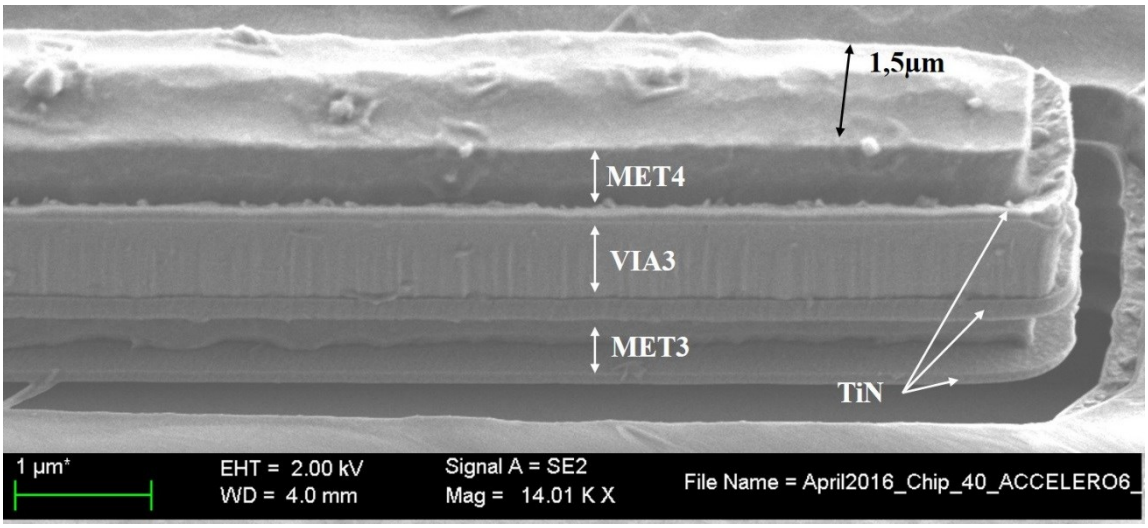

Figure 1.7 SEM image of a MET3-VIA3-MET4 stack, showing the different layers including the TiN.

Mechanical structures with electrical actuation can be fabricated using every conductive layer from polysilicon to MET4. Every material has different inherent mechanical properties (Young's modulus, density), with also different physical characteristics coming from the fabrication steps (inherent stress, robustness), and every layer /material follows different sets of design rules. These design rules are given in section 1.2.5 for the VIA structures used in this work.

To release a structure (regardless of its material) from the surrounding SiO_2, it is convenient to first define a PAD layer on top of the structure. This indicates the foundry to etch the two Si_3N_4 passivation layers (PROT1 and PROT2 in Figure 1.4) at this location. The PAD must be at least 15µm*15µm. After the chip is fabricated, a wet etching step using hydrofluoric acid is then performed, as it is the simplest solution to etch away the unprotected SiO_2:

- The chip is placed in a solution of dissolved HF for a duration between 4 min and 20 min depending on the depth of the structure to be released. One must count 250nm/min, plus the time for the etching under the beam since the etching isotropic.
- The chip is then washed for 10 min in a flow of distilled water to get rid of the acid on the surface and inside the chip.
- To eliminate the remaining water, the chip is placed in two successive baths of isopropyl alcohol for respectively 3 and 5 min.

- Finally, it is heated at 100°C for 10 min to evaporate the remaining alcohol.

It should be noted that the etching time cannot exceed a certain time (25-30 min) for three reasons. First, the aluminum is etched by the HF as well. Even though the etch rate is smaller than for SiO_2, this can deteriorate the electrodes and the anchor of the structures. Second, the electrodes and anchors are under-etched (since the etching is isotropic as well) and may fall off (see Figure 1.8 and Figure 1.9). And last, if MET4 is used as metal layer connection for the rest of the CMOS circuitry, it is etched as well even under the passivation layers (tunneling effect) and can be affected by an over-etching. The entire release process lasts approximately 50 min depending on the etching time and can be performed without extensive knowledge of clean room equipment, which is a major asset when it comes to developing a proof of concept.

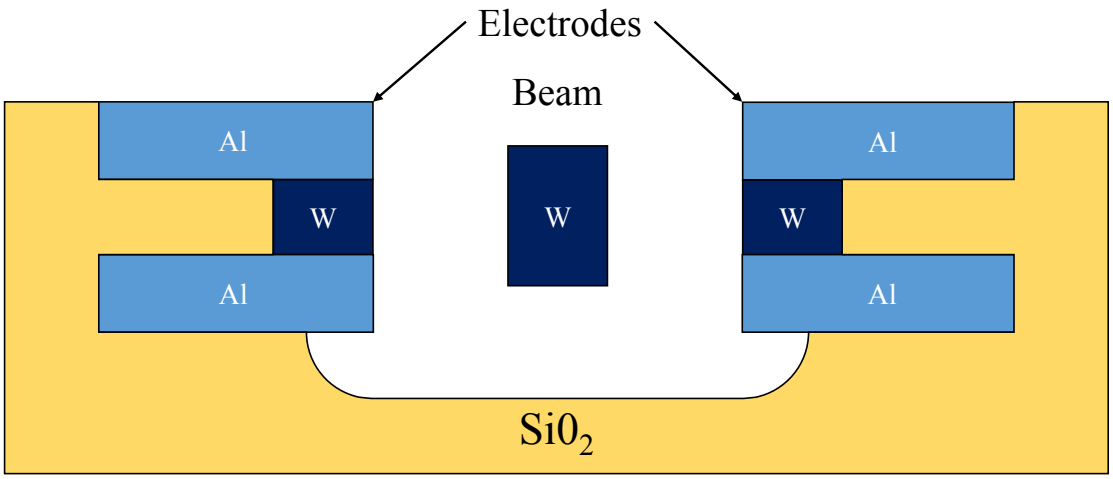

Figure 1.8 Cross section of a tungsten beam between two electrodes illustrating the effect of the isotropic wet etching: the electrodes can fall off.

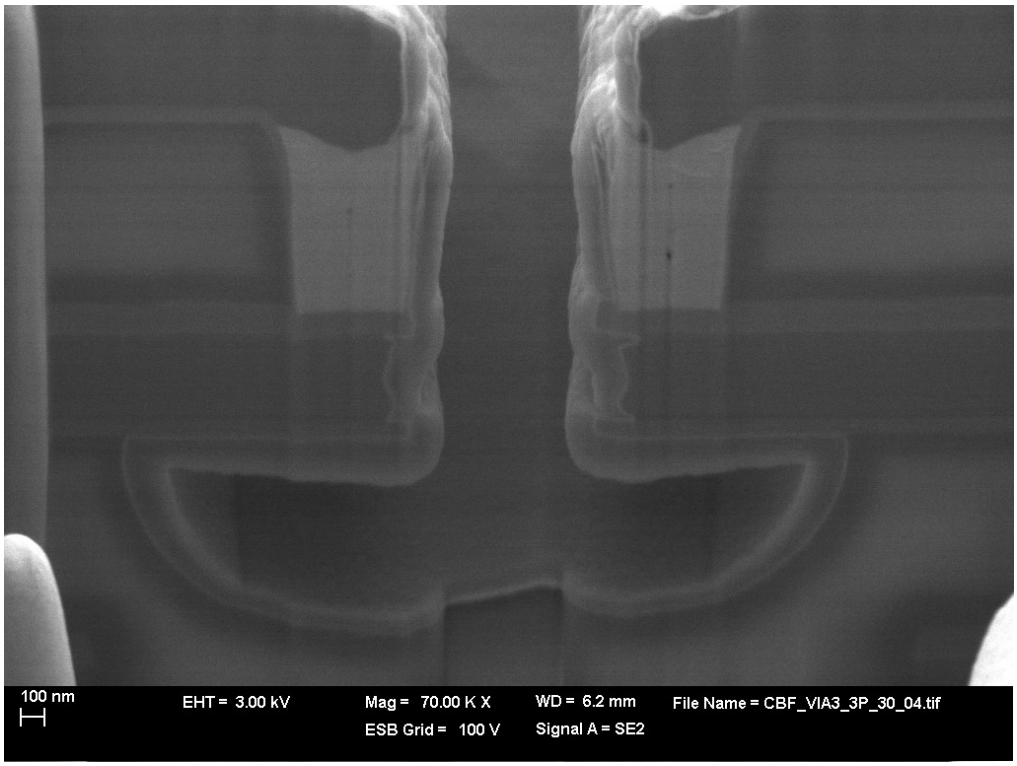

Figure 1.9 SEM image of two under-etched electrodes (MET-VIA-MET stack). The beam is not in the section of the FIB cut.

1.2.5 VIA structures

In the AMS 0.35um fabrication process, VIA layers are meant to connect two layers of metal by 500nm*500nm squares. Drawing a VIA with a larger area violates the design rules and suppresses AMS foundry-guarantee on the fabrication. Moreover, since they are meant to connect two layers of metal, defining geometries with no metal above or below violates the design rules as well. But after 15 years of playing with the rules, with more or less success, the ECAS group gathered a strong knowledge of what can be fabricated and what cannot. For VIA structures, this can be summed-up in 2 rules:

- Without metal above or below, the width and thickness of the VIA structure are fixed, respectively around 500 nm and 1200 nm with the 10% variability of the process. If a structure has more than one dimension wider than 500 nm, it must incorporate MET above and below otherwise only its edges are fabricated (cf. Figure 1.7, where the

width is 1.5 µm and it is well fabricated because of the metal above and below, while the seismic mass from Figure 1.11 does not, and only its edges are fabricated).

- The lateral gap between two VIA structures must be at least 450nm: it is the minimum gap achievable for VIA structures in AMS C35b4c3.

As long as these two rules are followed, any kind of structures (clamped-clamped beams, clamped-free beams, springs, switches, see-saw resonators [66]) can be fabricated. These rules are not the same for the other layers of material. A good example of both failure and success on one structure is shown in Figure 1.10 and Figure 1.11.

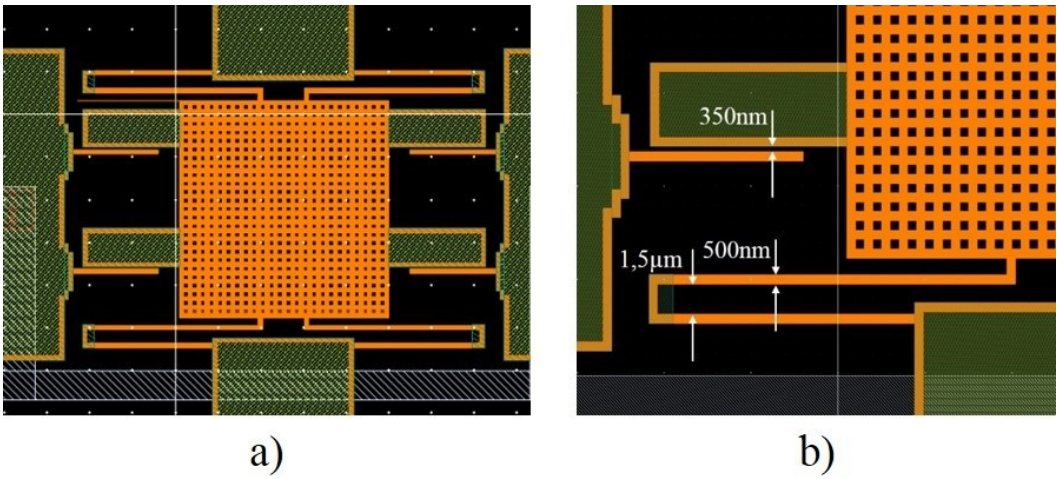

Figure 1.10 a) Layout of a resonant accelerometer: VIA3 Stack MET3-MET4 b) zoom with the layout dimensions.

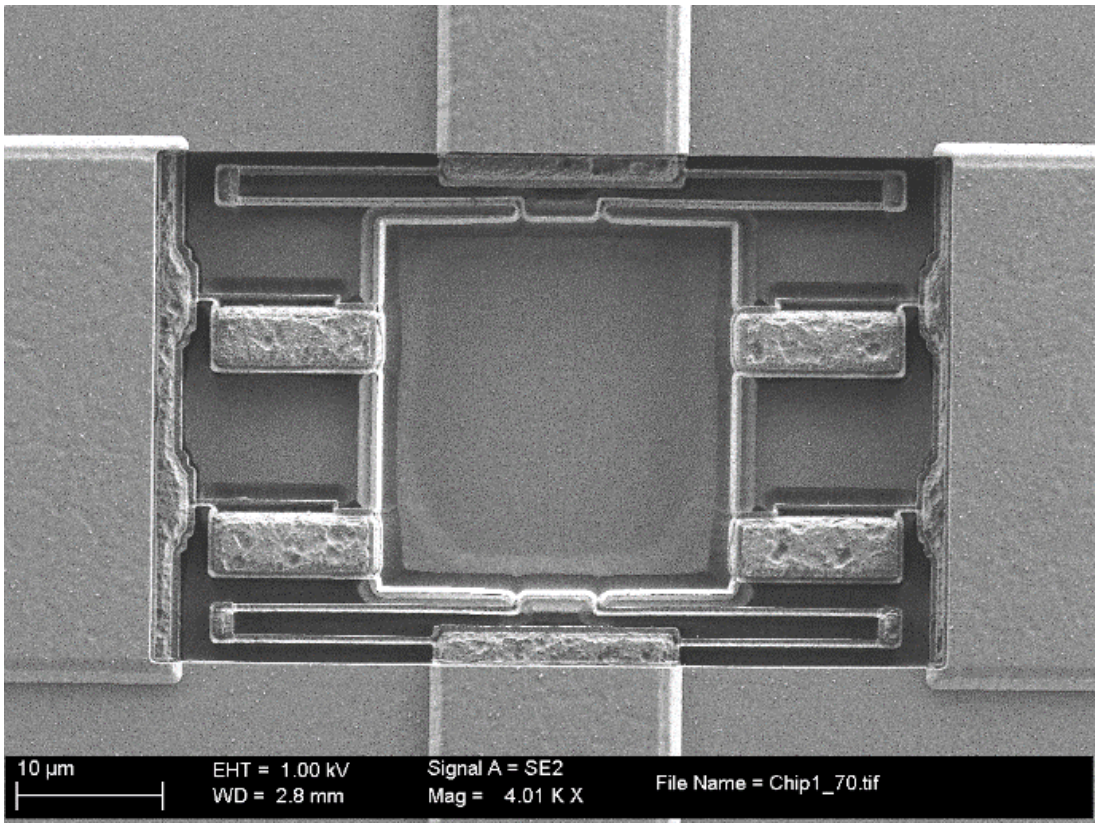

Figure 1.11 SEM image of the structure whose layout is presented in Figure 1.10. The spring of 500nm width and 1.5µm gap is well fabricated, but the resonator with 350nm is not. The seismic mass which is only made of VIA without any metal has only been fabricated on its edges.

In this work, two specific VIA3 structures are used: 10 µm-long clamped-free beams (CFB) and 30 µm-long clamped-clamped beams (CCB). The width is set at 500 nm and the lateral gap at 450 nm to obey the empirical rules. The layout of these two structures and SEM images of the fabricated resonators are presented in Figure 1.12 and Figure 1.13. As the fabrication process is not optimized for the fabrication of MEMS structures, the dimensions must be measured afterwards because they might be different from those specified in the layout. These measurements are shown in Figure 1.14 and Figure 1.15.

In the end, the lateral gap is always smaller than the one specified in the layout, at 370 nm for the CCB and 340 nm for a CFB. The width of the structure is smaller as well, 490 nm for the clamped-clamped beam, and 465 nm for the clamped-free beam. Finally, the clamped-free beam's length is longer than specified, at 10.5 um, while the clamped-clamped beam's length is slightly smaller than the specifications. The

thickness cannot be measured without specific techniques like FIB cutting. But since this quantity does not affect the natural frequency of the beams, as shown in section 1.3.2, this measurement is not performed here. It has been done in [63] for VIA relays, and the measured thickness is 1.3 µm. These dimensions are summed-up in Table 1.2, with the notations defined in Figure 1.16. Note that the SEM imaging includes small artifacts (like thermal drift during the imaging, leading to small curvatures), making it difficult to establish very precise dimensions (less than ~10 nm). However, it is clear that gap dimensions are much smaller than designed.

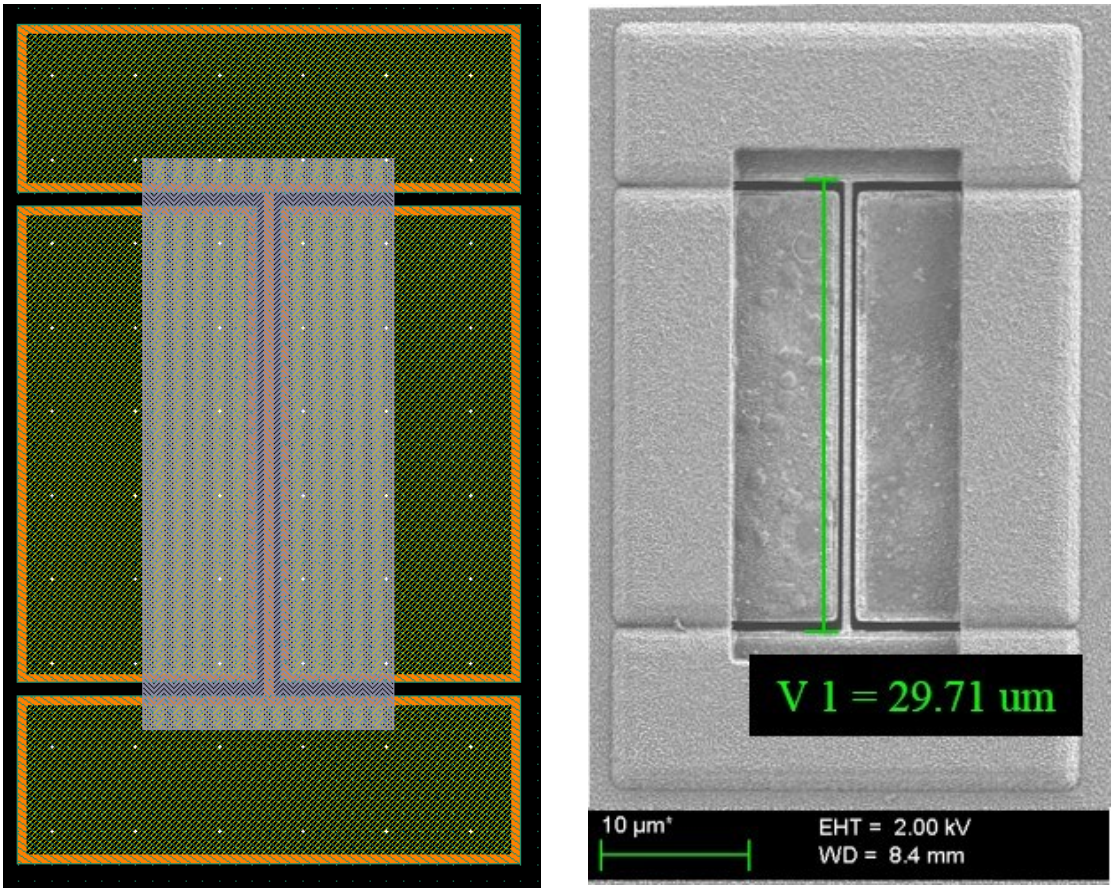

a) b)

Figure 1.12: a) layout of a 30µm*0.5µm clamped-clamped VIA3 beam (CCB) b) SEM image of this structure.

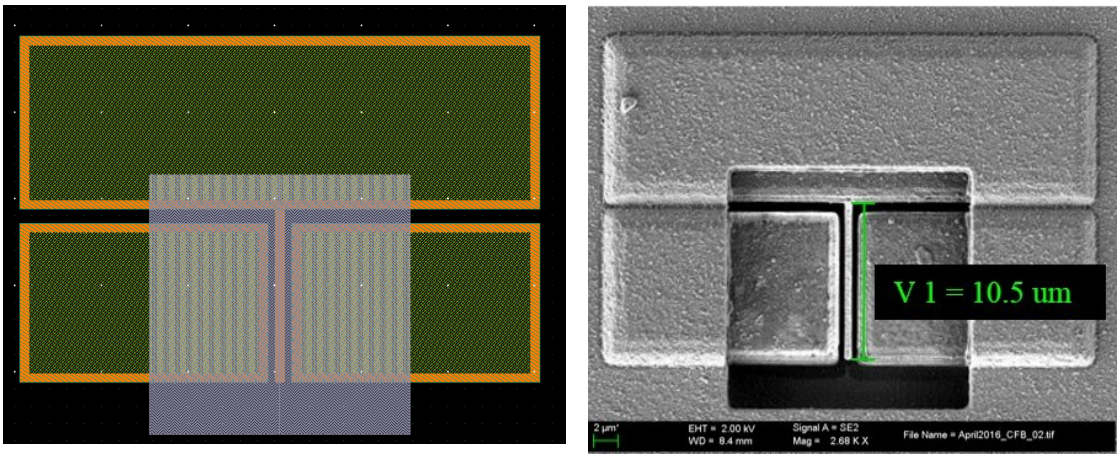

a) b)

Figure 1.13: a) layout of a 10µm*0.5µm clamped-free VIA3 beam (CFB) b) SEM image of this structure.

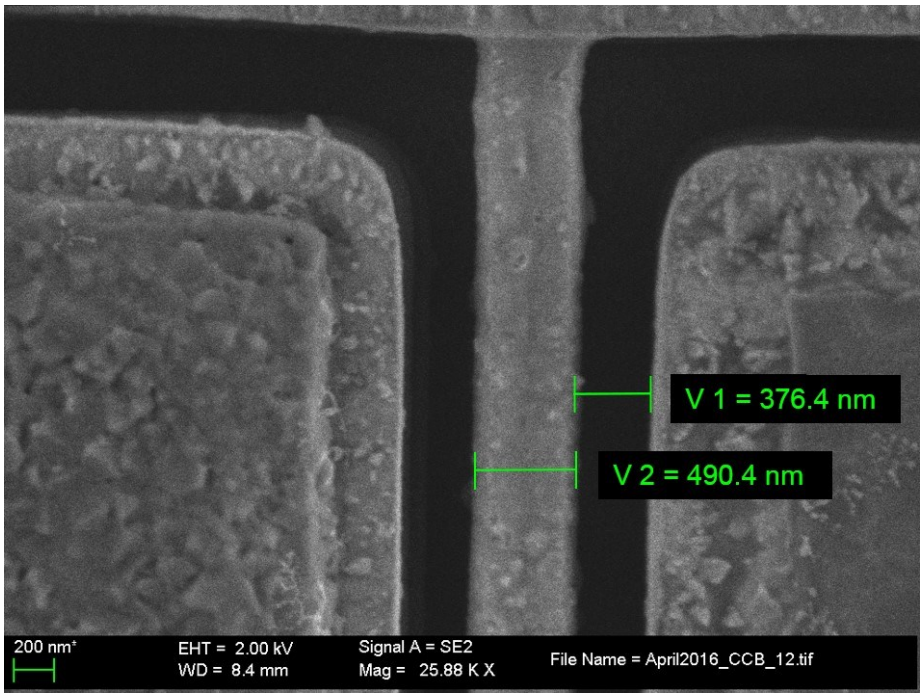

Figure 1.14 SEM image of a clamped-clamped beam close to the anchor, with a designed 450nm gap.

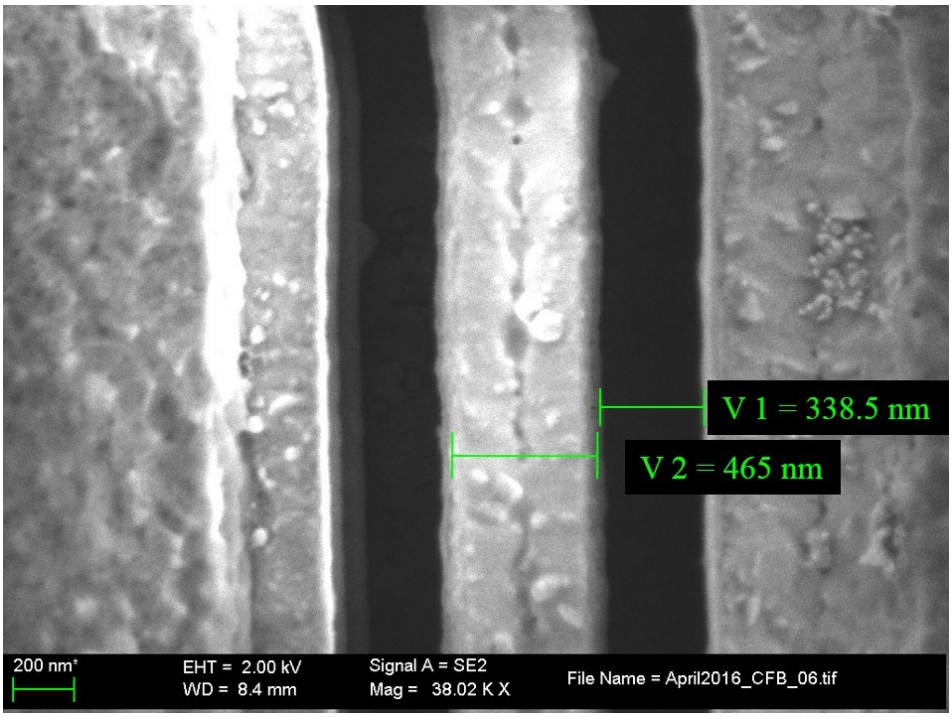

Figure 1.15 SEM image of a clamped-free beam away from the anchor, with a designed 450nm gap.

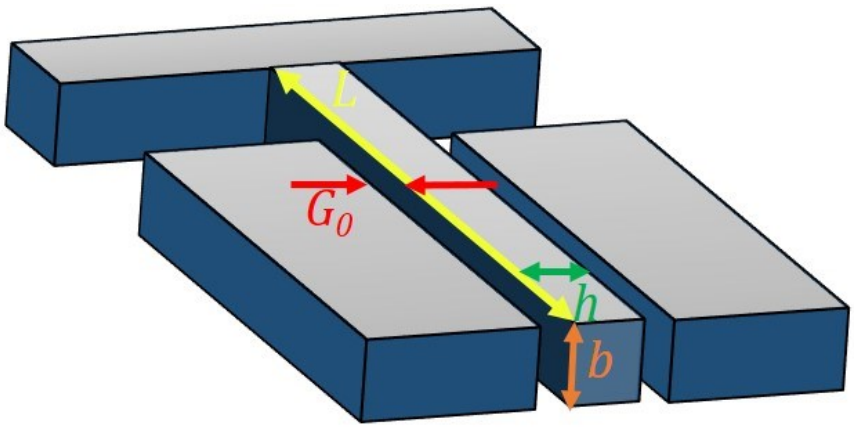

Figure 1.16 Schematic of the capacitive CFB with the different geometrical and electrical notations used in this work.

Geometry	L	h	b	G_0
CCB layout	30 µm	500 nm	900 nm	450 nm
CCB measured	29.7 µm	490 nm	1.3 µm	380 nm
CFB layout	10 µm	500 nm	900 nm	450 nm
CFB measured	10.5 µm	470 nm	1.3 µm	340 nm

Table 1.2 Dimensions for the considered geometries.

In the next section, reduced-order models of the fabricated resonators are established.

1.3 Modelling of capacitive MEMS beams

1.3.1 Framework and objectives of this section

The goal of this section is to obtain a compact equivalent electrical model with lumped elements (Butterworth-Van Dyke model) based on the geometry of the resonator, its dimensions, and external parameters (biasing voltage, temperature).

We consider the beams to be of uniform rectangular cross-section, initially straight, and with one large dimension, their length, compared to their width and thickness. The curvature of the beams as they bend is supposed to be very small, so that Euler-Bernoulli's beam equation [67] may be used to model them. It is supposed that the mechanical motion of the resonators can be modelled by taking into account the first in-plane flexural mode of the beams only, as illustrated in Figure 1.18 in the case of a CFB. The resonators are used in the three-port configuration (one electrode for excitation voltage and one for the output current readout). Energy is transduced from the electrical domain to the mechanical domain through the capacitance C_{in} formed by the resonator and the input electrode, as shown in Figure 1.17. A variation of the energy stocked inside the capacitance is obtained by applying an alternating voltage V_{in} which sets the resonator in motion. This motion is then read by another transfer of energy back to the electrical domain using the second capacitance formed by the resonator and the output electrode C_{out}: any change of C_{out} creates charges on the output electrode that are read by an appropriate circuitry, if the voltages V_b (bias voltage) and V_{out} (self-bias voltage of the electronic readout) are fixed.

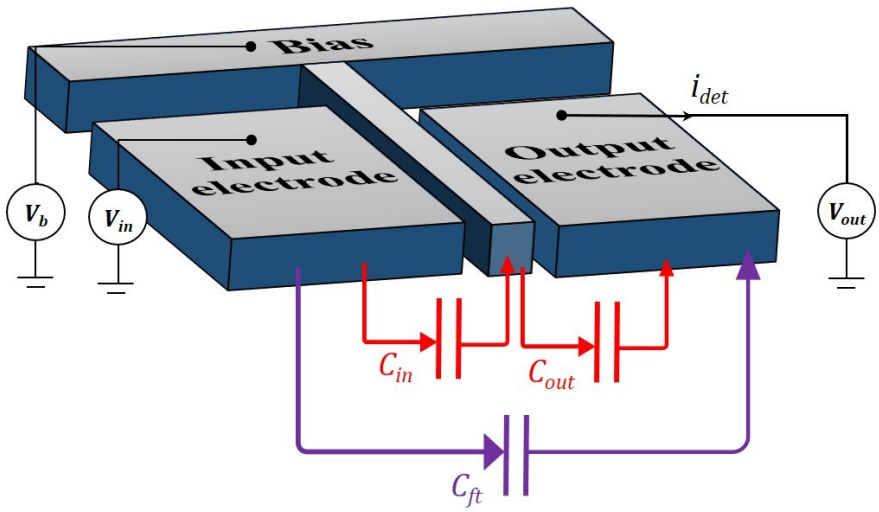

Figure 1.17: Electrostatic CFB in the three-port configuration.

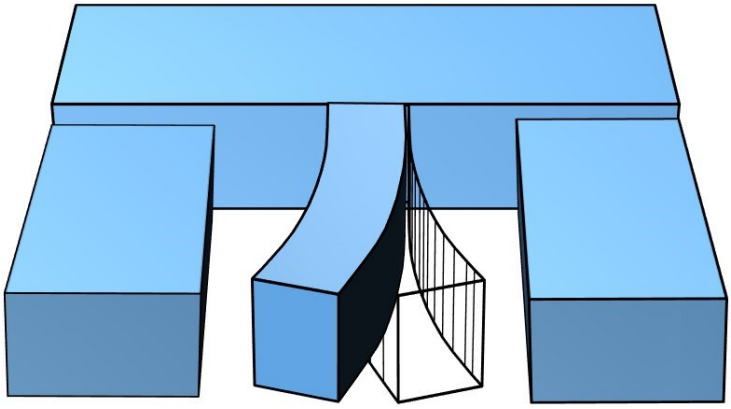

Figure 1.18: In-plane motion of the CFB

The voltages V_b and V_{out} are supposed to be fixed, only V_{in} can vary. As the movement of the beam is supposed to be very small, the capacitances C_{in} and C_{out} can be estimated by the plane capacitance method. A parasitic feedthrough capacitance C_{ft} exists that directly couples the input and output electrodes and must be considered as well. We first model the mechanical behavior of the beams under the assumptions made in this paragraph, and then exploit the modelling to make an electrical equivalent circuit of the device, which can be exploited for numerical simulations.

1.3.2 Reduced-order model of a three-port beam with electrostatic actuation

A reduced-order model of the resonator can be derived from its governing partial differential equation(s) by means of modal projection techniques. This is readily done in the case of bending bridges and cantilever beams in [68]. The case of electrostatically-actuated MEMS bending beams (with or without axial stress) is covered in [69], [70], in the case of a two-port configuration. The equations governing the motion of a beam in a three port configuration can directly be derived from these papers as:

$$\frac{d^2a}{dt^2} + \frac{\omega_0}{Q}\frac{da}{dt} + \omega_0^2 a\left(1 + \gamma_D a + \frac{\sigma_s}{\sigma_{crit}}\right) = \eta(V_b - V_{in})^2 N(a) - \eta(V_b - V_{out})^2 N(-a) \quad , \quad (1)$$

$$\begin{cases} C_{in} = \frac{\varepsilon_0 bL}{G_0}\Gamma(a) \\ C_{out} = \frac{\varepsilon_0 bL}{G_0}\Gamma(-a) \end{cases} \quad , \quad (2)$$

where a is the maximal deflection of the beam normalized with respect to the gap (position of beam's midpoint for a CCB, of beam's extremity for a CFB), and:

- $\omega_0 = 2\pi f_0$ is the natural pulsation of the beam.
- ε_0 is the vacuum permittivity.
- γ_D is the Duffing coefficient.
- η is the electromechanical coefficient.
- $N(a)$ and $\Gamma(a)$ represent the dependence of the electrostatic forces and of the input and output capacitances on the deflection of the resonator.
- σ_s is the residual stress in the beam.
- σ_{crit} is a critical value of the residual stress.
- Q is the quality factor of the beam.

These quantities are described hereafter.

The natural pulsation can be expressed by using the effective mass and stiffness of the considered eigenmode:

$$\omega_0 = \sqrt{\frac{k_e}{m_e}}. \quad (3)$$

The effective stiffness and mass are calculated by means of modal analysis and Galerkin projection of the Euler-Bernoulli's equation, as described in [71], [72] or [33]. The results are presented in Table 1.3, with the values for our two geometries, and the parameters for tungsten:

$$\begin{cases} \rho = 19300\ kg.m^{-3} \\ E = 411\ GPa \end{cases}. \quad (4)$$

Geometry	Effective mass (m_e)	Effective stiffness (k_e)	Natural frequency (f_0)
Clamped-free beam	$0.25\rho bhL$	$\frac{0.257Ebh^3}{L^3}$	$\frac{1.014}{2\pi}\frac{h}{L^2}\sqrt{\frac{E}{\rho}}$
CFB	$30.6\ pg$	$11.92\ N.m^{-1}$	$3.141\ MHz$
Clamped-clamped beam	$0.397\rho bhL$	$\frac{16.56Ebh^3}{L^3}$	$\frac{6.459}{2\pi}\frac{h}{L^2}\sqrt{\frac{E}{\rho}}$
CCB	$145\ pg$	$39.73\ N.m^{-1}$	$2.63\ MHz$

Table 1.3: Effective mass and stiffness of the first resonant mode of the resonating structures for the first vibrating mode, calculated for the considered structures presented in paragraph 1.2.5

When the amplitude of motion is important, nonlinearities become sensible. Nonlinear effects that enter the equation of motion in the form of a force proportional to the cube of the displacement are the most common [73]. The Duffing coefficient γ_D can either be positive, making the resonator stiffer and increasing its resonance frequency, or negative, decreasing its resonance frequency. The softening effect can be observed in capacitive MEMS at high amplitude of motion, since the electrostatic force is nonlinear with the displacement. The hardening effect can be observed in clamped-clamped beam because the beam necessarily stretches as it deflects in its transverse motion. In this work, we suppose that $a \ll 1$, so the coefficient $\gamma_D a^2 \ll 1$. This means that the resonator is kept in its linear regime.

The electromechanical coefficient η is, according to [70] :

$$\eta = \frac{\varepsilon_0 L b}{2 m_e G_0^3}. \tag{5}$$

Provided a "local" plane capacitance holds, one may find very accurate analytical approximations of $N(a)$ and $\Gamma(a)$, which respectively correspond to the dependence on a of the projection of the electrostatic force on the first eigenmode, and of the input and output capacitances. The methods for approximating these projection integrals are described in [69], [70]. The corresponding expressions are given in Table 1.4.

Geometry / Function	Clamped-free beam	Clamped-clamped beam
$N(a)$	$0.392\left(\frac{1+0.783a}{1-a} + (0.531+0.114a)\log(1-a)\right)$	$0.523\frac{1+0.017a}{(1-a)^{\frac{3}{2}}}$
$\Gamma(a)$	$1-0.505a-(0.888-0.201a)\log(1-a)$	$\frac{1+0.029a}{(1-a)^{\frac{1}{2}}}$

Table 1.4: Geometry-dependent functions N and Γ for the considered geometries.

The expression of σ_{crit} is explained in page 53.

Finally, Q represents the quality factor of the structure. A complete review of the different loss mechanisms is given by Imboden in [74]. In this work, resonators will always be operating in air. But it has been observed in other work that the same structures operating in vacuum have their quality factor multiplied by 10 [75]. This means that the principal loss mechanism is fluidic loss like the squeeze film damping described by Bao in [76]. Taking into account the border effects as well as the effective viscosity, one can write [76]:

$$Q = \frac{2\pi f_0}{\frac{2\mu}{1+6\lambda/G}\cdot\frac{(b+1.3G)^3}{G^3\rho b h}}. \tag{6}$$

In this equation: μ is the fluid's viscosity ($1.8.10^{-5}$ Pa.s in air at 20 °C), and λ is the mean free path at atmospheric pressure (64.10-9 m in air at 20 °C). The other quantity are related to the geometry, and detailed in Table 1.2.

Applied to our two geometries, the resulting theoretical quality factor are:

$$\begin{cases} Q_{CCB} = 153 \\ Q_{CFB} = 126 \end{cases}. \tag{7}$$

However, the thickness only 3.5 times bigger than the gap, which is not enough to perfectly fit into the modelling of the squeeze film damping made in [76]. This is why a measurement of the quality factor after the fabrication process and the release is always made.

The nonlinear model (1) can be further simplified by assuming:

$$\begin{cases} V_b \gg V_{in} \\ V_b \gg V_{out} \\ a \ll 1 \\ Q \gg 1 \end{cases}. \tag{8}$$

The equation (1) can be linearized close to the equilibrium and written again:

$$\ddot{a} + \frac{\omega_0}{Q}\dot{a} + \omega_{\sigma_s,V_b}^2 a = -2\eta V_b V_{in} N(0)\,, \tag{9}$$

where

$$\omega_{\sigma_s,V_b}^2 = \omega_0^2\left(1 + \frac{\sigma_s}{\sigma_{crit}}\right) - 2N'(0)\eta V_b^2\ . \tag{10}$$

and N' is the derivative of N. The resonance pulsation of the resonator can then be tuned "manually" after it has been fabricated, as illustrated in Figure 1.24. This can be advantageous for systems that seek to tune the resonant frequency electronically [77], or to make up for the variability of the fabrication process. On the other hand, noise affecting the bias voltage also affects frequency stability, which can be an issue in high-accuracy applications. Values of the resonance frequency for the CCB and CFB at a bias voltage V_b of 20 V are derived from the model, given the measured dimensions (see Table 1.2 and presented in Table 1.5.

Geometry	Resonance frequency
CCB ($V_b = 20\ V$)	2.560 MHz
CFB ($V_b = 20\ V$)	3.055MHz

Table 1.5: Resonance frequency for the CCB and CFB for 20 V of bias voltage.

The ultimate limit of this electrostatic softening phenomenon is static pull-in [78]. In our case, the static pull-in position is

$$a_{pi} = 0, \tag{11}$$

because of the symmetry of the three-port configuration. Static pull-in occurs when $\omega_{s,V_b} = 0$. We give, in Table 1.6 the values of the biasing voltage for this limitation for the geometries with the dimensions given in section 1.2.5

CFB	$V_b^{instability} = 123.91\ V$
CCB	$V_b^{instability} = 86.1\ V$

Table 1.6: Values of V_b to put the resonators to instability for the two considered geometries.

In equation (10), σ_s is the internal stress in Pa, and σ_{crit} a "critical" stress calculated by projecting the tensile term of the Euler-Bernoulli beam equation with axial stress on the first eigenmode according to [70]. The obtained value for the CCB is:

$$\sigma_{crit} = 3.39\frac{Eh^2}{L^2} = 358\ MPa. \tag{12}$$

This value is approximately equal to the opposite of the buckling stress corresponding to our geometry (-356 MPa according to [79], or -354 MPa according to [80]): when $\sigma_s = -\sigma_{crit}$, the first eigenfrequency of the beam drops to 0, as shown by equation (10), corresponding to the collapse of the beam under compressive stress.

No studies are found on the value of residual stress in tungsten VIA layers of CMOS fabrication process. However, in [81], Zhang measured an 112 MPa stress for boron-doped silicon (Young's modulus 133 GPa). In [82], Fedder a 69 MPa stress for a metal-stacked structure (effective Young's modulus 61 GPa). So finding a residual stress of the order of 1/1000 of the Young modulus seems normal. In Figure 1.19 are plotted the natural frequencies of every CCB released during this work, biased at 20 V, showing a mean resonance frequency of 3.90 MHz. Given the equation (10), this leads to a residual stress of 475 MPa. The various residual stress found in the literature as well as the one found in this work are summed-up in Table 1.7. The internal stress also has an effect on the instability voltage and the theoretical quality factor since it modifies (increases, in our case) the resonance frequency. Taking into account the 475 MPa tensile stress, the theoretical quality factor is estimated with Equation (6) at 157, and the instability voltage is adjusted at 130.74 V according to Equation (10).

In the case of clamped-free beams, SEM characterization shows no deflection. Moreover, the natural frequencies of the released beams (Figure 1.20) are according to the modelling (experimental mean value of 3.02 MHz, compared to the modelled 3.055 MHz), meaning that it can be assumed that if some level of stress coming from the fabrication was affecting the structure, it was released without gradient during the etching.

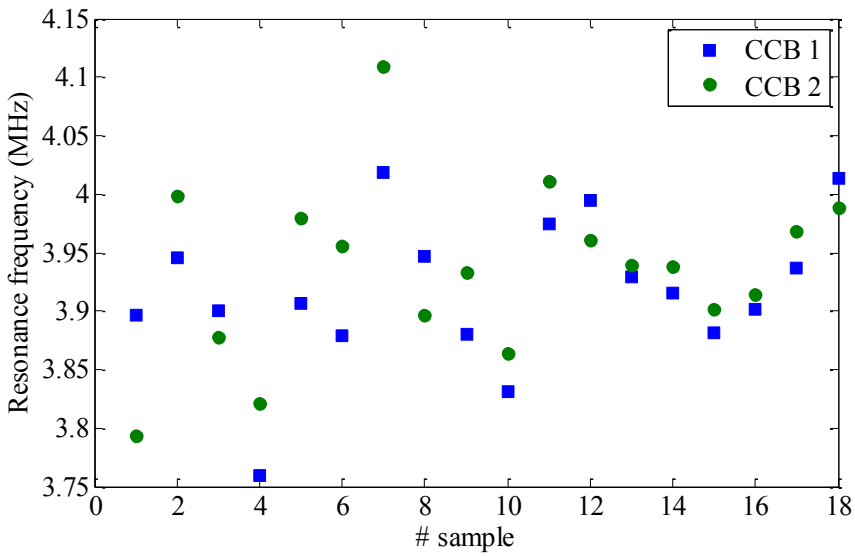

Figure 1.19: Resonance frequencies of the CCB for $V_b = 20V$. Each dot represents a CCB, and 2 active CCB are fabricated on each sample.

Material	Young' modulus E	Residual stress σ_s
Boron-doped silicon [81]	133 GPa	112 MPa
Metal stack [82]	61 GPa	69 MPa
Silicon oxide [83]	69 GPa	276 MPa
Tungsten (this work)	411 GPa	475 MPa

Table 1.7: Young's modulus and experimental residual stress of various materials used for MEMS resonators. Note that in this work, it is derived from the modelling.

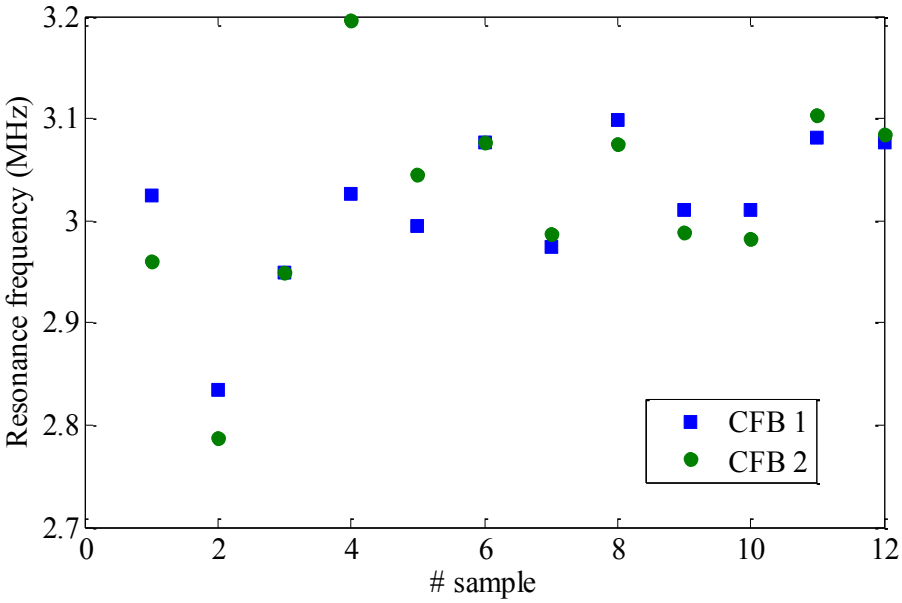

Figure 1.20: Resonance frequency of every CFB for $V_b = 20V$. Each dot represents a CCB, and 2 active CFB are fabricated on each sample.

1.3.3 Butterworth-Van Dyke model of electrostatically-actuated resonator with capacitive detection

One may establish a Butterworth-Van Dyke model (or equivalent electrical model) of the resonator by taking into account how its motion is converted into an electrical signal. To this end, we consider that the electric charges at the output electrode result from:

- The variation of the gap between the resonator and the output electrode with a fixed bias of $V_b - V_{out}$. As mentioned in p.47, V_{out} is an eventual bias voltage of the input of the analog front-end, which is fixed, as is the bias voltage.
- The variation of the voltage between the output electrode and the input electrode $V_{in} - V_{out}$ given the fact that both electrodes are capacitively coupled. This capacitance, C_{ft} (Figure 1.17) has many contributions, like direct capacitive coupling of the two electrodes with the screening of the resonator in between, coupling between the connections of the electrodes, or indirect coupling through the substrate.

One can write:

$$i_{det} = \frac{d\big(C_{out}(V_b - V_{out}) + C_{ft}(V_{in} - V_{out})\big)}{dt}. \tag{13}$$

Under assumptions (8), this simplifies to:

$$i_{det} = V_b \frac{dC_{out}}{dt} + C_{ft}\frac{dV_{in}}{dt}. \tag{14}$$

The output current is divided in two contributions: the motional current i_{mot} actually corresponding to the motion of the resonator, and the parasitic current i_{par} corresponding to the effect of the actuation voltage on the output electrode. As we suppose $a \ll 1$, we may also express the motional current as:

$$i_{mot} = -V_b C_{out}(0)\Gamma'(0)\dot{a}\,, \tag{15}$$

where Γ' represents the derivative of Γ, and $C_{out}(0)$ is the nominal value of the output capacitance.

The electrical equivalent of the resonator is represented in Figure 1.21. This simplified model can easily be used to simulate the resonator's behavior as well as the circuit at the same time.

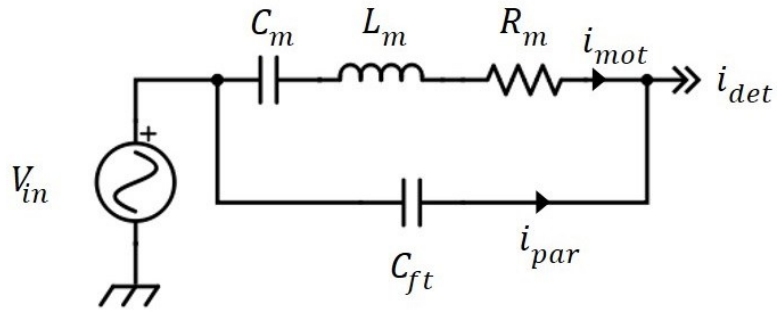

Figure 1.21 Butterwort-Van Dyke model of the capacitive MEMS resonator.

The governing equation of this model's behavior is:

$$\begin{cases} L_m \dfrac{di_{mot}}{dt} + R_m i_{mot} + \dfrac{1}{C_m}\displaystyle\int_0^t i_{mot}dt = V_{in} \\ i_{par} = C_{ft}\dfrac{d(V_{in})}{dt} \end{cases}. \tag{16}$$

To match the terms of equation (9), the motional elements must be defined as:

$$\begin{cases} R_m = \dfrac{\omega_0}{Q}\dfrac{1}{2\eta C_{out}(0)N(0)\Gamma'(0)V_b^2} \\ C_m = \dfrac{2\eta C_{out}(0)N(0)\Gamma'(0)V_b^2}{\omega_s^2 - 2N'(0)\eta V_b^2} \\ L_m = \dfrac{1}{2\eta C_{out}(0)N(0)\Gamma'(0)V_b^2} \end{cases} . \quad (17)$$

Using the functions Γ, N and the parameters defined throughout this section, we calculate the value of the motional elements for our two geometries (see Table 1.8 for the results and Table 1.9 for numerical applications)

Geometry	R_m	L_m	C_m
CFB	$1.6759\dfrac{h^2G^4}{Q\varepsilon_0 bV_b^2}\sqrt{E\rho}$	$1.665\dfrac{\rho hG^4}{\varepsilon_0^2 bLV_b^2}$	$\dfrac{\dfrac{\varepsilon_0^2 bLV_b^2}{1.665hG^4}}{\dfrac{1.02Eh^2}{L^4} - \dfrac{1.96\varepsilon_0}{hG^3}V_b^2}$
CCB	$\dfrac{1.43hG^4}{L^2Q\varepsilon_0^2 bV_b^2}\sqrt{\dfrac{41.71Eh^2\rho}{L^2} + 12.29\sigma_s\rho}$	$0.9036\dfrac{\rho hG^4}{\varepsilon_0^2 bLV_b^2}$	$\dfrac{\dfrac{\varepsilon_0^2 bLV_b^2}{0.9036hG^4}}{\dfrac{41.71Eh^2}{L^4} + \dfrac{12.29\sigma_s}{L^2} - \dfrac{3.173\varepsilon_0}{hG^3}V_b^2}$

Table 1.8: Values of the electrical equivalent components of the Butterworth-Van Dyke model of cantilever beam and bridge resonator given its dimension and material properties.

Geometry	R_m	L_m	C_m
CFB	$91\ M\Omega$	$460\ H$	$5.76\ aF$
CCB	$58\ M\Omega$	$233\ H$	$7.09\ aF$

Table 1.9: Numerical applications for our geometries, for $Q = 100$, $\sigma_s = 475\ MPa$ and $V_b = 20\ V$

1.3.4 Illustration

The effects of the different model parameters are now illustrated using simulations based on the BVD model we just developed and experimental results. First, the effect of the biasing voltage (electrostatic softening and gain modification) is drawn in Figure 1.22 and Figure 1.23. From these simulations, the resonance frequency for each bias voltage can be extracted. The theoretical dependence of the resonance frequency of CCB resonators and CFB resonators to the bias voltage are then plotted in Figure 1.24 and Figure 1.25, and compared to experimental results.

These measurements are obtained under a probe station, with the interface circuit depicted in section 2.2. The connection is made with an HTT Wedge 7 probe card, and a "home-made" SMA adapter. The precise description and influence of the experimental setup is discussed in section 3.1. The frequency responses of the resonators are obtained with an Agilent E5100 network analyzer, for different bias voltages (provided by a Keithley 2200 DC power supply). The corresponding resonance frequencies are extracted, and compared to the simulated ones, showing very good agreement

Finally, the effect of the feedthrough capacitance is illustrated in Figure 1.26. Concerning the gain, one can see that the resonance peak becomes less important due to the anti-resonance, and the quality factor harder to estimate with the cut-off frequency at -3dB estimation. The phase at resonance goes from -90° in the absence of feedthrough, to 90° when parasitic current is much greater than motional current.

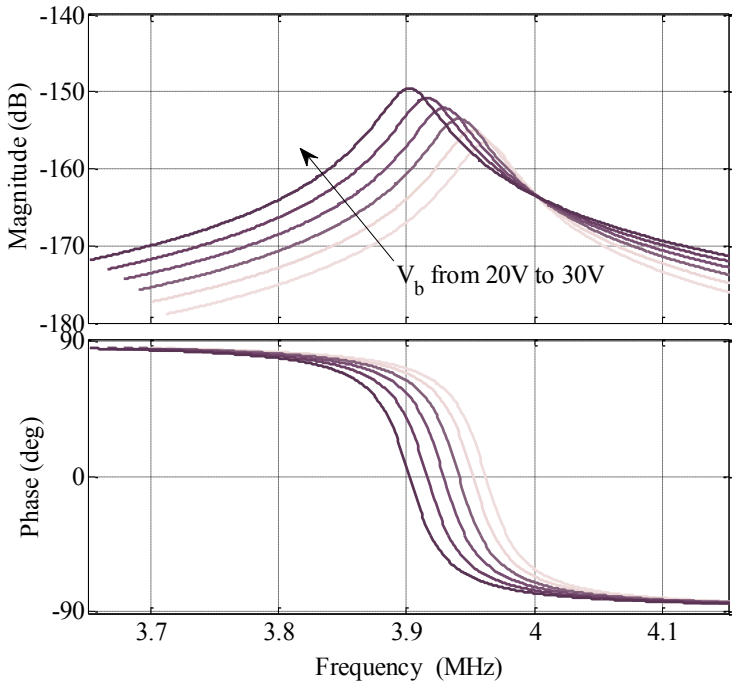

Figure 1.22: Simulated Bode diagram (input: V_{in}, output: i_{mot}) of the CCB at $Q = 100$, $\sigma_s = 475\ MPa$ for $V_b$varying from 20V to 30V.

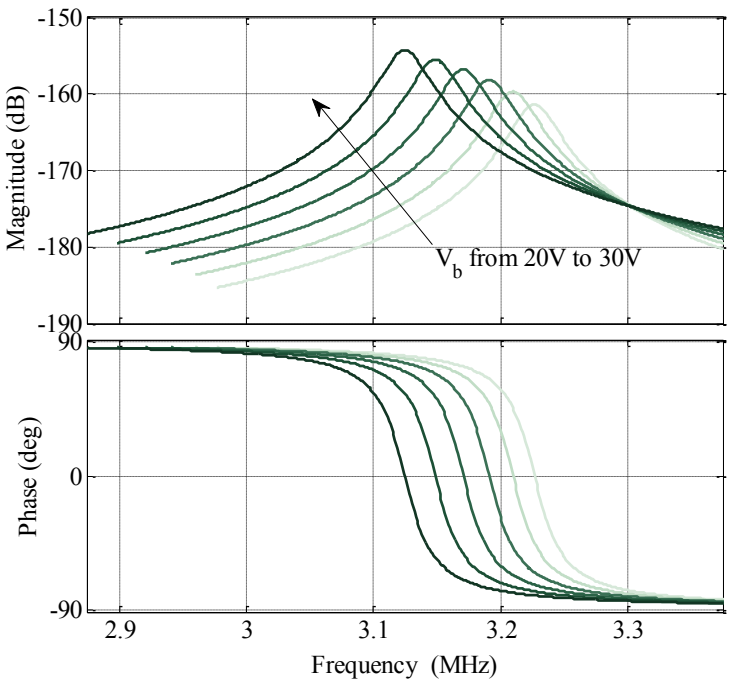

Figure 1.23: Simulated Bode diagram (input: V_{in}, output: i_{mot}) of the CFB at $Q = 100$ for $V_b$varying from 20V to 30V.

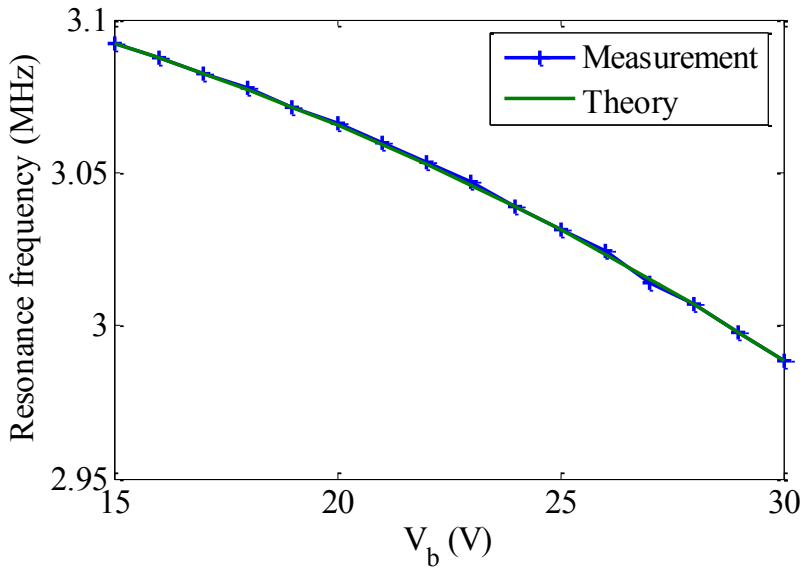

Figure 1.24: Measured electrostatic softening effect on a CFB, with simulated predictions.

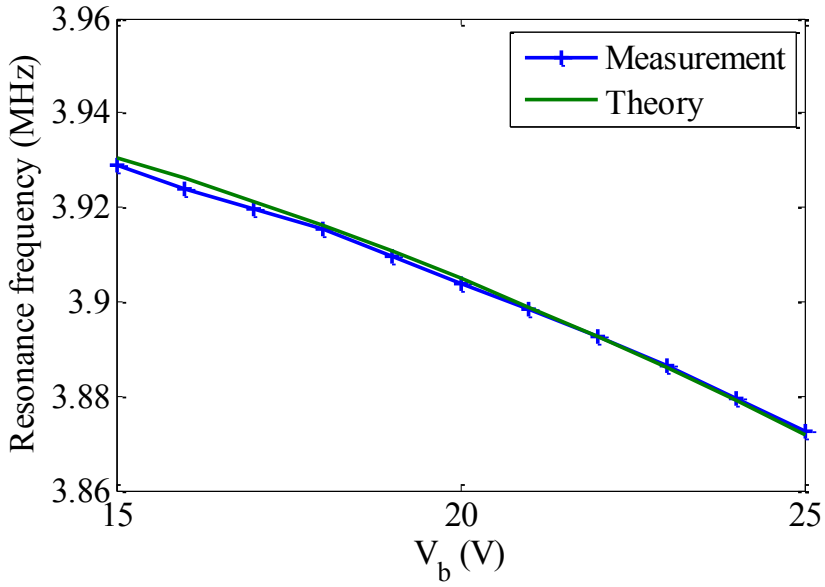

Figure 1.25: Measured electrostatic softening effect on a CCB, with simulated predictions.

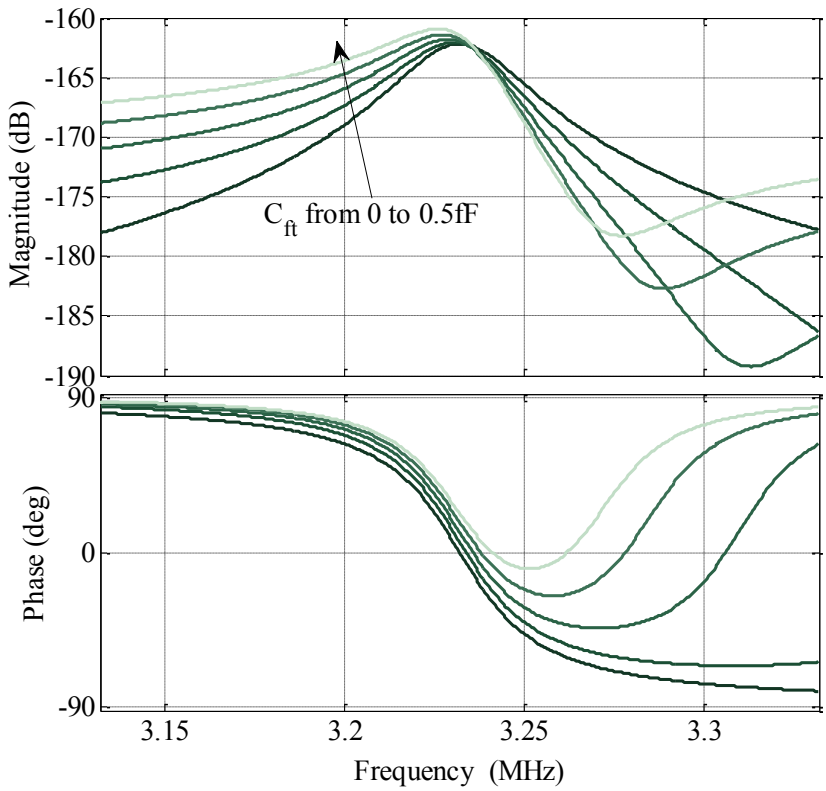

Figure 1.26: Simulated Bode diagram (input: V_{in}, output: i_{det}) of the CFB at $V_b = 20V$ and $Q = 100$ for C_{ft} varying from 0 to 0.5fF.

Note that the fully-nonlinear model of Equation (1) may also be simulated in the transient or in the steady-state regime to verify the consistency of our assumptions. For example, Figure 1.27 and Figure 1.28 shows the nonlinear steady-state amplitude response of the CCB and of the CFB for different values of the actuation voltage. This shows that the dominant nonlinearity in the CCB is the Duffing hardening nonlinearity, whereas the CFB is purely subject to softening phenomena. This also shows that by exciting the resonators with voltages lower than 1V, they remain inside their linear regime.

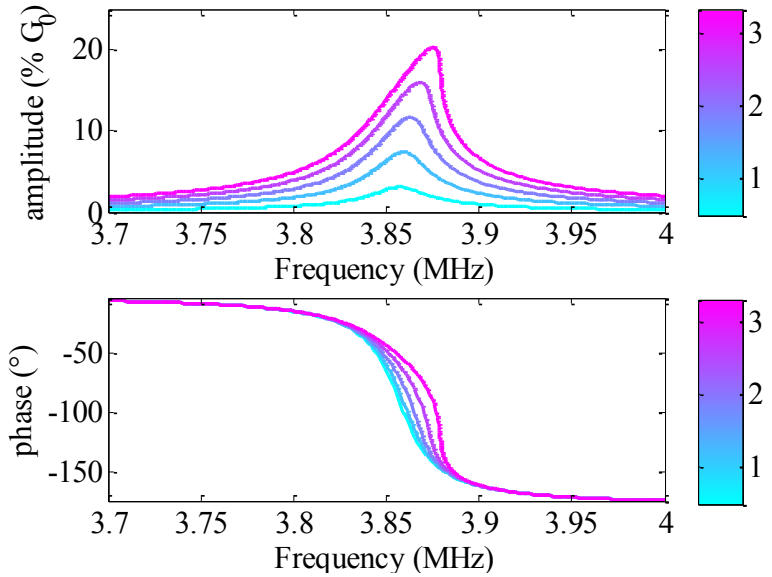

Figure 1.27: Fully nonlinear model of the CCB for different actuation voltage, at $V_b = 20\ V$, $Q = 100$ (scale from cyan to purple in Volt).

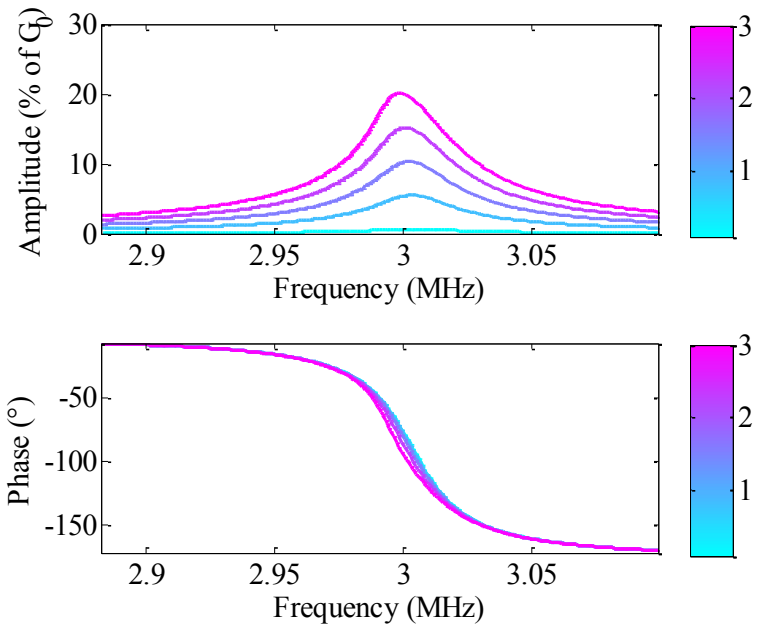

Figure 1.28: Fully nonlinear model of the CFB for different actuation voltage, at $V_b = 20\ V, Q = 100$ (scale from cyan to purple in Volt).

1.4 Differential architectures for temperature drift cancellation

This section begins by exploring the effect of temperature on the resonance frequency of the resonators, and how it is detrimental for the clocking and sensing applications. It then presents the existing architectures for cancelling this drift.

1.4.1 Effect of temperature

In Figure 1.29 and resp. Figure 1.30 is plotted the resonance frequency of a CCB structure (resp. CFB) over a 70°C temperature range. The results are obtained using the same equipment described in section 1.3.4, page 57, but since the probe-card does not handle well temperature changes, the chip was placed over a golden PCB and connected with wire bondings. The chip is then placed over a thermal chuck which enables precise temperature control. Frequency responses are extracted, and resonance frequencies obtained for different temperatures. Further details about the experimental set-up are given in section 3.6.

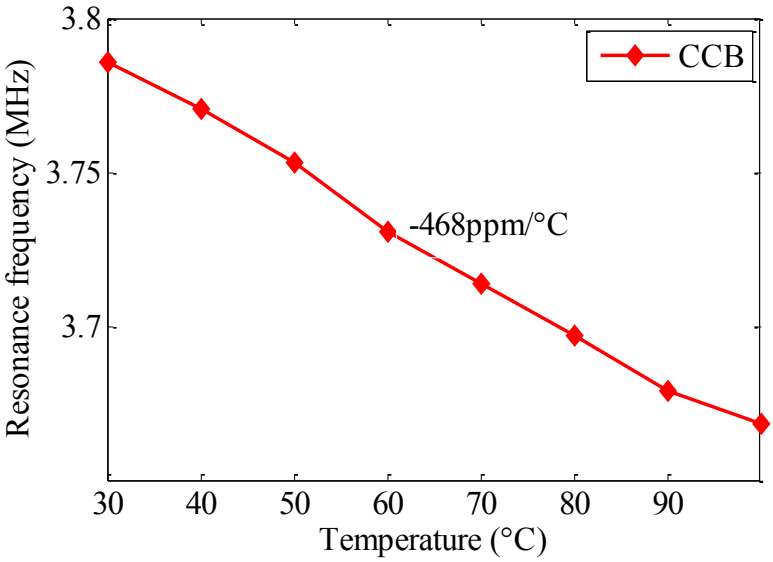

Figure 1.29: Experimental temperature dependence of the resonance frequency of one CCB.

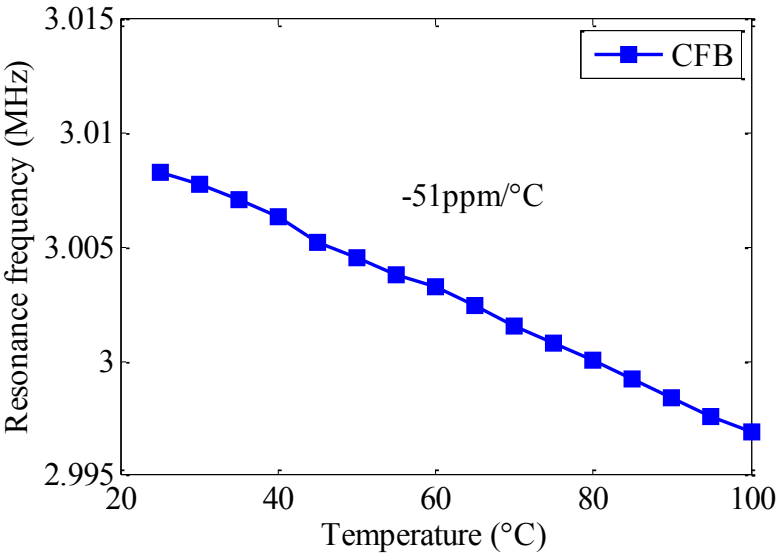

Figure 1.30 Experimental temperature dependence of the resonance frequency of one CFB.

To explain the dependence of resonance frequency on temperature, two effects are to be considered: the shift in Young modulus and the thermal expansion of the material. The dependence of Young modulus E, the density ρ, any dimension d that is not the gap and the residual stress σ_s on temperature can be expressed as:

$$\begin{cases} E(T) = E_0(1 + TCE.\Delta T) \\ \rho(T) = \rho_0(1 - 3.TCd.\Delta T) \\ d(T) = d_0(1 + TCd.\Delta T) \\ \sigma_s(T) = \sigma_{s_0}(1 + TC\sigma_s.\Delta T) \end{cases} \quad (18)$$

In this equation, TCE, $TC\sigma_s$ and TCd are the thermal coefficients expressed in °C^{-1}, $E_0, \rho_0, d_0, \sigma_{s_0}$the values measured at ambient temperature (20 °C) and ΔT the temperature shift in °C. One can write the natural pulsation of a resonator with the temperature dependence of its dimension and Young Modulus:

$$\omega_{\sigma_s,V_b}(T) = \sqrt{k_1 \frac{E(T)h(T)^2}{\rho(T)L(T)^4} + k_2 \frac{\sigma_s(T)}{\rho(T)L(T)^2} - k_3 \frac{\varepsilon_0 V_b^2}{\rho(T)h(T)G(T)^3}} \quad (19)$$

For the gap, as it shrinks when the temperature rise because the resonator thickens, its evolution with the temperature is:

$$G(T) = G_0(1 - TCd.\Delta T) \quad (20)$$

In this equation, the coefficient k_1, k_2 and k_3 are the coefficients from the denominator of the motional capacitance C_m from Table 1.8 for our geometries. The results are given in Table 1.10.

Geometry	k_1	k_2	k_3
CFB	1.02	0	1.96
CCB	41.7	12.3	3.17

Table 1.10 Values of constants k_1 and k_2 for our geometries.

The values of the temperature coefficients found in the literature, for bulk tungsten, are presented in Table 1.11. No references about the shift in the residual stress with the temperature can be found.

Material	TCd [84]	TCE [85]	TCE [86]
Tungsten	4.3ppm/°C	-87.1ppm/°C	-86ppm/°C

Table 1.11: Values of the temperature coefficients found in the literature.

In Table 1.12 we present the numerical applications of the thermal shift for the two causes (Young's modulus shift and thermal expansion) that are present in the literature, and the experimental results of the Figure 1.29 and Figure 1.30.

Cause of the shift / Geometry	Young's modulus ([85], [86])	Thermal expansion ([84])	Theoretical thermal drift	Experimental results
CFB	-45.83 ppm/°C	-4.7 ppm/°C	-50.66 ppm/°C	-51ppm/°C
CCB	-43.84 ppm/°C	-4.2 ppm/°C	-48.23 ppm/°C	-468ppm/°C

Table 1.12: Theoretical thermal drift only taking into account the Young's modulus shift and the thermal expansion, and experimental results of the thermal drift.

For the clamped-free beam structure, the experimental results fit with the values found in the literature. For the clamped-clamped beam structure, the experimental thermal drift is ten times higher than the theoretical predictions, which does not take into account the shift in the residual stress. The thermal coefficient of the residual stress to fit the experimental results for the CCB is:

$$TC\sigma_s = -1595 ppm/°C \quad (21)$$

It is explained by the fact that a tensile stress is lowered by an expansion of the length of the structure. The effect of this thermal drift on MEMS-based oscillators for clocking and sensing applications is now investigated.

1.4.2 MEMS-based oscillating loop

A MEMS oscillator is composed of a MEMS resonator and of an electronic feedback loop, as drawn in Figure 1.31. The purpose of the feedback loop is to deliver to the resonator an actuation voltage that compensates for its losses, and to maintain it in a steady-state oscillation state. The primary purpose of the feedback loop is to maintain a certain phase relation between the detected signal (motional + parasitic current) and the actuation voltage: for example, in the absence of capacitive feedthrough, imposing 0° phase-difference between V_{in} and i_{mot} ensures that the oscillation frequency is equal to the natural resonance frequency of the device. This purpose can be met by appropriate filtering of the detected signal (so-called self-oscillating loop approach, as in [87]), or by using a phase-locked loop (PLL) in the feedback loop (as in [88] or [89]). The secondary purpose of the feedback loop is to regulate the amplitude of the electromechanical oscillation. This is achieved by the use

of nonlinear elements, such as automatic amplitude control loops [90] or saturating nonlinearities [91], [92].

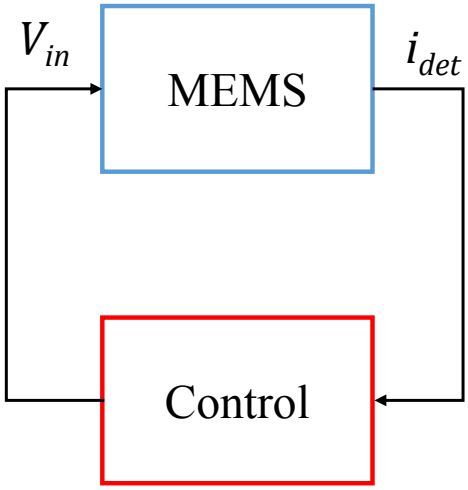

Figure 1.31 Structure of a MEMS oscillator based on a control feedback.

For timing applications, such an oscillator can be directly embedded into a digital system to provide a timing reference [93]. For resonant sensing applications, the oscillation frequency must be compared to an external frequency either through a PLL [94] or another frequency reference, or even both [42] to give an information on the measurand.

For both applications, MEMS oscillators suffer from the intrinsic defect of the MEMS resonator: its dependence on temperature, or more generally its dependence on environmental conditions (temperature, humidity, pressure). Indeed, for clocking applications, a frequency stability over an 80°C temperature range around 100ppm is required for cheap embedded systems (MP3 music players, digital cameras), around 1ppm for laptops, GPS and mobile phones, and around 10ppb for military or aerospace applications [95]. The numerical applications made in section 1.4.1 show that a MEMS resonator without compensation cannot match such requirements. On the other hand, oscillators based on quartz crystal resonators, whose temperature dependence can be diminished by choosing a proper cut [96] as shown in Figure 1.32, are used for the 100ppm node. For higher stability requirements, a compensation scheme must be embedded in any case. For sensing applications, the same drawback exists, making it a challenge to discriminate the cause of a natural frequency change.

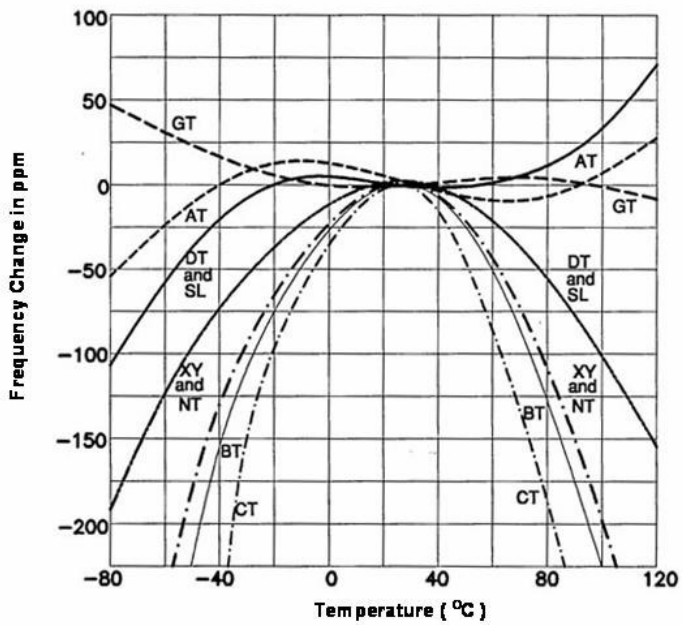

Figure 1.32 Frequency-temperature characteristics for a variety of common quartz resonator cuts [96]

1.4.3 Temperature sensors in Integrated Circuits technology

Thermal drift can be either compensated *in-situ* i.e. controlling the resonator's atmosphere with oven-based system, or compensated afterward with a post processing of the information. In both case, the temperature must be sensed. Makinwa gives a review of all existing temperature sensors available in standard CMOS technology in [97]. Two physical phenomena are exploited: the bandgap energy sensitivity to the temperature in bipolar junction transistor or the temperature-dependent propagation delay of a chain of CMOS inverters. They have a resolution between 20 mK and 1 K depending on the technology [97]. In [98] , a thermistor is used because of its 10 µK resolution, but it is not CMOS-compatible and comes at a cost of in increased electrical consumption. Using the quality factor of an encapsulated MEMS resonator in vacuum, where its dependence to the temperature is high (see [99]) has been proposed by Hopcroft [100] with the intrinsic limitation on a quality factor measurement in term of time and resolution. Moreover, these analog sensors require ADC which lowers the resolution and the time response. In the case of our CFB, reaching 1 ppm frequency stability means being able to sense a 16 mK variation for the CFB, given the -50.66 ppm/K which is already too much for the temperature sensors described in [97]. But

as seen in Section 1.4.1, one could use the resonant frequency of a MEMS resonator to sense the temperature. For example, Roshan in [101] presents a solution using two MEMS resonators with different temperature dependence, achieving a 40 μK resolution, which is close to the thermistor-based temperature sensor but is CMOS-compatible. The information given by this temperature sensor can then transferred to a micro-oven or a microprocessor to compensate the information of the MEMS-based oscillator.

1.4.4 Differential measurement and temperature compensation for clocking and sensing applications

One could think of using simultaneously the two resonators (the temperature sensor and the resonator for the dedicated application). For instance, one idea was developed by Kenny's group in Stanford. It relies on the co-integration into a micro-oven of two MEMS resonators with different temperature dependence and nearly identical natural frequencies (a block diagram of this architecture is given in Figure 1.33).When the operating temperature changes, the oscillation frequencies f_1 and f_2 change, and the difference $f_2 - f_1$ provides a high-accuracy temperature measurement. This measurement can then be used to control the temperature of the micro-oven (and also adjust the mechanical oscillation amplitude).

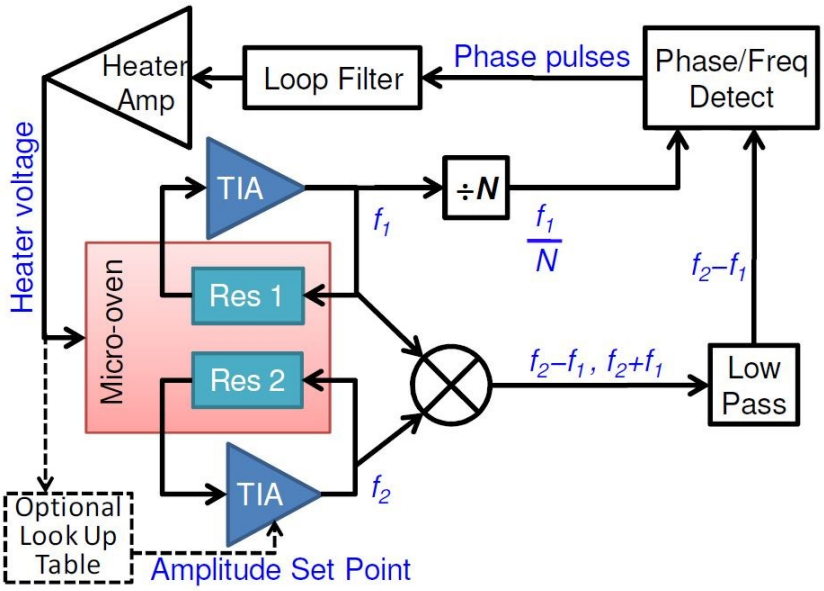

Figure 1.33 Block diagram of temperature compensation system using two MEMS resonators with different temperature dependence [102].

A frequency stability of 0.05ppm over a 100°C temperature range is achieved with this architecture. This is the same order of performance as commercially-used ovenized quartz crystals, such as C4550 (from Vectron Inernational, Inc.), but it comes at the cost of a 130mW power consumption and a level of complexity which is not necessarily desired for VLSI applications. But the main drawback is elsewhere. To fit into the same micro-oven and endure the exact same thermal drift, both resonators must be placed close to each other, and packaged into the oven. This leads to capacitive coupling between the resonators and, because of the closeness of their oscillation frequencies, may result frequency pulling and locking, and dead zones in the temperature sensing scheme. A solution was developed to address this problem: using two (or more) modes of a single MEMS, whether two bulk modes [103] with a 0.25 ppm stability over a 100 °C range, or three flexural modes [104] with a 14ppm stability over a 120 °C. It comes at the cost of more complexity. Using two MEMS with different temperature dependence is also proposed by SiTime in the Elite DualMEMS Architecture [105], with a post-processing of the information using a fractional PLL (see Figure 1.34). A 0.1ppm variation over an 80 °C temperature range is obtained.

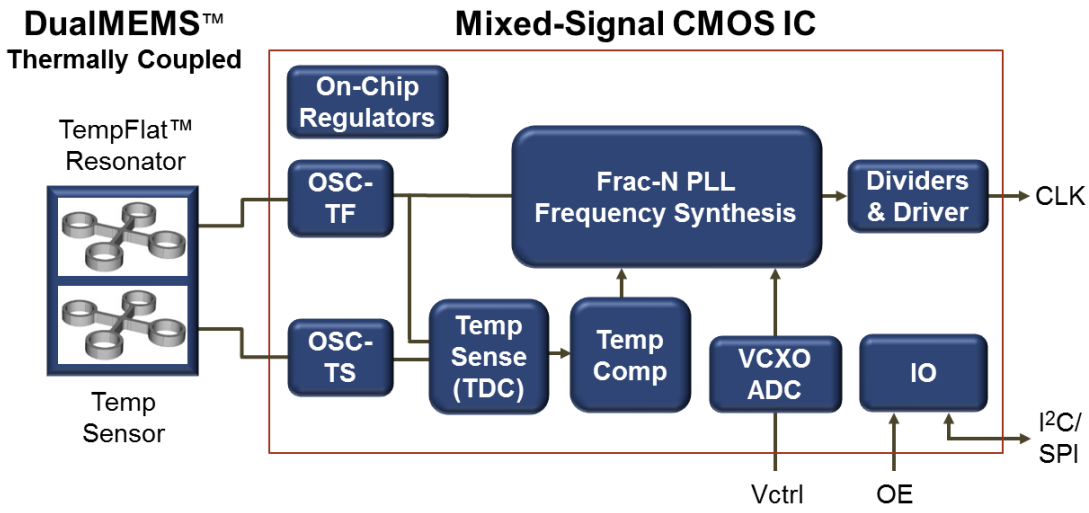

Figure 1.34 Dual MEMS temperature compensation by post-processing scheme [105].

For resonant sensing, the challenge is slightly different, since one must discriminate whether the oscillation frequency change is caused by the measurand or by an environmental change. Performing a differential measurement between two oscillators appears to be a good solution but it must be thought differently. Indeed, thermal drift (or all kind of bias that is not the measurand) must be suppressed from the output frequency. The differential approach based on two oscillators with the same dependence on the environmental drifts, but a different sensitivity on the measurand has been developed by Trusov [106], the principle and experimental results of which are presented Figure 1.35 & Figure 1.36, Chun [107] for accelerometer applications, and Cobianu [108] for gas detection.

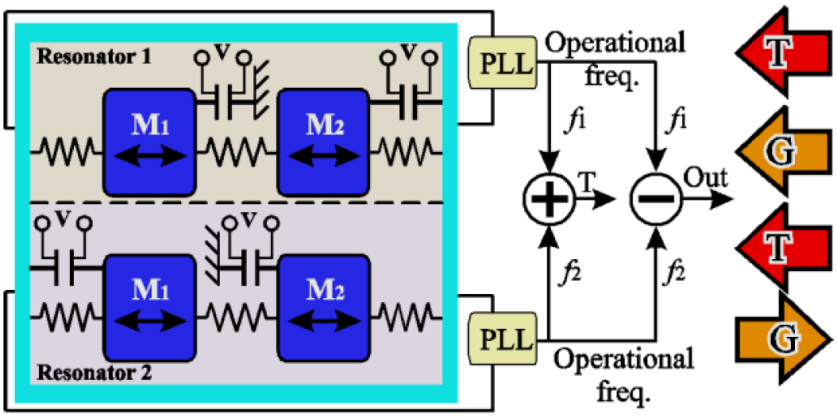

Figure 1.35: Concept of the differential resonant accelerometer of Trusov [106]. Red and orange arrows show axes of sensitivity to external acceleration and temperature (i.e. the resonators have the same temperature dependence but opposite acceleration dependence).

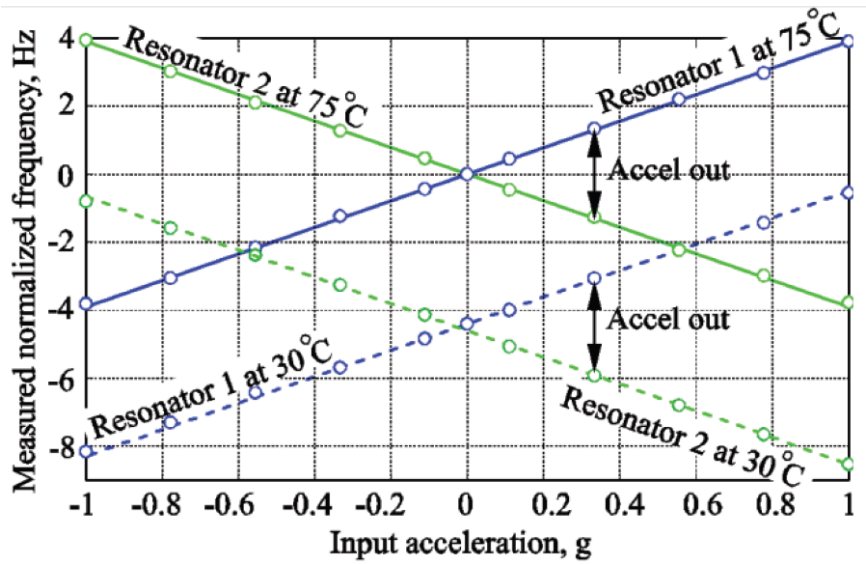

Figure 1.36 Experimental results of Trusov [106]: Differential frequency split is invariant to temperature

All these solutions enable theoretical drift-free measurement, at the cost of complex double PLL architectures, and frequency or phase comparators. Depending on the closeness of the frequencies of the two oscillators, they may also suffer from spurious couplings as described in section 1.4.4. In fact, coupling is the fundamental phenomenon limiting the use of separate oscillators for differential measurements: the only way to ensure a proper drift cancelation is to fabricate the resonators as close as possible (in order to guarantee that they are exposed to the same environmental drifts), which results in increased electrical or mechanical coupling and its resulting issues

(e.g. dead zones in the device response, as described in [102]). Dual-mode architectures with different resonant frequencies are proposed in the case of resonant strain gauge [109] (see [110] for a review).

Alternatively, some authors have proposed to enforce coupling between two resonators (or oscillators) to perform differential measurements, as described in the next section.

1.4.5 Mode localization of coupled MEMS resonators

The idea of mode localization is to enforce the intrinsic coupling of two or more MEMS resonators by either adding a mechanical coupling element [111] or fabricating them close to each other [112], [113]. In the latter case, biasing the resonators at a different voltage creates an electrostatic coupling, as shown Figure 1.37 b). In both cases, this leads to a possible transfer of energy between the resonators, represented by a stiffness element in the lumped element model of such systems (see Figure 1.38). Zhao gives an extensive review of the state of the art of this technique in [114].

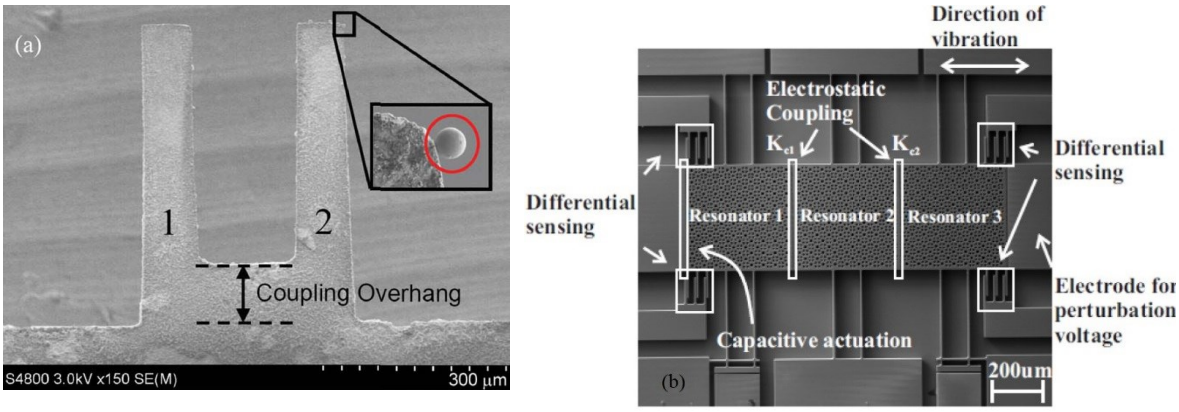

Figure 1.37 (a): mechanical coupling two resonators through an overhang [111]. (b): coupling three resonators by placing them very close one to the other [113].

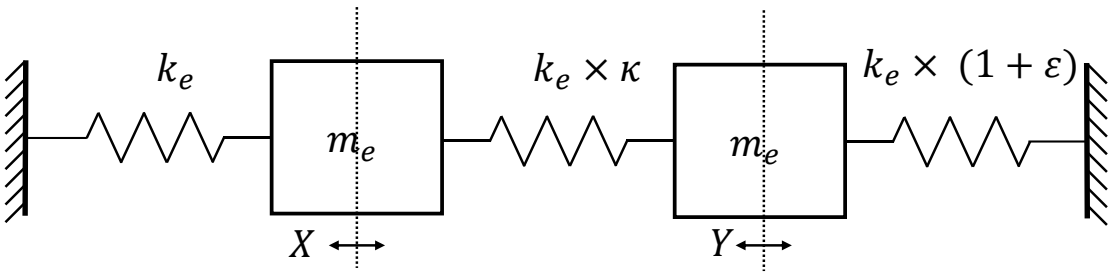

Figure 1.38 Lumped model of two coupled MEMS resonators (without the dampers). K_e is the mechanical stiffness of the resonators, κ is the constant corresponding to the coupling restoring force and ε a mechanical stiffness change corresponding to the measurand.

Such a system presents (in the case of two resonators) two vibrating modes, one mode where both oscillate in phase, and the other mode where both oscillate out of phase. The frequencies are spaced by a factor $1 + 2\kappa$. A relative change ε of the mechanical stiffness of either one of the resonators results in breaking the symmetry of the system, and generates a shift in the modal frequencies and in other output metrics as well (e.g. amplitude at resonance). In [115], Zhao gives a review of the different output metrics for three weakly coupled MEMS resonators, and their advantages and drawbacks in term of sensitivity, linearity and range. In the case of the eigenvector change, the sensitivity is [116]:

$$\frac{\partial u_i}{\partial \varepsilon} = \frac{1}{4\kappa}. \tag{22}$$

In this equation, u_i is the normalized eigenvector of the ith mode. In [114] is proved that Equation (22) leads to a sensitivity enhancement of $1/2\kappa$ if the change in eigenvector is used as the output signal. One would want a κ as small as possible to enhance the sensitivity (hence the common name "weak coupling" of this technique), but to be able to spectrally separate both modes, the condition is [117]:

$$\kappa > \frac{1}{2Q}. \tag{23}$$

This means that the quality factor of the resonators is also the maximum sensitivity of such an architecture. Typical frequency response, when one resonator is actuated, is given Figure 1.39, with and without a stiffness mismatch. The amplitude ratio is greatly increased by a small stiffness mismatch. But this sensitivity

enhancement entails no resolution enhancement, as it is proven in [117]. In fact, [117] proves that coupling two resonators for sensing applications cannot lead to any resolution enhancement if the dominant noise process is thermomechanical noise, whatever the coupling strength or mode. This is experimentally proven in the case of mutual-injection locking in this work (see sections 3.7.1 and 3.7.2)

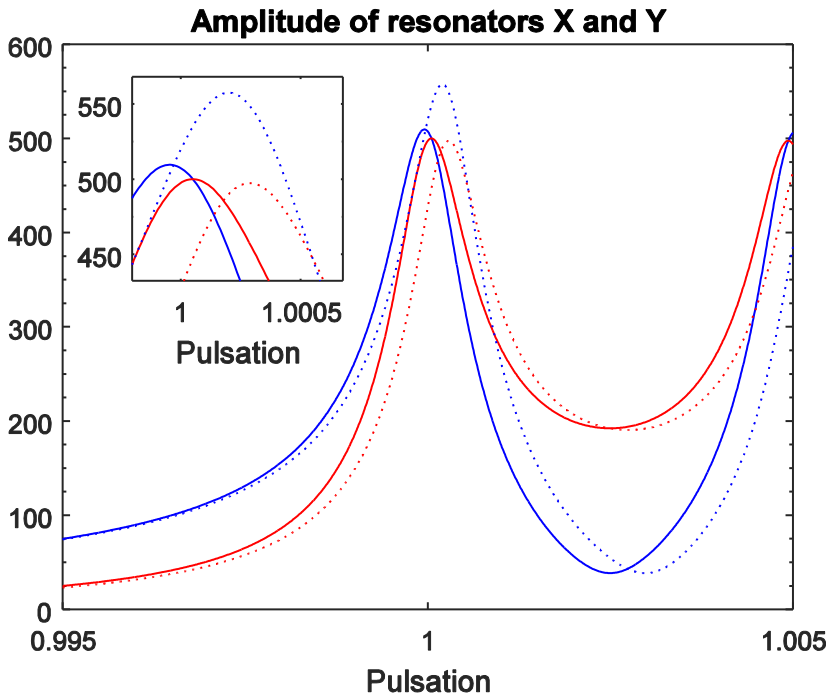

Figure 1.39 Simulated amplitude responses of X (blue) and Y (red) as defined in Figure 1.38 for varying pulsation, when $Q = 1000, \kappa = 5.10^{-3}$, $\varepsilon = 0$ (full curves) or $\varepsilon = 10^{-3}$ (dotted curves) [117].

Another benefit of this technique is the fact that it is intrinsically differential, because only ε affects the output metrics. This enables drift-free measurements, as experimentally demonstrated by Thiruvenkatanathan in [116]. This differential sensing is usually conducted in open-loop configuration: an input frequency is swept at the input of one or both of the resonators, and the output amplitudes are recorded and exploited (see Figure 1.40). Some research is being conducted to make this technique "closed-loop" [118], with the first experimental results [119]. In this case, two amplitude measurements need to be performed at the same time. Recently, a phase measurement was suggested [117], with no experimental results so far. An alternative approach is to actively couple the resonators through their actuation voltages, and force

them to oscillate at the same frequency. The benefits to be drawn from the synchronized operation of MEMS oscillators is described in the next section.

1.4.6 Synchronization of oscillators

The synchronization of two clocks was first observed by Huygens during the XVII century, as reported in [120]. It involves two independent clocks placed close to each other. The movement of one of them (i.e. its output) will affect the actuation of the other (i.e. its input) and vice versa. If their natural frequencies are close enough, and depending on the coupling mechanism, they will eventually synchronize into oscillating at the exact same frequency, even though a slight mismatch in their natural frequencies remains. A very simplified schematic of such systems is given Figure 1.40, to be compared with the mode localization approach described in the section 1.4.5.

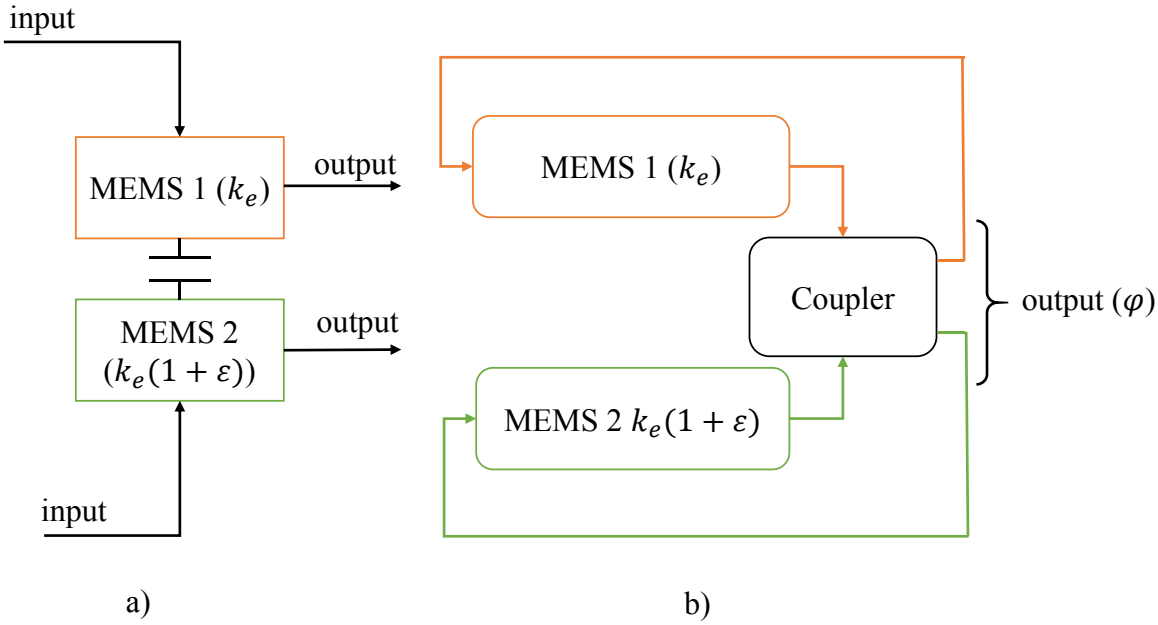

Figure 1.40 a): block diagram of two passively coupled MEMS resonators (mode localization technique) for the sensing of a mechanical stiffness mismatch ε. b): block diagram of two actively coupled MEMS resonators through their actuation for the sensing of a stiffness mismatch ε.

The first extensive study of these injection locking phenomena was done by Adler in 1946 [121]. It deals with the case of an oscillator into which a current is injected from an external frequency reference, whereas in Huygens' case, both oscillators were affecting each other (i.e. were in "mutual injection"). The fundamental

equation (known as "Adler's equation") governing the dynamics of the phase difference between the synchronized external frequency reference and the oscillator is derived in [121] and experimentally validated using LC tank oscillators. It is extended to LC oscillators in mutual injection by Mazzanti [122] and Mirzaei [123], in order to study the properties of quadrature oscillators, which produce two synchronous periodic signals with a stable, 90 ° phase-difference, as required in QAM modulation and demodulation, with a 3 dB reduction of phase noise arising from white and flicker noise. Soshani extended this phase noise reduction property to any pair of synchronized oscillator in [124], and Mattheny proved it experimentally in the case of NEMS resonators in [125]. Finally, Chang proved in [126] that, in the case of N synchronized resonators, the phase noise is divided by N. The frequency locking range was studied by Agrawal in [127].

Mirzaei also proved in [123] that the exact value of the phase difference depends on the natural frequency mismatch between the oscillators (resulting from the fabrication process for instance). While this sensitivity to mismatch of the phase difference of quadrature oscillators may be a drawback for quadrature clocking applications, it can be turned into advantage for adjusting the phase difference manually [128], or for sensing purposes. In [129], it was shown that the phase-difference of a quadrature MEMS oscillator could be used as a high-sensitivity measurement of the stiffness mismatch between the resonators. A generic expression for the phase difference variation in this case is [123]:

$$\frac{\partial \varphi}{\partial \varepsilon} = \frac{Q}{m}. \tag{24}$$

In this generic equation, m is a coupling factor which depends on the coupler's architecture (possibly $m \leq 1$). This means that tracking the phase difference can enhance the sensitivity by a factor higher than Q (depending on the coupling architecture), but comes at the cost of a reduced locking range. Finally, it is intrinsically differential as well, since any physical quantity equally affecting both resonators' natural frequency leaves the phase difference unchanged.

This section presented the physical concept of resonance, and how it could be used to make powerful tools for embedded systems (clocks and sensors). Then it gave

an overview of the MEMS resonators, and why they are good candidates for such systems. A mathematical modelling of the two MEMS resonators used in this work was given. And as the thermal drift raised as an issue for sensing and clocking application, three techniques were analyzed for drift free resonant sensing: the frequency difference, the mode localization and the synchronization, each one with benefits and drawbacks, as summed-up in Table 1.13. The next part describes the theoretical framework of the synchronization and one possible implementation for a co-integrated synchronized oscillator.

Technique	☺	☹
Frequency difference	- Infinite range. - Ease of implementation. - "Quasi-digital" output (frequency difference).	- Extensive electronics (double PLL, divider, subtraction). - Parasitic coupling.
Mode localization	- Sensitivity enhancement ≤ Q. - Good locking range.	- Analog output (amplitude, amplitude ratio). - Open-loop.
Synchronization	- Sensitivity enhancement potentially ≥ Q. - Close-loop - "Quasi-digital" output (phase difference). - Simple electronics (digital coupler).	- Reduced locking range (compromise with the sensitivity).

Table 1.13: Advantages and drawbacks of three techniques for drift-free resonant sensing

Chapter 2 Design and integration of a monolithic CMOS/MEMS Mutually Injection-Locked Oscillator

This section gives an account of the electronic design of an integrated CMOS/MEMS mutually injection-locked oscillator (MILO). Sub-section 2.1 addresses the design constraints that must be met by the electronic part of the system in order to operate CMOS/MEMS MILOs as differential resonant sensors in an optimal manner. Sub-section 2.2 describes the integration of the CMOS readout associated with the MEMS resonators described in section 1.2.5 to form the "so-called" CMOS-MEMS resonators. Section 2.3 and 2.4 detail block-by-block the integration of the digital coupler, and each block's performance. The layout of the entire device is then designed and additional simulations are operated, described in section 2.5 yielding slightly different performances. The simulated dependence of the electronics to the temperature is finally investigated in section 2.6.

2.1 Design guidelines for MILOs

In [130], the synchronization of two resonators by mutual injection is studied in depth, in the case when each resonator is driven with a signal which is a nonlinear mixture of the two resonator outputs. Since [130] is extensively used in this work, it is recalled in Annex 1. Under specific mixing conditions, provided the natural frequencies of the resonators are tuned, synchronization occurs: the two resonators oscillate at the same frequency, and are locked in phase. As already mentioned, in this synchronized state, the phase difference between the resonator outputs is highly sensitive to any natural frequency mismatch between the two resonators. The main properties of such architectures (locking range, response time, sensitivity and resolution) are established in [130]. This sub-section tries to take a different approach,

aimed at electronic designers, instead of re-going through the control-theoretical calculations of [130].

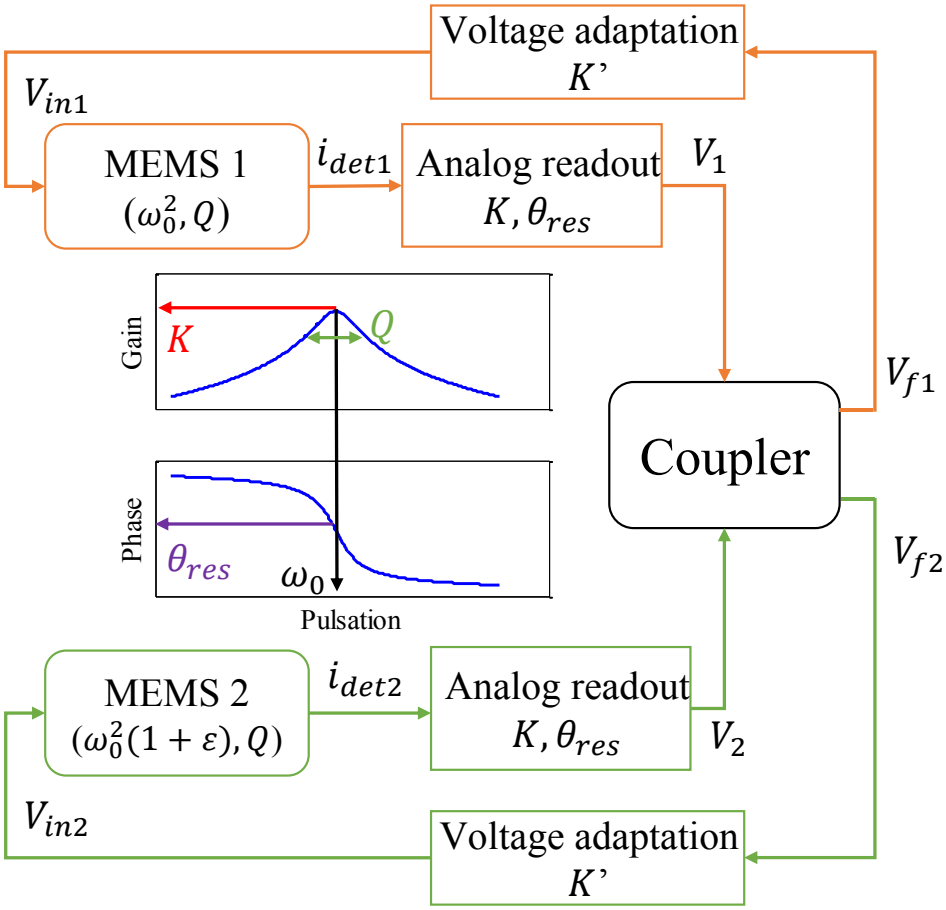

Figure 2.1: High-level schematic of our proposition for the synchronization of two resonators by injection-locking.

A high-level schematic of a MILO architecture is shown in Figure 2.1. The resonators, readouts and voltage adaptation stages of each branch have the same nominal characteristics. The resonators (a detailed model of which was given in section 1.3) are characterized by their quality factor Q and natural pulsation ω_0. The analog readouts have transimpedance gain $K > 0$ (between the current output by the resonator and the readout output voltage) and phase θ_{res} at ω_0. The voltage adaptation stages are characterized by a non-dimensional gain $K' > 0$. The system-level architecture of the coupler is shown in Figure 2.2. It is characterized by a cross-coupling gain γ and two phase-shifting elements Ψ_{self} and Ψ_{mut}.

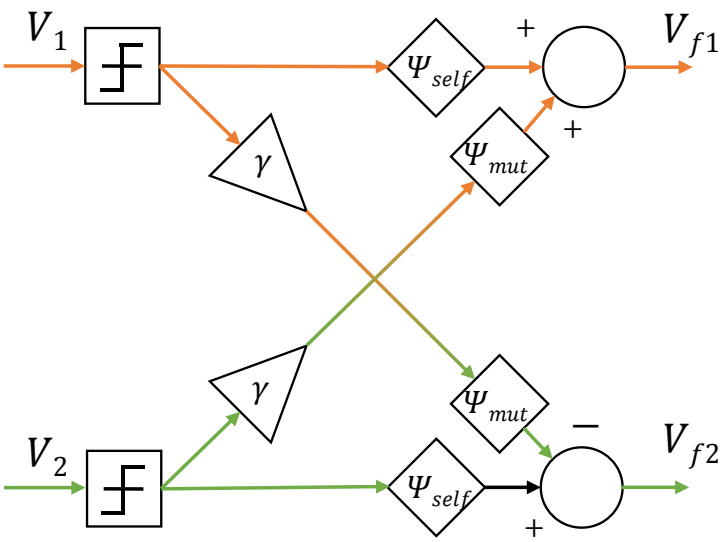

Figure 2.2: Low-level schematic of the architecture of a generic coupler.

When $\gamma = 0$, the system of Figure 2.1 reduces to two uncoupled self-oscillating loops. Because of the comparator in each loop, the Barkhausen criterion reduces to a single condition on the feedback phase, which is valid provided $K > 0$ and $K' > 0$. The pulsation of oscillation ω is equal to ω_0 provided:

$$\Psi_{self} = -\theta_{res} \,. \tag{25}$$

Note that, if this criterion is not exactly met, each loop still oscillates, but at a pulsation slightly off from ω_0, and with a decreased frequency stability. Thus, equation (25) can be used as a guideline for a designer, aiming at the best oscillator performance.

A similar approach can be used when $\gamma > 0$, i.e. when the two loops are in mutual injection. The drive voltage of each resonator is then a linear combination of the phase-shifted comparator outputs. As in the single oscillator case, the best performance is obtained by setting the pulsation of oscillation ω to ω_0 [130]. Since a MILO has three design degrees of freedom instead of one for a single oscillator, it is also possible to choose the nominal value φ_0 of the phase difference φ between V_1 and V_2. This is useful in the context of a resonant sensing application.

Because of the comparators, as in the single oscillator case, the Barkhausen criterion in each loop reduces to:

$$\begin{aligned} &\sin\left(\theta_{res} + \Psi_{self}\right) - \gamma \sin(\theta_{res} + \Psi_{mut} + \varphi_0) = 0 \\ &\sin\left(\theta_{res} + \Psi_{self}\right) + \gamma \sin(\theta_{res} + \Psi_{mut} - \varphi_0) = 0, \end{aligned} \tag{26}$$

provided K, K' and γ are positive. With the nominal phase difference $\varphi_0 = \pi/2$, this boils down to a single equation:

$$\sin\left(\theta_{res} + \Psi_{self}\right) - \gamma \cos(\theta_{res} + \Psi_{mut}) = 0. \tag{27}$$

In the present work, the choice to impose $\Psi_{mut} = \Psi_{self} \triangleq \Psi_{res}$ is made, leading to:

$$\Psi_{res} = -\theta_{res} + \tan^{-1}(\gamma)\,. \tag{28}$$

The case $\gamma = 1$ is optimal as far as frequency stability is concerned and also is of practical interest, since the mixer can then be implemented with digital blocks [130] [1], as shown in sub-section 2.3.1. Equation (28) then reduces to:

$$\Psi_{res} = -\theta_{res} + \pi/4\,. \tag{29}$$

Thus, provided (29) is verified, the nominal self-oscillation state of the MILO is $\omega = \omega_0$, and $\varphi = \pi/2$. When a relative stiffness mismatch ε exists between the two resonators, the phase difference and the pulsation shift away from their nominal values. From [130], the oscillation remains stable provided:

$$|\varepsilon| < \varepsilon_{lock} = \frac{\sqrt{2}}{\mathrm{Q}}\,. \tag{30}$$

The nominal sensitivities of ω and φ to the relative stiffness mismatch ε are then:

$$\begin{cases} S_\varphi \triangleq \dfrac{1}{\varphi_0}\dfrac{\partial\varphi}{\partial\varepsilon}\Big|_{\varepsilon=0} = \dfrac{2}{\pi}Q \\ S_\omega \triangleq \dfrac{1}{\omega_0}\dfrac{\partial\omega}{\partial\varepsilon}\Big|_{\varepsilon=0} = \dfrac{1}{4} \end{cases}, \tag{31}$$

[1] It should be mentioned that, in [122], the phase-shifting elements Ψ_{self} and Ψ_{mut} are chosen so that both terms on the left-hand side of (27) vanish independently of the cross-coupling coefficient, i.e.:

$$\Psi_{self} = \Psi_{mut} - \pi/2 = -\theta_{res}.$$

Although this approach has a slightly better stability compared to the one used in the present work and the same sensitivity to ε, when $\gamma = 1$, it cannot be implemented with digital blocks, which is the main reason why it was not chosen.

One can finally define the sensitivity enhancement ratio, corresponding to the ratio between the two outputs of the MILO (the phase difference and the frequency). These quantities are normalized, and one can write:

$$S_{MILO} \triangleq \frac{\omega_0}{\varphi_0}\frac{\partial\varphi}{\partial\omega} = \frac{8Q}{\pi}, \tag{32}$$

Since $Q \gg 1$, it is clear that the phase difference is much more sensitive to ε than the pulsation.

For $Q_1 \neq Q_2$, the model from [130] can be derived, yielding:

$$\begin{cases} S_\varphi = \frac{4}{\pi}\frac{Q_1 . Q_2}{Q_1 + Q_2} \\ S_\omega = \frac{1}{2}\frac{Q_2}{Q_1 + Q_2} \end{cases}. \tag{33}$$

It means that S_φ is mainly determined by the lower quality factor of both resonators. However, the sensitivity ratio S_{MILO} is only affected by Q_1:

$$S_{MILO} = \frac{8Q_1}{\pi}. \tag{34}$$

Note that, if (29) is not exactly met or if the quality factors of the resonators differ, the oscillation state and sensitivities will be slightly off from their nominal values, and the stability of both φ and ω may be decreased. On the other hand, the exact values of the transimpedance gains and the voltage adaptation gains have in theory no impact on the performance of the MILO.

Equation (29) is used in the rest of this work as a design objective. One can present the coupler as composed by perfect blocks (i.e. no delay, no rise & fall time) and two phase-shift blocks, one for each side, merging the delays and rise & fall time of every blocks (see Figure 2.3). The sum of all the phase shifts in these blocks is Ψ_{res}, it is supposed to be equal for both sides since the architecture is symmetrical.

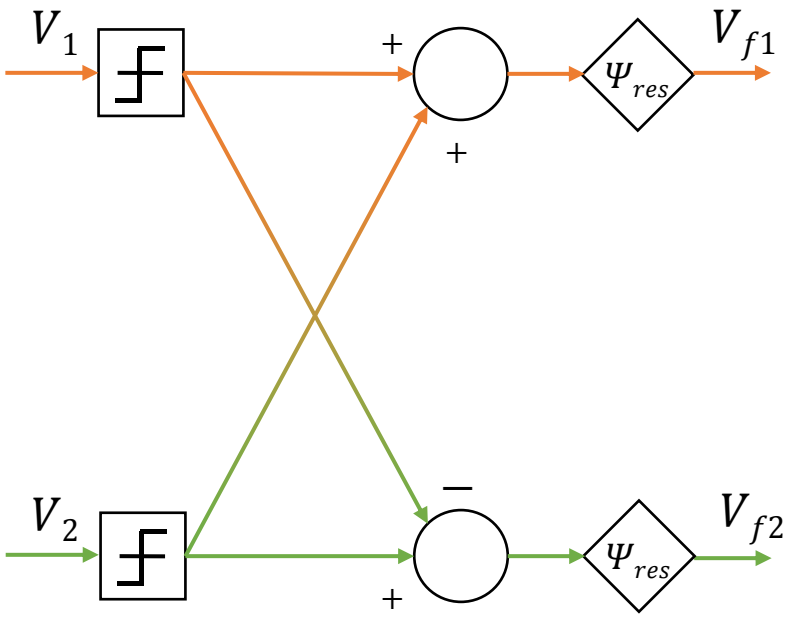

Figure 2.3: Low-level schematic of the coupler implemented in this work

In the following section, the design of the analog readouts is addressed. The design of the digital coupler taking (29) into account is addressed in sub-section 2.3. The resulting MILO is schematically represented in Figure 2.4. Most of it is monolithically co-integrated. Besides the expertise of the ECAS group in monolithic CMOS/MEMS integration, there are several reasons why this is an interesting choice for a MILO-based differential sensor:

- fabricating the two resonators on the same chip reduces the fabrication variability in terms of resonance frequency, as shown in section 3.2.1.
- the distance between the resonators is reduced, thus ensuring that temperature drifts affect them equally.
- precise extraction of the parasitic elements of the design is made possible at the simulation stage. This enables accurate estimation of the phase of the coupler, and an optimization according to Equation (29).

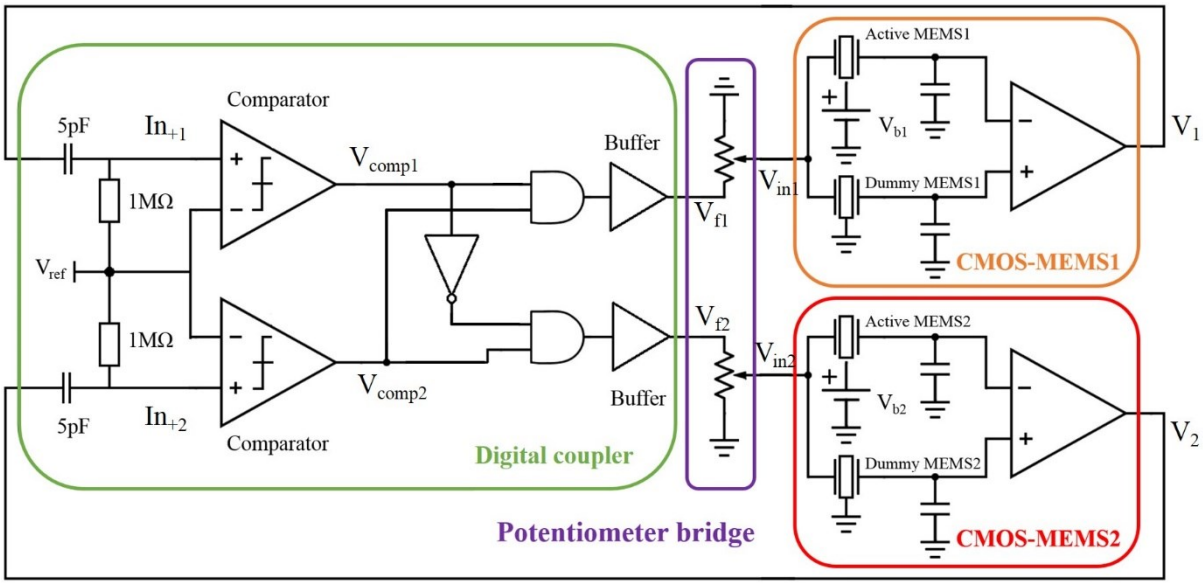

Figure 2.4: Schematic of the MILO. Only the potentiometer bridge is not co-integrated.

In fact, previous implementations of this architecture with separately fabricated blocks (i.e. one PCB for the coupler, and one for each resonator) [129], [131] were shown to be limited because of imperfect drift cancellation due to the distance separating the resonators, and phase delay estimation due to the interconnections between the PCBs.

In this work, the potentiometer bridge is not co-integrated because, as this work is the group's first experience of complex co-integration (i.e. analog and digital with multiple blocks), precise open-loop characterization is required to ensure to well-function of several blocks that are co-integrated for the first time. One must be able to open the loop, and the connection between the coupler and the resonators' excitation makes the most sense because it's digital thus robust to noises and interferences. Moreover, this allows for an easier control of the actuation voltage of the resonators. However, the digital coupler must be able to output enough current to load the connection pad and the wiring to connect the bridge to the chip. This is detailed in subsection 2.3.3.

2.2 CMOS-MEMS readout design

This section describes the design and the co-integration of a CMOS amplifier with the MEMS resonator described in sub-section 1.2.5. The design of the readout is presented, and some extracted simulation results are given (i.e. post-layout model of the amplifier, with extracted resistance and capacitance arising from the design, coupled with the BVD model of the resonators developed in section 1.3). These simulation results, in particular the value of θ_{res}, can be used to design the digital coupler according to Equation (29) as presented in section 2.3.

As shown in sub-section 1.3.4, the output current i_{det} of the MEMS resonators considered in this work is of the order of 10 nA at the resonance (for a CFB, given $V_b = 20\ V$, and $V_{in} = 1\ V$). A transimpedance amplifier is required to transform this current into an exploitable voltage (i.e. with amplitude high enough to trigger the comparators of the coupler). The impedance in which the output current is sensed fixes the phase delay of the amplifier, as long as the resonance frequency is inside the bandwidth of the amplifier. In the case of a capacitive readout, in which the current is integrated into the parasitic capacitances of the output electrode of the MEMS and of the input transistor of the amplifier (see Figure 2.5), the phase delay between the detected current and the output voltage V_1 should then be $\pm 90°$, depending on the sign of the gain of the amplifier. Since, at resonance, the phase between the input voltage V_{in1} and the output current of the resonator is 0 °, the value of θ_{res} should also be $\pm 90°$.

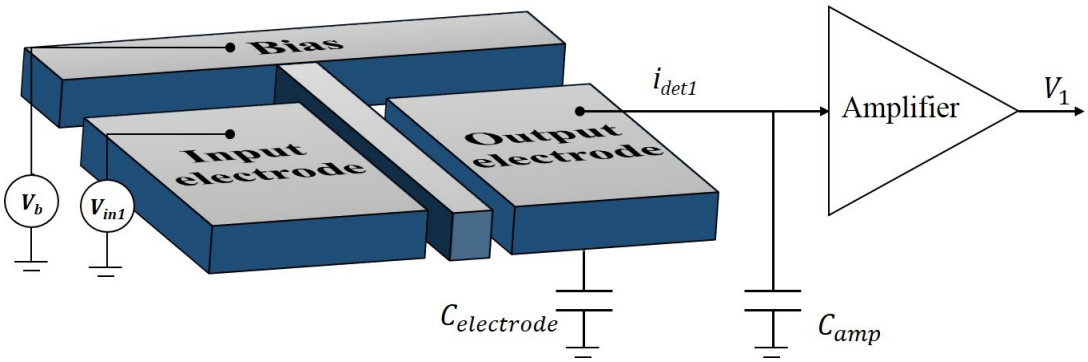

Figure 2.5: Capacitive current sensing scheme. The resonator's output current i_{det} is the sum of the motional current, generated by the movement of the beam, and

of the parasitic current, generated by the feedthrough capacitance (not represented here).

The amplifier used in this work was previously designed and presented in [132]. Its transistor-level schematic is given in Figure 2.6.

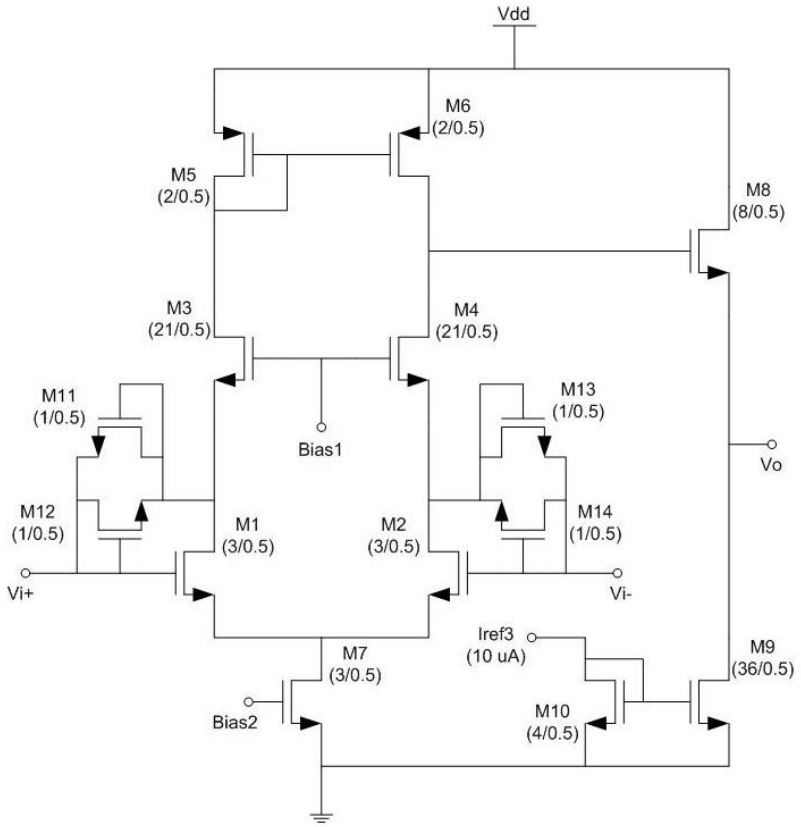

Figure 2.6: Transistor-level circuit scheme of the differential sustaining circuit based on a cascode voltage amplifier [132].

The biasing of the amplifier inputs (Vi+ and Vi- in Figure 2.6) is achieved by the implementation of two NMOS transistors (M11 to M14 in Figure 2.6) in anti-parallel configuration working in their sub-threshold region [62], [133], [132]. It exhibits a high resistance (10^{12} Ω [132]), thus a low input-referred current noise (80 fA/Hz [132]).

The input stage is a differential pair (M1 to M6 in Figure 2.6), which allows for a compensation of the feedthrough effect described in section 1.3.3. At each input one resonator is connected: both resonators are nominally identical and excited by the same voltage, but only one of them is biased (see Figure 2.7). Thus, according to Equation (14), the biased (or active) resonator outputs the sum of the parasitic and the motional

current $i_{par} + i_{mot}$, whereas the unbiased (or dummy) resonator outputs the parasitic current i_{par} only. In the differential stage of the amplifier, a subtraction is operated. Thus, the output voltage is nominally free of the effect of the parasitic current i_{par}. This scheme is only valid as long as the two MEMS are identical, in order to have the exact same parasitic current for a given excitation voltage. This is ensured by fabricating them as close as possible (see Figure 2.8 for the layout). In this work, the active MEMS is placed on the inverter input (see Figure 2.7). This means that inside the bandwidth of the amplifier, in this configuration and supposing a good feedthrough cancellation, $\theta_{res} = 90°$.

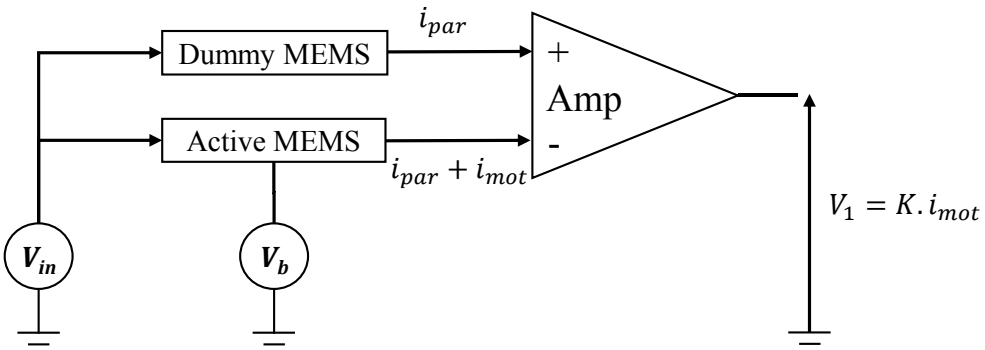

Figure 2.7: block-level schematic of the feedthrough compensation scheme

The amplification is provided by a differential cascode amplifier (M1 to M6), and is buffered by a source-follower output stage (M8 and M9, biased by M10).

The electrical consumption is 1.5 mW for a supply voltage of 3.3 V [132]. The size is 300 µm × 150 µm. A microphotograph and layout image of the entire amplifier (i.e. sustaining amplifier + biasing block + buffer) is presented in Figure 2.8.

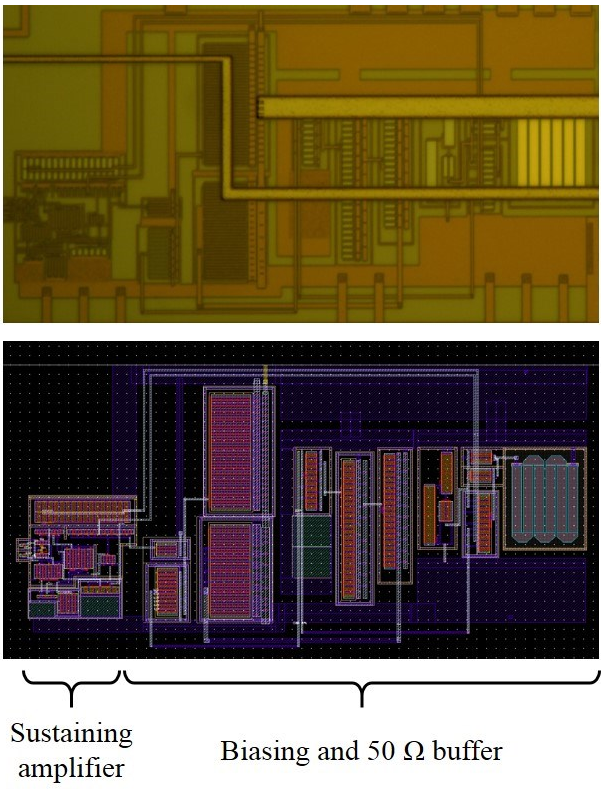

Figure 2.8: Entire amplifier: up) microphotograph, down) layout

The transimpedance gain is set by the parasitic capacitance in which the input current is integrated. As presented in the layouts of Figure 1.12 and Figure 1.13, the electrodes do not have the same size for the CCB and the CFB, thus the amplifier gain is different in both cases. To take this parasitic capacitance into account in the amplifier's extracted model, it must be added manually. It is estimated geometrically, given the electrode's dimensions (without considering any fringing fields) and the distance between the substrate and the MET3 (3 µm). The relative permittivity of the SiO_2 is 3.9. The parasitic capacitances corresponding to CCB and CFB resonators are given in Table 2.1. In order to have the lowest value of the parasitic capacitance (and thus, the highest transimpedance gain), the resonators are placed as close as possible to the input of the amplifier.

The actual value of θ_{res} is determined by the bandwidth of the amplifier, and the natural frequencies of the MEMS resonators (CFB and CCB). The simulated Bode diagram of the amplifier in gain and phase is given in Figure 2.9 and Figure 2.10, and the values of gain and phase for the CCB and CFB are presented in Table 2.1. The

bandwidth of the amplifier is estimated at 9.7 MHz thanks to the same type of simulation with a wider range.

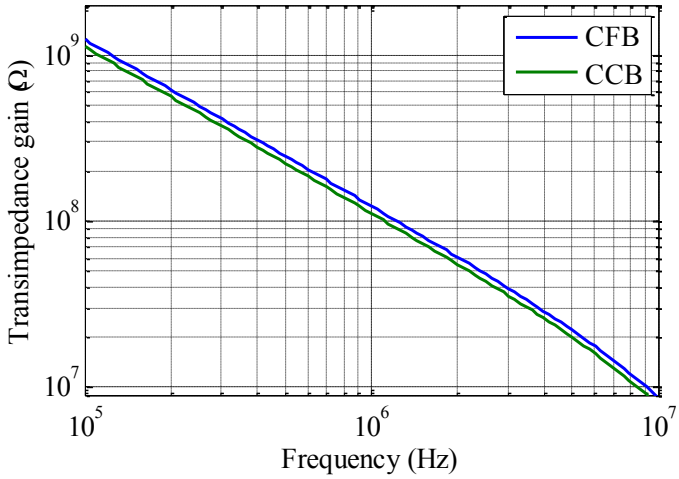

Figure 2.9: Transimpedance gain of the amplifier: extracted simulation + added $C_{electrode}$ capacitance corresponding to the resonator's geometry for the two cases.

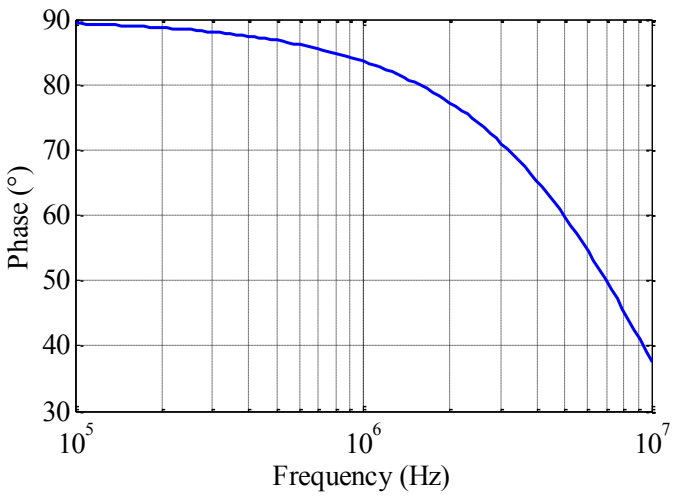

Figure 2.10: Phase of the amplifier: extracted simulation, which is not affected by $C_{electrode}$.

Geometry	f_0	$C_{electrode}$	Gain K @ f_0	Phase @ f_0: θ_{res}
CCB ($\sigma_s = 0$)	2.6 MHz	4.6 fF	41 MΩ	72.5 °
CCB ($\sigma_s = 475\ MPa$)	3.9 MHz	4.6 fF	26 MΩ	65 °
CFB	3.05 MHz	1.3 fF	39 MΩ	71 °

Table 2.1: Electrode's parasitic capacitance, transimpedance gain and phase of the amplifier at the resonance frequency of the MEMS.

As it is seen in Figure 2.10, the CCB and CFB are working on the edge of the bandwidth of the amplifier. This means that its phase depends on the considered frequency. This is a difficulty in the design of the feedback loop in the case of the CCB, because the resonance frequency is a priori unknown since it is related to the residual stress arising from the fabrication process, which is not necessarily predictable (see the difference of θ_{res} arising from the residual stress in the case of CCB resonators in Table 2.1). Concerning the gain, it depends on the frequency as well but the amplifiers load comparators (Figure 2.4). As long as the gain is high enough to trigger them, the gain's dependence on the frequency does not matter. Given the motional resistances at a bias voltage of 20 V (58 MΩ for the CCB, 91 MΩ for the CFB for a quality factor of 100 in both cases), the CMOS-MEMS resonators should behave like voltage dividers of ratio 0.7 for the CCB and 0.3 for the CFB (i.e. output 700 mV (resp. 300 mV) for an excitation voltage of 1 V for the CCB (resp. CFB). Finally, the amplifier's output is auto-biased, and this DC voltage is related to the input charge of the amplifier.

2.3 Integration of the NOT QUADDRO coupler

2.3.1 Digital mixer principle

In the case $\gamma = 1$, the operations (+|+) and (+|−) of Figure 2.2 can be done by combining logic gates instead of using analog adders / subtractors. Two "equivalent" mixer architectures based on logic gates are represented in Figure 2.12. In Figure 2.11, the output signals of these digital architectures are compared to those output by the analog mixer of Figure 2.3. Although the digital mixers output binary-valued signals, as opposed to the three-valued output of the analog mixer, the input-output phase-relationship is the same.

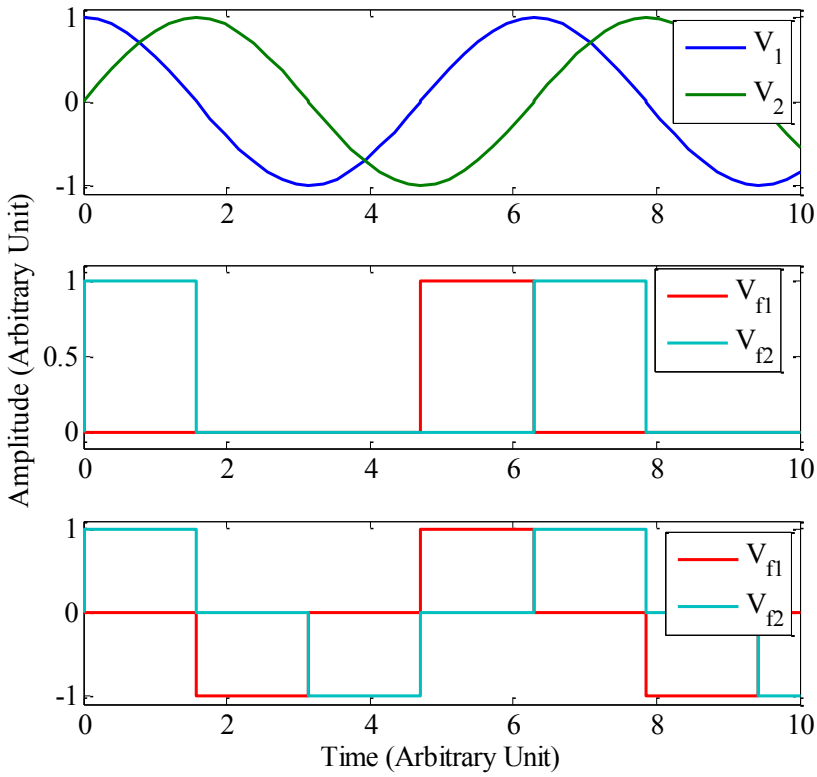

Figure 2.11: High-level Simulink simulation. Top: mixer's inputs V_1 and V_2. Middle: output voltages of the digital mixer of Figure 2.12 with $\Psi_{res} = 0$. Down: output voltages of the analog mixer of Figure 2.3 with $\Psi_{res} = 0$.

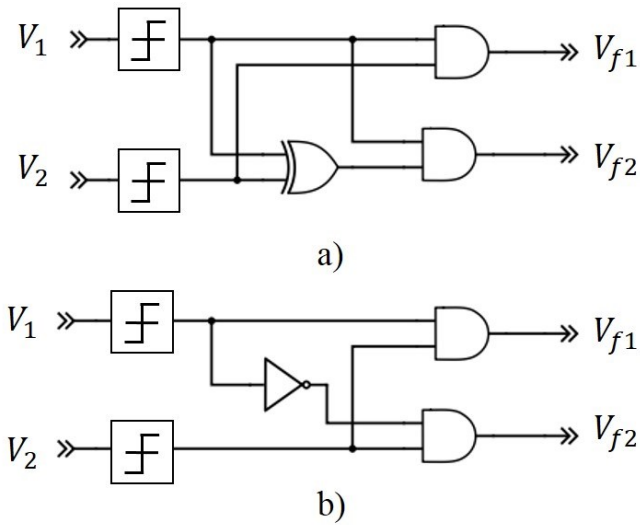

Figure 2.12: Two possible implementations for the QUADDRO coupler phase and gain conditions: a) is implemented in [129] and [131], while b) is studied in [134] and implemented in this work.

The XOR QUADDRO (Figure 2.12 a) has the exact same truth table as the NOT QUADDRO (Figure 2.12 b) but if the propagation delays in the logical gates is not negligible, the XOR gate can lead to apparition of unwanted spikes at the mixer output [129]. This is why the NOT QUADDRO architecture was chosen for implementation.

Another benefit from this architecture is the fact that the phase difference φ can be calculated from the values of the duty cycles of V_{f1} and V_{f2}: DC_1 and DC_2 according to :

$$\varphi = 90 \cdot \left(1 + \frac{DC_1 - DC_2}{DC_1 + DC_2}\right). \tag{35}$$

Given the fact that the sum $DC_1 + DC_2$ is fixed (nominally 0.5, but which value can vary due to the saturation of the amplifiers, as described in subsection 3.3), one can calculate φ (in degrees) based on the knowledge of either DC_1 or DC_2 :

$$\begin{cases} \varphi = 180 \cdot (1 - 2DC_2) \\ \varphi = 360 \cdot DC_1 \end{cases}. \tag{36}$$

The relation between φ, DC_1 and DC_2 is illustrated with high-level simulation of the mixer presented in Figure 2.13 and Table 2.2, showing perfect agreement, which is expected since the high-level simulation does not take any non-ideality into account. This is a great asset when it comes to VLSI implementation since V_{f1} can be directly fed into the digital system, without requiring any analog-to-digital converter or counter. The resulting coupling circuit is composed of two comparators, two AND gates, one inverter gate (i.e. the mixer), but also requires two bias tees, if only to eliminate the DC component of the amplifier outputs, and a two-sided digital buffer. The design of these blocks is detailed in the following sub-sections, with a focus on how much each block contributes to the phase-shift in the loop, in order to verify (29). The results in this sub-section are based on schematic-level simulation to extract the theoretical performances of every block. In section 2.5, the complete chip design is explained, and the performance of each block is simulated taking into account the parasitic elements arising from the overall layout (i.e. the resistive connections between the blocks, the capacitive coupling with the substrate, the capacitance corresponding to the connection pads).

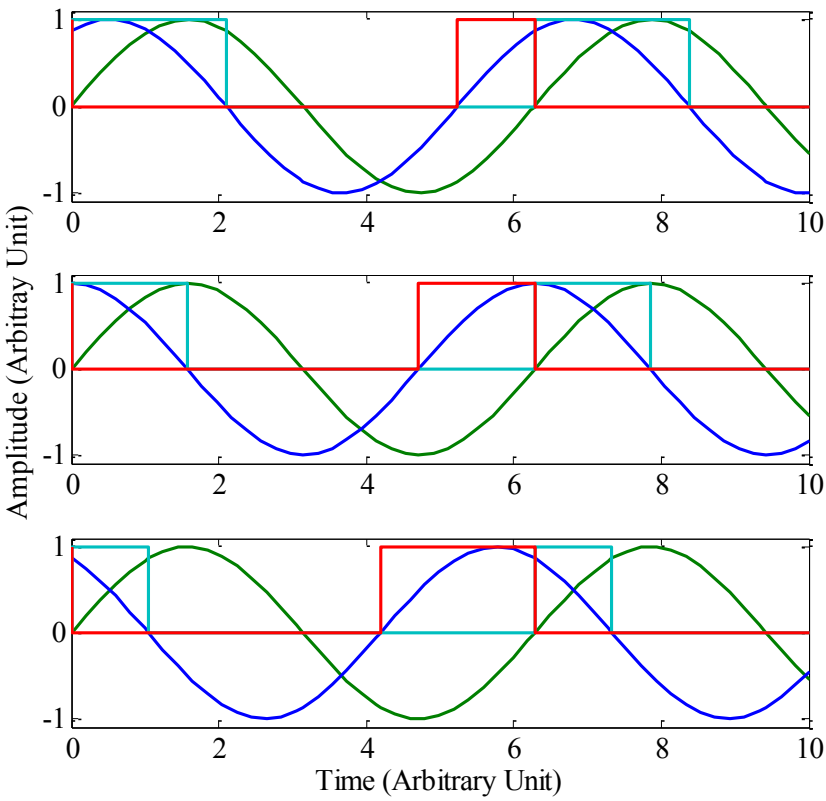

Figure 2.13: High-level Simulink simulation of V_1 (blue), V_2 (green), V_{f1} (red) and V_{f2} (teal). Top: $\varphi = 60$ °; middle: $\varphi = 90$ °; bottom: $\varphi = 120$ °.

φ	DC_1	DC_2	$DC_1 + DC_2$	Calculated φ
60 °	0.166	0.334	0.5	60 °
90 °	0.25	0.25	0.5	90 °
120 °	0.334	0.166	0.5	120 °

Table 2.2: Measured duty cycle from the three cases of Figure 2.13 and calculated φ according to (35).

2.3.2 Comparator and bias tee design

The comparator is found in the library Analog Standard Cells (A_CELLS) from AMS C35. It is composed of a differential pair followed by a common source for the amplification and two inverter gates for the saturation and the ability to drive large capacitive loads (see Figure 2.14 for a transistor-level schematic of the comparator). A feedback is provided by the transistor Q15 to set a 17 mV hysteresis on the negative threshold. The bias current I_{bias} is provided by the BBIAS block from the same library.

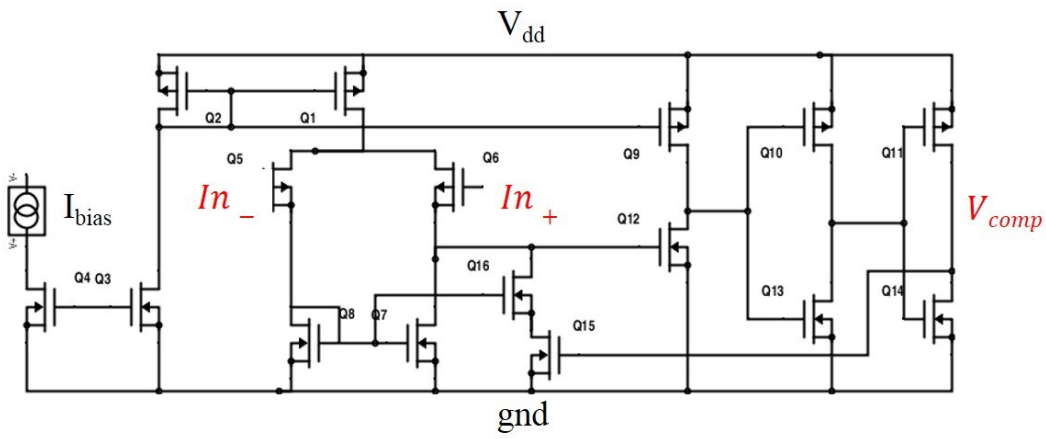

Figure 2.14: Transistor-level schematic of the A_CELLS comparator.

As the power supply is asymmetrical (V_{dd} to ground), the input voltage must be biased to ensure the fact that the totality of its amplitude remains within the V_{dd} to ground range. Schematic simulation of the comparator is performed with slow sinewaves (1 kHz) without load with successive 0 V biasing and 1 V biasing of the input signal, and 200 mV peak-to-peak amplitude to illustrate the hysteresis value and the performance degradation if the signal is outside the [0 V-3.3 V] interval. The results, shown in Figure 2.15, illustrate hysteresis is 17 mV for the 1 V-biased input, but jumps to 25 mV with a 30 mV offset for the 0 V-biased input.

To prevent this degradation, an integrated bias tee composed of a 1 MΩ resistance and a 2 pF capacitor is designed. The resistance is a 1500 µm × 2 µm rpoly layer (the most resistive layer available in the technology) wrapped around itself to save space. The capacitance is an octagonal cpoly layer of 56 µm side length, surrounded by an N-well biased at V_{dd} and a P-well biased at GND to prevent any current leakage. The block is routed as illustrated in Figure 2.16, with V_{ref} chosen to make sure that V_1 remains inside the [0 V-3.3 V] interval. The bias tee is a high-pass filter with a cutoff frequency of 79 kHz which adds a positive phase-shift depending on the frequency (theoretically 1.16 ° at 3.9 MHz and 1.52 ° at 3 MHz).

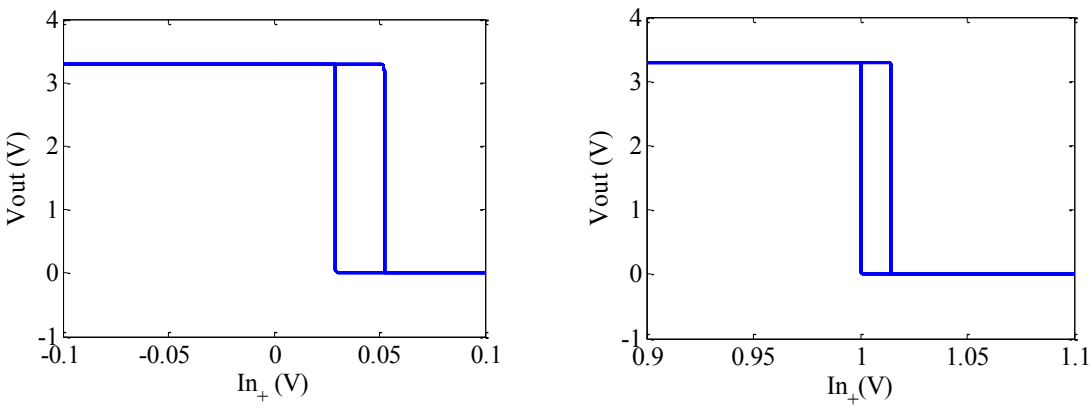

a) b)

Figure 2.15: Transient schematic simulation to illustration the hysteresis and the input biasing requirement: a) 0V bias, b) 1V bias.

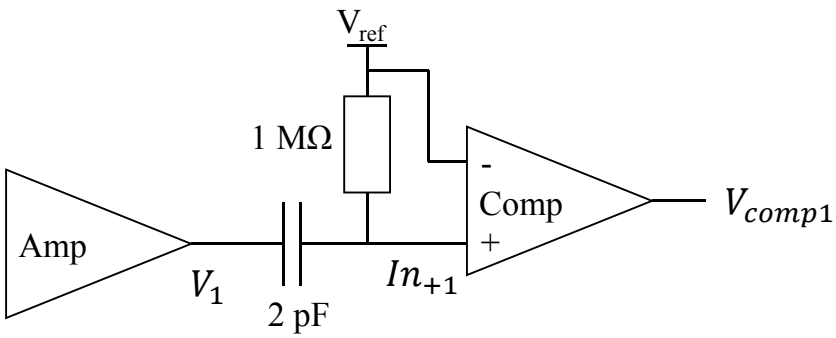

Figure 2.16: Schematic of the bias tee routing.

Simulations are then performed based on the schematic model of the comparator with fast sinewaves (3 MHz) with various loads to estimate the delay and rise & fall time of the comparator. The result is shown in Figure 2.17, exhibiting a 5 ns delay for the positive threshold and a 7 ns for the negative one (corresponding to the hysteresis). This is according to the AMS datasheet. A rise & fall time between 2 ns and 8 ns depending on the load is found. The comparator nominally consumes 0.86 mW, while the current bias block consumes 105 μW.

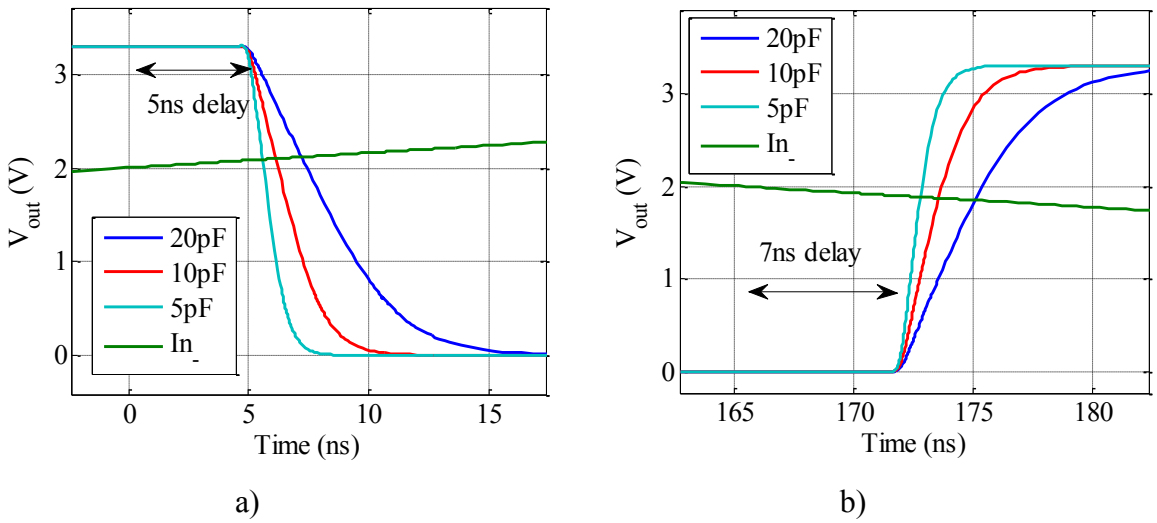

Figure 2.17: Transient schematic simulation of the A_CELLS comparator for various capacitive loads at 3 MHz: a) positive threshold, b) negative threshold (2ns added delay corresponding to the 17mV hysteresis).

2.3.3 Digital mixer and buffer design

The digital mixer is composed of three logical gates which are taken from the library CORELIBD from AMS C35. A digital buffer is designed as well because, as mentioned in section 2.1, the coupler loads a potentiometer bridge placed outside the chip. This means that the coupler needs to output enough current to drive the connection PADs and the wiring to go to the bridge.

Concerning the mixer, it is composed of the smallest gates available in the technology (AND2X1, INVX1), to have the smallest delay, since they are not perturbed by possible capacitances to load. The two AND2X1 are composed of 6 transistors (2 PMOS, 2 NMOS for the NAND, 1 PMOS, 1 NMOS for the inverter), and the INVX1 is composed of 2 transistors (1 PMOS, 1 NMOS). The transistors dimensions are 0.35 µm × 0.45 µm for the NMOS, and 0.35 µm × 0.7 µm for the PMOS.

The digital buffer is composed of 4 stages of increasingly larger inverter gates, whose dimensions are given in Table 2.3.

Stage	PMOS	NMOS
1	0.35 µm × 0.7 µm	0.35 µm × 0.45 µm
2	0.35 µm × 22.4 µm	0.35 µm × 12.55 µm

3	0.35 µm × 44.8 µm	0.35 µm × 25 µm
4	0.35 µm × 179 µm	0.35 µm × 100 µm

Table 2.3: Size of the transistors from the digital buffer.

The different transition times and delays are estimated through transient simulations of the schematic model of the coupler. After the 7 ns delay of the comparator are extracted:

- 0.3 ns delay for the mixer (since the gates are the smallest).
- 1.2 ns delay for the digital buffer.

The mixer and the buffer are simulated for various capacitive loads (Figure 2.18 a)), showing better loading capabilities than the comparator (3 ns of rise time instead of 5 ns at 20 pF), at the cost of a very high AC current consumption. The steady-state consumption of the coupler is 0.48 mA (corresponding to 1.6 mW at 3.3 V) but there is a short surge at every transition (Figure 2.18 b)), which exact value depends on the load. These results are summed up in Table 2.4. The current spikes, because of the RLC behavior of the BNC wire bringing the supply voltage to the chip, generate oscillation in the effective voltage supply. Hence, the current spikes lead to voltage oscillations on every block of the chip. This is illustrated in section 2.4.2.

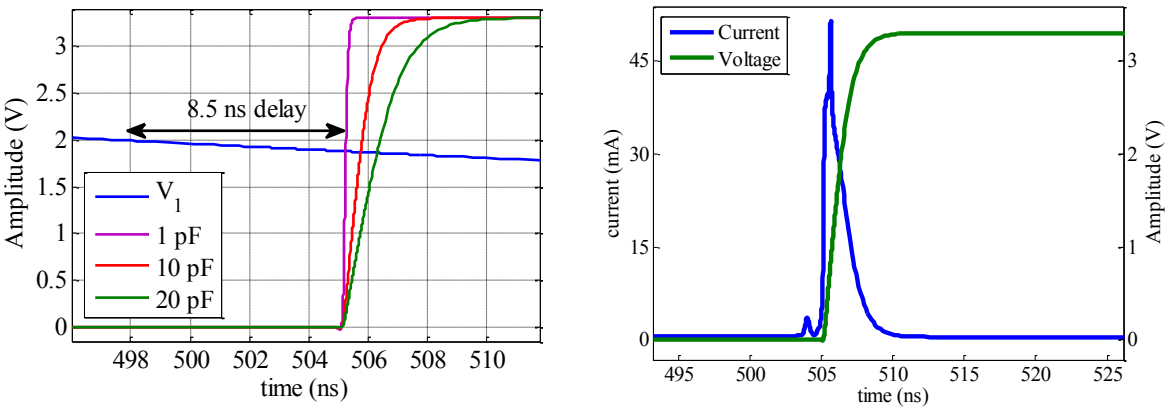

a) b)

Figure 2.18: Transient schematic simulation of the complete coupler at 3MHz: a) for various loads, b) current consumption at the transitions for a load of 20pF.

Load (pF)	1 pF	2 pF	10 pF	20 pF
Delay + Rise & Fall time	1.5 ns	1.5 ns	2.6 ns	3 ns

Ψ @ 3 MHz	1.6 °	1.6 °	2.8 °	3.24 °
Ψ @ 3.9 MHz	2.1 °	2.1 °	3.65 °	4.21 °
Current spikes (mA)	25 mA	31 mA	39 mA	48 mA

Table 2.4: Simulated delays and current spikes at each coupler's transition, and extracted added phase by the association mixer + buffer for various capacitive loads.

2.4 Miscellaneous design issues

2.4.1 Decoupling capacitances and low-resistance access matrix

To lower the access resistance of the power supply voltage and absorb a part of the AC consumption presented in the previous paragraph, a block composed of a NMOS-based capacitance towered by three levels of metal routed as illustrated in Figure 2.19 has been designed. The dimension of one block is 10 µm × 10 µm, producing a 50 fF decoupling capacitance between the supply voltage V_{dd} and the ground. These blocks are placed all over the chip and ensure the low-resistance distribution of the power supply and a distributed decoupling capacitance of 40 pF in total. By the standard "rule of thumb", this 40 pF decoupling capacitance allows the digital buffer to load a 4 pF capacitance without major perturbations even with the current spikes, which are "absorbed" by the distributed capacitance. Moreover, these blocks bias the substrate at 0 V and prevent any current leakage from affecting the other blocks.

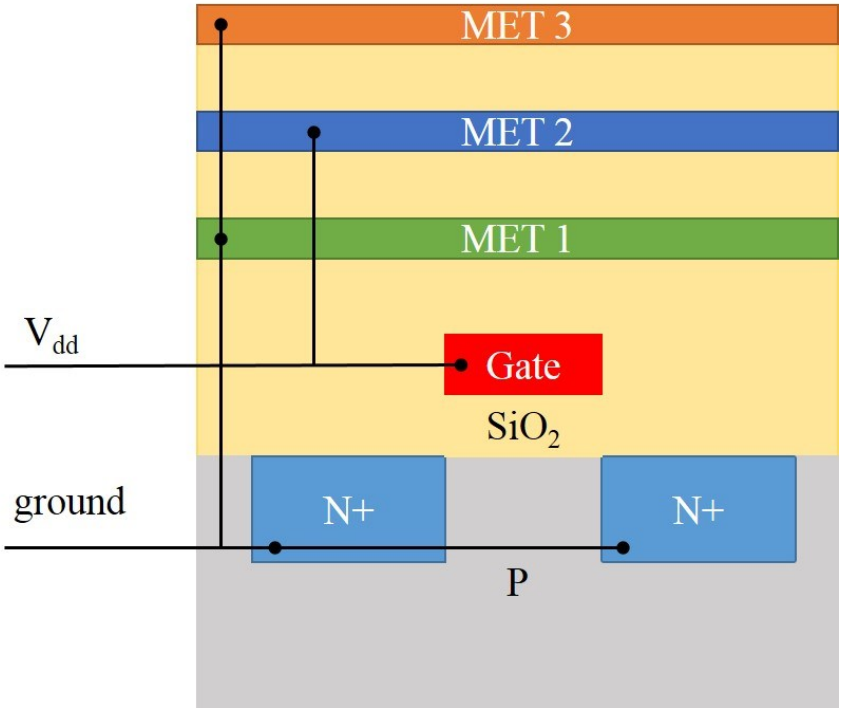

Figure 2.19: Design and routing of the decoupling capacitance.

2.4.2 Potentiometer bridge

The digital buffer outputs 3.3 V logic signals that would drive the resonators outside of their linear range, even for moderate values of the bias voltage (see Figure 1.27 and Figure 1.28): this voltage must then be reduced for nominal operation. To this end, an off-chip voltage divider bridge (corresponding to gain K' in Figure 2.1) consisting of a 1 kΩ potentiometer is used. The exact impact of this off-chip component on the value of the feedback phase-shift Ψ_{res} is very dependent of the experimental connection set-up. Two set-ups (Figure 2.20) are used to connect it to the chip:

- the output of the digital buffer is connected to the bridge with an 8 cm SMA wire. The PCB carrying the bridge is placed over the chip, and the output of the bridge is connected back to the chip (to the input port of the MEMS resonator) with a 12 cm SMA wire.
- the output of the digital buffer is connected to the bridge with a 1 cm SMA connector. The PCB carrying the bridge is in the same plane as the

chip, and the output bridge's output is connected back to the chip with a 15 cm SMA wire.

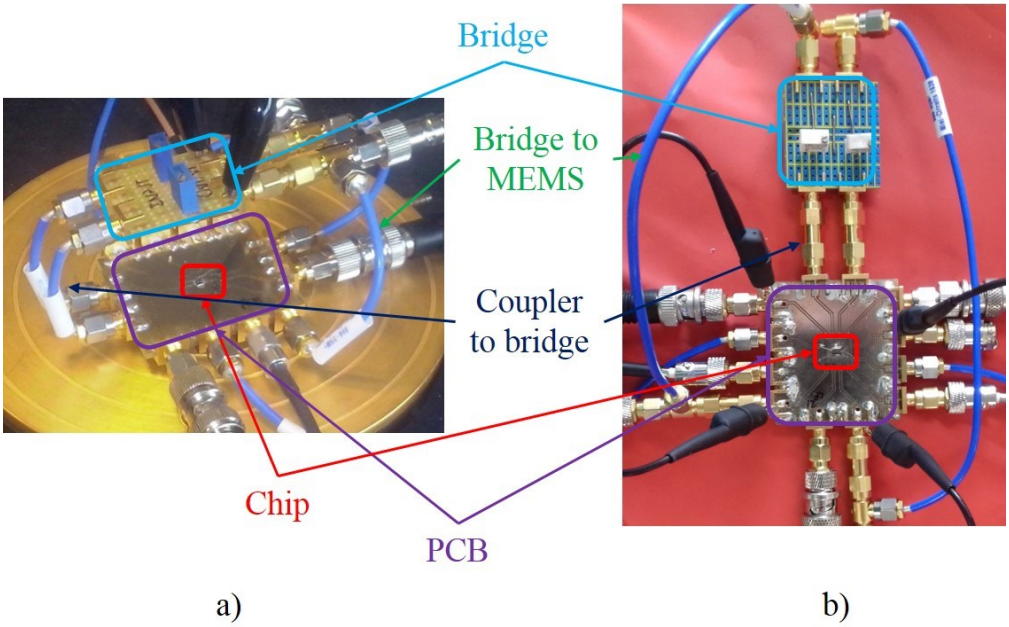

Figure 2.20: Two experimental set-ups.

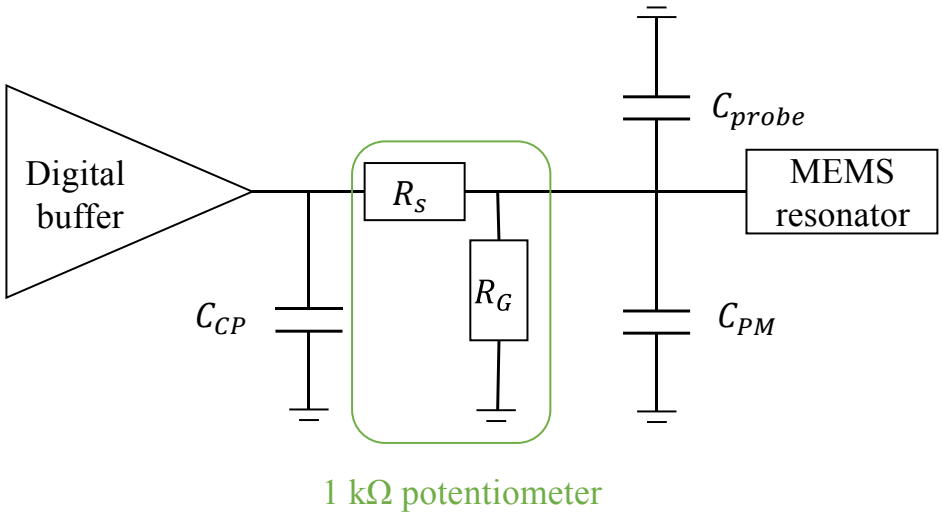

Figure 2.21: Connection of the potentiometer's bridge.

The two connections can be modelled as parasitic capacitances C_{CP} and C_{PM}, as shown in Figure 2.21. Capacitance C_{CP} should be as small as possible so that the current spikes mentioned in sub-section 2.3.3 are minimized. Transient simulation of the entire coupler are performed for the two set-ups and presented in the Figure 2.22.

As predicted, the 8 pF load of set-up a) leads to major perturbations while the perturbations are well-absorbed for the 2 pF load of set-up b).

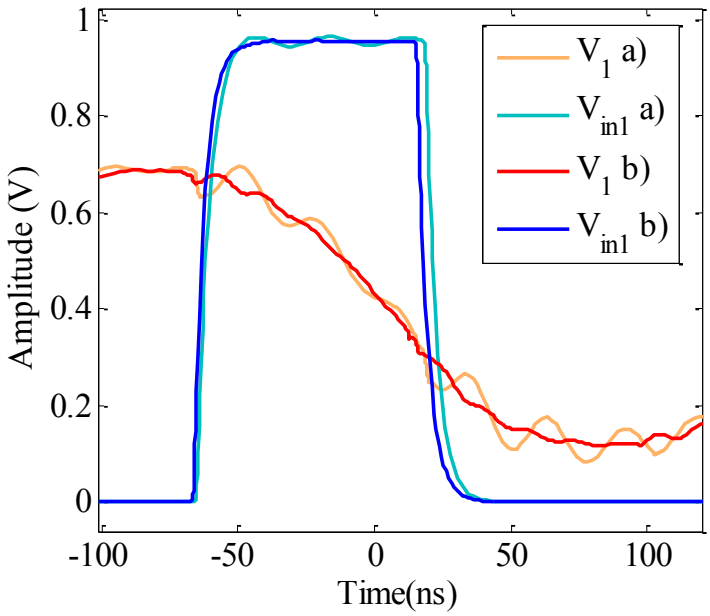

Figure 2.22: Transient closed-loop simulation of the MILO at 3.9 MHz for the two set-ups, taking into account the RLC equivalent of the wire which supplies V_{dd} (10 nH, 80 pF, 0.3 Ω)

On the other hand, C_{PM} acts as a low-pass filter when combined with the potentiometer. Moreover, a probe is always placed after the potentiometer to control the amplitude and record the signal, adding another capacitance. Suppose that the bridge divides by 3.3 to have a 1 V excitation signal. The series resistance R_s is at 700 Ω, and the ground resistance R_G at 300 Ω. The results of the added phase delay at each frequency, for each set-up is given in Table 2.5.

Set-up	C_{CP}	C_{PM}	C_{probe}	Phase @ 3 MHz	Phase @ 3.9 MHz
a	8 pF	12 pF	3.9 pF	-3.7 °	-4.6 °
b	1 pF	15 pF	3.9 pF	-4.2 °	-5.2 °

Table 2.5: Capacitances to load and theoretical phase delay added by the potentiometer's bridge connection for the two set-ups.

The set-up b) is preferred, mainly due to the perturbations reduction, since the phase delays are almost equal in both case.

2.5 Final chip layout and extracted simulation

The overall chip organization (see Figure 2.23) results from the fact that connection pads must be set in a straight line in order to use the HTT Wedge7 probe card at our disposal. Indeed, even if the probe card is not suited for closing the loop, it is the best suited tool to check if the MEMS releasing occurred properly. The etching process does not work 100 % of the time, and the hand-made bonding process is very time consuming. Then, the critical connections between the resonator and the amplifier, and between the amplifier and the comparator have to be as small as possible, because they are analog connections, susceptible to noise interference. Three pads are routed to the ground to properly evacuate parasitic currents from the substrate. The routing is carefully made so that no two AC signals with different phase or waveform types (i.e. analog and digital) are connected to neighboring pads, and thus avoid parasitic coupling. This organization comes at the cost of having a rather long (1 mm) connection between the comparator output and the mixer input, since the comparators are at each extremity of the chip and the mixer in the center. This connection is the bottleneck of the device as it is designed in Metal4, the highest layer or the back end of the line process, and is subject to etching even under the silicon nitride protection layer for long etching time (> 15 min.). This etching leads to narrowing of the connection at some places, and an increased current density, and eventually electromigration and breaking of the connection. It is discussed in section 4.2.

Transient open-loop simulations of the entire chip plus the model of the potentiometer bridge are performed. The BVD equivalent of the two MEMS resonators are excited with sinewaves in quadrature (V_{exc1} and V_{exc2}), at their resonance frequency. Every external non-idealities are taken into account (RLC behavior of the power supply cord, capacitances C_{PM} and C_{CP} of the SMA wiring connecting the potentiometer bridge to the chip, capacitances C_{probe} of the oscilloscope at the output of the amplifiers and at the input of the MEMS resonators. The internal non-idealities (PADs capacitances, substrate capacitance and resistive connections) are taken into account in the extracted model of the chip. The results are presented in Figure 2.24 for

a CCB working at 3.9 MHz and for a CFB working at 3 MHz. In these figures, the amplitudes were normalized for better readability. Indeed, some signals (like V_{comp1} or Vf1 are digital signals from 0 V to 3.3 V while the amplitude of In_{+1} is of the order of 200 mV_{pp}).

The phase delays in the different blocks for the two respective resonance frequency of the CCB and CFB are presented in Table 2.6, in the case of schematic simulations from section 2.3.2 to section 2.4.2 and post layout extracted simulation of the entire chip. The delay in the comparator is much higher than the one found in the schematic model. This is due to the long connection between the comparator's output and the mixer's input. The positive phase in the bias tee is higher than expected as well, possibly due to inductive effects in the "wrapped-up" shape of the resistance. The delay in the mixer + buffer block is slightly higher as well, due to the fact that its output is connected to a pad which represents a 0.3 pF capacitance to load. Overall, the architecture is optimized for a resonance frequency around 3 MHz, which is the frequency of the CFB and the unstressed frequency of the CCB (2.6 MHz).

Unfortunately, due to the unpredicted tensile stress, the oscillation frequency of CCB MILOs is around 3.9 MHz, instead of 2.6 MHz, where the architecture is not optimized. Indeed, at 3.9 MHz, the phase in the amplifier is not 71 ° but 65 ° (according to post layout simulations, see Figure 2.10). Moreover, the fixed temporal delays in the digital blocks of the coupler lead to higher phase delay at 3.9 MHz (compared to 3 MHz). The two effects (-6 ° in the amplifier's phase and +3 ° in the coupler's phase) add up, leading to a supplementary 9 ° in the loop compared to the optimized value.

The simulated consumption of the device has a static value of 9.8 mA with spikes at 29 mA.

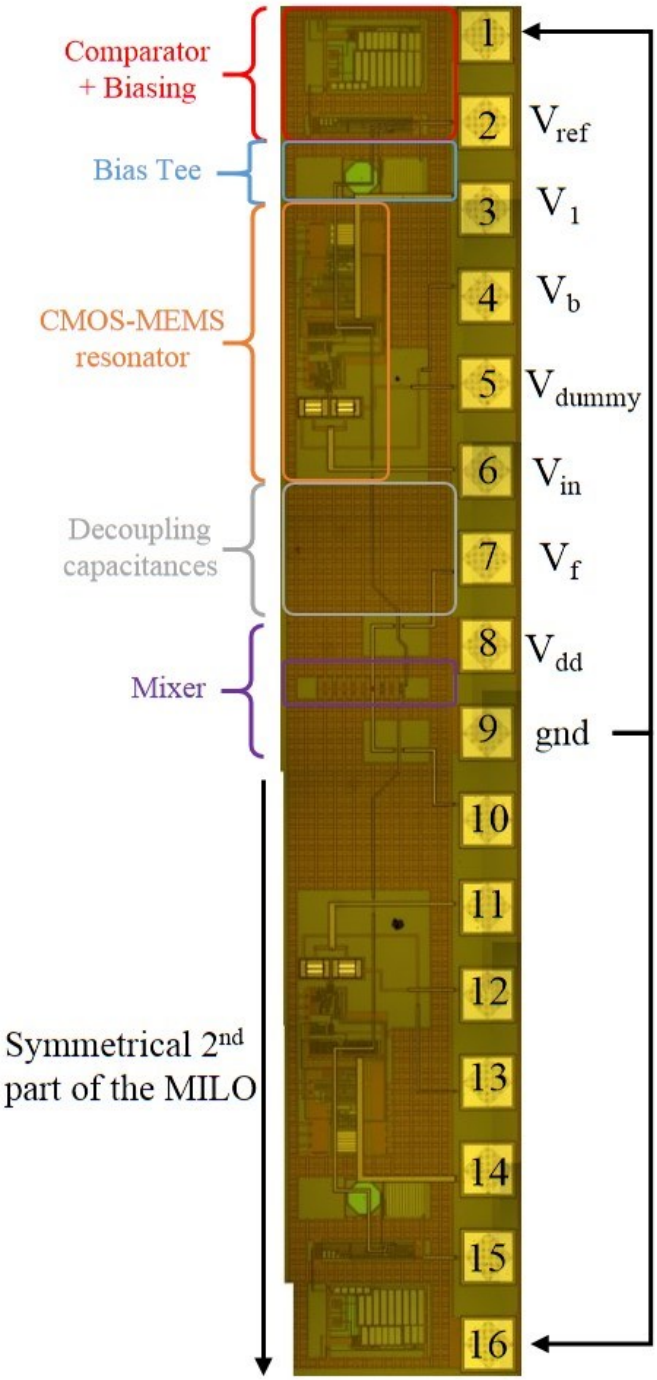

Figure 2.23: Microscopic image of a co-integrated CMOS-CCB MILO (dimensions: 2.4 mm × 375 µm).

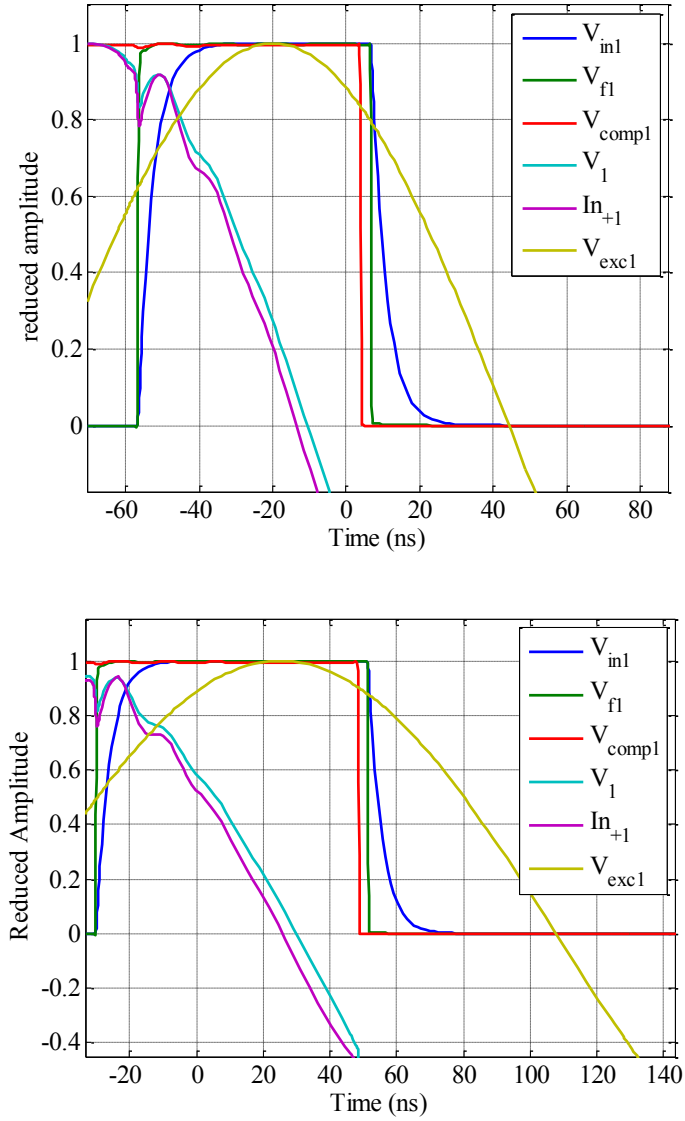

Figure 2.24: Open loop transient simulation of the entire chip. The amplitudes are reduced for better readability. Top: CCB (3.9 MHz). Bottom: CFB (3 MHz)

Frequency	Mode	Bias Tee	Comparator	Mixer + Buffer	Bridge	Ψ_{res}	Optimal Ψ_{res}
3 MHz	schematic	1.52 °	-7.56 °	-1.94 °	-4.6 °	-12.58 °	-26 °
	extracted	4.3 °	-24 °	-2.4 °	-4.2 °	-26.3 °	-26 °
3.9 MHz	schematic	1.16 °	-9.83 °	-2.53 °	-5.2 °	-16.4 °	-20 °
	extracted	2.2 °	-25 °	-3.2 °	-5.2 °	-29.2 °	-20 °

Table 2.6: Phase delays in the different blocks for the complete extracted model of the chip.

2.6 Electronics' dependence on the temperature

The variation of the resonance frequency of the MEMS resonators with the temperature has been detailed in section 1.4.1. But due to the fact that the bandgap energy of MOS transistors are temperature-dependent, charge carriers' mobility changes with the temperature as well [135]. Temperature has an effect on the performances of the CMOS blocks. This section explores the temperature dependence of the blocks of our circuitry, based on simulations.

As it is seen throughout this part, the phase of the amplifier is the important parameter as long as its gain is high enough to trigger the amplifier. In Figure 2.25 is shown the results of frequency simulations of the extracted model of the amplifier for various temperatures. It is seen that there is a 5 ° shift over the 80 °C range. The phase for two temperatures (20 °C and 100 °C) are extracted at 3 MHz and 3.9 MHz and presented in Table 2.7.

Slow-varying simulations also show the fact that the comparator's hysteresis linearly shifts from 17 mV to 27 mV between 20 °C and 100 °C, which has no impact as long as amplifiers' signals are large enough, but be quite detrimental otherwise.

Various transient simulations are then conducted on the extracted model of the device for two temperatures at 3 MHz and 3.9 MHz. The extracted phase values are presented in Table 2.7 for 3 MHz and Table 2.8 for 3.9 MHz. It can be seen that the architecture which was optimized for 3 MHz, is not when the temperature rises.

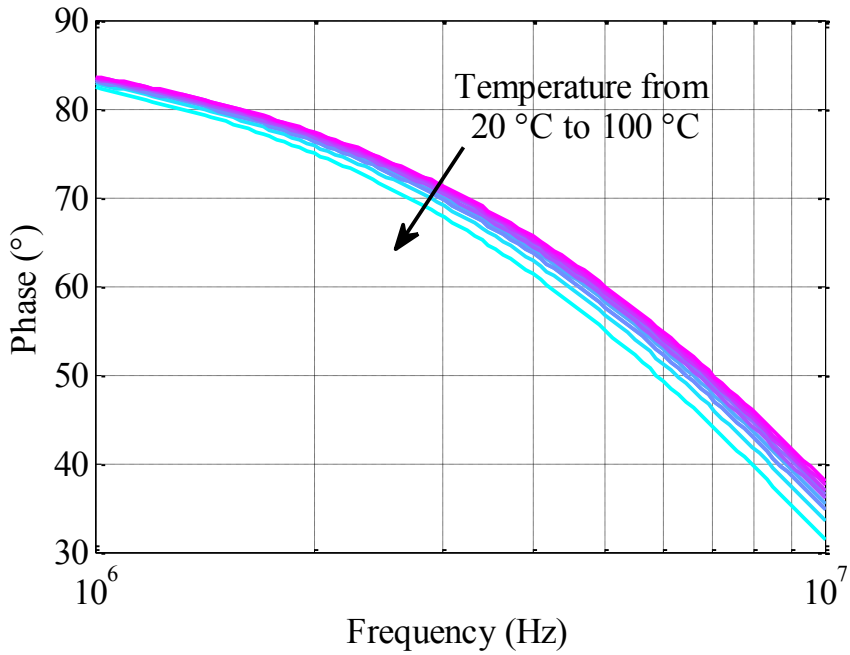

Figure 2.25: Extracted simulation of the phase of the amplifier for different temperatures.

T (°C)	θ_{res}	Comparator + Bias tee	Mixer + Buffer	Bridge	Ψ_{res}	Optimal Ψ_{res}
20	71 °	-19.7 °	-2.4 °	-4.2 °	-26.3 °	-26 °
100	67 °	-21.2 °	-3.2 °	-4.2 °	-28.6 °	-22 °

Table 2.7: Phase delays in the blocks for two temperatures extracted from transient simulations of the device at 3 MHz.

T (°C)	θ_{res}	Comparator + Bias tee	Mixer + Buffer	Bridge	Ψ_{res}	Optimal Ψ_{res}
20	65 °	-19.8 °	-3.2 °	-5.2 °	-28.2 °	-20 °
100	61 °	-22.4 °	-4.3 °	-5.2 °	-31.9 °	-16 °

Table 2.8: Phase delays in the blocks for two temperatures extracted from transient simulations of the device at 3.9 MHz.

The fact that the condition of Equation (29) is lost when the temperature rises in the case of CFB, or the phase imbalance increases with the temperature in the case of CCB might leads to a decreased sensitivity S_φ and stability. But as long as the mismatch between the optimal case of Equation (29) and the measured phase is the same for both sides of the MILO, it has no effect on φ_0.

In this chapter, a simplified model of a generic Mutually Injection-Locked oscillator using the phasor notations has been developed. Some choices were made for a VLSI-compatible implementation of the device ($\gamma = 1, \Psi_{self} = \Psi_{mut}$), and a design constraint was extracted in order to drive both resonators at their resonance frequency, and to have $\varphi_0 = 90\,°$. This constraint, presented in Equation (29) acts as a guideline throughout the design of the device. This design was then presented, block by block first and of the entire device afterward, alongside schematic and extracted simulations to ensure the compliance with the design constraint. The difficulties arising from the design (e.g. the *a priori* unknown resonance frequency of the CCB, the differences between schematics and extracted simulations) were presented as well as the choices that were made. The next chapter presents the experimental characterization of the device in comparison with extracted simulations and theoretical performances derived from the modelling of the architecture.

Chapter 3 Experimental results

In this chapter the performances of the fully co-integrated MILO as a resonant differential sensor are analyzed and compared to the theory. First, the open-loop characterization of the CMOS-MEMS resonators and of the entire circuitry (CMOS-MEMS + coupler) is performed experimentally and compared to simulation results in section 3.1. Then, section 3.2 explores the co-integration of two CMOS-MEMS resonators on one single chip. The potential advantages in term of resonance frequency and quality factor matching are emphasized. After that, the loop is closed (see section 3.3), experimental waveforms are compared to simulated ones in order to verify the accuracy of the phase parameters that were estimated in the open-loop measurements. The MILO is then characterized as a differential sensor: the quantities of interest defined in Equation (30), (31) and (32): S_{φ}, S_{ω}, S_{MILO} and ε_{lock} are analyzed for various samples in section 3.4 and 3.5, given the phase parameters found in the previous steps. The thermal drift rejection of φ is assessed in section 3.6. Finally, the MILO is characterized as an oscillator in section 3.7, with short-term stability measurements in term of phase noise, frequency noise, and noise over the phase difference φ.

3.1 Open-loop characterization of the MILO.

In this first section, the CMOS-MEMS resonators are characterized experimentally and compared to the association of the BVD model obtained in section 1.3 and the readout Cadence model depicted in section 2.2. The emphasis is put on the importance of the experimental set-up for the extraction of knowledge on the blocks. Then, the entire circuitry (CMOS-MEMS resonators + coupler) is characterized experimentally and compared to the global model (BVD + readout model + coupler models).

3.1.1 Open-loop characterization of the CMOS-MEMS resonators

The resonators and their readouts (see the microscopic images in Figure 3.1) are experimentally characterized with a probe station, using a HTT Wedge7 probe card, a

“home-made” connector and an Agilent E5100 network analyzer. This network analyzer is generally sets with a resolution bandwidth of 50 Hz and its trace noise is 0.01 dBrms[2], which means that noises appearing on the frequency response comes from the device (or the experimental set-up) rather than from the analyzer. It also comes with a built-in quality factor calculator (-3 dB bandwidth method) benefiting from the intrinsic low trace noise of the analyzer, and allowing for high accuracy measurement (less than 0.1). This module is used in section 3.2.2.

The set-up is shown in Figure 3.2. The input and output of the network analyzer are 50 Ω impedances, and they are connected to the device under test (DUT) with 80 cm SMA wires, as schematically illustrated in Figure 3.3. Those capacitances and resistances are taken into account in the Cadence model of the test bench. The two RC filters thus created generates phase delays of -5.3 ° at 3 MHz and -7 ° at 3.9 MHz. In Figure 3.4, the spectra of CMOS-CFB 1 and 2 are recorded for $V_{b1} = V_{b2} = 40\ V$, and for $V_{b1} = 20\ V$ and $V_{b2} = 0\ V$ in Figure 3.5.

[2] http://www.keysight.com/en/pdx-x201702-pn-E5100A/high-speed-network-analyzer?pm=spc&nid=-32493.1150116&cc=FR&lc=fre

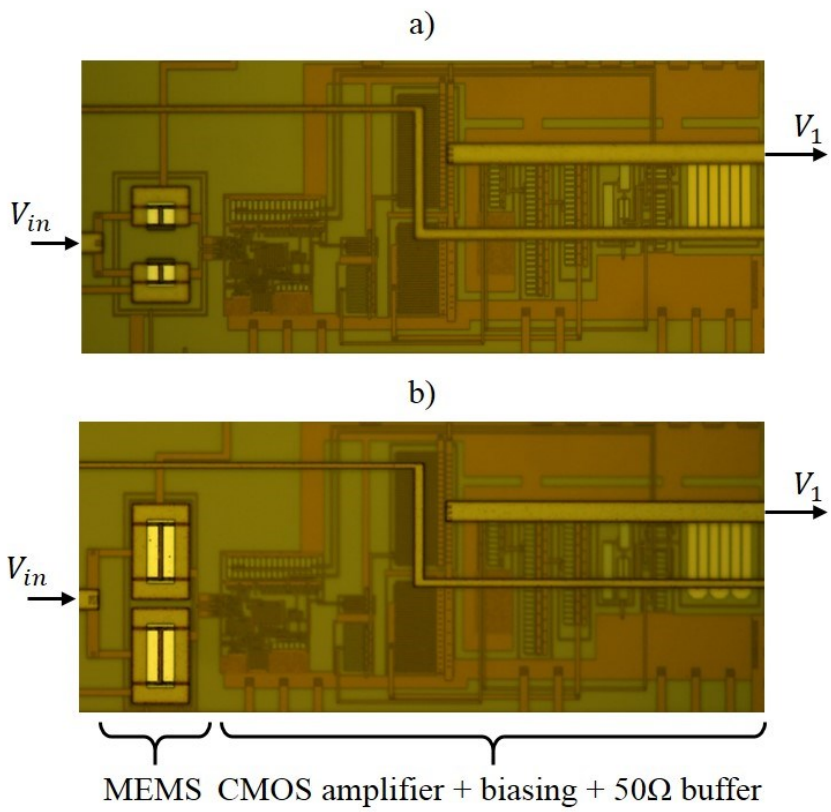

Figure 3.1: Microscopic images of the two CMOS-MEMS resonators: a) CFB b) CCB.

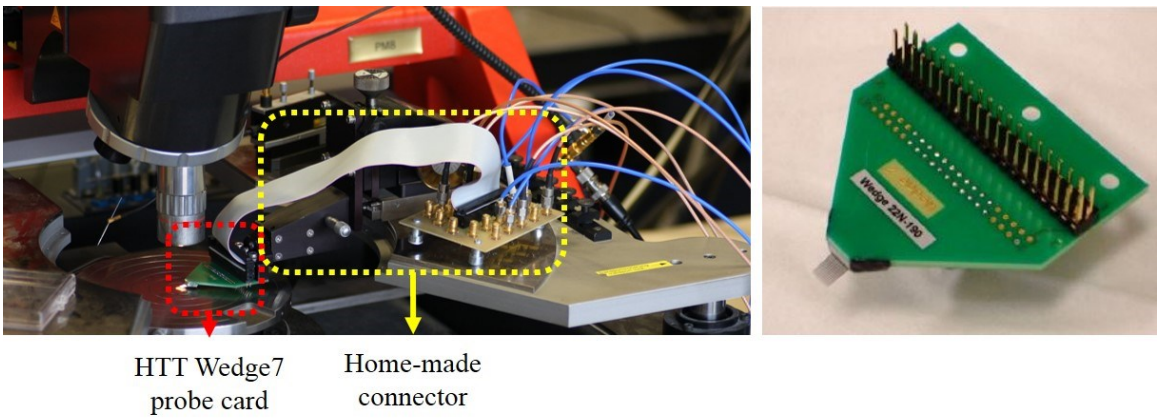

Figure 3.2: Experimental set-up for the CMOS-MEMS resonators characterization: entire set-up (left), and zoom on the Wedge7 probe card (right).

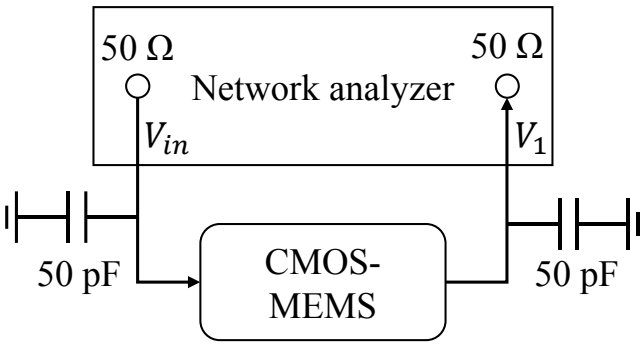

Figure 3.3: Experimental set-up for the extraction of CMOS-MEMS frequency responses.

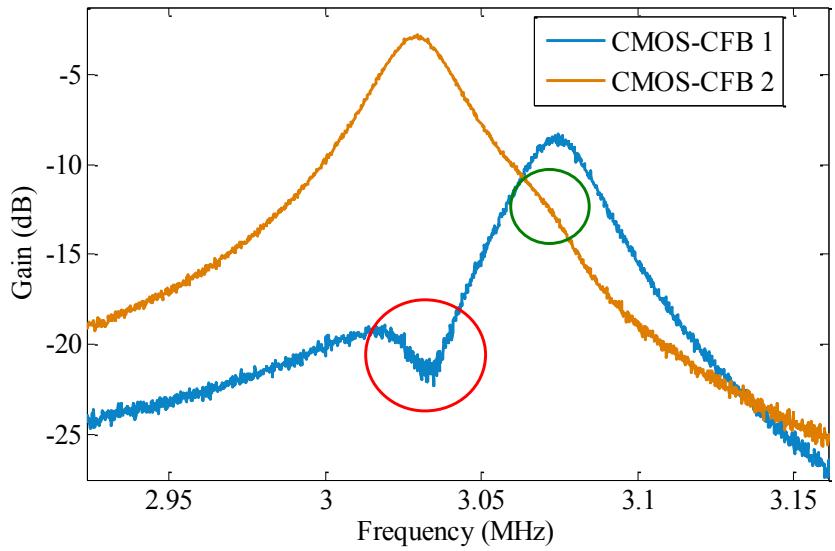

Figure 3.4: Experimental frequency responses of the CMOS-CFB 1 and 2 for $V_{b1} = 40\ V$ and $V_{b2} = 40\ V$ (both are excited simultaneously, excitation level: -20 dBm = 63 mVrms).

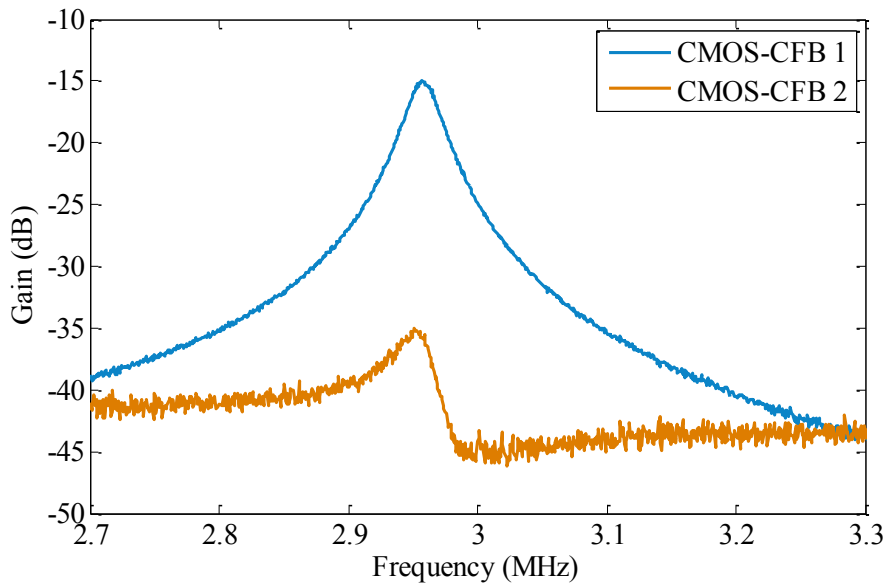

Figure 3.5: Experimental frequency responses of the CMOS-CFB 1 and 2 for $V_{b1} = 20\ V$ and $V_{b2} = 0\ V$ (both are excited simultaneously, excitation level: -20 dBm = 63 mVrms).

Several points emerge from this characterization:

- The gain is not as high as expected. For instance, in the case of the CFB at $V_b = 40\ V$, the model gives a motional resistance of 18 MΩ, and given the transimpedance gain of 39 MΩ, the gain at the resonance should be at 6.7 dB. The measurement at $V_b = 40\ V$ exhibits a gain at the resonance of -4 dB.
- There is a coupling between the outputs of both CMOS-CFB. This coupling generates first an anti-tone (i.e. a gain drop, red circle in Figure 3.4) in the output of the resonator with the highest resonance frequency, due to the other resonator's resonance peak. The coupling then generates a tone (i.e. gain peak, green circle in in Figure 3.4) in the output of the resonator with the lowest resonance frequency due to the other resonator's peak. According to the spectra plotted in Figure 3.5, this coupling is of the order of -20 dB.
- Feedthrough is not effectively cancelled, especially in the case of the CFB resonators, since there is a clear asymmetry on each side of the resonance, even though the anti-resonance is outside the measured span.

These phenomena are explained hereafter.

The gain loss is due to the bad contact between the chip and the probe card. Indeed, the probe card is an array of 22 parallel probes, all connected to the chip. A small tilt between the chip and the probe card leads to a poor contact of some probes, thus an increased contact resistance and a gain loss.

The coupling, which generates the unwanted tone, is due to the probe card and the "home-made" connector. Indeed the array of parallel probes very close to each other (150 µm pitch) followed by an unshielded connection bus generates capacitive coupling between the lines (see Figure 3.6 for an illustration of the configuration: each line number corresponds to the position of the pads, according to the device's layout in Figure 2.23). Three coupling must be taken into account: the one between the two outputs of the CMOS-MEMS (the blue arrow in Figure 3.6: from line 3 to line 14), the one between the output of CMOS-MEMS 1 and the input of CMOS-MEMS 2, and vice versa (the two orange arrows in Figure 3.6, from lines 3 to 11 and 14 to 6). The capacitances between each line of the connector alone (i.e. not connected to the chip) are measured with the network analyzer, the test bench is schematically drawn in Figure 3.7. The capacitance values are extracted and the result is presented in Figure 3.8. The measured capacitances between line 3 and line 11 and line 6 and line 14 (both equivalent to line 1 to 9) are 12 pF. The capacitance between line 3 to 14 was not measured but can be interpolated at 10 pF given the other results. One can then add these capacitances to simulate the coupling through the connector between the two CMOS-MEMS resonators.

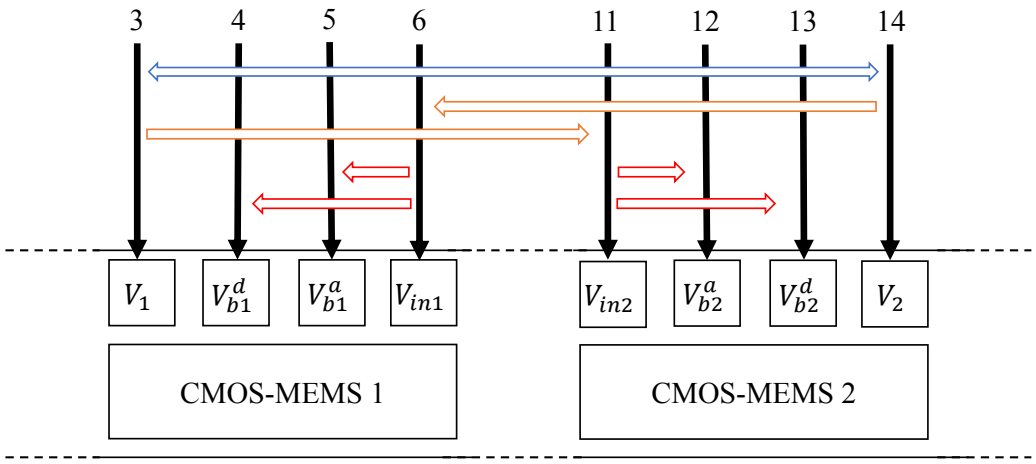

Figure 3.6: Schematic of the wedge probe card experimental set-up. Illustration of the capacitive coupling between the lines. The black arrows represent the probes.

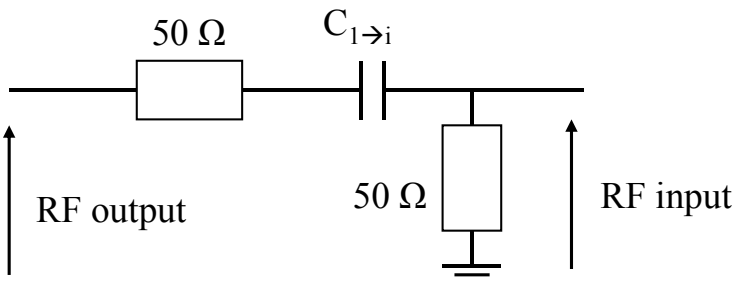

Figure 3.7: Experimental test-bench for the measurement of the coupling capacitances between the lines of the wedge probe card and the connector

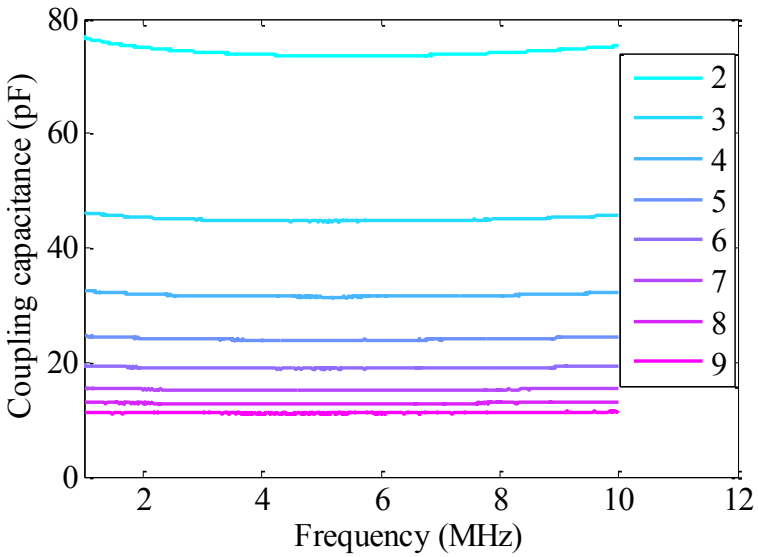

Figure 3.8: Measured coupling capacitance between line 1 and lines from 2 to 9 of the wedge probe card and the connector.

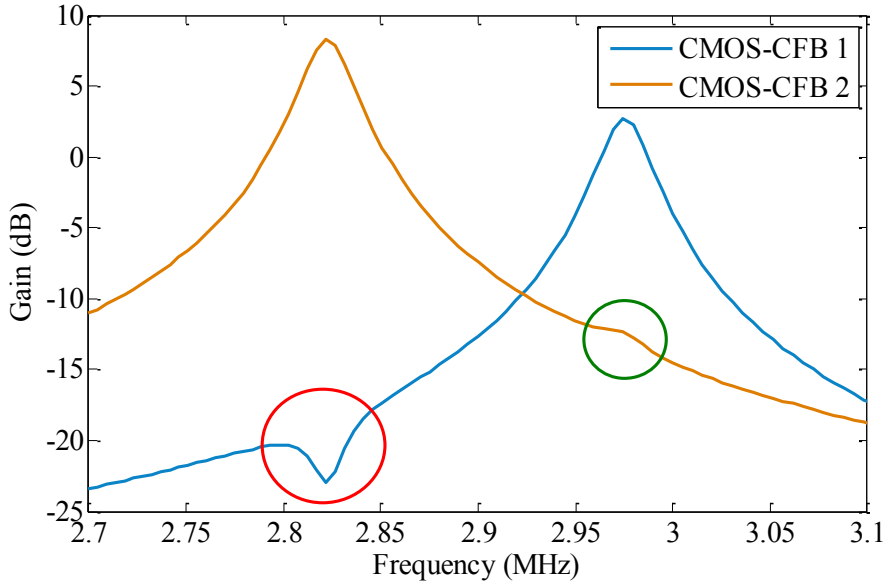

Figure 3.9: Simulated frequency responses of the extracted model of the amplifier + BVD model of the CFB ($V_{b1} = 11\ V, V_{b2} = 30\ V$) + coupling capacitances between the lines.

The simulation are according to the measurement, showing the anti-tone and the tone, meaning that the -20 dB coupling is effectively due to the capacitive coupling between the lines in the connector, and not an effect inside the chip (current leakage, coupling through the substrate for instance. In theory, the MILO should not affected by such couplings, since both resonators are working at the same frequency. However, the chip integrates a digital coupler composed of logic gates thus exhibiting transitions from 0 V to 3.3 V, generating high frequency harmonics. The parasitic coupling of these harmonics to the analog outputs of the amplifiers generates spikes at every transition. Figure 3.10 presents the experimental open-loop waveforms of V_1, V_2, V_{in1} and V_{in2} taken with the probe card: the two MEMS resonators are excited in quadrature using a sinewave generator. They are biased in order to have the same resonance frequency, and excited at this precise frequency. The waveforms of Figure 3.10 are taken with 20 MHz probes, thus smoothing out the high frequency perturbations, but showing the spikes on the amplifiers' output at every transition. Theses spikes are such as the loop cannot be closed with such a set-up.

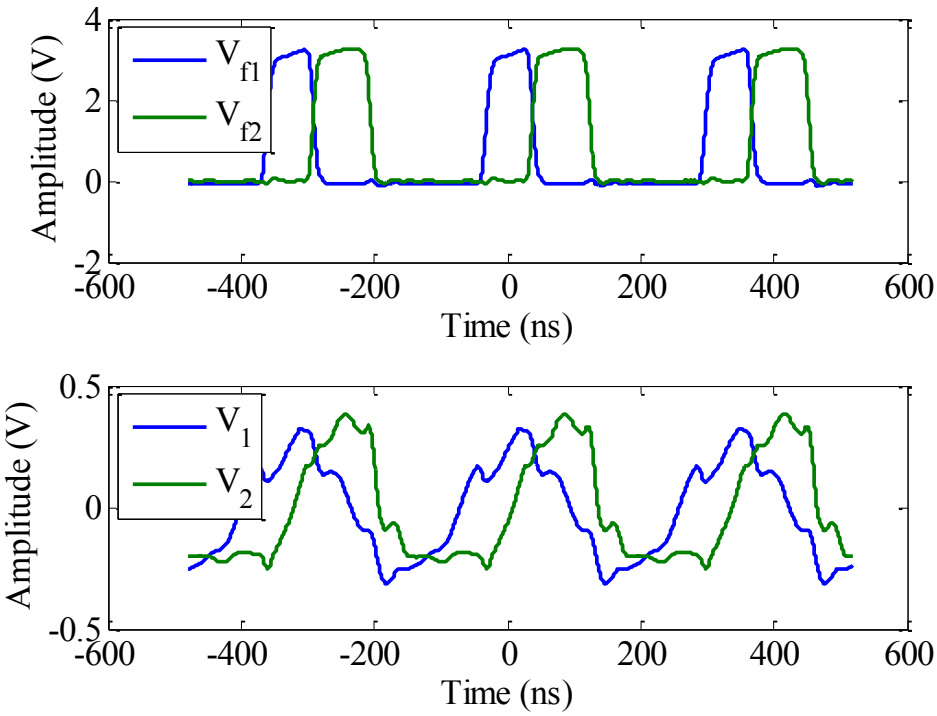

Figure 3.10: Experimental open-loop oscillogram extracted with the wedge probe card set-up: chip 2, $V_{b1} = 30\ V$, $V_{b2} = 48\ V$, $V_{exc} = 200\ mVrms$ @ 3.05 MHz.

Finally, the bad feedthrough cancellation is also due to parasitic coupling: the excitation signal is capacitively coupled to the bias electrodes of the active and of the dummy MEMS resonators. As shown by the red arrows in Figure 3.6, the coupling capacitance is different between the excitation signal and the dummy bias, and between the excitation signal and the active bias, resulting in different values of their parasitic currents and in poor feedthrough cancellation, regardless of the biasing voltage.

To perform better open-loop characterization, the chip is placed over a PCB, and wire-bonded as shown in Figure 3.11.

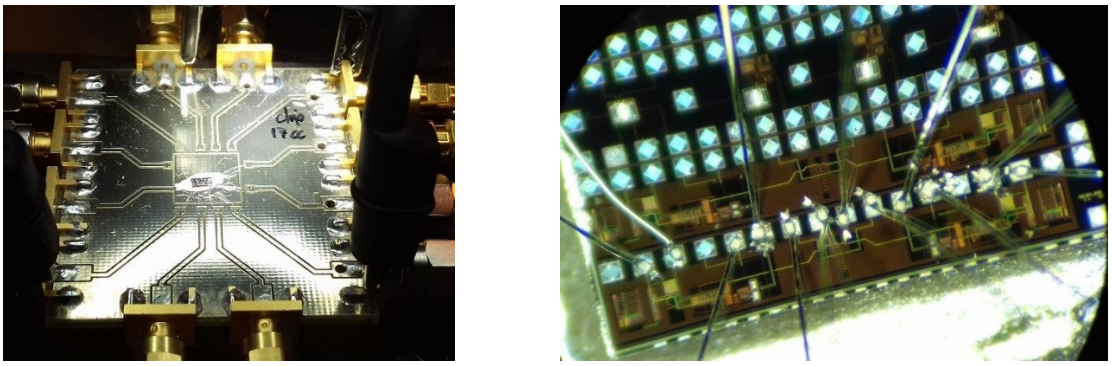

a) b)

Figure 3.11: a) image of the chip wire-bonded on a PCB, b) details on the aluminum wire bondings.

Experimental frequency responses are extracted, presented with their modelled counterparts in Figure 3.12 and Figure 3.13.

- For bias voltages under 20 V, some level of feedthrough remains due to the fabrication mismatch between the dummy and the active resonator.
- For bias voltages higher than 20 V, the parasitic current mismatch at the two inputs of the amplifier begins to surpass the motional current of the active resonator, thus a better agreement is found between the simulated and the experimental results.
- For bias voltages of the order of 30 V (in Figure 3.13), the parasitic current is negligible compared to the motional one, and the agreement between simulations and measurements is good.
- The dimensions of the modelled beams are adapted to fit the measured resonance frequency, because the fabrication process's variability is around 10 %, and it is seen in section 1.2.5 that the fabricated dimensions are different from the specified ones.
- The model predicts accurately the resonance frequency decrease and the gain increase with the biasing voltage.
- The phase is well predicted by the model provided the two RC filters depicted in Figure 3.2 are taken into account. One can then extrapolate a phase at the resonance without the analyzer's and SMA's effect: 70.4

° for the CFB and 64 ° for the CCB. The results for the measured phase, the contribution of the experimental set-up, the extrapolated value of θ_{res} and a comparison with the simulated phase of the amplifier alone is made in Table 3.1, showing a correct agreement for the different techniques of evaluation of θ_{res} (0.9 % difference between simulation and measurements)

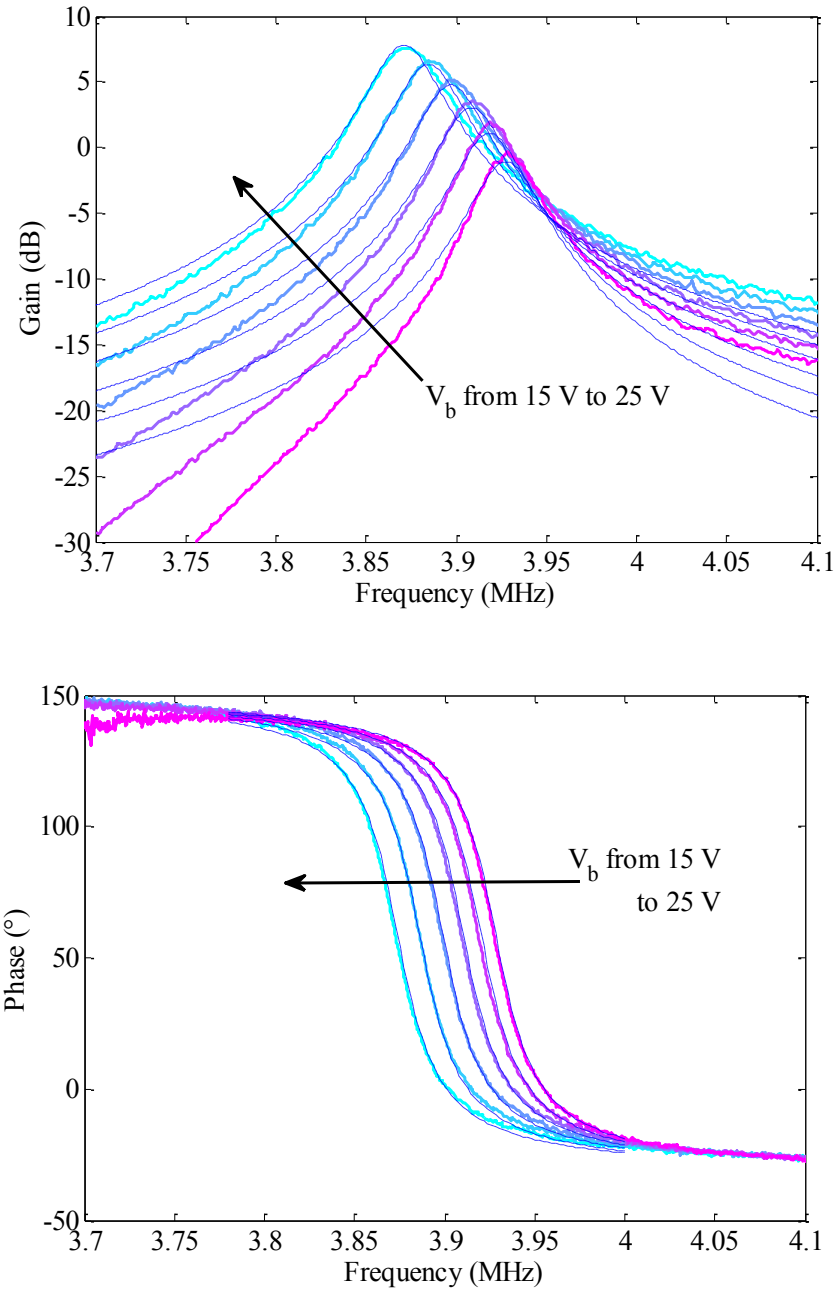

Figure 3.12: Experimental frequency response (full lines) and model (dashed lines, dimensions L=29.6 µm, b=1.3 µm, h=0.5 µm, G_0 :370 nm, Q=120) of a CCB for V_b from 15 V to 25 V in 2 V steps, input power of -20 dBm.

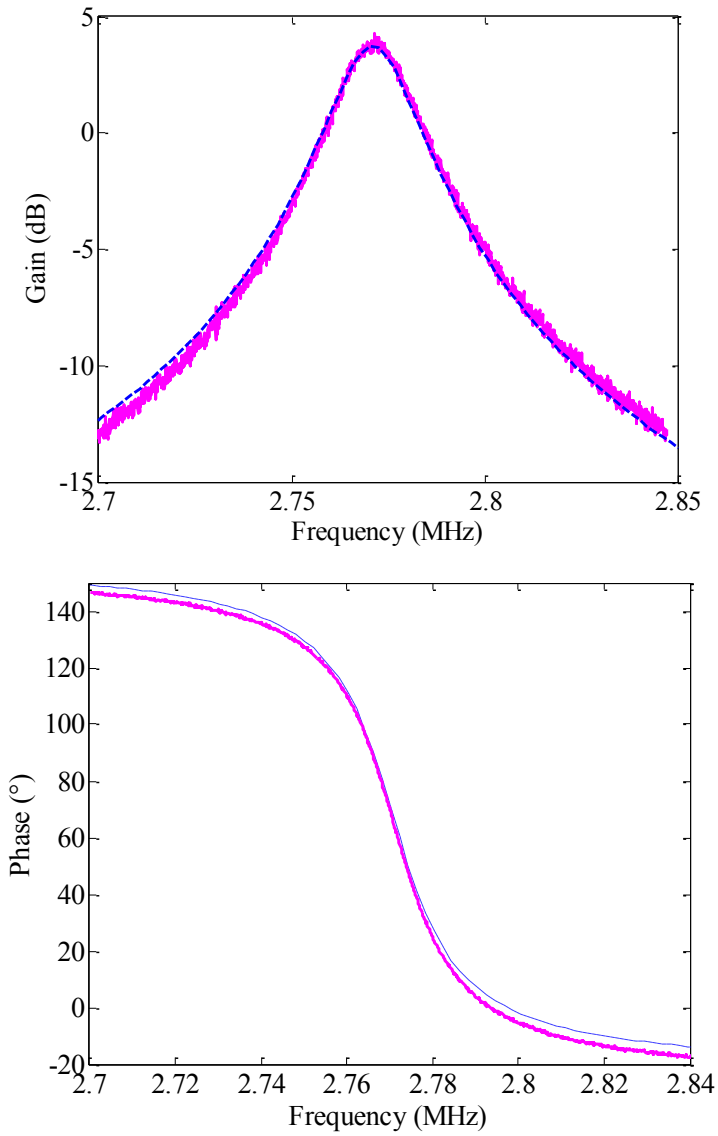

Figure 3.13: Experimental frequency response (full lines) and model (dashed lines, dimensions L=10.57 µm, b=1.3 µm, h=0.45 µm, G_0 :330 nm, Q=100) of a CFB for $V_b = 30\ V$, input power of -20 dBm.

Resonator	Measured θ_{res}	Calculated setup contribution	Extrapolated θ_{res}	Simulated θ_{res}
CFB	65 °	-5.3 °	70.3 °	71 °
CCB	57 °	-7 °	64 °	64.8 °

Table 3.1: Measured θ_{res} for the two geometries, with the estimated contribution of the experimental set-up, an extrapolation of the actual θ_{res}, and the evaluation of θ_{res} with the simulated phase of the amplifier alone made in Table 2.1.

Finally, in Figure 3.14 the experimental spectra of two co-integrated resonators are plotted, simultaneously excited but where only one is biased. This figure is to be compared with Figure 3.5. The resulting coupling ratio is -45 dB while it is between -16 dB and -20 dB with the wedge probe card (see Figure 3.4 and Figure 3.5). This remaining coupling factor might be due to some level of coupling through the substrate or inductive coupling between the wire bondings. Simulations shows that it is small enough to be neglected, since the impact of digital signals' harmonics on amplifiers waveforms is very small.

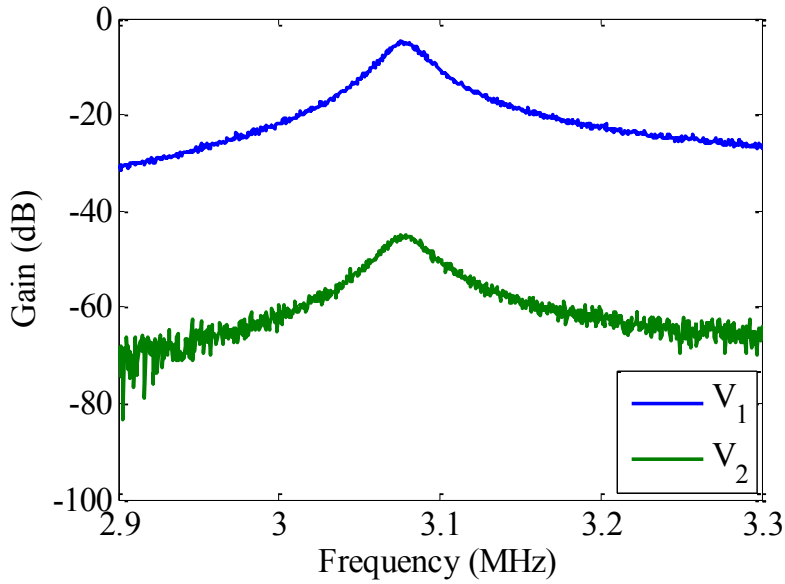

Figure 3.14: Experimental frequency response of a wire-bonded CFB MILO where the CMOS-CFB 1 and 2 are simultaneously excited at -20 dBm, with $V_{b1} = 20\ V$ and $V_{b2} = 0\ V$.

The experimental results coming from the characterization of the CMOS-MEMS resonators show good agreement with the association of the BVD modelling of the resonators and the extracted model of the amplifier, provided every component of the experimental set-up has been taken into account.

3.1.2 Open-loop characterization of the entire circuitry

To make sure that everything has been taken into account in the model, an open-loop characterization of the MILO is performed. The two resonators' frequency responses for various bias voltages are obtained, the matching condition is found (i.e.

values of V_{b1} and V_{b2} so the two resonators' resonance frequencies are matched). The MEMS resonators are biased according to the matching condition, and excited by a Tektronix AFG3052C waveform generator at this resonance frequency. The signals are recorded on a Tektronix MSO5024B oscilloscope. The oscilloscope has a 2 GHz bandwidth, and when used for phase measurements, set with a 128 samples averaging. In total, the accuracy of the measurement is at 0.1 °.

The waveform generator outputs two signals with a fixed 90 ° phase shift. The open-loop measurements are presented in Figure 3.15 for a CFB and Figure 3.16 for a CCB, and compared to their simulated counterparts. Overall, the simulations fit the measurements well, with 3 % difference, even though the delay seems slightly underestimated by the simulations. The negative transition of V_{in2} is a bit overestimated by the simulation, this might come from an underestimation of the saturation of the amplifiers, as described in section 3.3. The simulated value of Ψ_{res} found in simulations in Table 2.6 and the simulated value of θ_{res} found in Table 3.1 are according to the measurements. They are summarized in Table 3.2

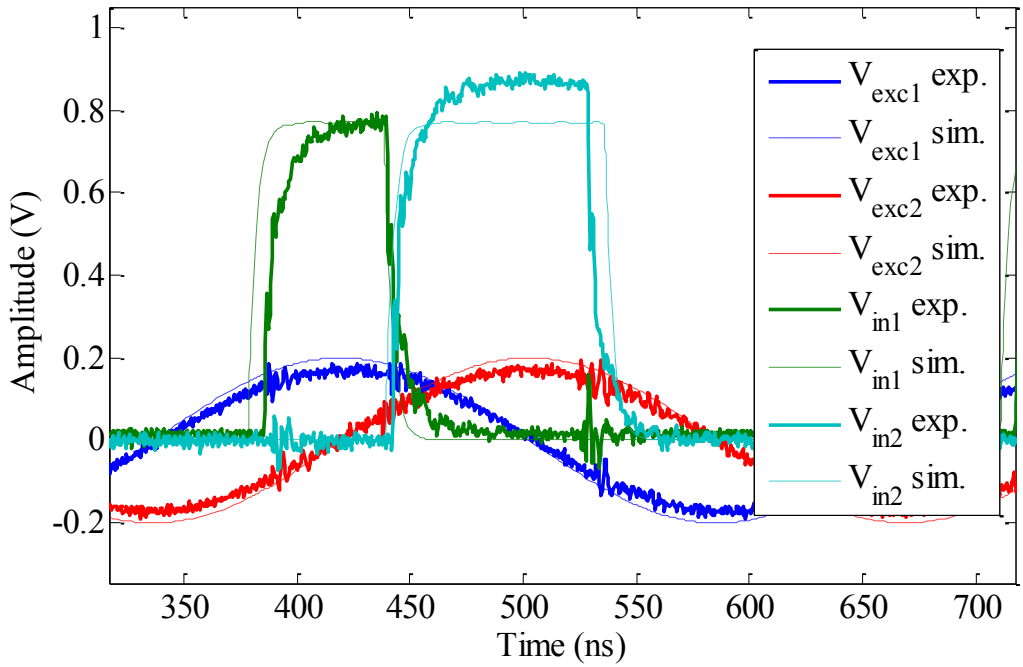

Figure 3.15: open loop waveform of a CFB (chip 12) with the following adjustment: $V_{b1} = 28\ V$, $V_{b2} = 30\ V$, excitation voltage: 170 mVrms, 3.0059 MHz, and comparison with the transient extracted simulations

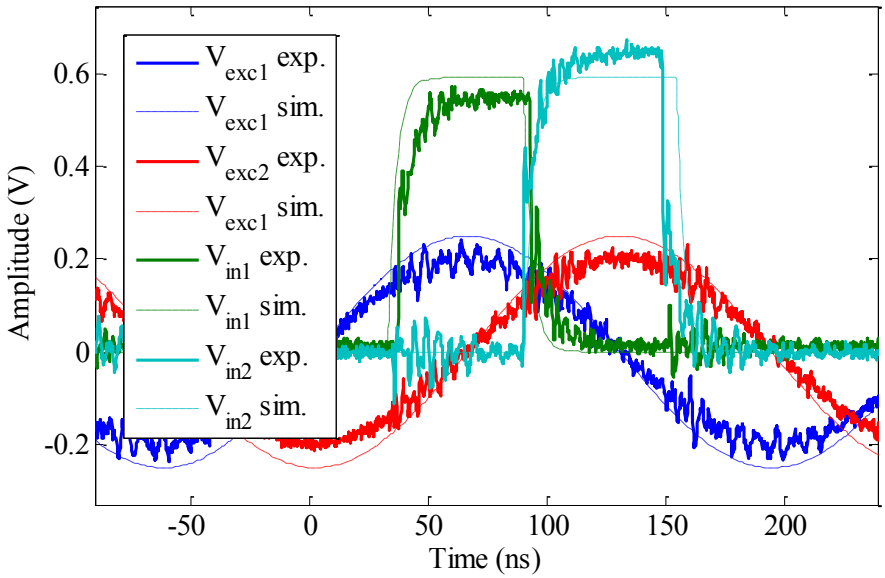

Figure 3.16: open loop waveform of a CCB (chip 17) with the following adjustment: $V_{b1} = 28\ V$, $V_{b2} = 29.2\ V$, excitation voltage: 200 mVrms, 3.854 MHz, and comparison with the transient extracted simulations

Resonator	Frequency (MHz)	θ_{res}	Ψ_{res}	Optimal Ψ_{res}
CFB	3.006	70.3 °	-26.3 °	-25.3 °
CCB	3.854	65 °	-28.2 °	-20 °

Table 3.2: Summarized measured phase delays across the loop and comparison with the optimal value according to Equation (29).

3.2 Characterization of two co-integrated CMOS-MEMS resonators

In this section, the effect of co-integrating two CMOS-MEMS resonators on one single chip is explored.

3.2.1 Matching of resonance frequencies

As pointed out at the beginning of section 2.1 the resonators of the MILO must be nominally matched in term of resonance frequency. Considering the fabrication process variability, having two co-integrated MEMS resonators at close proximity should lower their mismatch in term of dimensions, thus, natural frequency. However,

since AMS 0.35 is not a specific MEMS technology and the structures are fabricated in spite of being out of the design rules check, some level of variability remains. Figure 3.17 recalls the resonance frequency for a bias voltage of 20 V of the two CMOS-MEMS resonators of every sample released in the case of CFB geometry (12 samples) and CCB geometry (18 samples).

Concerning the CCB, the standard deviation of the resonance frequency error of all 630 resonator pair combinations is 59.4 kHz, or 1.5% relatively to the mean resonance frequency of 3.93 MHz. On the other hand, if we consider only the frequency mismatch of each of the 18 co-integrated pairs relatively to its average frequency, the standard deviation is 27.2 kHz, or 0.69 %. Discounting the first 10 chips, for which the fabrication "recipe" was still under development, the first figure drops to 1.03 %, and the second to 0.36 %. This shows that co-integration improves the match between resonators by a factor between 2.18, or 2.85 if only the "well-etched" chips are taken into account.

Concerning the CFB, the same figures can be obtained, yielding a mean resonance frequency of 3.02 MHz, a total variation of 2.6 % considering every possible pair or 1.48 % considering only the co-integrated pairs (gain of 1.76). And discounting the first 5 chips, these results adjust to 1.37 % for every possible pair and 0.31 % for the co-integrated pairs (gain of 4.36). Overall, there is a clear matching enhancement due to the co-integration. The results are presented in Table 3.3.

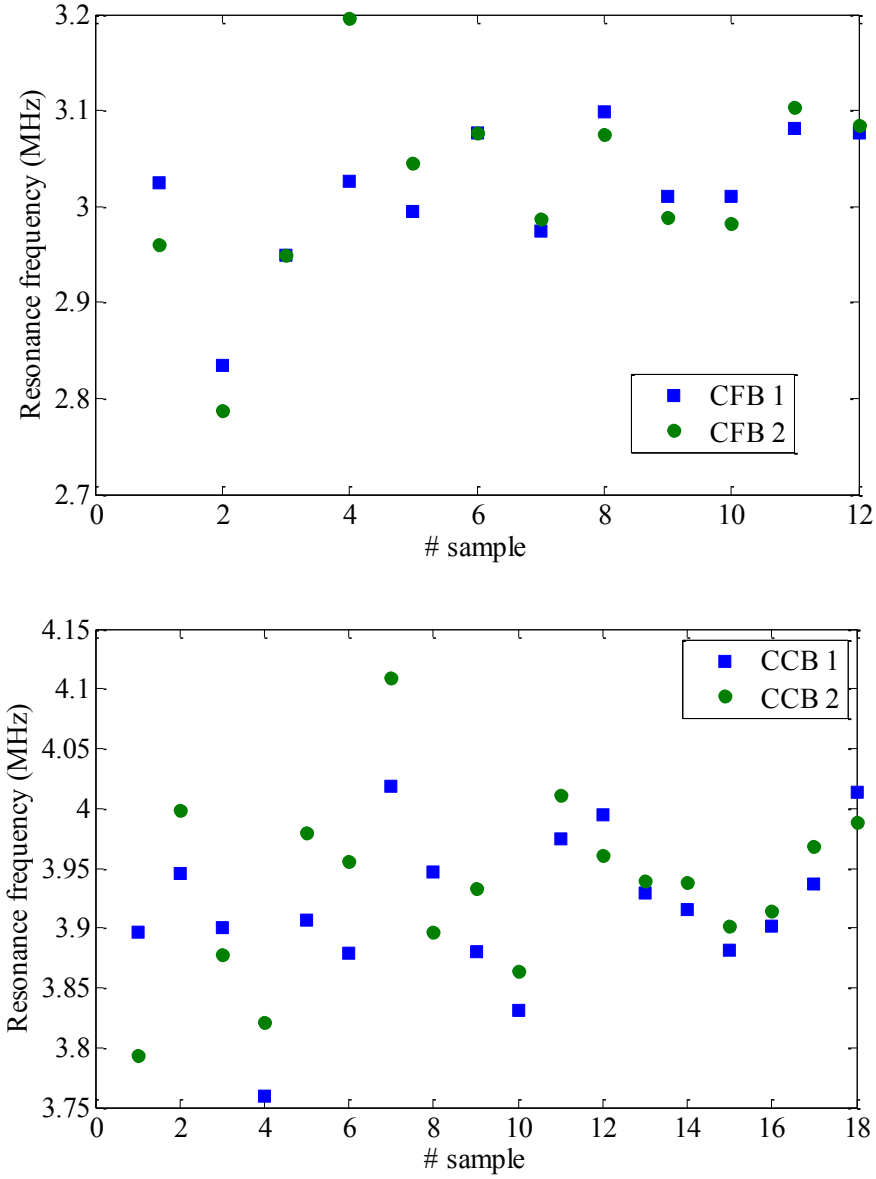

Figure 3.17: Resonance frequency at $V_b = 20\,V$ of the different resonators released in this work.

Resonator	Total deviation	Co-integrated deviation	Well-etched total deviation	Well-etched co-integrated deviation
CCB	1.5 %	0.69 %	1.03 %	0.36 %
CFB	2.6 %	1.48 %	1.37 %	0.31 %

Table 3.3: Matching improvement in term of resonance frequency due to co-integration

3.2.2 Matching of quality factors

The same operation can be made with the quality factors of the released CFB and CCB resonators. The measured quality factors (using the -3 dB bandwidth technique on the network analyzer) of every released CCB and CFB resonators are presented in Figure 3.18. In neither case is there any clear gain from co-integrating the resonators: the calculated standard deviations are equivalent whether one considers every possible combination or only co-integrated pairs, on the order of 10 % for CFB resonators, and 20 % for CCB resonators. The mean value of the CCB's quality factor is 119, which is 25 % smaller from the theoretical value (157, see section 1.3.2) but of the same order of magnitude. Concerning the CFB's quality factor the mean value is 110 which is 12 % from the theoretical value (126, see section 1.3.2).

The difference between the theoretical predictions and experimental results may be explained by the fact that the considered MEMS resonators are at the limit of the validity of the squeezed-film damping model developed in [76]. Indeed, the mean ratio of thickness over gap is only 3.5 for the CCB and 3.8 for the CFB while a ratio of 10 is in general expected for the assumptions of the squeezed-film damping model to hold, or slightly less when length-extension effects are taken into account (as in our model). This interpretation seems to be confirmed by the fact that the predictions are closer to the measurement in the CFB case, whose thickness/gap ratio is larger than in the CCB case.

Another explanation for the fact that the difference between the predictions obtained by [76] is higher in the case of CCB resonators than for CFB resonators might be due to the fact that other damping sources are not considered in [76]. For instance, anchor losses are more important in the case of CCB since there are two anchors. Moreover, in general, CCB resonators require more etching time, leading to more under-etching and potentially poorer anchors, thus increased damping.

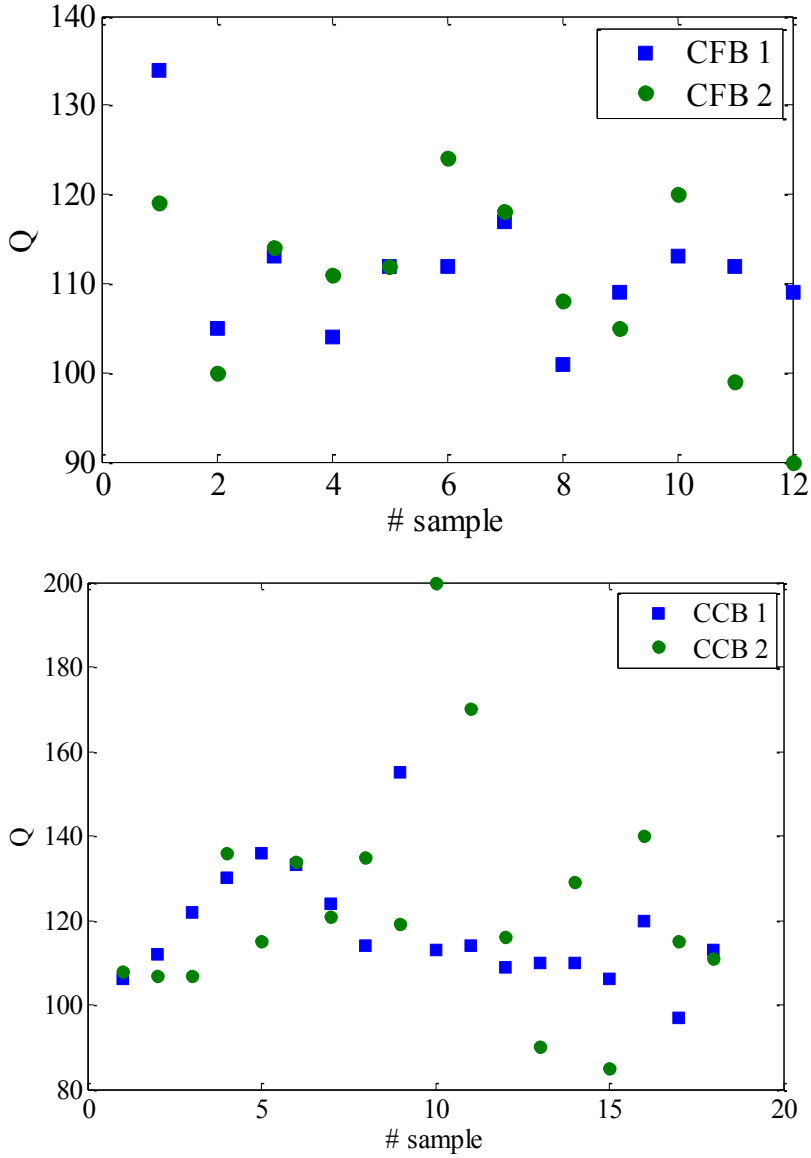

Figure 3.18: Quality factor in air of the different CMOS-MEMS resonators released in this work.

3.2.3 Consequences for the MILO

Supposing Equation (29) is verified, the measured quality factors and resonance frequencies can be used to estimate the theoretical optimal locking range. Using Equation (30), this yields:

$$\begin{cases} \varepsilon_{lock}^{CCB} = 0.012 \\ \varepsilon_{lock}^{CFB} = 0.013 \end{cases}. \tag{37}$$

The change of oscillation frequency induced by a stiffness mismatch ε is:

$$\Delta f(\varepsilon) \approx f_0 \times S_\omega \times \varepsilon \ . \tag{38}$$

This change of oscillation frequency is roughly equal to half the resonance frequency mismatch between the two resonators (if $Q_1 = Q_2$):

$$\Delta f(\varepsilon) \approx \frac{1}{2}(f_0 - f_{res2}) \ . \tag{39}$$

In this equation, f_0 is the nominal resonance frequency of both resonators, thus the nominal oscillation of the MILO (without mismatch), and $f_{res2} = f_0\sqrt{1+\varepsilon}$ the resonance frequency of the second resonator once a stiffness mismatch ε is applied. Given the value of S_ω=1/4, the non-dimensional locking ranges derived from the measured quality factors, and the mean resonance frequencies for the two geometries found in section 3.2.1, the maximum resonance frequency mismatch for which the MILO is locked is:

$$\begin{cases} \Delta f_0^{CCB}(\pm\varepsilon_{lock}) = \pm\, 23.35\ kHz \rightarrow \dfrac{\Delta f_0^{CCB}}{f_0^{CCB}} = 0.6\ \% \\ \Delta f_0^{CFB}(\pm\varepsilon_{lock}) = \pm\, 19.41\ kHz \rightarrow \dfrac{\Delta f_0^{CCB}}{f_0^{CCB}} = 0.64\ \% \end{cases} . \tag{40}$$

It should thus always be possible to lock two co-integrated resonators at the same bias voltage, since the average resonance frequency mismatch between co-integrated resonators is 0.36 % for CCB resonators and 0.31 % for CFB resonators. However, this would not be true if the resonators were not co-integrated (1.03 % resonance frequency mismatch for CCB resonators and 1.37 % for CFB resonators). Note that, for most couples of co-integrated resonators, there remains a resonance frequency mismatch ($\varepsilon \neq 0$), so that the MILO is not at equilibrium when the same bias voltage is used. One can then precisely tune the resonance frequency of the resonators by changing the bias voltage of one of the resonators, in order to set the MILO at the equilibrium or sweep through the MILO's entire locking range.

Close to $V_b = 20\ V$, the electrostatic softening formula of Equation (10) can be linearized, yielding:

$$\begin{cases} \left.\frac{\partial f^{CCB}}{\partial V_b}\right|_{V_b \approx 20\,V} = 5.68\,kHz.V^{-1} \\ \left.\frac{\partial f^{CFB}}{\partial V_b}\right|_{V_b \approx 20\,V} = 6.09\,kHz.V^{-1} \end{cases}. \tag{41}$$

Thus, the entire locking range can be swept by a +/− 4.17 V bias voltage sweep in the case of a CCB resonator, and a +/− 3.2 V bias voltage sweep in the case of CFB resonator.

Note that these values are valid close to the bias voltage of 20 V for which the resonance frequencies were obtained, and should be adjusted depending on the actual value of the bias voltage. For example, at 40 V, the locking range (in terms of bias voltage) should be twice as small as at 20 V.

3.3 Closed-loop characterization

3.3.1 Closed-loop waveforms

For each sample, the matching condition is obtained with frequency response measurements (Figure 3.19 and Figure 3.20 on the left-hand side). After that, the loop is closed, using the setup b) (where the coupler and the bridge are connected by 1 cm SMA connectors, and the bridge is connected to the MEMS resonators by 15 cm SMA wires) described in Figure 2.20 in section 2.4.2, the resonators are biased with appropriate voltages and the oscillation builds up naturally. The excitation voltage of the resonators is controllable with the potentiometers. Oscilloscope probes are put at the input of both resonators and at the output of both amplifiers (Figure 3.19 and Figure 3.20 on the right-hand side). The measurements are compared to the transient simulations, showing good agreement except for the saturation of V_1 in the CFB MILO. This leads to a slight discrepancy between the measured and simulated duty cycles of V_{f1} and V_{f2}. When the amplifiers are not saturated, as in the CCB MILO, the model describes accurately the system. The steady-state consumption is 9.5 mA which corresponds to the simulated value (estimated in section 2.5).

As illustrated in the experimental oscillograms from Figure 3.20, there are some perturbations at the transitions, especially in the case of the CCB MILO, with a higher

oscillation frequency, even though they are reduced when using setup b) instead of setup a) (Figure 3.21).

Once the loop is closed, the only measurable phase shift is the one between the amplifiers' output and the bridge's output. In the case of the CFB MILO (Figure 3.20 top) this measured phase shift is -25 °, and -28 ° in the case of the CCB MILO (Figure 3.20 bottom). This goes accordingly to the simulated results (-25.3 ° for the CFB, and -28.6 ° for the CCB) given the measurement's uncertainty.

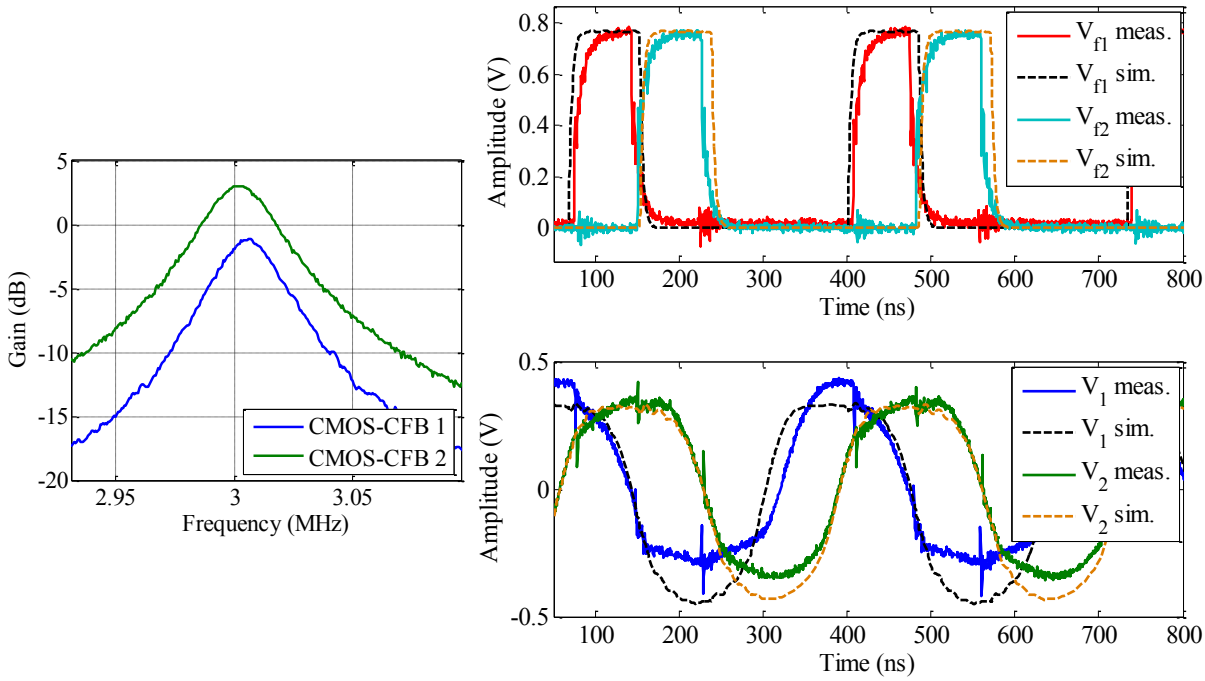

Figure 3.19: CFB MILO: sample 12, $V_{b1} = 30\,V$, $V_{b2} = 28\,V$ CMOS-MEMS frequency response and closed-loop waveforms (simulated and measured)

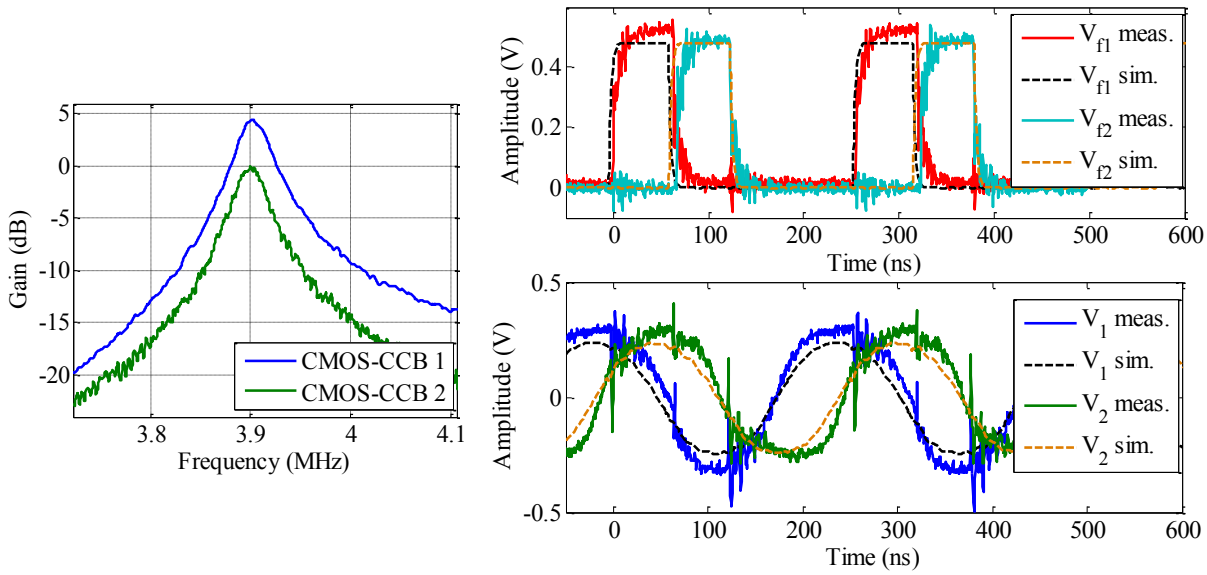

Figure 3.20: CCB MILO: sample 16, $V_{b1} = 20\ V$, $V_{b2} = 22.3\ V$: CMOS-MEMS frequency response and closed-loop waveforms (simulated and measured).

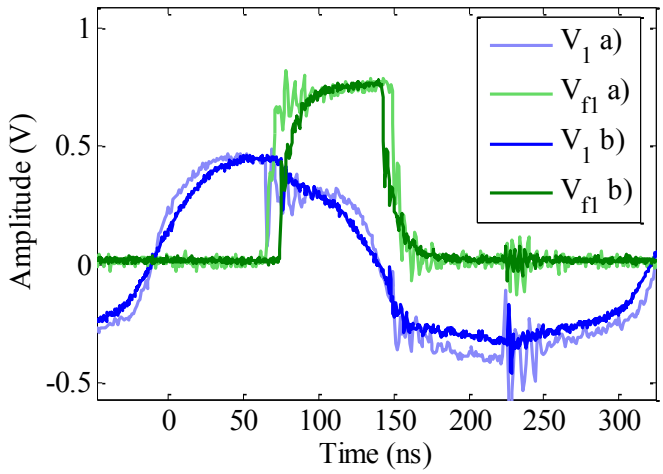

Figure 3.21: Closed loop experimental oscillogram of CFB MILO (sample 12, $V_{b1} = 30\ V$, $V_{b2} = 28\ V$) obtained with setup a) and setup b).

3.3.2 Amplitude, saturation and hysteresis

The amplifiers begins to saturate around 200 mV_{peak}, but the saturation is asymmetrical since the dynamic range is limited by V_{dd} and the output DC value of the amplifier is 2.7 V (i.e. the upper part of the waveform is saturated due to the proximity of the DC value and V_{dd}). This means that when the output signal of the amplifier goes through the bias tee, its DC value does not correspond to the "true" zero crossing, but a slightly higher value. Thus, when the output signal of the bias tee is

compared to its DC value, the duty cycle of the comparator's output is not 50 % but slightly less, leading to duty cycles of less than 25 % at the coupler's output. This point is illustrated in Figure 3.22, with two transient open loop simulations with two different input amplitudes, showing the reduction of the duty cycle due to the saturation of the amplifier.

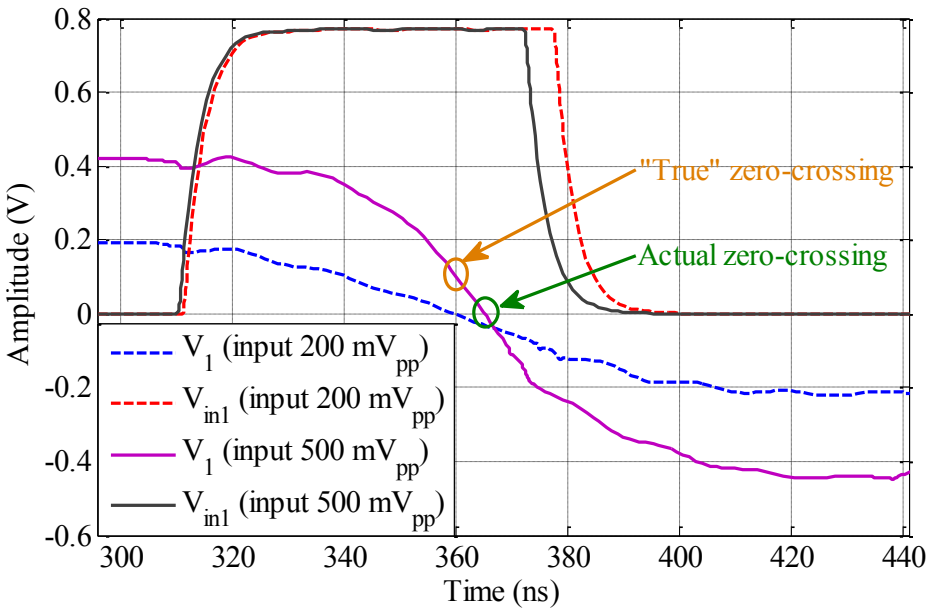

Figure 3.22: Transient simulation of a CCB MILO with two different input amplitudes. The dashed blue waveform is not saturated, showing the true zero crossing, while the purple full waveform is highly saturated, showing a 5 ns shift from the true zero crossing, leading to a reduction of the duty cycle.

As long as both amplifiers are identically saturated, when passing through the coupler, DC_1 and DC_2 are equally affected, thus not the estimated phase difference φ as mentioned in section 2.3.1. This point is illustrated in Figure 3.23 and Table 3.4. Waveforms of the same CCB MILO (sample 16) are taken for various bias voltages V_{b1} and V_{b2}, resulting in various amplitudes of the amplifiers' output and various saturation levels. It is seen that both DC_1 and DC_2 decrease, due to the saturation, but the calculated φ remains unchanged.

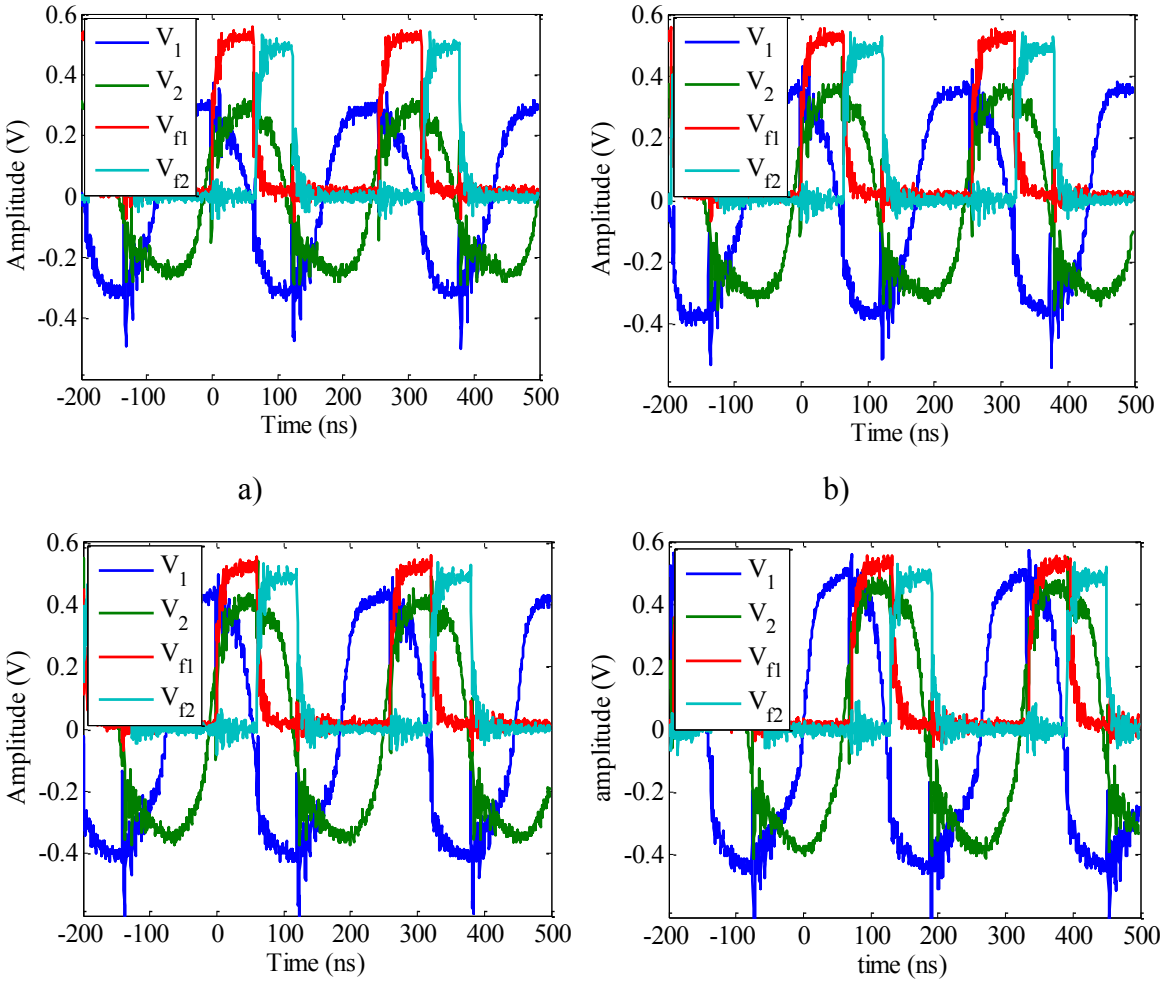

Figure 3.23: Experimental oscillograms of a CCB MILO (sample 16) for different biasing voltages. V_{b1} and V_{b2} are respectively: a) 20 V and 22.3 V; b) 25 V and 25.3 V; c) 30 V and 32.3 V; d) 35 and 37.3 V.

Vrms (mV)	DC_1 (%)	DC_2 (%)	$DC_1 + DC_2$ (%)	φ (°)
600	24.88	22.7	47.58	94.12
700	24.69	22.48	47.17	94.2
800	24.1	22	46.1	94.1
900	23	21	44	94.1

Table 3.4: Calculated phase difference φ based on duty cycles measurements for different levels of amplitudes of the outputs of the amplifiers.

Without any saturation, the sum is nominally 0.5, however no saturation means low amplitudes (i.e. less than 0.4 $V_{peak\text{-}peak}$). However, only DC_2 is affected by the 17 mV hysteresis on the negative transition (see section 2.3.2), since DC_1 starts at the

positive threshold of V_1, ends at the positive threshold of V_2, while DC_2 starts at the positive threshold of V_2 and ends at the negative threshold of V_2. This is illustrated in Figure 3.24, with an arbitrary 0.2 A.U. hysteresis on the negative threshold, resulting in $DC_1 \neq DC_2$ while having $\varphi = 90\,°$. Having low-amplitude signals compared to the hysteresis thus creates an asymmetry between DC_1 and DC_2 which is not related to a phase difference between V_1 and V_2. Since DC_1 and DC_2 is the way used to calculate this phase difference, the choice is made to have higher amplitudes, thus saturation in order to avoid this effect.

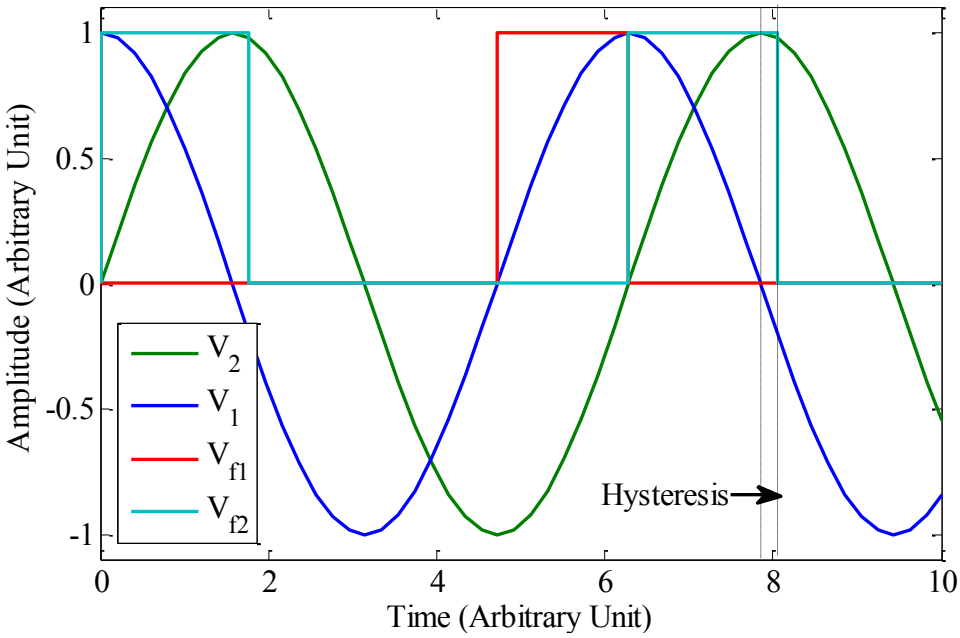

Figure 3.24: Simulink high-level simulation of the coupler, illustrating a potential drawback of the hysteresis.

3.4 Phase difference sensitivity to mismatch

To characterize a differential resonant sensor, one must first assess the output sensitivity to the measurand. Concerning the MILO, the output quantity is the phase difference between the two resonators φ, measured thanks to the duty cycle of the resonators' excitation voltage DC_1 and DC_2 according to Equation (35). An illustration of this sensing scheme is provided in Figure 3.25 and described hereafter:

- The steady-state is fixed through the tuning of V_{b1} and V_{b2} as described in subsections 3.2.1 and 3.3. The steady-state phase difference φ_0 is nominally 90 °.
- A variation of the CMOS-MEMS 2's bias voltage ΔV_{b2} is applied, generating a stiffness mismatch ε thus a resonance frequency mismatch Δf_0 according to the electrostatic stiffness phenomenon.
- The resonance frequency mismatch Δf_0 leads to a change in the MILO's oscillation frequency (approximately $\Delta f_0/2$, if $Q_1 = Q_2$) and a phase difference change $\Delta\varphi$. Close to $\varepsilon = 0$, the dependence of the resonance frequency (or pulsation) and of the phase difference to ε are theoretically given by Equation (33).

In the next two subsections, the quantities S_φ, S_ω and S_{MILO} are experimentally measured, and compared to the theory for the two geometries. As mentioned in section 2.1, these quantities of interest should be equal to:

$$\begin{cases} S_\varphi = \dfrac{4}{\pi}\dfrac{Q_1 . Q_2}{Q_1 + Q_2} \\ S_\omega = \dfrac{1}{2}\dfrac{Q_2}{Q_1 + Q_2} \\ S_{MILO} = \dfrac{8Q_1}{\pi} \end{cases}, \tag{42}$$

provided the phase condition of Equation (29) is verified. It has been proven experimentally that the condition is verified for the CFB MILO but is not for the CCB MILO. One should expect different experimental results for the two cases, as illustrated in subsections 3.4.1 and 3.4.2. The frequency is measured by an Agilent 53230a counter, and the phase difference is calculated based on the duty cycles measurements provided by the same counter. The frequency counter has a 20 ps time interval resolution and a 12 digits/s precision. The resolution of the counter is not the bottleneck for the estimation of duty cycles and oscillation frequency. The standard deviation of measured oscillation frequencies is always between 30 Hz and 100 Hz in our experiments, and the standard deviation of measured duty cycles is around and 0.5% (+/-0.2 %), corresponding to a phase difference standard deviation around 1.8 ° (+/- 0.7 °). For oscillation frequency, error bars are not placed because they would be

too small (30 Hz compared to 3 MHz) to be readable. For phase difference and duty cycles, error bars are not placed because the standard deviation is rather constant over all the measurements made during this work, so they do not add any supplementary information. One should keep in mind the 1.8 ° precision of the measurements when reading this part.

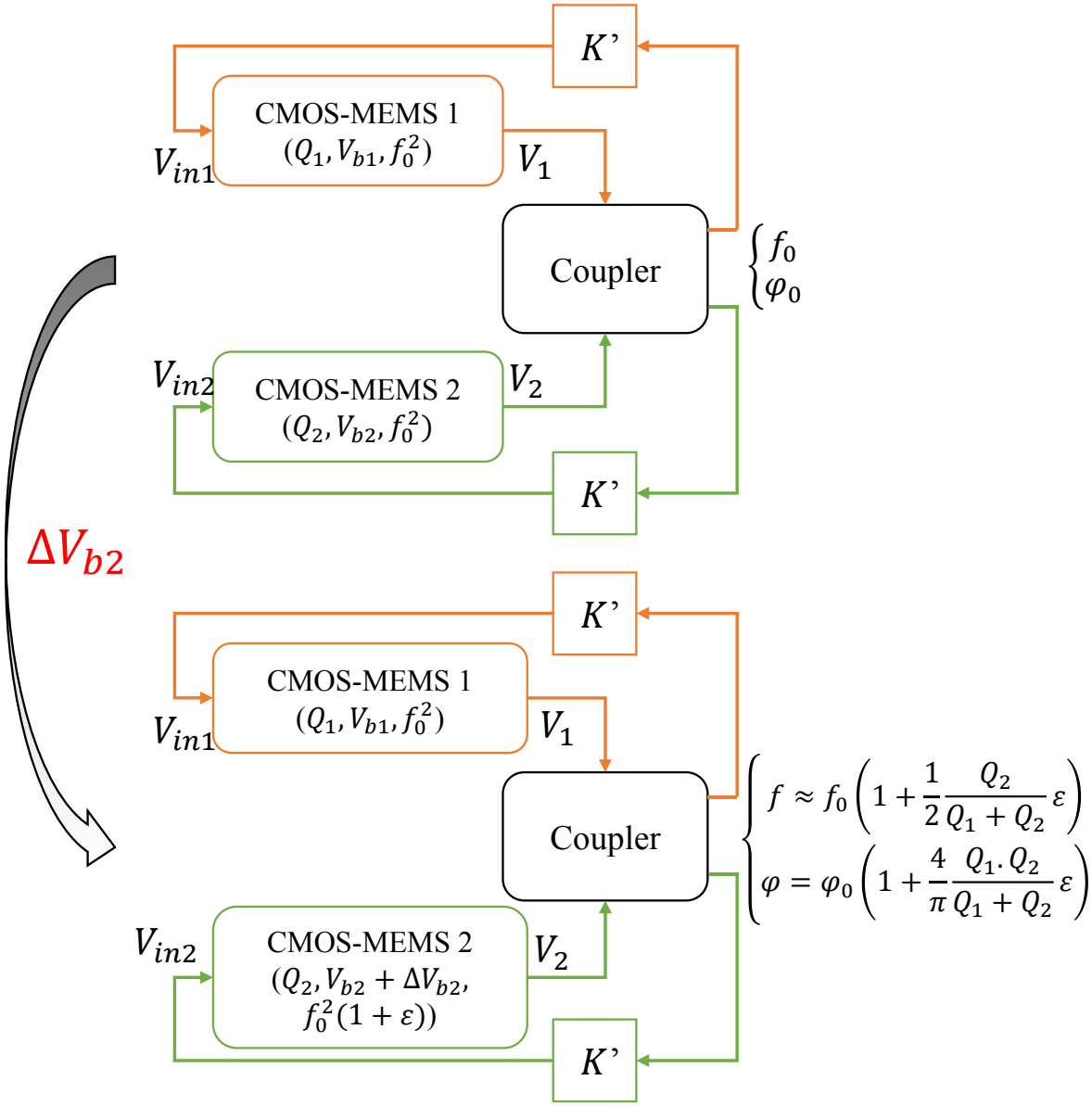

Figure 3.25: Differential resonant sensing scheme of the MILO.

3.4.1 Sensitivity to mismatch of CFB MILO

This section aims to assess the sensitivity to mismatch of CFB MILO and the validity of the theoretical predictions. These predictions (Equations (33) and (34)) are

made provided the MILO is close to $\varepsilon = 0$, which means that it is the case in this section as well. The edges of the locking range are explored in section 3.5.

The experiments are conducted on sample 12 ($Q_1 = 110$, $Q_2 = 90$) whose steady-state response is shown in Figure 3.20. The resonators are biased at $V_{b1} = 30\ V$, $V_{b2} = 28\ V$, in order to have a resonance frequency at $f_0 = 3.008\ MHz$. The oscillation frequency and duty cycles are recorded as V_{b2} is swept, and plotted in Figure 3.26. As mentioned in section 2.1 and recalled in Figure 3.25, ε is defined as a stiffness mismatch between the resonators. Since the resonance frequency is proportional to the square root of the stiffness, it follows that the variation of the second resonator's resonance frequency with ε is

$$\left.\frac{\partial f_{res2}}{\partial \varepsilon}\right|_{\varepsilon=0} \approx \frac{f_0}{2}, \tag{43}$$

where f_0 is the nominal value of the resonance frequency of both resonators, and also the oscillation frequency of the MILO (without mismatch). The BVD model predicts, around 28 V, an electrostatic softening of -9.6 kHz.V^{-1}, which means that the relation between V_{b2} and ε can be written:

$$\left.\frac{\partial \varepsilon}{\partial V_{b2}}\right|_{\varepsilon=0} \approx \frac{2}{f_0}.\frac{\partial f_{res2}}{\partial V_{b2}} \Longrightarrow \varepsilon \approx -6.4.10^{-3}\Delta V_{b2}\ . \tag{44}$$

One can then use Equation (33) to predict the variation of the oscillation frequency of the MILO f with V_{b2}:

$$\left.\frac{\partial f}{\partial V_{b2}}\right|_{\varepsilon=0} \approx \frac{\partial f}{\partial \varepsilon}\frac{\partial \varepsilon}{\partial V_{b2}}. \tag{45}$$

$$\left.\frac{\partial f}{\partial V_{b2}}\right|_{\varepsilon=0} \approx \frac{f_0}{2}\frac{Q_2}{Q_1+Q_2}\frac{2}{f_0}\frac{\partial f_{res2}}{\partial V_{b2}} \approx -4.32\ kHz.V^{-1}\ . \tag{46}$$

As presented in Figure 3.26, the measurement are in good agreement with the theory.

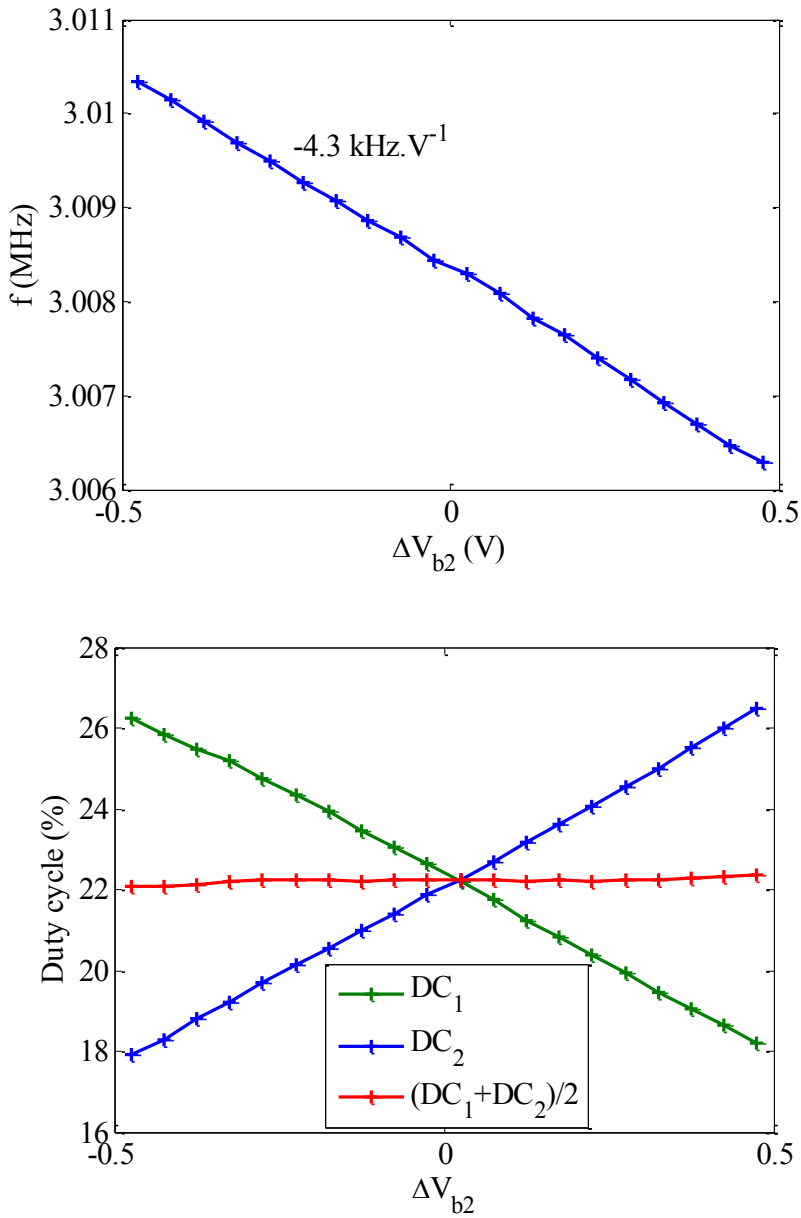

Figure 3.26: Measured oscillation frequency (Top) and duty cycles (Bottom) for different values of ΔV_{b2}.

Then, using equation (35), one can calculate the phase difference based on the duty cycles measurement. In Figure 3.27 the phase variation with ε (calculated according to Equation (44)) is plotted alongside the frequency variation with ε, as well as the theoretical predictions from Equations (33) and (34). Overall, the theory predicts the behavior of the MILO very well. For an electrometer, where one seeks to measure the quantity ΔV_{b2}, the sensitivity of the phase difference to the measurand is -36°.V^{-1}, or -4.10^{5} ppm.V^{-1}, while the sensitivity of the frequency to the measurand is -4.3

kHz.V^{-1}, or -1.39.10^{3} ppm.V^{-1}. Both show good linearity, but the sensitivity enhancement is 278 if the phase difference is taken as the output signal.

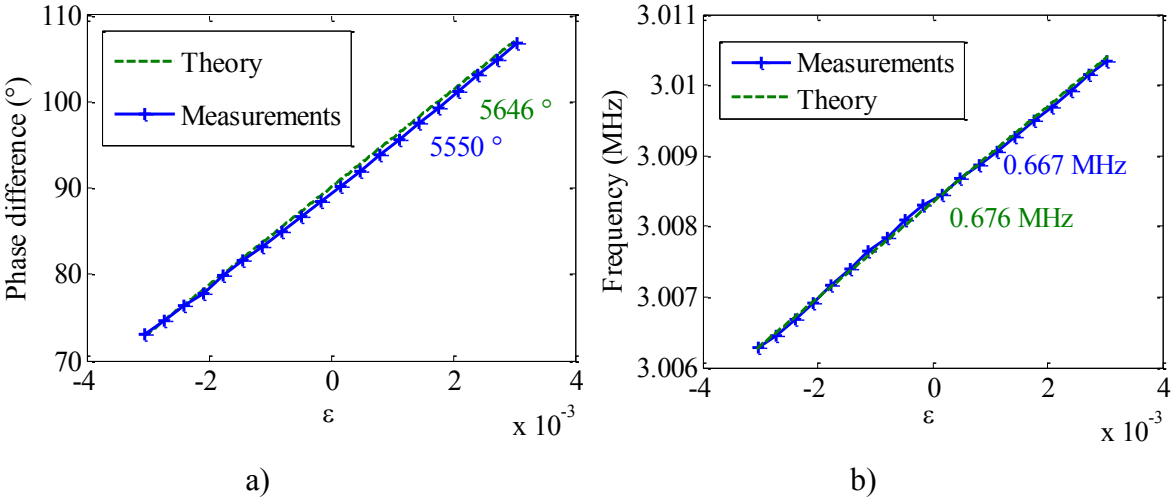

a) b)

Figure 3.27: a) calculated φ VS calculated ε; b) measured f VS calculated ε.

This is confirmed by plotting the fractional phase (i.e. $\varphi/\varphi_0 - 1$) versus the fractional frequency (i.e. $f/f_0 - 1$) and compare it to the theoretical value of S_{MILO} found in Equation (34). The resulting figure is plotted in Figure 3.28, showing excellent agreement (0.7 % difference), which is expected given the fact that the architecture is optimized for an oscillation frequency around 3 MHz.

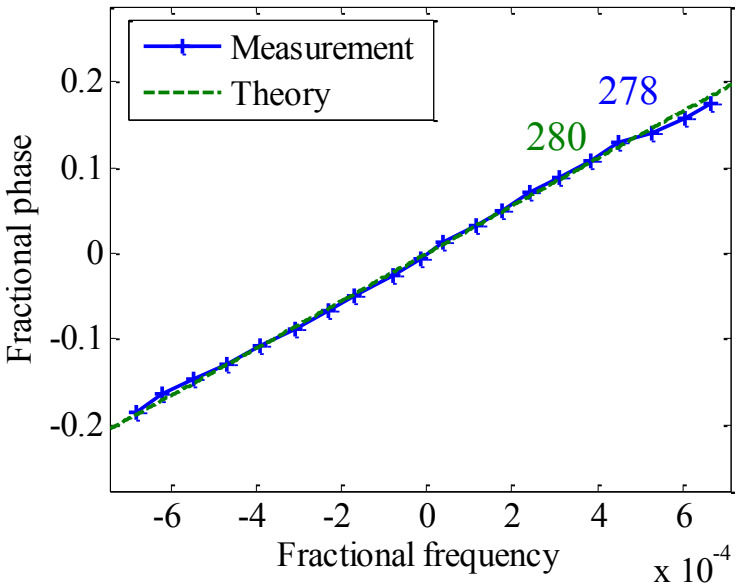

Figure 3.28: Fractional phase VS fractional frequency for the CFB MILO, measurement and theoretical predictions.

3.4.2 Sensitivity to mismatch of CCB MILO

The same experiments are performed on CCB MILO of sample 16 ($Q_1 = 120$, $Q_2 = 140$). The resonators are biased at $V_{b1} = 35\ V$ and $V_{b2} = 37.3\ V$, yielding $f_0 = 3.791\ MHz$. The second resonator's bias voltage is the swept around its steady-state value. The oscillation frequency and duty cycles are recorded and plotted in Figure 3.30. The BVD predicts an electrostatic softening of -10.2 kHz.V^{-1} around a bias voltage of 37 V, meaning that one can write, according to Equation (44):

$$\varepsilon \approx -5.4.10^{-3}\ \Delta V_{b2}\ . \tag{47}$$

one can predict a variation of the oscillation frequency of the MILO with V_{b2} of:

$$\left.\frac{\partial f}{\partial V_{b2}}\right|_{\varepsilon=0} \approx -5.5\ kHz.V^{-1}\ . \tag{48}$$

The measured value of the decrease of the oscillation frequency (-5.7 kHz.V^{-1}, see in Figure 3.29) is slightly higher than expected. This might be due to a gap smaller in the second resonator, increasing its electrostatic softening phenomenon. Then, using equation (35), one can calculate the phase difference based on the duty cycles measurement from Figure 3.30, and plot it versus ε alongside the oscillation frequency as illustrated in Figure 3.31, and compare it to the theory.

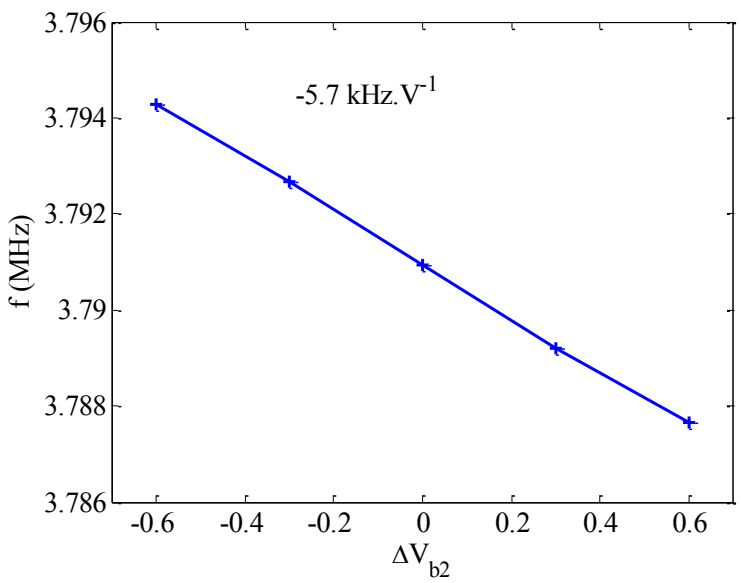

Figure 3.29: Measured oscillation frequency of the CCB MILO for different values of ΔV_{b2}

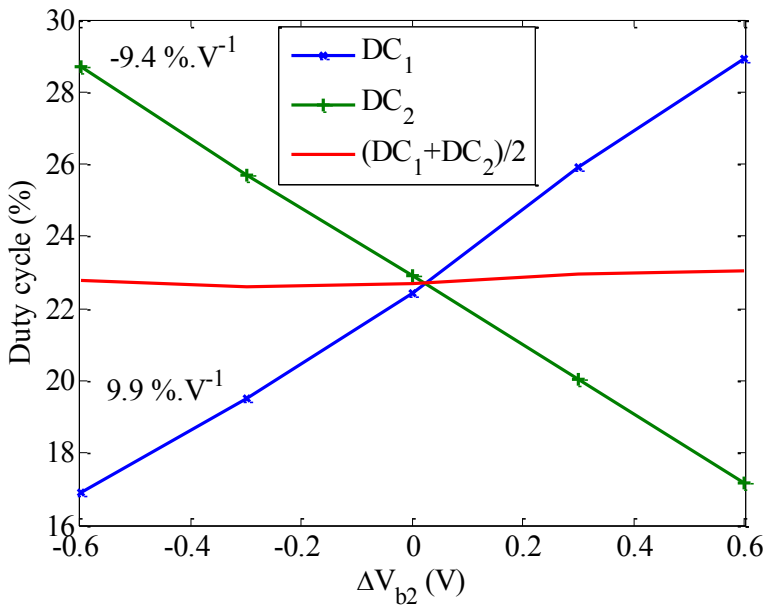

Figure 3.30: Measured duty cycles of V_{in1} and V_{in2} for different values of ΔV_{b2}.

The measured phase difference variation with ε (slope 7048°) is 2 % inferior to the theoretical predictions from Equation (33) (i.e. Simplified Theory, with a slope of 7191°). This is explained by the fact that the modelling is made assuming Equation (29) is valid. Yet, it is seen in section 2.5 that it is not the case for the CCB MILO. The experimental results are also compared to the complete theory [130] (the code to obtain the figures is presented in Annex 2), which takes into account the different quality factors and the different values of θ_{res} and Ψ_{res}. The variation of the oscillation frequency with ε is not related to θ_{res} and Ψ_{res}, and is accurately predicted by both the simplified theory and the complete theory.

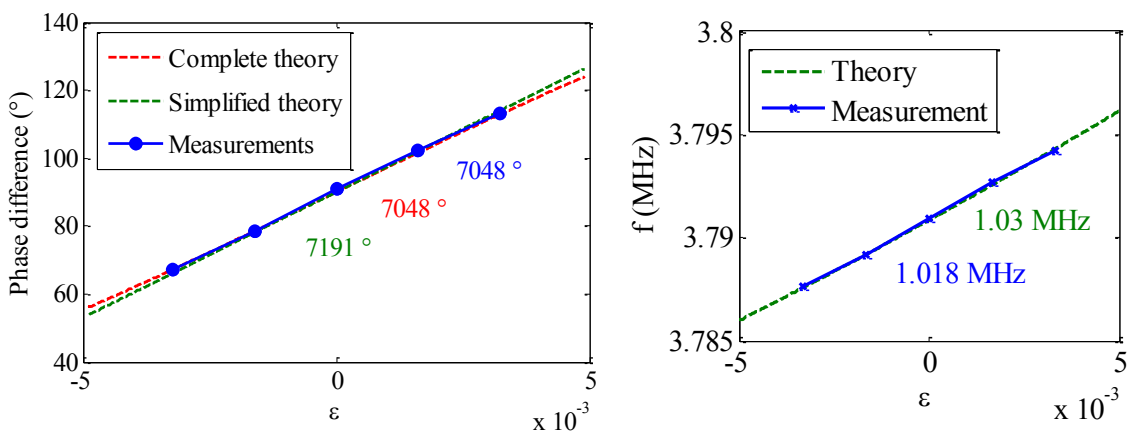

a) b)

Figure 3.31: a) Measured φ VS measured ε; b) measured f VS calculated ε.

Taking the electrometer application, the sensitivity of the phase difference (resp. oscillation frequency) to ΔV_{b2} is -38.07 °.V^{-1}, or -4.27.10^{5} ppm.V^{-1} (resp. -5.56 kHz.V^{-1}, or -1.46.10^{3} ppm.V^{-1}), showing a sensitivity enhancement of 294. This is illustrated by plotting the fractional phase versus the fractional frequency in Figure 3.32. As expected, the sensitivity enhancement is 4 % smaller than the theoretical predictions (294 to 305) from (34) since the phase delay inside the loop is not optimal. However, the complete theory developed in [130], where the non-optimal phase delays is taken into account, predicts the sensitivity enhancement very accurately. This shows the robustness of the architecture, since an important phase gap between the optimal value and the obtained value (-28.2 ° instead of -20 °, or 41 %) results in a small performance degradation since the phase difference sensitivity to mismatch is decreased by only 4 % compared to its optimal value.

According to the comparison between the predictions and the measurements made in this subsection and in subsection 3.4.1, one can conclude that the simplified model developed in section 2.1 predicts accurately the MILO's sensitivity enhancement if the phase condition from equation (29) is met. If not, one should employ the complete theory developed in [130] to obtain the accurate matching between the prediction and the measurement. However, no analytical expression of the sensitivity enhancement, given the values of θ_{res}, Ψ_{res}, Q_1 and Q_2 is provided in [130], only a system of equations that needs to be solved numerically to obtain the curves displayed in Figure 3.32.

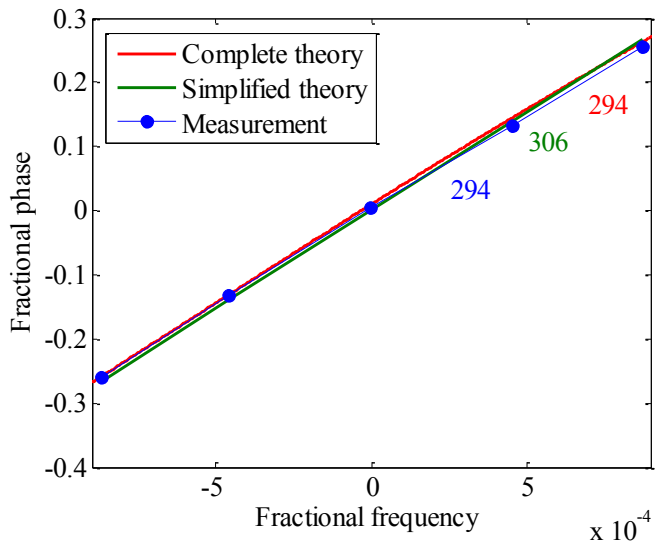

Figure 3.32: Fractional phase VS fractional frequency: measurements, simplified theory from Equation (34) and complete theory from [130], with the extracted linear slopes.

3.5 Locking range

The locking range experiment is conducted on the same sample as in the last subsection (CCB MILO, sample 16), following the same procedure (i.e. setting the equilibrium, then changing V_{b2} and recording the phase difference and frequency). However, the biasing voltage is changed up to the point where the oscillation is lost. The same quantities as in the last subsection are plotted in Figure 3.33 and in Figure 3.34.

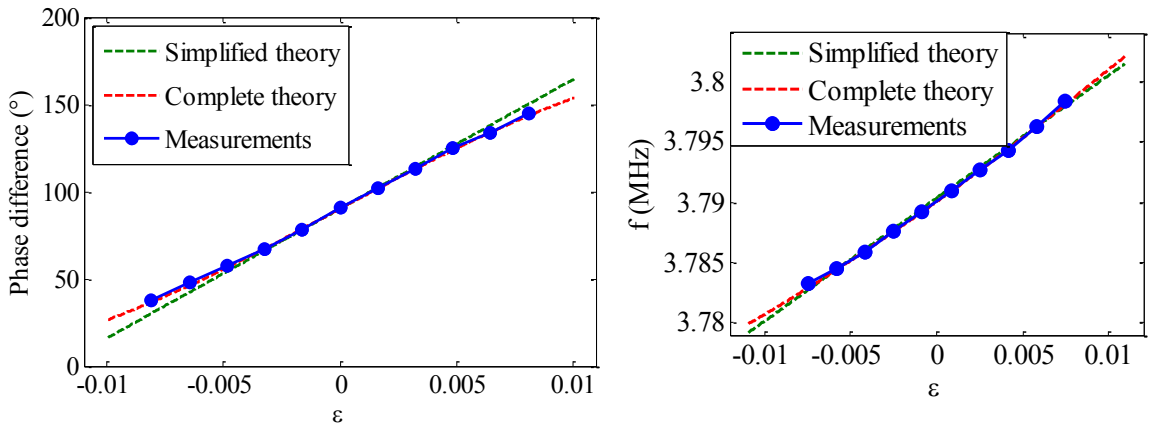

a) b)

Figure 3.33: Measurements, predictions from the simplified theory and the complete theory: a) Phase difference vs. epsilon; b) Frequency vs. epsilon, each time

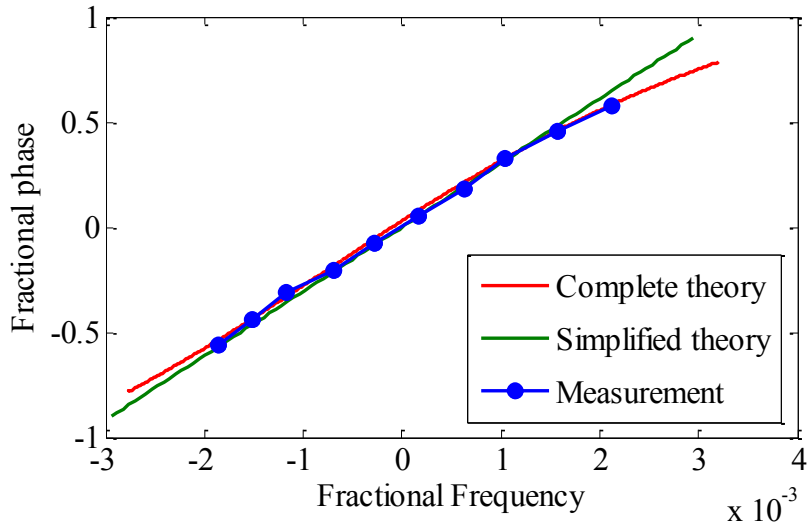

Figure 3.34: Measurements and predictions of the fractional phase vs. fractional frequency.

Overall, the experimental locking range [-8.055×10^{-4}: 8.429×10^{-4}] is 20 % smaller than predicted, either by the simplified theory or the complete theory ([-1.08×10^{-3}: 1.08×10^{-3}]). This might be due to the fact that, on the edges of the locking range, one pulse width becomes very small, leading to small actuation forces and small amplitude. The comparators' hysteresis which is not taken into account, might cause instabilities, leading to early quenching of the loop.

The measured "saturation" in Figure 3.34 is predicted by the complete theory from [130]. One should note that the saturation is only for positive fractional phases due to the fact that, in CCB MILOs, $\theta_{res} < 45\,° - \Psi_{res}$. If we had $\theta_{res} > 45\,° - \Psi_{res}$, the saturation would have appeared on for negative fractional phases. For a balanced architecture, slight saturations are theoretically present on both sides, but less marked. This is illustrated in Figure 3.35. Unfortunately, due to reliability issues (described in section 4.1) the results of such experiments were not made on the CFB MILO.

Taking again the electrometer application, the experimental locking range is 3V, compared to a theoretical 3.7 V for both modellings. One can think of controlling the loop with a second feedback loop in order to ensure the fact that the system is kept close to the quadrature, where the sensitivity is maximal, and the above-mentioned "saturation" caused by a $\theta_{res} \neq 45\,° - \Psi_{res}$ are avoided. Some leads about this topic are given in the last chapter.

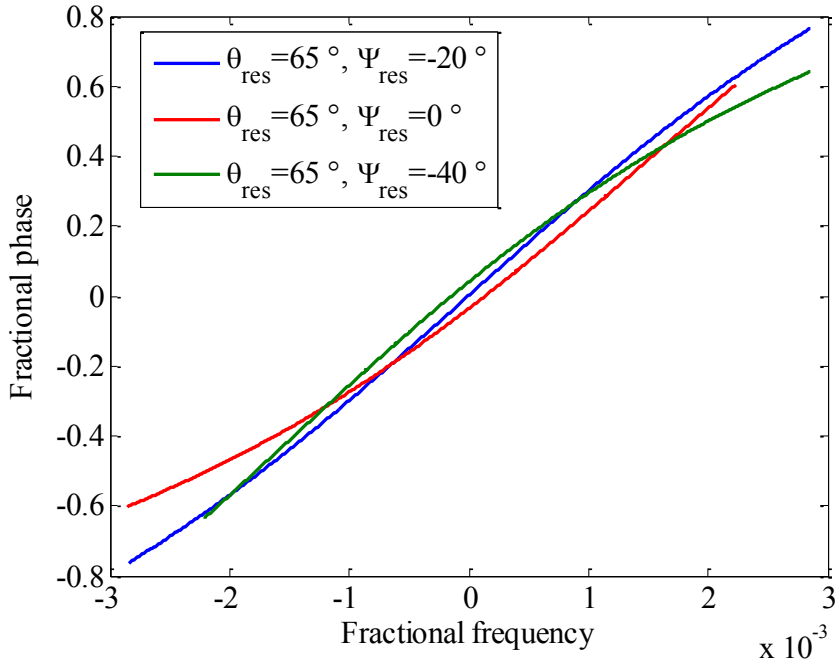

Figure 3.35: Simulated fractional phase vs. fractional frequency according to [130] for a balanced architecture (blue line) and two imbalanced architectures (red and green lines).

3.6 Common-mode rejection

The next step in order to characterize the MILO as a differential sensor is to assess its common-mode rejection capabilities. Theoretically, any physical quantity equally affecting both resonators has no effect on φ. This section aims to demonstrate experimentally the common-mode rejection capabilities of the co-integrated MILO through the rejection of the thermal drift of the MEMS resonators presented in section 1.4.1. The chip, placed and wire-bonded on a PCB, is placed over a thermal chuck, as presented in Figure 3.36.

The resonators are biased to meet the matching condition, and the MILO is started. The heating is set on the thermal chuck, and as in the last three sections, the frequency and duty cycles are recorded. The temperature is increased by 10 °C steps. On each step, a mismatch is applied with ΔV_{b2} in order to ensure the fact that the drift is rejected whatever the value of ε (as long as the $\varepsilon < \varepsilon_{lock}$).

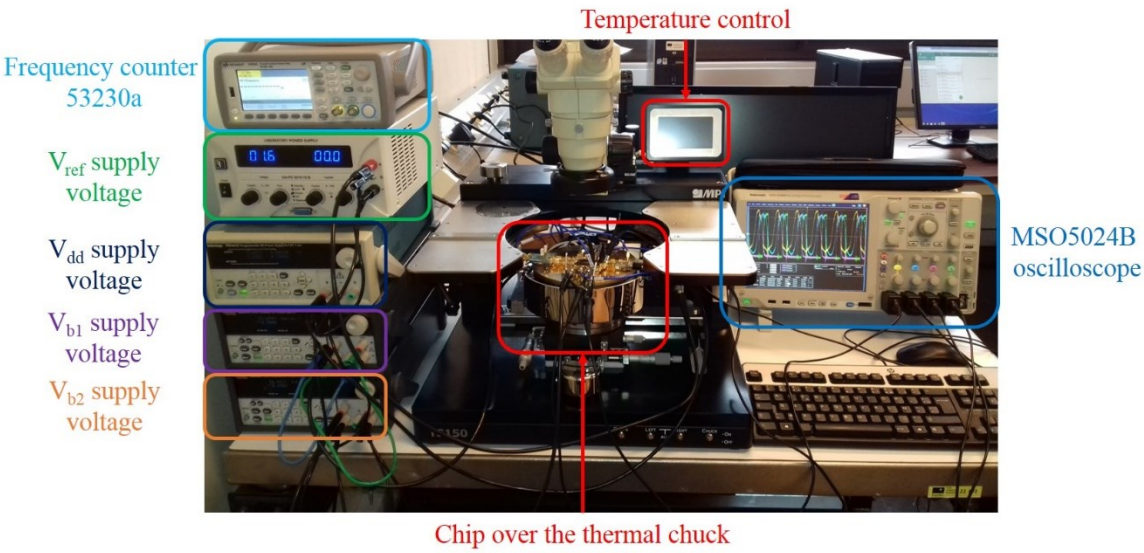

Figure 3.36: Experimental set-up for the drift rejection measurements.

3.6.1 Common-mode rejection of CFB MILOs

The experiment is performed on the sample 1 ($Q_1 = 134$ and $Q_2 = 119$). The equilibrium is set for with $V_{b1} = 23\ V$ and $V_{b2} = 30\ V$, yielding $f_0 = 2.769\ MHz$ as illustrated in the experimental spectra plotted in Figure 3.37.

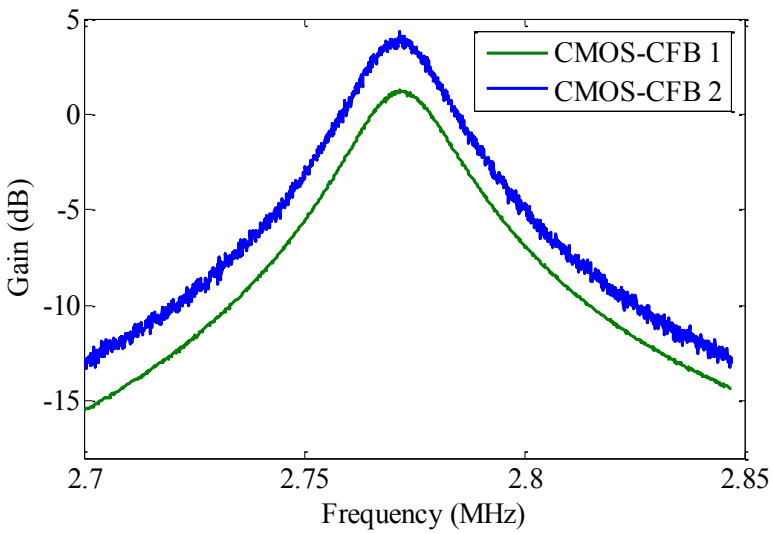

Figure 3.37: Experimental spectra of the CMOS-CFB resonators (sample 1) with $V_{b1} = 23\ V$, $V_{b2} = 30\ V$.

Then, the temperature is increased by 10 °C step, and for each step, a ±0.6 V is applied on V_{b2} with 0.2 V steps. The frequency and phase are recorded and calculated,

and plotted in Figure 3.39. Transient simulations of the device are also conducted for $\varepsilon = 0$, at the same temperatures (the models of the resonators are modified at each temperature step, and the circuitry's temperature is taken into account in the simulation engine of Cadence). The results are plotted in red dashed lines in Figure 3.39, and in Table 3.5, the phase and frequency dependence with the temperature are extracted with a linear fit for the different values of V_{b2}.

As expected, the frequency decrease with the temperature is not related to V_{b2}. There is a clear phase difference drift with the temperature for low values of V_{b2}, and the system rejects the thermal drift more efficiently for a ΔV_{b2} of +0.4. Two factors can explain the phase difference drift, supported by two Cadence simulations.

Mechanically, there is a stiffness mismatch between the resonators, which is compensated by the electrostatic tuning. When the temperature increases, the mechanical stiffness variation is not the same for both resonators. The resulting resonance frequency mismatch with the temperature leads to a phase difference shift with the temperature. In this case, the resonance tuning is obtained for $V_{b1} < V_{b2}$, meaning that the mechanical stiffness of the second resonator is higher than the first resonator's. When the temperature increases, it proportionally affects more the second resonator, i.e. its resonance frequency decreases faster than the first resonator's. This leads to a negative ε, and a decrease of the phase difference with the temperature. To prove this, a Cadence simulation is performed, where first two BVD models are obtained in order to have the same resonance frequency but with the bias voltage chosen for this experiment (i.e. respectively 23 V and 30 V). To this end, the width of each beams are adapted. Then, for each step of temperature, each one of the BVD models is changed according to the modelling made in section 1.4.1, and the simulation is started. For each step, the phase is extracted, and plotted in green dotted lines in Figure 3.39. This phenomenon leads to a -0.03°/°C phase difference drift (3 % difference from the measurements).

Electronically, simulations show that the hysteresis goes from 17 mV at 20 °C to 27 mV at 100 °C. It is demonstrated in section 3.3 that the hysteresis can decrease the estimation of φ based on the duty cycles measurements which is not related to the phase difference between the resonators. The other Cadence simulations, which is made with two identical BVD models (i.e. same dimensions and bias voltage), but

where only the temperature of the circuitry changes show that this phenomenon leads to a -0.01 °/°C drift (red dotted lines in Figure 3.39).

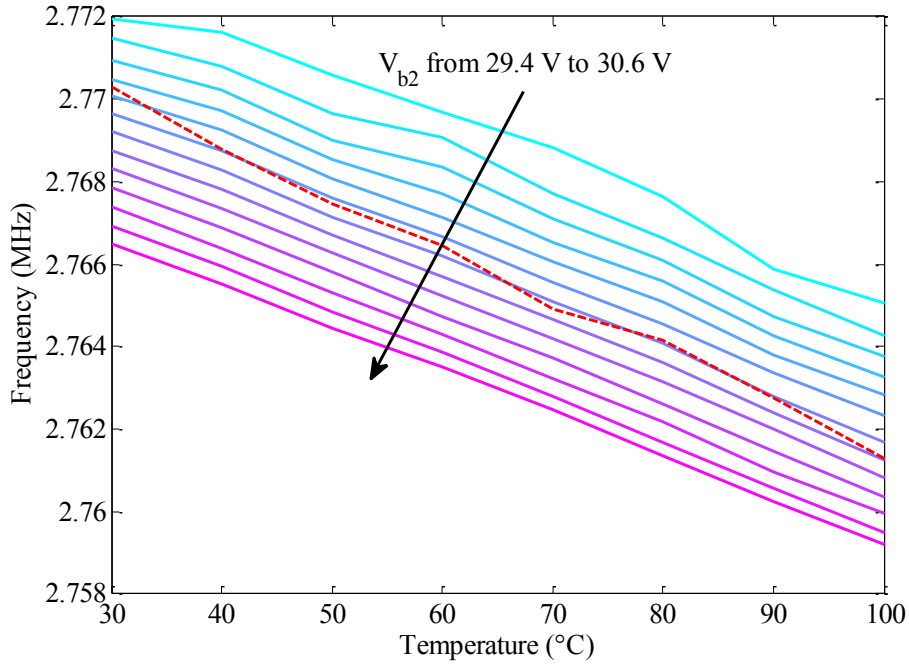

Figure 3.38: Experimental oscillation frequency of the CFB MILO of sample 1 for various temperature and V_{b2}. In red dotted lines, Cadence transient simulations, both setups (different BVD and same BVD) shows same results.

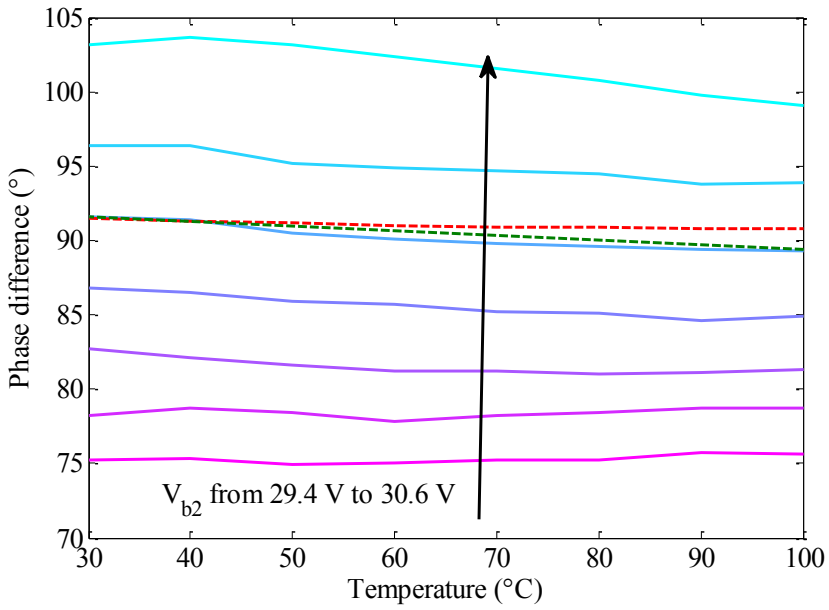

Figure 3.39: Experimental phase difference for the CFB MILO of sample 1 for various temperature and V_{b2}. In red dotted lines, Cadence transient simulations for two similar BVD models which change equally with the temperature. In green dotted line, Cadence transient simulations for two different BVD models.

ΔV_{b2} (V)	$\frac{\Delta f}{\Delta T}$ (Hz.°C^{-1}), linear fit	$\frac{1}{f_0}\frac{\Delta f}{\Delta T}$ (ppm.°C^{-1}), linear fit	$\frac{\Delta \varphi}{\Delta T}$ (°.°C^{-1}), linear fit	$\frac{1}{\varphi_0}\frac{\Delta \varphi}{\Delta T}$ (ppm.°C^{-1}), linear fit
-0.6	-103	-37.24	0.007	67
-0.4	-104.5	-37.78	0.0048	47
-0.2	-104.4	-37.74	-0.021	216
0	-104.7	-37.85	-0.031	340
0.2	-104.8	-37.9	-0.035	389
0.4	-105.1	-38	-0.04	470
0.6	-107	-38.7	-0.066	880
Cadence simulation				
Same BVD	-120.5	-43.4	-0.01	111
≠ BVD	-120.5	-43.4	-0.03	333

Table 3.5: Extracted dependence of the frequency and phase difference with the temperature for the CFB MILO (sample 1) for various values of ΔV_{b2}.

The quantities calculated in Table 3.5 must be compared to the dependence of the phase difference and oscillation frequency to the differential mode measured in subsection 3.4.1. In Table 3.6, the electrometer application is taken again and the effect of the thermal drift on the measurement ΔV_{b2} is calculated, if this measurement is made using the phase difference and the oscillation frequency.

ΔV_{b2} (V)	$\frac{\Delta f}{\Delta T}\frac{\Delta V_{b2}}{\Delta f}$ (mV.°C^{-1})	$\frac{\Delta \varphi}{\Delta T}\frac{\Delta V_{b2}}{\Delta \varphi}$ (mV.°C^{-1})	Rejection enhancement
-0.6	-26.8	0.17	166
-0.4	-27.2	0.12	232
-0.2	-27.2	0.54	50
0	-27.2	0.8	33.1
0.2	-27.3	1	27.9
0.4	-27.3	1.17	23.1
0.6	-27.8	2.2	21
Cadence simulation			
Total	-31.2	0.83	37

Table 3.6: Effect of the temperature on the measurement of ΔV_{b2} with a CFB MILO if the output signal is the f or φ, and ratio between these two.

3.6.2 Common-mode rejection of CCB MILOs

The same experiment is conducted on the CCB MILO of sample 16, also used in subsection 3.4.2. The resonators are biased at $V_{b1} = 35\ V$ and $V_{b2} = 37.3\ V$, with a ΔV_{b2} sweep performed at each 10 °C step. The oscillation frequency and phase difference are measured, and plotted in Figure 3.40 and Figure 3.41. The effect of temperature on phase difference and oscillation frequency is summarized in in Table 3.7.

The same Cadence simulations are performed, showing a -0.0143 °/°C phase difference shift due to the hysteresis increase with the temperature (red dotted lines), which is this time much smaller than the experimental phase difference shift. The phase difference shift due to the mechanical stiffness mismatch (green dotted lines) is -0.073 °/°C. The total simulated phase difference shift is -0.087 °/°C, which is according to the measurements.

The gap between V_{b1} and V_{b2} (which reflects the mechanical stiffness mismatch between the two resonators) is only 2 V, but the mechanical stiffness change with the temperature (illustrated by the oscillation frequency change with the temperature) is 10 times higher than in the CFB MILO case. This leads to a higher phase difference variation with the temperature. One can also observe that the phase difference variation with the temperature is less important for lower values of V_{b2}.

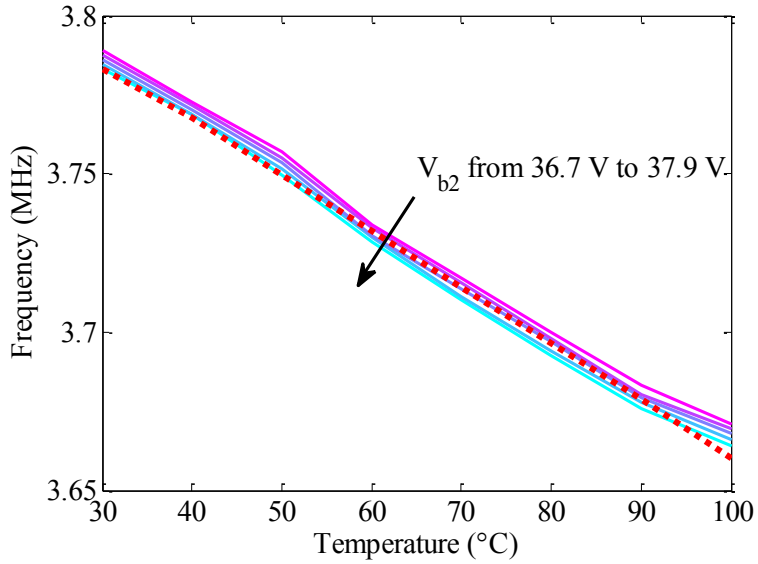

Figure 3.40: Full lines: experimental oscillation frequency of the CCB MILO of sample 16, for various temperature and V_{b2}. Red dotted line: simulated phase difference (both simulations show the same frequency variation)

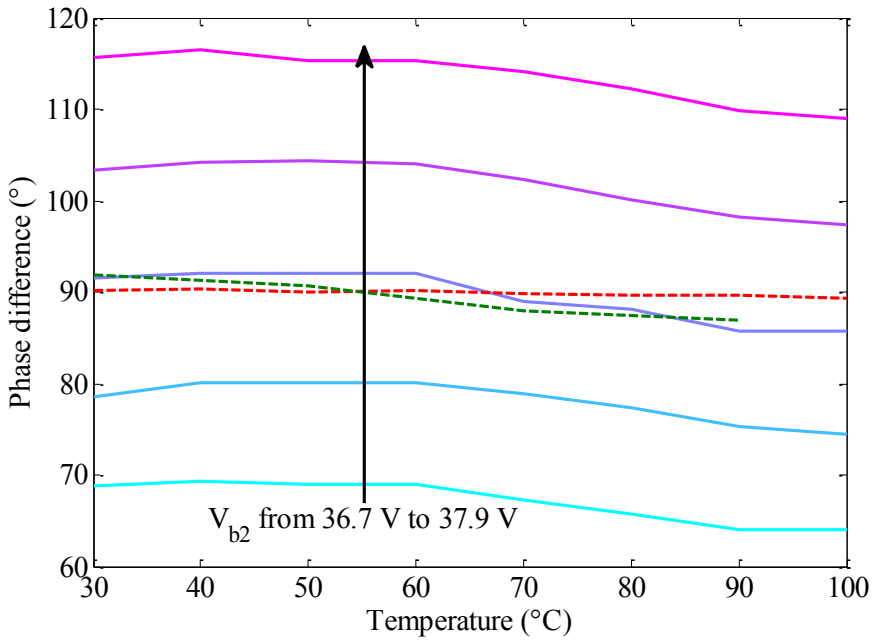

Figure 3.41: Full lines: experimental phase difference for the CCB MILO of sample 16, for various temperature and V_{b2}. Red dotted line: simulated phase difference with same BVD models. Green dotted line: simulated phase difference with different BVD models.

ΔV_{b2} (V)	$\frac{\partial f}{\partial T}$ (Hz.°C^{-1}), linear fit	$\frac{1}{f_0}\frac{\partial f}{\partial T}$ (ppm.°C^{-1}), linear fit	$\frac{\Delta\varphi}{\Delta T}$ (°/°C), max. var.	$\frac{1}{\varphi_0}\frac{\Delta\varphi}{\Delta T}$ (ppm.°C^{-1}), max. var.
-0.6	-1768	-466	0.071	1060
-0.3	-1756	-463	0.075	974
0	-1745	-460	0.08	888
0.3	-1750	-461	0.1	1000
0.6	-1740	-459	0.1	909
Cadence simulation				
Same BVD	-1769	-466	0.0143	158
≠ BVD	-1769	-466	0.0727	945

Table 3.7: Extracted dependence of the frequency and phase difference with the temperature for the CCB MILO (sample 16) for various values of ΔV_{b2}.

The data collected are applied in the framework of the electrometer application in Table 3.8, showing a rejection enhancement of the same order (10 % difference) as in the CFB MILO case, in Table 3.6.

ΔV_{b2} (V)	$\frac{\Delta f}{\Delta T}\frac{\Delta V_{b2}}{\Delta f}$ (mV.°C^{-1})	$\frac{\Delta\varphi}{\Delta T}\frac{\Delta V_{b2}}{\Delta\varphi}$ (mV.°C^{-1})	Rejection enhancement
-0.6	-319	1.83	173
-0.3	-317	1.93	163
0	-315	2.06	152
0.3	-315	2.58	122
0.6	-314	2.58	122
Cadence simulation			
Total	-319	1.9	167

Table 3.8: Effect of the temperature on the measurement of ΔV_{b2} with a CCB MILO if the output signal is the f or φ, and ratio between these two.

3.7 Frequency noise, phase difference noise and resolution

3.7.1 Noise and resolution of CCB MILOs

The last step in the closed-loop characterization of the MILO is to obtain the resolution of the MILO as a differential sensor. The resolution is the smallest quantity that can be sensed. It is limited by the influence of unavoidable noises on the system, making the detection of small measurands impossible. For resonant sensors, it is well-described by figures like phase noise, frequency noise or Allan Variance [136]. These three figures contain the same information, but presented in different ways, in order to be best suited for different applications [137], [138]. For instance, for sensors tracking sinusoidal phenomena, which generates phase modulations in the carrier frequency, the phase noise is suited to estimate the influence of noise on the output signal. For sensors tracking slow-varying signals, away from the carrier, and allowing averaging of the output signal, the Allan variance is suited to estimate the best averaging time (i.e. the best tradeoff between the reduction of the influence of noise due to the averaging and the apparition of slow drifts that are not suppressed by averaging).

In the case of the MILO, the output signal is a phase difference. An algorithm is developed to extract the power spectral density of the variations of the period and of the variations of the duty cycle, thus extrapolate the frequency (or phase) noise and noise over the phase difference. It is based on a "very" long waveform recording of V_{in1} (up to 40 ms, corresponding to 150k periods for the CCB MILO), as depicted in Figure 3.42. One should note that the estimation of the phase difference is different in this case, because recording simultaneously V_{in1} and V_{in2} decreases the number of points by a factor 2. So only one waveform is recorded, and the phase difference is estimated based on one duty cycle measurement. This measurement is performed on the sample 17 ($Q_1 = 97$, $Q_2 = 115$), with $V_{b1} = 40\ V$ and $V_{b2} = 40.6\ V$, and $V_{in} = 500\ mV$ unless specified.

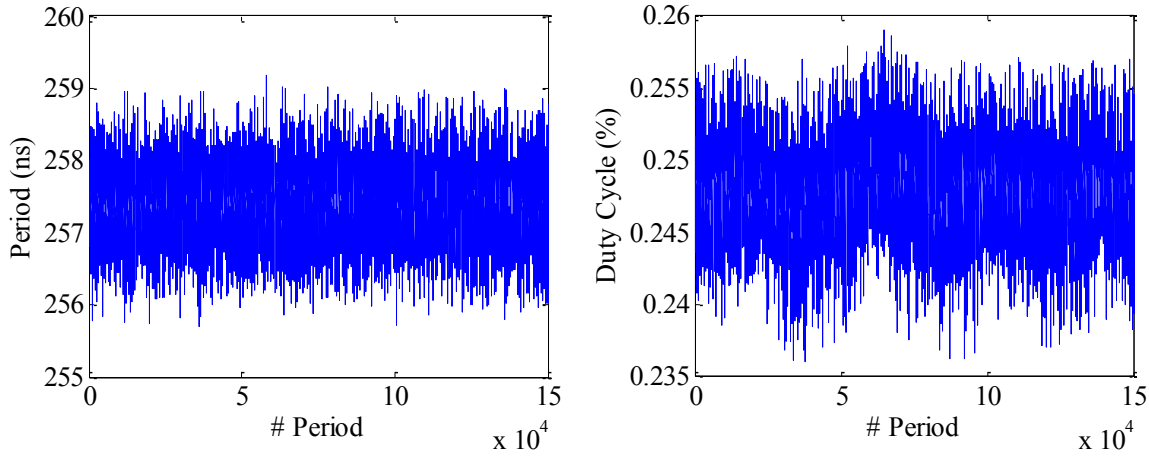

a) b)

Figure 3.42: Extracted periods and duty cycles for 150000 periods of the CCB MILO of sample 18.

Then, the power spectral density of the duty cycle (S_ϕ) and the period (S_f) are calculated using Matlab's routine Periodogram (the code is given in Annex 3). This algorithm is compared to the built-in algorithm DPOJET proposed by the oscilloscope to calculate the power spectral density of the period and the duty cycle. The DPOJET enables an averaging over several non-consecutive acquisitions.

Finally, the theoretical thermomechanical fractional frequency noise is, according to [139], for a single clamped-clamped beam:

$$S_f^{thermomecha} = \frac{k_b.T}{8.\pi.P_c.Q^2}, \tag{49}$$

where P_c is the kinetic power at the carrier frequency, $P_c = \omega_0.E_c/Q$, and E_c is the carrier energy: $E_c = \frac{1}{2}.m_e.\omega_0^2.\max a\,.G_0$. The maximum position of the resonator inside the gap is estimated with the "rule of thumb" $Q.F = k_e.\max a\,.G_0$, where F is the actuation electrostatic force, as described in Equation (9). Merging these terms, one can apply the formula to our geometries:

$$S_f^{thermomecha} = \frac{k_b.T.k_e}{2.f_0.Q^3.\left(\frac{\varepsilon_0^2.L.b}{G^2}\right)^2.V_b^2.V_{in}^2.N'(0)^2}, \tag{50}$$

where V_{ac} represents the harmonic content of V_{in} at f_0, or ${}^{\sqrt{2}}/_{\pi}\,V_{in_{peak-peak}}$, given the fact that V_{in}'s waveform is composed of pulses of duty cycle 0.25 for $\varepsilon = 0$. In our case, the system is composed of two synchronized resonators, meaning that the

floor noise is twice as small [126] as the value given in Equation (50). Given the two different quality factors, the floor noise is

$$S_f^{floor} = \frac{1}{2}\frac{k_e.k_b.T}{2.f_0.\left(\frac{2Q_1.Q_2}{Q_1+Q_2}\right)^3.\left(\frac{\varepsilon_0.L.b.V_b.V_{ac}.N(0)}{G^2}\right)^2}, \tag{51}$$

The resulting curves ("home-made" algorithm, DPOJET algorithm, and theoretical thermomechanical noise) are plotted in Figure 3.43.

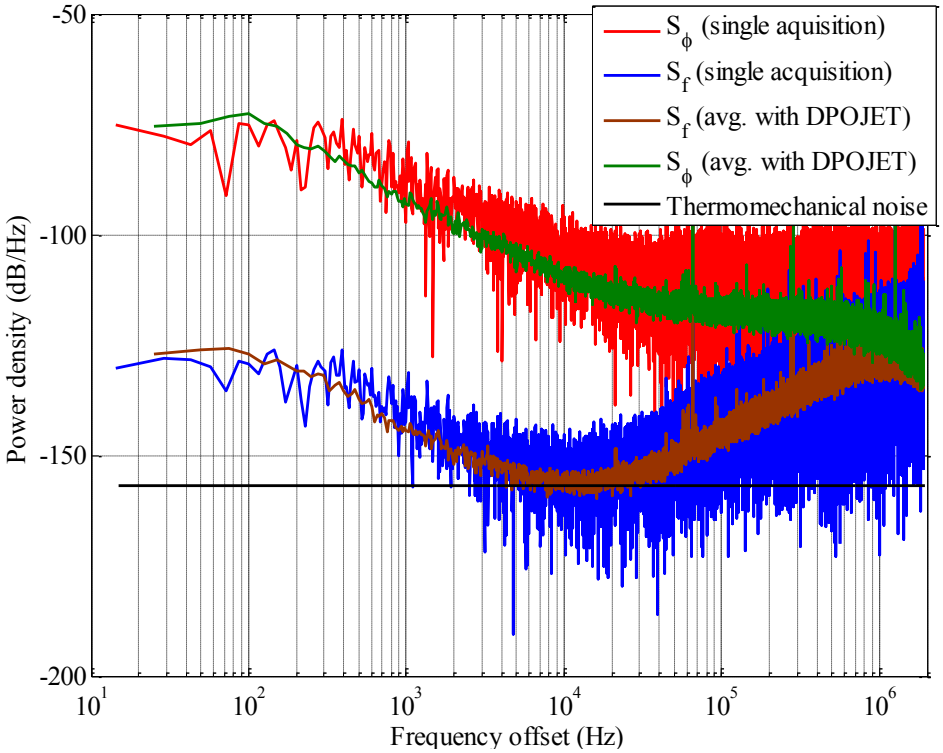

Figure 3.43: Frequency noise S_f and phase difference noise S_ϕ measured using the Periodogram (single acquisition) or DPOJET (averaged on 5 acquisitions) algorithm, and theoretical floor noise.

Several points emerge from these measurements and calculations.

- The results obtained with the averaged periodogram (obtained with the oscilloscope) and with the Matlab processing of a single acquisition are coherent. The discrepancies can be explained by the different settings used in the two cases (filtering, and threshold levels).
- At the corner $f_0/2\frac{2Q_1.Q_2}{Q_1+Q_2} = 17.8\ kHz$, S_f reaches the thermomechanical noise, which is the ultimate noise value reachable for an oscillator for a given quality factor. This is because the oscillator works in air, thus with

"low" quality factor, and the thermomechanical noise is higher than electronic noise.

- S_ϕ is, as illustrated in Figure 3.44, $S_{MILO} = 49\ dB$ higher than S_f. This result is in agreement with the theory [130], [117] in the sense that there is no expected gain in terms of resolution in using a MILO over a frequency-based resonant sensor.
- Below the frequency corner, both S_f and S_ϕ have the same behavior (a plateau at small frequency offsets, followed by a $1/f^2$ drop). This is an unexpected phenomenon, showing that there are unidentified lowpass noise sources in the system affecting the two resonators (or their associated electronics) independently. In fact, a single noise source, or two correlated noise sources, should have no impact on S_ϕ thanks to the common mode rejection property of the MILO. Possible noise sources are investigated hereafter.

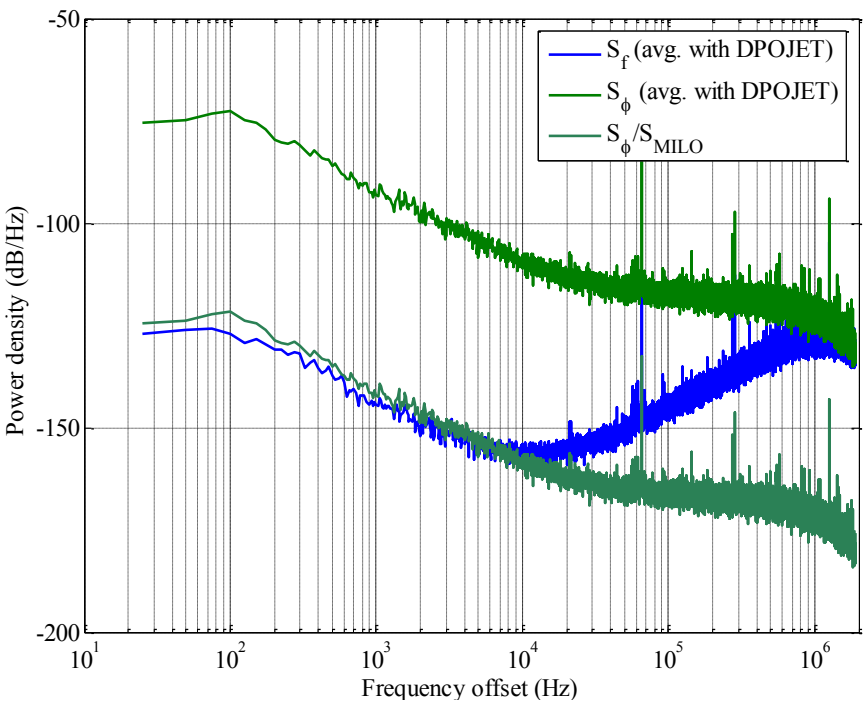

Figure 3.44: S_f, S_ϕ and calculated S_ϕ/S_{MILO}.

One could think that the uncorrelated noise comes from the bias voltage source, since $V_{b1} \neq V_{b2}$, and the resonators are biased using two voltage generators. Indeed, independent voltage generators lead to independent voltage fluctuations, which are

translated into independent parametric frequency fluctuations due to the electrostatic softening phenomenon. Such a parametric frequency fluctuations would be translated into phase difference fluctuations and amplified by the factor S_{MILO}.

The phase PSD is then extracted for $V_{b1} = V_{b2} = 44.6\,V$ with two voltage generators and a single voltage generator. The results are plotted in Figure 3.45.

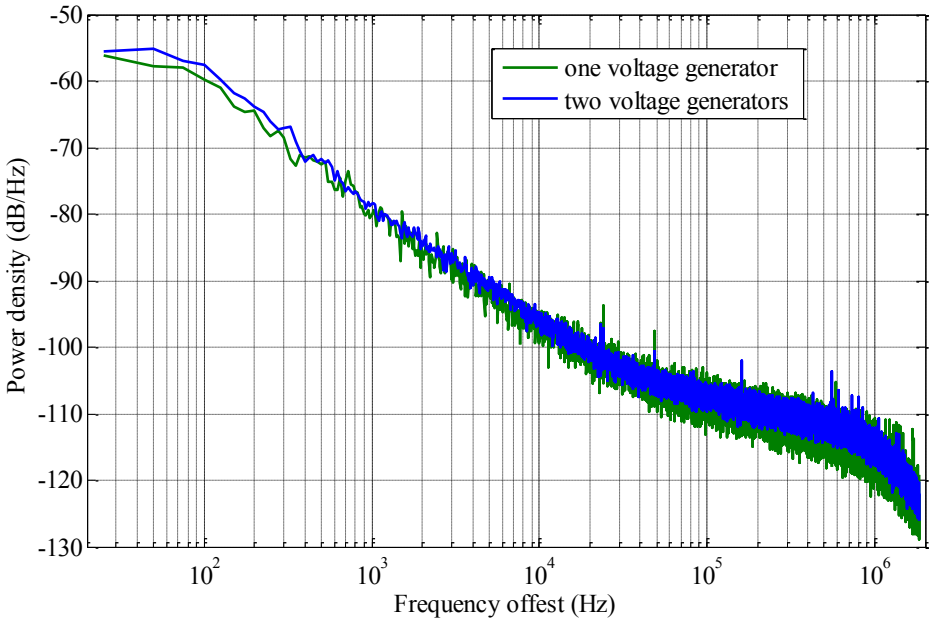

Figure 3.45: Phase difference PSD for $V_{b1} = V_{b2} = 44.6\,V$, using one or two voltage generators for the bias voltages.

The experiment show that there is no decrease of the close-to-the-carrier noise even with only one voltage generator as bias voltage source, and eliminates bias voltage fluctuations as a possible noise source.

Other experiments are then performed in order to find the cause of this unfiltered noises.

- First, the biasing voltage of both V_{b1} and V_{b2} are progressively decreased, in order to decrease the amplitude of motion and output signal amplitude. For each bias voltage pair, the period and phase PSD are calculated using the built-in DPOJET algorithm. The results are plotted in Figure 3.46.
- Then, V_{b1} and V_{b2} are respectively fixed at 28 V and 28.6 V, but the actuation voltage is increased from 500 mV to 1 V, and the period and phase PSD are calculated with DPOJET and plotted in Figure 3.47.

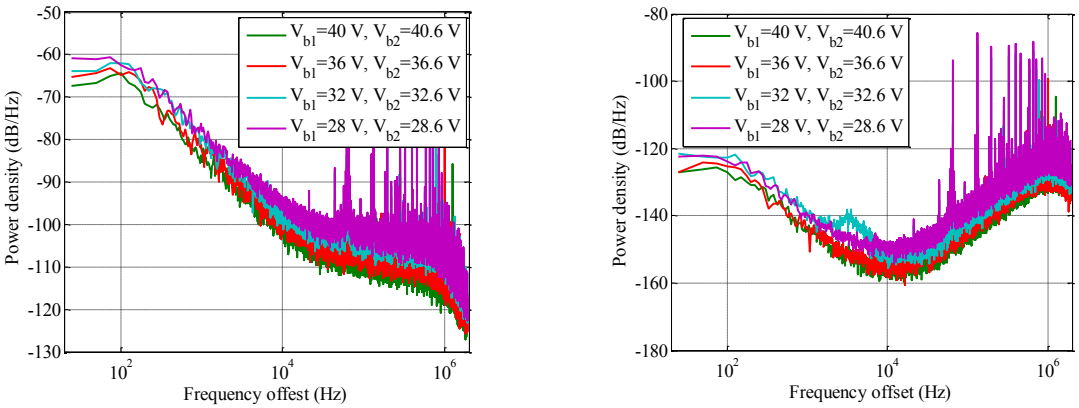

a) b)

Figure 3.46: S_ϕ (a) and S_f (b) measured with the DPOJET algorithm for several bias voltage pairs, for $V_{in} = 500\ mV$

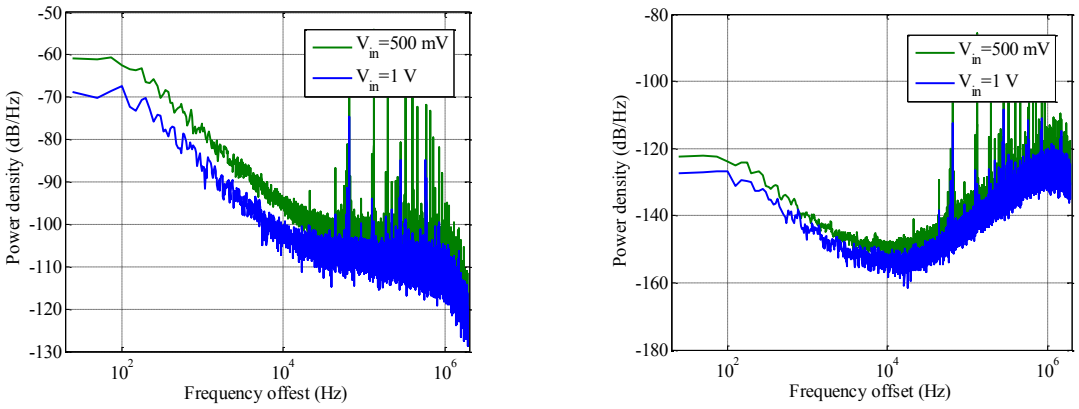

a) b)

Figure 3.47: S_ϕ (a) and S_f (b) measured with the DPOJET algorithm for $V_{b1} = 28\ V$, $V_{b2} = 28.6\ V$, and two values of V_{in}.

Overall, both the phase PSD and period PSD decreases when the voltages (whether bias or actuation) increases. This means that the period and phase difference noise are correlated to the amplitude of the output signals. This may be caused by additive noise sources or by parametric amplitude fluctuations, converted to frequency noise through a nonlinearity. This may typically be the result of the hysteresis of the comparators described in subsection 2.3.2, modulating a fluctuation of the output voltage of the amplifier into jitter at the comparator output. However, this is only a hypothesis that must be tested with further simulations and experiments. The resolution is then estimated by calculating the Allan Deviation (plotted in Figure 3.48) from the duty cycles and period samples presented in Figure 3.42.

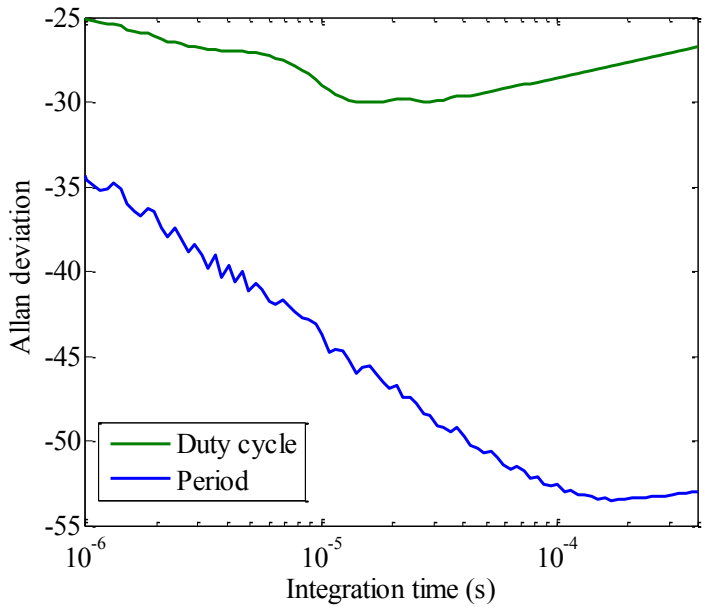

Figure 3.48: Allan deviation of the period and duty cycles.

Then, the minimum of the deviation corresponds to the maximum of the resolution. For the period, the -53 dB corresponds to a 19 Hz minimum of the Allan Deviation (given the 3.8 MHz oscillation frequency). And, according to the -5.5 kHz.V^{-1} sensitivity found in section 3.4.2, this translates into a resolution of 3.5 mV for the oscillation frequency output of the MILO. For the duty cycle, the -30 dB corresponds to a 25 m%, or a 0.09 ° minimum of the Allan Deviation. The 38.07 °.V^{-1} sensitivity found in section 3.4.2 was with the respective quality factors of 120 and 140 from the sample 16. In the case of the sample 17, with quality factors of 90 and 117, this sensitivity theoretically drops to 31.8 °.V^{-1}, which leads to a resolution of 3 mV.

The resolution can also be obtained by integrating the power spectral densities between 0 Hz and the corner frequency, and taking the square root of the result. This gives a resolution for the frequency of 34.5 Hz, and of 0.23 ° for the phase difference. Given the sensitivities of the frequency and phase difference to ΔV_{b2}, these resolutions, translated into the electrometer example, are 6.5 mV if the frequency is used 7.2 mV if the phase difference is used.

The two methods are not totally coherent but they show that the sensitivity enhancement when the phase difference output is chosen entails no increase in term of resolution.

3.7.2 Noise and resolution of CFB MILOs

Unfortunately, this analysis was not extensively carried out on the CFB MILOs chips. Only "long" recordings of V_{in1} were taken on the sample 12 ($Q_1 = 110$, $Q_2 = 90$), with $V_{b1} = 28\ V$, $V_{b2} = 30\ V$ and $f_0 = 3.009\ MHz$. Only single acquisition PSD figures (i.e. with the Periodogram algorithm) and Allan Deviation can be plotted. They are respectively presented in Figure 3.49 and Figure 3.50. The same behavior is observed, but no further investigation on the noise sources can be made. By doing the same reasoning as in the last paragraph, and given the sensitivities found in subsection 3.4.1, the experimental resolutions extracted from the Allan Deviation figures are 10 mV tracking the phase difference, and 10.9 mV tracking the oscillation frequency, showing the absence of resolution enhancement. The resolution is poorer than in the CCB case of section 3.7.1 because the bias voltages and quality factors are smaller.

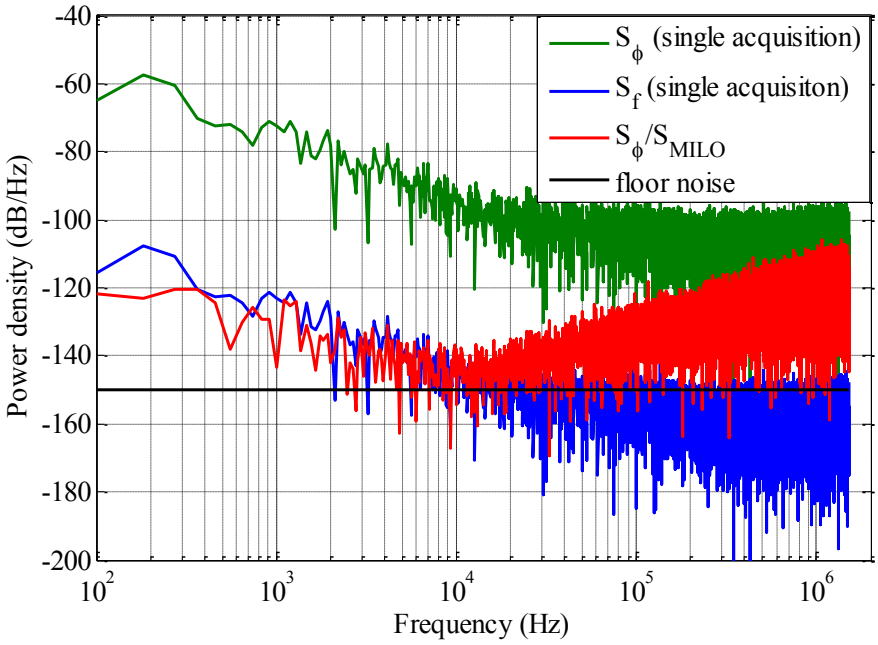

Figure 3.49: S_f, S_ϕ, calculated S_ϕ/S_{MILO}, and calculated floor noise according to Equation (51) for the CFB MILO (sample 12).

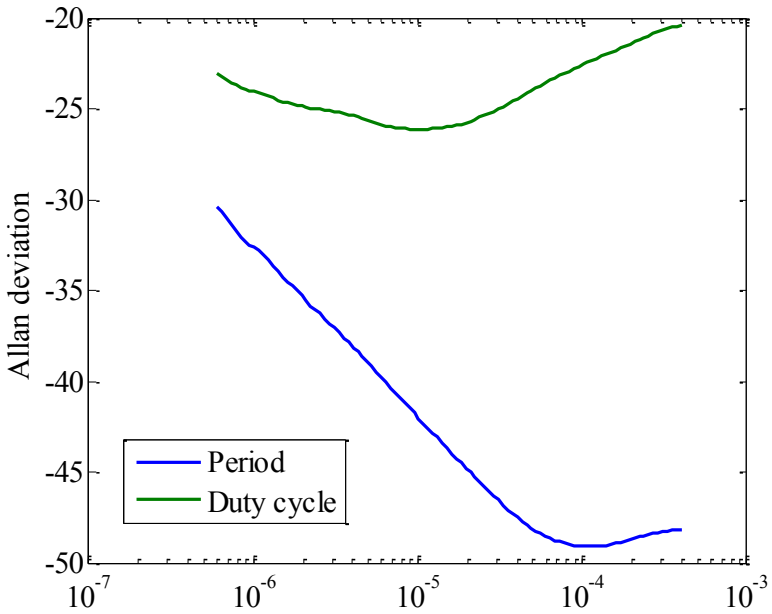

Figure 3.50: Allan deviation of the period and duty cycles for the CFB MILO (sample 12).

3.8 Electrometer application

This section sums-up the numbers derived from the different experiments for a MILO-based electrometer application. These numbers are presented in the case of the CFB MILO in Table 3.9 and in the case of the CCB MILO in Table 3.10. The theoretical resolution is calculated assuming the thermomechanical noise is the only source of noise. By integrating the value of the fractional thermomechanical frequency noise found in Equation (51) between 0 Hz and the corner frequency, one can obtain the best resolution achievable for this system if the frequency is the chosen output, and infer the best resolution achievable is the phase difference is the chosen output.

CFB	$\frac{\partial\varphi}{\partial V_{b2}}$ (°.V^{-1})	$\frac{\partial f}{\partial V_{b2}}$ (kHz.V^{-1})	S_{MILO} (diff. mode)	$\frac{\partial\varphi}{\partial T}$ (°.°C^{-1})	$\frac{\partial f}{\partial T}$ (Hz.°C^{-1})	Rejection ratio	Resolution
Exp.	-36	-4.3	280	0.03	104	31→230	$\begin{cases}\varphi: 10\ mV \\ f: 10.9\ mV\end{cases}$
Model	-36.3	-4.32	280	0.01	120	117	$\begin{cases}\varphi: 2.2\ mV \\ f: 2.2\ mV\end{cases}$

Table 3.9: Table characterizing a CFB MILO-based electrometer.

CCB	$\frac{\partial\varphi}{\partial V_{b2}}$ (°.V^{-1})	$\frac{\partial f}{\partial V_{b2}}$ (kHz.V^{-1})	S_{MILO} (diff-mode)	Locking range	$\frac{\partial\varphi}{\partial T}$ (°.°C^{-1})	$\frac{\partial f}{\partial T}$ (Hz.°C^{-1})	Rejection ratio	Resolution
Exp.	-38.1	-5.5	294	3 V	0.07	1745	120→170	$\begin{cases}\varphi: 6.5\ mV \\ f: 7.2\ mV\end{cases}$
Model	-36.8	-5.5	306	3.7 V	0.01	1769	167	$\begin{cases}\varphi: 1.3\ mV \\ f: 1.3\ mV\end{cases}$
[130]	-38.1	-5.5	294	3.7 V				

Table 3.10: Table characterizing a CCB MILO-based electrometer.

- Concerning the differential mode, the CFB MILO is very well described by the simple modelling made in this work. The CCB MILO, because of the added phase delay in the loop, differs slightly from this simple modelling, but is well described by the complete modelling made in [130]. The robustness of the architecture to design issues is proved, since an important unwanted phase delay in the design leads to small performance reduction.
- Concerning the common mode, the different models do not take into account the possible mechanical stiffness, thus showing much better drift rejection than what is experimentally observed.
- As predicted, the sensitivity enhancement entails no resolution enhancement due to the fact that the dominant noise sources applied to both resonators seems to be not correlated.

In this part, the experimental characterization of the MILO as an oscillator and as a differential resonant sensor was made. The open-loop and closed-loop characterizations show a good agreement with simulations, provided the set-up is characterized as well and taken into account into the model. This agreement enables a precise reading of the phase equilibrium in the loop, in order to adapt the parameters of the MILO's modelling made in the last chapter. Then, the sensitivity to mismatch and drift rejection properties of the MILO is experimentally demonstrated. The sensitivity goes according to the simplified theoretical predictions in the case of a optimized architecture (CFB MILO) and to the complete theoretical predictions in the

case of a non-optimized architecture (CCB MILO). The robustness of the architecture is shown, since an important missing phase delay in the loop leads to a small performance degradation. The drift rejection's capabilities are assessed, and the limits are understood, coming from the circuitry's dependence to the temperature and the mechanical stiffness mismatch between the resonators coming from the fabrication process. Finally, the noise figures are extracted and analyzed, showing the fact that the sensitivity enhancement entails no resolution enhancement. The main noise source of each side of the MILO, close to the carrier, are uncorrelated and are not filtered by the differential structure. In the next and last part, this work is concluded and some leads are given for its continuation.

Chapter 4 Conclusion and perspectives

4.1 Conclusion

Thermal drift is one of the limiting factors in the design of MEMS-based resonant sensors for embedded systems. Several approaches exist in order to either suppress or compensate for this drift, such as the control of the resonator temperature by ovenizing it, digital compensation with microprocessors and temperature sensors, or differential sensor architectures. Differential architectures target the amplification of difference in mass or stiffness of two resonators, while being unaffected by variations equally affecting both resonators. Several strategies have been developed: frequency difference, mode localization and synchronization. In this thesis, the synchronization technique was chosen because of its potential for sensitivity enhancement and VLSI capabilities.

This thesis aimed at proving the feasibility as a VLSI-compatible differential sensor of a mutually injection-locked oscillator, whose output signal (the phase difference between two synchronized resonators) is not affected by thermal drift. Most of the critical components were monolithically co-integrated, using AMS 0.35 µm fabrication process. This work relied on the experience of CMOS-MEMS co-integration of the ECAS group, on the analog/digital CMOS integration knowledge of the GEEPs group, and on the mathematical modelling of the MILO architectures made at the beginning of the thesis.

This work demonstrates that the MILO architecture is a good candidate for VLSI-compatible differential resonant sensor applications. It benefits from potentially higher than Q sensitivity enhancement compared to a traditional resonant sensor, drift rejection capabilities (in this work limited by the electronics' dependence to the temperature and by the fabrication process variability), at the cost of a reduced locking range. An excellent agreement was found between the experimental results and the theoretical predictions, provided the model parameters are accurately derived, based

on a proper physical model of the resonators, extracted simulation of the entire device, and accounting for the imperfections of the experimental setup. Furthermore, it was shown that, in spite of the existence of several unknowns at an early design stage (e.g. residual stress) making it difficult to optimize the design, the system performance is close to optimal even when critical parameters (such as loop delay) are far from their nominal values. The drift rejection capabilities, and the sensitivity enhancement were experimentally assessed for various samples, showing the repeatability of the device, and its robustness in spite of the variability of the fabrication process. An unexpected result comes from the existence of as yet unidentified noise sources, which degrade the performance of the sensor, regardless of which output signal (phase difference or frequency) is used.

This work may be pursued in several different directions. First of all, improvements to the existing device may be made, as discussed in the following section. Then, as discussed in sub-section 4.3, longer-term perspectives may also be addressed.

4.2 Device improvements

Several upgrades can be made directly on the chip, in order to obtain better results and more reliable device.

- Equip the connection pads with electrostatic discharges protections. Since it was the first time the group co-integrated a CMOS-MEMS analog/digital device, the protections were forgotten, leading to ESD at the input of the comparator (only pad connected to a transistor's gate). A microscopic image of the burnt input of the comparator after an ESD is given in Figure 4.1.

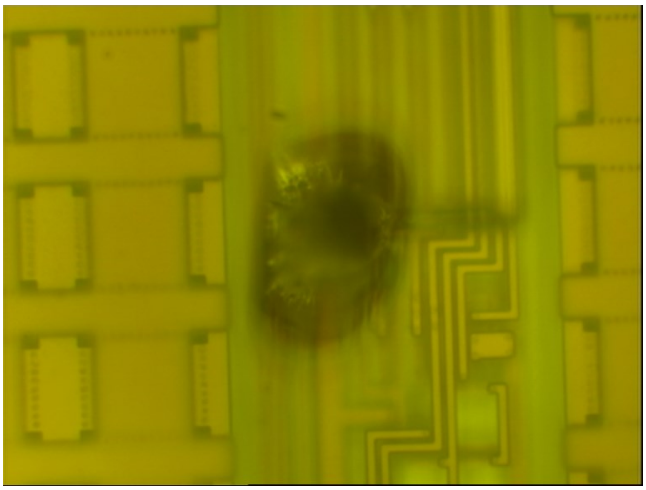

Figure 4.1: effect of an ESD on the input transistor's gate of the transistor.

- Think differently the decoupling capacitances. Indeed, they are connected with the MET3 layer, leaving only the MET4 to connect the different blocks. This layer is attacked by the HF wet etching, even under the Si_3N_4 protection layer, leading to reduced section at some points, thus increased density of current and potentially break-down. It has been observer in the connection between the comparator and the mixer, as illustrated in Figure 4.2.

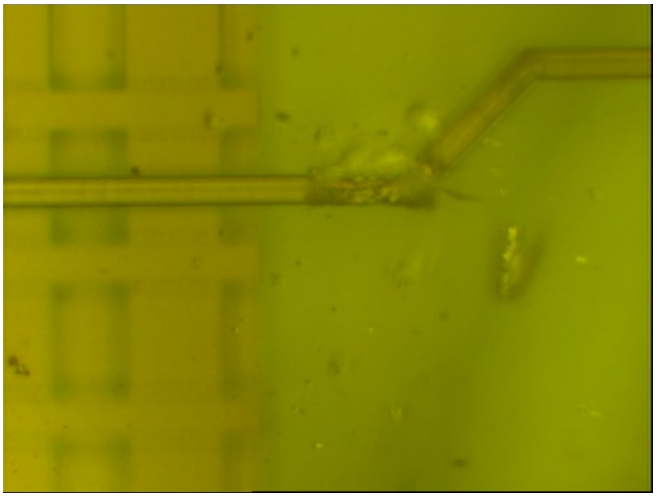

Figure 4.2: attacked MET4 connection between the comparator and the mixer

- Add a rail-to-rail amplifier after the bias tee. The amplifier's dynamic range is limited by the output's DC value (2.7 V), which is close to V_{dd}. Adding a rail-to-rail amplifier after the bias tee, without necessarily an

important gain but with an important dynamic range would allow smaller actuation or bias voltage while having the same amplitude at the input of the comparator. This could decrease the transimpedance amplifier' saturation. This would reduce the phase and period noise induced by the comparator's hysteresis, and maybe reveal other noise sources.

- Separate the analog power supply from the digital power supply, or add extra decoupling capacitance. At 3.9 MHz, major perturbations are still present at every transition of the digital buffer, leading to difficulties in the reading of the phase difference and frequency. Decoupling the two power supply or adding extra decoupling capacitance would reduce these perturbations even further.
- Identify the major sources of system imbalance, parametric fluctuations and additive noise in the system, through the use nonlinear oscillator noise analysis CAD tools, and optimize the design consequently. This may be done at several levels: optimization of the symmetry of the digital mixer or of the comparators, optimization of the readout, and stabilization of the (bias) voltage supplies, etc.
- Identify the major electronic sources of drift in the ASIC and design CMOS components that are less affected by temperature variations, or whose variations compensate for each other (e.g. added phase shift in the comparator, compensated by a reduced phase shift in the amplifier).

Those improvements can be made using AMS 0.35 technology, with the limitations due to the variability of the process, or using a MEMS-dedicated technology. Finally, some insights are given for potential future works around the MILO as a differential sensor.

4.3 Future work

Various leads can be followed for the development of the MILO as a differential sensor.

4.3.1 Investigation on the concept

Various leads can be followed for the development of the MILO as a differential sensor. First of all, one should try to investigate the limits of the proposed concept. We have shown that a MILO is only as good as the resonators are well-matched in terms of natural frequencies, which ensures frequency locking and proper thermal drift rejection, and as their quality factor is high, which ensures a good sensitivity to the frequency of interest. However, increasing the quality factor to boost sensitivity also results in increased sensitivity to variability in the fabrication process, since the locking range of a MILO is inversely proportional to Q. In fact, while the accuracy and the repeatability of our fabrication process is adequate for designing MILOs with fairly low quality factors, it would probably be less appropriate if one sought to increase the quality factor of the resonators (for example by operating them in vacuum). This issue could be partly addressed by designing the active resonators closer to each other, thus reducing fabrication uncertainties, or larger resonators (farther from the limits of the technology), but this would also have consequences on the whole system design (because of spurious couplings, weaker signals, smaller oscillation frequencies, etc.). Alternatively, one may also think of using other processes (MEMS-dedicated or not) for the design of the resonators alone, probably with the objective of a gain in intrinsic Q, in accuracy and repeatability. Still another perspective would be to explore alternative mixer architectures, such as the analog architectures with coupling factor smaller than 1 mentioned in section 1.4.6, in order to achieve higher sensitivity, at the cost of reduced locking range: this would put less constraints on the design of the resonator or of the packaging of the system (for example, the resonators could still be operated at ambient pressure, but the system would still benefit from an increased sensitivity) but would still be demanding in terms of fabrication accuracy.

4.3.2 Locking-range extension

Another perspective, which is not completely disconnected from the previous one, is the investigation of architectures with extended locking range, and hence extended dynamic measurement range. This could be achieved by having a second feedback loop continuously track the phase difference between the resonators and adapt the bias voltage of either of them in order to maintain them locked in quadrature, by adjusting their electrostatic stiffness (this loop could also be used to automatically

start the oscillation by sweeping bias voltages at startup). This bias voltage adaptation would become the output signal of the MILO. The concept is illustrated in Figure 4.3. Several challenges arise from this idea. First, the frequency to bias voltage relation is non-linear, even though it can be linearized close to a certain value. A compromise would then have to be found between linearity and range. Moreover, the dynamic range would still be limited by other practical limits (e.g. static pull-in, low motional currents). Also, even if the resonators remained matched in terms of electromechanical stiffness, they would still be mismatched as far as mechanical stiffness, and hence thermal sensitivity, is concerned, probably leading to poorer drift rejection as the dynamic range increases.

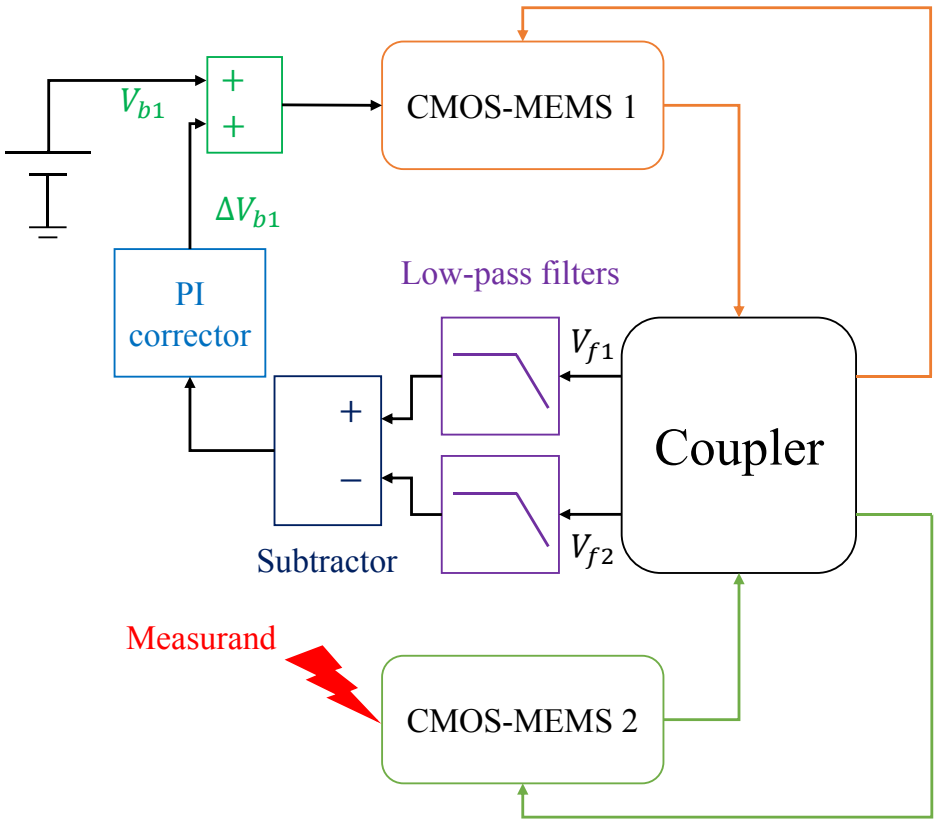

Figure 4.3: High-level schematic of a second feedback loop proposition, details on the analog extraction of φ.

4.3.3 Resonant accelerometer

Finally, once these questions are addressed, it would be interesting to go from a proof of concept to a "real" sensor. Several ideas can be pursued for the fabrication of a MILO-based resonant sensor. As an example, and to test the limits of the fabrication

process, the design of an accelerometer-like device was tentatively explored during this thesis (Figure 4.4)[3]. The device consists in a seismic mass and in a CFB resonator separated by a gap that varies as the mass undergoes an external acceleration. If the bias voltage of the seismic mass is different from that of the resonator, an acceleration then results in a modification of the resonator's resonance frequency. By placing one resonator on each side of the seismic mass (in the direction of motion), one obtains a differential acceleration sensor structure, in which the resonators can be synchronized using the solution developed in this thesis, thus making a drift-free resonant accelerometer. The concept is illustrated in Figure 4.5.

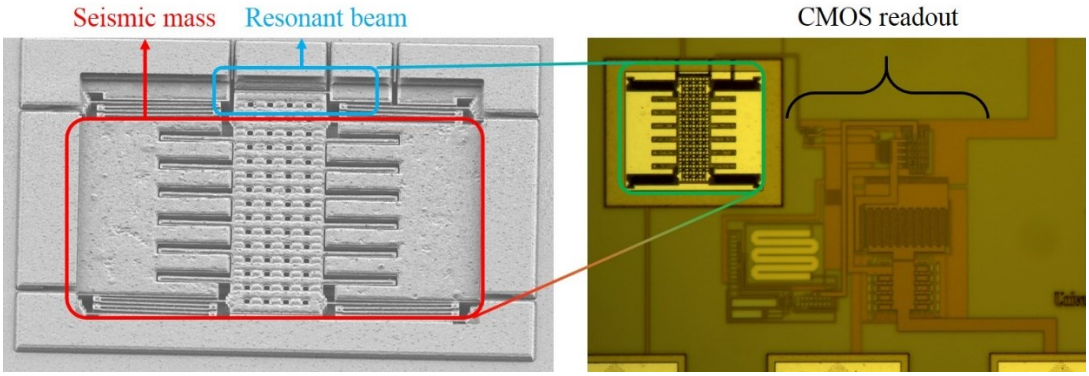

Figure 4.4: Resonant accelerometer (seismic mass and resonant beam electrostatically coupled) and the CMOS readout. Left: SEM image; right: microscopic image.

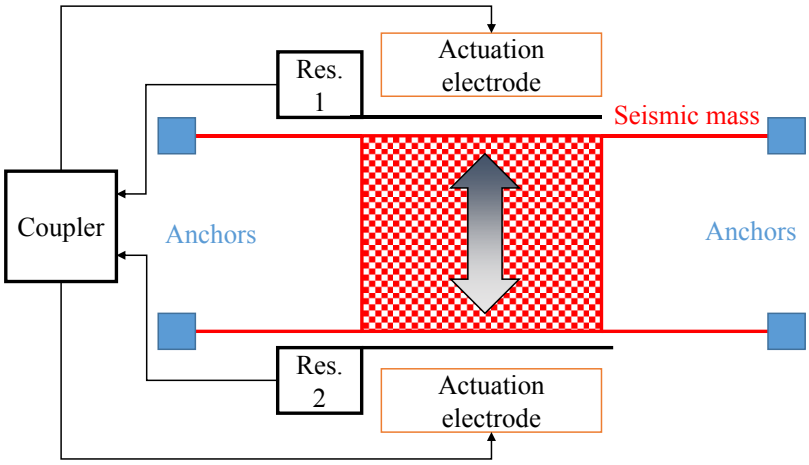

Figure 4.5: MILO-based resonant accelerometer principle.

[3] However, the characterization of the successfully-released structures could not made due to lack of time and equipment.

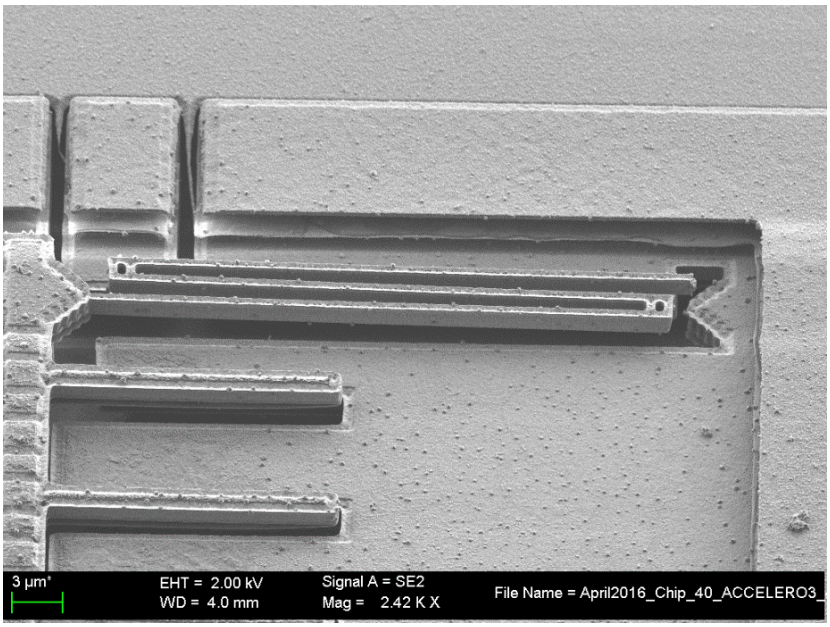

Figure 4.6: SEM image of a seismic mass which anchor broke out due to the residual stress.

Although most of the structures broke due to the residual stress (see Figure 4.6 for an example), some of them were successfully released (Figure 4.4), highlighting the potential of the AMS 0.35 µm process for the fabrication of monolithically-integrated resonant MEMS sensors.

Layout AMS C35B4C3

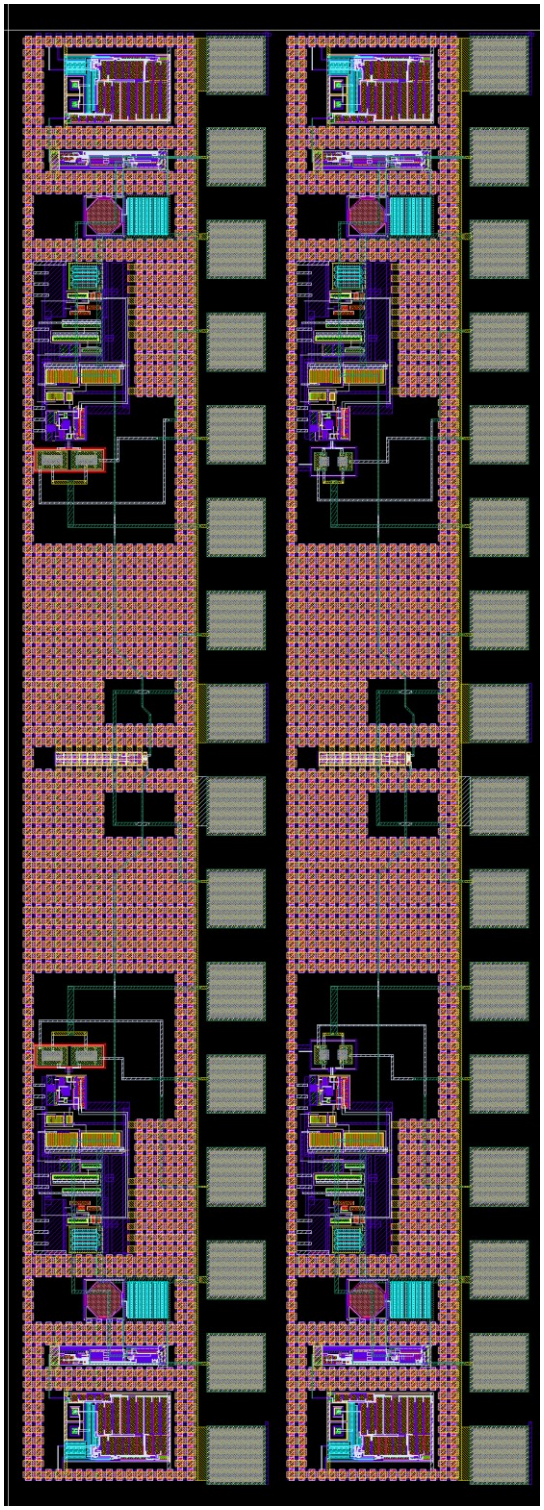

Figure 4.7: Layout of the two CMOS-MEMS MILO.

Annex 1: Analysis of Mutually Injection-Locked Oscillators for Differential Resonant Sensing [130]

IEEE TRANSACTIONS ON CIRCUITS AND SYSTEMS—I: REGULAR PAPERS, VOL. 63, NO. 7, JULY 2016 1055

Analysis of Mutually Injection-Locked Oscillators for Differential Resonant Sensing

Jérôme Juillard, *Member, IEEE*, Pierre Prache, and Núria Barniol, *Member, IEEE*

***Abstract*—The potential benefits of oscillator synchronization are receiving increased interest in the resonant MEMS community, for clocking or sensing applications. In this paper, we explore the possibilities of differential resonant sensing applications based on the phase-difference between two injection-locked resonators, strongly coupled through an electronic mixer. A general model of such oscillators is established, and their static and dynamic performance is determined. The design space offered by the mixing scheme is then investigated at the system-level, in the weak and strong coupling cases. The practical implementation of the corresponding architectures in the context of a MEMS application is discussed. The theoretical results are supported by simulations and experimental data.**

***Index Terms*—Coupling circuits, injection-locked oscillators, microelectromechanical systems, system-level design.**

I. Introduction

MUTUALLY injection-locked oscillators (MILOs) are receiving increased interest in the resonant micro- or nano-electromechanical system (M/NEMS) community, for clocking or sensing applications [1]–[9]. In clocking applications, this interest is driven by the possibility of taking advantage of the intrinsically large quality factor of MEMS devices (typically larger than 100), while benefitting from the phase noise characteristics of injection-locked oscillators [10]–[14]. In sensing applications, the motivation is either to improve phase noise through injection-locking, or to use the large sensitivity to mismatch of injection-locked oscillators to provide a drift-free measurement of a quantity of interest (such as mass, acceleration, etc.) based on the phase difference between the oscillators rather than on their oscillation frequency. In this paper, we focus on the latter sort of resonant sensing application.

To eliminate drift, the two MEMS sensors need to have the same operating conditions, and, hence, need to be in close proximity to each other. An unwanted consequence of this proximity is the existence of parasitic couplings (electrostatic, mechanical, electrical...) between the two resonators. In sensors based on nominally-uncoupled oscillators (i.e., frequency-based sensors), these parasitic effects, which one may also describe as weak injection signals, can result in spurious tones in the spectrum of the resonator, or in dead-zones in the sensor response [15]. These weak couplings may be overcome by enforcing a stronger injection signal, which motivates our research into resonant sensing architectures based on two strongly-coupled resonators. Several solutions for enforcing coupling between two (or more) resonators have been studied in the MEMS literature, either in theory or in practice: linear electric coupling [6], [16], coupling through smooth nonlinear phenomena, such as electromagnetic [3], electrostatic [4], [5], [9], or optomechanical forces [17], and coupling through non-smooth phenomena, such as mechanical impacts [18], or saturated electronics [7]. The purpose of this paper is to provide a theoretical framework and some practical insight for the design of electronically-coupled MILOs for M/NEMS-based resonant sensing applications. Although MILOs and their characteristics have been extensively described elsewhere in different contexts [11]–[14], [19]–[26], these references are largely ignored by the MEMS community, because of their differences in focus; for example, the purpose of a multiphase oscillator in a clocking application is to provide two or more periodic signals with specific, guaranteed phase-differences. On the other hand, in a MILO-based sensing application, as proposed in [7], one seeks to maximize the sensitivity of this phase difference to the physical quantity that must be measured (mass, acceleration, etc.). Hence the design paradigms of MILOs should be revisited in view of differential resonant sensing applications. Furthermore, as mentioned above, the existence of weak parasitic couplings in such applications requires relatively larger injection levels for robust MILO operation: consequently, in this paper, we aim at covering all the cases from weak to very strong injection signals.

The outline of the paper is as follows: in Section II, the framework of the analysis and the notations are introduced. In Section III a phase-domain model of the system, valid in the strong-coupling case, is established, and then used, in Section IV, to determine the static and dynamic performance of the system. Section V is dedicated to a qualitative comparison of specific MILO architectures for resonant sensing in cases of very weak to very strong injection signals and remarks about their practical implementation. Section VI is dedicated to an experimental validation of our theoretical results, with MEMS resonators strongly-coupled through a digital mixer architecture. Finally, some concluding remarks and perspectives are given in Section VII.

Manuscript received November 22, 2015; revised March 1, 2016; accepted March 16, 2016. Date of publication June 21, 2016; date of current version July 22, 2016. This paper was recommended by Associate Editor F. Bizzarri.

J. Juillard is with the GEEPS, UMR 8507, CNRS, CentraleSupelec, UPSud, UPMC, 91190 Gif sur Yvette, France (e-mail: jerome.juillard@supelec.fr).

P. Prache is with the GEEPS, UMR 8507, CNRS, CentraleSupelec, UPSud, UPMC, 91190 Gif sur Yvette, France, and also with the Department Enginyeria Electronica, University Autonoma de Barcelona (UAB), 08193 Bellaterra, Spain (e-mail: pierre.prache@supelec.fr).

N. Barniol is with the Department Enginyeria Electronica, University Autonoma de Barcelona (UAB), 08193 Bellaterra, Spain (e-mail: nuria.barniol@uab.cat).

Color versions of one or more of the figures in this paper are available online at http://ieeexplore.ieee.org.

Digital Object Identifier 10.1109/TCSI.2016.2553298

1549-8328 © 2016 IEEE. Personal use is permitted, but republication/redistribution requires IEEE permission.
See http://www.ieee.org/publications_standards/publications/rights/index.html for more information.

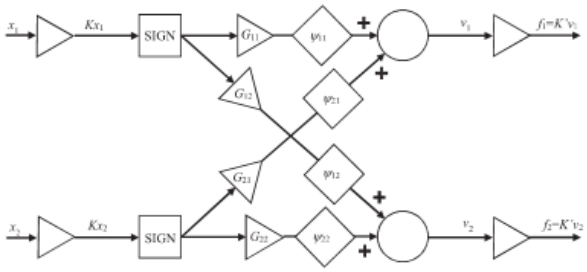

Fig. 1. Generic mixer architecture.

II. Framework and Notations

Let us consider two MEMS resonators, modeled with *linear* 2nd-order dynamics:

$$x_1 + \frac{\dot{x}_1}{Q_1} + \ddot{x}_1 = f_1$$
$$(1+\varepsilon)x_2 + \frac{\dot{x}_2}{Q_2} + \ddot{x}_2 = f_2 \qquad (1)$$

where all quantities have been non-dimensionalized: x_i, Q_i, and f_i respectively correspond to the displacement of the ith resonator, its quality factor and the force acting on it, a dot denotes differentiation with respect to (non-dimensional) time, and the quantity ε is the relative stiffness mismatch between the two resonators.[1] The derivation of this non-dimensional model in the case of an electrostatically-actuated/capacitively-detected MEMS is given in Appendix A. The forces applied to the resonators follow a certain control law, imposed by an electronic mixer. The behavior of the mixer and the transduction mechanisms are idealized. First, it is assumed that the electronic readout of each resonator outputs a voltage equal to Kx_i, $K > 0$. It is also assumed that voltage- or position-related actuation nonlinearities [27]–[29] can be neglected, so that the forces acting on the resonators can be written as $K'v_i$, $K' > 0$, where v_i is the actuation voltage delivered by the mixer to the ith resonator. These assumptions concerning the transduction scheme may for example apply to a resonator with electrostatic actuation and purely capacitive readout, provided the displacement of the resonator is small compared to the electrostatic gap, and the bias voltage is large with respect to the actuation voltage. It is also implicit in our model that higher-order modal interactions and super- or subharmonic resonances are neglected, although it is known that these may play a role in synchronization phenomena.

A system-level representation of the mixer used to generate the forces and enforce injection-locking is shown in Fig. 1: the phase-shifting elements ψ_{ij} act as ideal lag/lead blocks, so that the forces f_i are linear combinations of the phase-shifted signs of x_1 and x_2. The implementation of these blocks is discussed in Section V. Throughout the rest of the paper, we suppose without losing generality that all the G_{ij} coefficients are i) positive, since it is equivalent to have G_{ij} followed by a ψ_{ij} phase-shift, and $-G_{ij}$ followed by a $\psi_{ij} + \pi$ phase-shift, and ii) smaller than 1, the feedback amplitude being set by the transduction coefficient K'.

Finally, we will use a superscript ε to denote a dependency to the mismatch ε of one of the system's states or characteristics. For example, "ϕ^ε" designates the value of the phase difference ϕ for a given value of ε. A superscript 0 corresponds to the $\varepsilon = 0$ (no mismatch) case.

III. Modeling of MILOs Close to the Steady-State

In this section, we develop a model of the slow-time dynamics of MILOs "close" to a periodic regime of self-sustained oscillations. We can then determine stability conditions that are more general than those established, with more restrictive hypotheses, in previous work [19], [20].

A. Existence of Steady-State (Synchronized) Solutions

We start by studying the existence of a non-trivial steady-state regime corresponding to a periodic solution of (1). To this end, we use a harmonic balance approach, justified if the harmonic content of f_1 and f_2 is filtered out by the transfer functions of the resonators (the so-called "filter hypothesis" [30]). One may then write

$$\begin{cases} x_1 = A_1^\varepsilon \sin(\omega^\varepsilon t) \\ x_2 = A_2^\varepsilon \sin(\omega^\varepsilon t + \phi^\varepsilon) \end{cases} \qquad (2)$$

where A_i^ε is the amplitude of the ith resonator, ω^ε is the pulsation, ϕ^ε is the phase difference between the resonators, and t denotes non-dimensional time. From (2), one may derive expressions for the velocity $\dot{x}_i$ and the acceleration $\ddot{x}_i$. Equation (1) can then be projected on $\sin(\omega^\varepsilon t)$ and $\cos(\omega^\varepsilon t)$, which yields the following set of four equations:

$$A_1^\varepsilon(1-\omega^{\varepsilon 2}) = f_1^\varepsilon,\ A_2^\varepsilon(1+\varepsilon-\omega^{\varepsilon 2}) = f_2^\varepsilon \qquad (3)$$

$$\frac{A_1^\varepsilon \omega^\varepsilon}{Q_1} = g_1^\varepsilon,\ \frac{A_2^\varepsilon \omega^\varepsilon}{Q_2} = g_2^\varepsilon \qquad (4)$$

[1]The case of a relative mass mismatch (of interest in mass sensing applications) can also be studied but it has the same qualitative impact on the system as a stiffness mismatch (of interest in acceleration or pressure sensing applications).

where the right-hand sides of (3), (4) are

$$f_1^\varepsilon = \frac{4}{\pi} K' \left(G_{11} \cos \psi_{11} + G_{21} \cos(\psi_{21} + \phi^\varepsilon) \right) \quad (5)$$

$$g_1^\varepsilon = \frac{4}{\pi} K' \left(G_{11} \sin \psi_{11} + G_{21} \sin(\psi_{21} + \phi^\varepsilon) \right) \quad (6)$$

$$f_2^\varepsilon = \frac{4}{\pi} K' \left(G_{22} \cos \psi_{22} + G_{12} \cos(\psi_{12} - \phi^\varepsilon) \right) \quad (7)$$

$$g_2^\varepsilon = \frac{4}{\pi} K' \left(G_{22} \sin \psi_{22} + G_{12} \sin(\psi_{12} - \phi^\varepsilon) \right). \quad (8)$$

The amplitude and pulsation can readily be eliminated from (3), (4) to obtain an implicit relation defining ϕ^ε

$$\frac{f_1^\varepsilon}{2Q_1 g_1^\varepsilon} - \frac{f_2^\varepsilon}{2Q_2 g_2^\varepsilon} = \sqrt{1 + \left(\frac{f_1^\varepsilon}{2Q_1 g_1^\varepsilon} \right)^2} - \sqrt{1 + \varepsilon + \left(\frac{f_2^\varepsilon}{2Q_2 g_2^\varepsilon} \right)^2}. \quad (9)$$

For a given value of the mismatch parameter ε, one may then solve (9) for ϕ^ε. Expressing ϕ^ε as a simple function of ε is only possible for specific values of the coefficients G_{ij} and phase-shifts ψ_{ij}. Yet, one may express the reciprocal relation with greater ease. Defining

$$E(\phi^\varepsilon) \triangleq \frac{1}{Q_2} \frac{f_2^\varepsilon}{g_2^\varepsilon} - \frac{1}{Q_1} \frac{f_1^\varepsilon}{g_1^\varepsilon} (= E^\varepsilon) \quad (10)$$

we have

$$\varepsilon = E^\varepsilon \Big/ \left(\sqrt{1 + \left(\frac{f_1^\varepsilon}{2Q_1 g_1^\varepsilon} \right)^2} + \frac{f_1^\varepsilon}{2Q_1 g_1^\varepsilon} \right). \quad (11)$$

The corresponding steady-state pulsation ω^ε is then governed by

$$\omega^\varepsilon = \sqrt{1 - \frac{1}{Q_1} \frac{f_1^\varepsilon}{g_1^\varepsilon} \Big/ \left(\sqrt{1 + \left(\frac{f_1^\varepsilon}{2Q_1 g_1^\varepsilon} \right)^2} + \frac{f_1^\varepsilon}{2Q_1 g_1^\varepsilon} \right)} \quad (12)$$

and the steady-state amplitudes can be calculated from (4).

B. Stability of Synchronized Solutions

The stability of this solution can be assessed by studying a small perturbation of the system. Letting

$$x_1 = (A_1^\varepsilon + a_1(t)) \sin(\omega^\varepsilon t + \theta_1(t)) \quad (13\text{-a})$$

$$x_2 = (A_2^\varepsilon + a_2(t)) \sin(\omega^\varepsilon t + \phi^\varepsilon + \theta_2(t)) \quad (13\text{-b})$$

the calculations conducted in Appendix A result in the following model of the perturbed system dynamics:

$$\dot{\xi} + \left(\frac{1}{2Q_2 g_2^\varepsilon} \frac{df_2}{d\phi}\bigg|_{\phi^\varepsilon} - \frac{1}{2Q_1 g_1^\varepsilon} \frac{df_1}{d\phi}\bigg|_{\phi^\varepsilon} \right) \xi = \omega^\varepsilon \left(\frac{f_2^\varepsilon}{2(Q_2 g_2^\varepsilon)^2} a_2 - \frac{f_1^\varepsilon}{2(Q_1 g_1^\varepsilon)^2} a_1 \right) + \frac{b_{\sin,2}}{2Q_2 g_2^\varepsilon} - \frac{b_{\sin,1}}{2Q_1 g_1^\varepsilon} \quad (14)$$

$$\dot{a}_i + \frac{1}{2Q_i} a_i = \frac{1}{2\omega^\varepsilon} \frac{dg_i}{d\phi}\bigg|_{\phi^\varepsilon} \xi + \frac{1}{2\omega^\varepsilon} b_{\cos,i} \quad (15)$$

where $\xi = \theta_2 - \theta_1$ is the perturbation of the phase-difference ϕ^ε, and $b_{\sin,i}$ and $b_{\cos,i}$ are the projections of the perturbative forces. If $Q_1 = Q_2 \triangleq Q$, a single equation governing the phase-difference can be derived from (14) and (15)

$$2Q\ddot{\xi} + \left(1 + \frac{1}{g_2^\varepsilon} \frac{df_2}{d\phi}\bigg|_{\phi^\varepsilon} - \frac{1}{g_1^\varepsilon} \frac{df_1}{d\phi}\bigg|_{\phi^\varepsilon} \right) \dot{\xi} + \frac{1}{2} \frac{dE}{d\phi}\bigg|_{\phi^\varepsilon} \xi = \frac{\dot{b}_{\sin,2}}{g_2^\varepsilon} - \frac{\dot{b}_{\sin,1}}{g_1^\varepsilon} + \frac{1}{2Q} \left(\frac{1}{g_2^\varepsilon} \left(b_{\sin,2} + \frac{f_2^\varepsilon}{g_2^\varepsilon} b_{\cos,2} \right) - \frac{1}{g_1^\varepsilon} \left(b_{\sin,1} + \frac{f_1^\varepsilon}{g_1^\varepsilon} b_{\cos,1} \right) \right). \quad (16)$$

The stability of the steady-state solution is then trivially derived from the characteristic polynomial of the left-hand side of (16). This can be compared to the model constructed in [19] with more restrictive hypotheses ($Q_i \gg 1, G_{12} \ll G_{11}, G_{22} \ll G_{21}$), the so-called "generalized Adler's equation," whose perturbed form is given hereafter

$$\dot{\xi} + \frac{1}{2} \frac{dE}{d\phi}\bigg|_{\phi^\varepsilon} \xi = \frac{1}{2Q} \left(\frac{b_{\sin,2}}{g_2^\varepsilon} - \frac{b_{\sin,1}}{g_1^\varepsilon} \right). \quad (17)$$

Under the hypotheses of [19], the steady-state phase-difference and pulsation are given by

$$\varepsilon = E^\varepsilon \quad (18)$$

$$\omega^\varepsilon = 1 - \frac{1}{2Q_1} \frac{f_1^\varepsilon}{g_1^\varepsilon} \quad (19)$$

instead of (11) and (12). This steady-state solution is stable if

$$\frac{dE}{d\phi}\bigg|_{\phi^\varepsilon} > 0. \quad (20)$$

In the following section, we establish general characteristics of MILOs as resonant sensors.

IV. Characteristics of MILOs as Resonant Sensors

In what follows, subsections A, B, and C are dedicated to a study of the equilibrium state of MILOs, notably the sensitivity of this state to variations of ε and to variations of the other system parameters, in the neighborhood of $\varepsilon = 0$, and the determination of the locking range. Subsection D addresses the dynamic characteristics of MILOs, such as response time and phase noise, and proposes a tentative figure-of-merit.

In order to simplify the expressions in this section, we assume that, nominally, $Q_1 = Q_2 \triangleq Q \gg 1$, unless otherwise specified.

A. Sensitivity of the Synchronized State to ε

Under the assumption that $Q \gg 1$, (11) reduces to (18), from which the nominal phase-difference ϕ^0 can be calculated. An infinitesimal variation of ε then leads to a change of ϕ^0 equal to $S_\phi^0 \times \varepsilon$ where the phase sensitivity S_ϕ^0 is given by

$$S_\phi^0 = \frac{1}{\frac{dE}{d\phi}\Big|_{\phi^0}} = \frac{Q}{\frac{d}{d\phi}\left(\frac{f_2}{g_2} - \frac{f_1}{g_1} \right)\Big|_{\phi^0}}. \quad (21)$$

Similarly, one can calculate the (non-dimensional) pulsation sensitivity from (19) as

$$S_\omega^0 = -\frac{S_\phi^0}{2Q} \frac{d}{d\phi} \left(\frac{f_1}{g_1} \right)\bigg|_{\phi^0} \quad (22)$$

and the sensitivity of amplitude to mismatch is

$$S^0_{\mathcal{A}_i} = QS^0_\phi \left.\frac{dg_i}{d\phi}\right|_{\phi^0}. \tag{23}$$

Using (21) and (22), we find that all MILO architectures which verify the following three assumptions: i) $\psi_{12} = \psi_{21} + \pi$; ii) $\psi_{11} = \psi_{22}$; iii) $G_{12}/G_{22} = G_{21}/G_{11} \triangleq \gamma$ have at least two solutions corresponding to $\phi^0 = \pm\pi/2$, with the following sensitivities:

$$S^0_\phi = -\frac{Q}{2} \Big/ \frac{d}{d\phi}\left(\frac{f_1}{g_1}\right)\Bigg|_{\phi=\pm\pi/2},\ S^0_\omega = \frac{1}{4}. \tag{24}$$

Thus, phase sensitivity S^0_ϕ is on the order of Q times larger than S^0_ω, which motivates our use of phase difference rather than pulsation for sensing ε. It can be noted that pulsation sensitivity S^0_ω is twice as small as that of a single resonator in an oscillator loop. It is independent of the mixer parameters and MEMS quality factor.

Finally, it should be mentioned that several existing architectures, such as those studied in [19], verify

$$\left.\frac{dg_i}{d\phi}\right|_{\phi^0} = 0 \tag{25}$$

so that the oscillation amplitude is independent of ε at first order.

B. Sensitivity of the Synchronized State to Non-Idealities

In practice, because of fabrication dispersions, no two resonators exactly have the same quality factor, nor is it usually possible to guarantee the exact values of the phase delays ψ_{ij} or coupling coefficients G_{ij}. The impact of such non-idealities on the synchronized state can be estimated by perturbing (11) or (18). For any system parameter Θ other than ε, (for example, $\Theta = \psi_{ij}$) we find that

$$\frac{\partial\phi}{\partial\Theta} = -S^0_\phi \frac{\partial E}{\partial\Theta}. \tag{26}$$

From (10), the partial derivative on the right-hand side of (26) is of the order of $1/Q$ (or $1/Q^2$ if $\Theta = Q$). Thus, one may conclude that the phase difference is of the order of Q times more sensitive to ε than *to any other of the system's parameters*. This result is in fact a restatement of (38) in [19], highlighting that MILOs are robust to non-idealities, such as parameter drift or mismatches, including quality factor drift or mismatch. Finally, the ratios f_i/g_i depend on neither K' or K, so that, in our linear framework, these two gains have no influence on ϕ^ε or on ω^ε.

C. Locking Range

The locking range of a MILO, i.e., the range of values of ε for which there exists a stable synchronized regime, can be determined with the results of Section III-B. Our model (16) predicts that the phase-difference has second-order dynamics, whereas the generalized Adler's approach (17) predicts first-order dynamics. Significantly different results can be expected when

$$\left(1 + \frac{1}{g_2^\varepsilon}\left.\frac{df_2}{d\phi}\right|_{\phi^\varepsilon} - \frac{1}{g_1^\varepsilon}\left.\frac{df_1}{d\phi}\right|_{\phi^\varepsilon}\right)^2 - \frac{4Q}{S^\varepsilon_\phi} < 0 \tag{27}$$

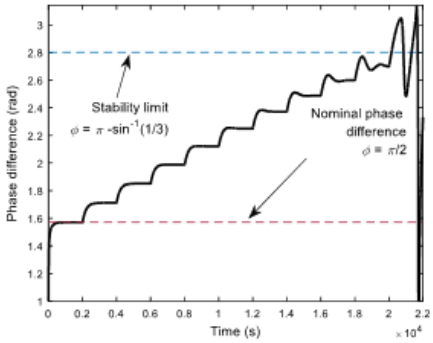

Fig. 2. Evolution of $\phi(t)$ obtained by transient simulation of (1). The value of ε is stepped up by $\sqrt{2}/10Q$, starting from 0, every 2×10^3 s.

in which case the characteristic polynomial of the left-hand side of (16) has complex conjugate roots. The steady-state solution is then stable if

$$1 + \frac{1}{g_2^\varepsilon}\left.\frac{df_2}{d\phi}\right|_{\phi^\varepsilon} - \frac{1}{g_1^\varepsilon}\left.\frac{df_1}{d\phi}\right|_{\phi^\varepsilon} > 0. \tag{28}$$

If the roots are real [which will typically be the case when the cross-coupling coefficients are small, as can be inferred from (5)–(8) and (21)], the stability criterion boils down to $S^\varepsilon_\phi > 0$, which is also the stability criterion derived from (17). To illustrate these results, let us consider a MILO with the following parameters:

$$G_{ij} = 1,\ \psi_{21} = -\pi/4,\ \psi_{11} = \psi_{22} = \psi_{12} = \frac{3\pi}{4},\ Q = 100.$$

For these parameters, there exists only one stable solution corresponding to $\phi^0 = \pi/2$, $S^0_\phi = Q$, and $S^0_\omega = 1/4$. The generalized Adler's model predicts that this MILO is stable for all values of ϕ^ε. On the other hand, (28) implies that the locking range of this MILO is limited to values of ϕ^ε such that $\sin\phi^\varepsilon > 1/3$, i.e., $|\varepsilon| < \sqrt{2}/Q$. This is confirmed by transient simulations of (1), as shown in Fig. 2. The second-order character of the phase-difference response can also be appreciated, in particular toward the end of the simulation.

If the coupling coefficients G_{12} and G_{21} are small compared to the values of G_{11} and G_{22}, the second- and first-order models tend to agree, as far as the locking range is concerned. For example, let $G_{12} = G_{21} = 0.1$ in the previous example, and leave all other parameters unchanged: in this case, two stable solutions corresponding to $\phi^0 = \pm\pi/2$ are found.

The real part of the corresponding eigenvalues is plotted in Fig. 3: the first- and second-order models predict approximately equal locking ranges, even though the eigenvalues at $\varepsilon = 0$ are still significantly different.

The locking range is usually found to be inversely proportional to Q, although it may be theoretically infinite for some architectures (discussed in Section V).

A more exhaustive discussion on the determination of the locking-range of phase-locked systems may be found in [31], [32].

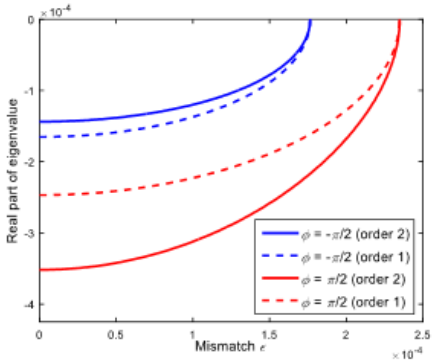

Fig. 3. Real part of the eigenvalues corresponding to first- and second-order models, respectively (16) and (17), in the case $G_{12} = G_{21} = 0.1$.

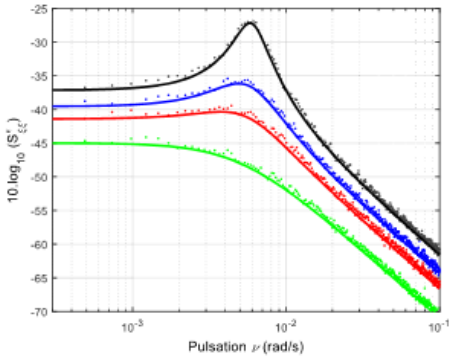

Fig. 4. Spectra of the phase difference noise $\xi(t)$ extracted from transient simulations of (B-1) (dots) and calculated from (30) (thick lines), with the same parameters as in Fig. 2, with $\varepsilon = 0$ (green), $\varepsilon = 0.9 \times 10^{-2}$ (red), $\varepsilon = 1.1 \times 10^{-2}$ (blue), and $\varepsilon = 1.3 \times 10^{-2}$ (black).

D. Response Time, Resolution and Figure of Merit

The response time of the MILO is proportional to Q, as can be trivially derived from (16). If the roots of the characteristic polynomial are real, two time-constants τ_1^ε and τ_2^ε are found

$$\tau_{1,2}^\varepsilon = S_\phi^\varepsilon \left[-\left(1 + \frac{1}{g_2^\varepsilon}\frac{df_2}{d\phi}\bigg|_{\phi^\varepsilon} - \frac{1}{g_1^\varepsilon}\frac{df_1}{d\phi}\bigg|_{\phi^\varepsilon}\right) \pm \sqrt{\left(1 + \frac{1}{g_2^\varepsilon}\frac{df_2}{d\phi}\bigg|_{\phi^\varepsilon} - \frac{1}{g_1^\varepsilon}\frac{df_1}{d\phi}\bigg|_{\phi^\varepsilon}\right)^2 - \frac{4Q}{S_\phi^\varepsilon}} \right]. \quad (29)$$

The sensor resolution can be determined by assuming b_1 and b_2 to be independent and white with variance σ_b^2, as would be the case of thermomechanical noise [27]. Neglecting the short-term correlation of $b_{\sin,i}$ and $b_{\cos,i}$ which results from averaging over one period, the phase-difference spectrum $S_{\xi\xi}^\varepsilon$ is derived from (16) by summing the contributions of $b_{\sin,1}$, $b_{\sin,2}$, $b_{\cos,1}$, and $b_{\cos,2}$

$$S_{\xi\xi}^\varepsilon \approx \frac{\sigma_b^2}{\pi} \frac{\left(\frac{1}{4Q^2}+\nu^2\right)\left(\frac{1}{g_2^{\varepsilon 2}}+\frac{1}{g_1^{\varepsilon 2}}\right)+\frac{1}{4Q^2}\left(\frac{f_2^{\varepsilon 2}}{g_2^{\varepsilon 4}}+\frac{f_1^{\varepsilon 2}}{g_1^{\varepsilon 4}}\right)}{\left(1+\frac{1}{g_2^\varepsilon}\frac{df_2}{d\phi}\Big|_{\phi^\varepsilon}-\frac{1}{g_1^\varepsilon}\frac{df_1}{d\phi}\Big|_{\phi^\varepsilon}\right)^2\nu^2+4Q^2\left(\frac{1}{4QS_\phi^\varepsilon}-\nu^2\right)^2} \quad (30)$$

where $\nu \ll 1$ is the pulsation of the fluctuations of ξ. The spectra obtained with (30) are represented in Fig. 4, showing excellent match to the ones obtained by transient simulation of (B-1). The variance $\sigma_\xi^{\varepsilon 2}$ of the phase difference noise can then be calculated from (30) by integrating $S_{\xi\xi}^\varepsilon$ over ν

$$\sigma_\xi^{\varepsilon 2} = \frac{\sigma_b^2}{2Q} \frac{\frac{S_\phi^\varepsilon}{Q}\left(\frac{1}{g_2^{\varepsilon 2}}+\frac{1}{g_1^{\varepsilon 2}}+\frac{f_2^{\varepsilon 2}}{g_2^{\varepsilon 4}}+\frac{f_1^{\varepsilon 2}}{g_1^{\varepsilon 4}}\right)+\frac{1}{g_2^{\varepsilon 2}}+\frac{1}{g_1^{\varepsilon 2}}}{\left|1+\frac{1}{g_2^\varepsilon}\frac{df_2}{d\phi}\Big|_{\phi^\varepsilon}-\frac{1}{g_1^\varepsilon}\frac{df_1}{d\phi}\Big|_{\phi^\varepsilon}\right|}. \quad (31)$$

Thus, close to a given value of ε, the measured phase behaves as:

$$\phi(t) \approx \phi^\varepsilon + \xi(t) \quad (32)$$

where the spectrum of ξ is given by (30) and its variance by (31). A small variation δ of ε can be detected if the resulting change of $\phi(t)$, equal to $S_\phi^\varepsilon \times \delta$, is significantly larger than the standard deviation of ξ. Assuming a Gaussian distribution for ξ, the resolution of the sensor (in terms of mismatch ε) is then

$$\delta_{\min}^\varepsilon = \frac{3\sigma_\xi^\varepsilon}{S_\phi^\varepsilon}. \quad (33)$$

For a given architecture, $\delta_{\min}^0$ scales as $1/Q^{3/2}$. This may be compared to the case of a "classical" resonant sensor based on a single oscillator, whose resolution in terms of mismatch scales as $1/Q$. Since this improvement comes at the cost of an increased response time, we define the following figure of merit, which also scales as $1/Q$:

$$\text{FOM} = \delta_{\min}^0 \times \sqrt{\tau_{\text{resp}}^0} \quad (34)$$

where τ_{resp}^0 is the nominal response time of the sensor (29), corresponding to $\varepsilon = 0$, and $\delta_{\min}^0$ its nominal resolution, calculated assuming $\sigma_b^2 = 1$, $K' = 1$ and $G_{ii} = 1$, except in the case $\gamma = \infty$, where we take $G_{ij} = 1, i \neq j$. Note that this FOM does not take into account the fact that, in most practical cases, the locking range is finite. Furthermore, it does not take into account the fact that the variance of thermomechanical noise is inversely proportional to Q [27].

V. Qualitative Study of Different MILO Architectures

In this section, several MILO architectures are described and compared in terms of sensor performance, as defined in Section IV, and of ease of implementation. Important design parameters to adjust sensor performance are the ratios of mutual-injection to self-injection

$$\gamma_{21} = \frac{G_{21}}{G_{11}}, \ \gamma_{12} = \frac{G_{12}}{G_{22}} \quad (35)$$

TABLE I
CHARACTERISTICS OF THE MILO ARCHITECTURES OF SECTION V. FOR ALL THESE ARCHITECTURES, $S_\omega^0 = 1/4$

ψ_{ii}	ψ_{12}	ψ_{21}	γ	ϕ^0	S_ϕ^0 $(\times Q)$	τ_{resp} $(\times Q)$	$\delta_{\min}^\phi$ $(\times 1/Q^{3/2})$	FOM $(\times 1/Q)$	ε_{lock} $(\times 1/Q)$
N/A	0	π	∞	$\pi/2$	1/2	2	3.33	4.71	∞
N/A	$\pi/2$	$\pi/2$	∞	0	1/2	2	3.33	4.71	∞
N/A	$-\pi/2$	$-\pi/2$	∞	π	1/2	2	3.33	4.71	∞
0	π	0	1	$\pi/2$	1/2	2	3.84	5.43	∞
$\pi/4$	$5\pi/4$	$\pi/4$	1	$\pi/2$	1	2	1.66	2.35	$\pm\sqrt{2}$
$\pi/2$	$3\pi/2$	$\pi/2$	1	$\pm\pi/2$	1/2	4	6.66	13.32	$\pm\sqrt{2}$
$\pi/2$	$3\pi/2$	$\pi/2$	$\gamma \ll 1$	$\pm\pi/2$	$1/2\gamma^2$	$1/\gamma^2$	3.33γ	3.33	$\pm\gamma^2$
$\pi/2$	π	0	1	$\pi/2$	1	2	1.18	1.66	$\pm 2\sqrt{2}$
$\pi/2$	π	0	$\gamma \ll 1$	$\pi/2$	$1/2\gamma$	$1/\gamma$	$3.33\gamma^{1/2}$	3.33	$\pm\gamma$

which set the value of the phase sensitivity of the system, as can be inferred from (21) or (24). Architectures obtained in the case $\gamma_{12} = \gamma_{21} \triangleq \gamma$, for different values of γ, are described hereafter and their characteristics are summarized in Table I.

A. Case $\gamma = +\infty$

This case is obtained in practice when $G_{11} = G_{22} = 0$, i.e., the phase-shifted sign of the output of each resonator is fed to the input of the other resonator. Because of the "sign" nonlinearity, the exact values of the coupling coefficients have, in theory, no impact on the behavior of the architecture: a variation of G_{21} or G_{12} affects the oscillation amplitudes, but leaves ϕ^ε unchanged. This robustness to coefficient mismatch is the main interest of this configuration.

Let us first consider the case i) $\psi_{12} = \pi$, $\psi_{21} = 0$. There exists a single stable solution with $\phi^0 = \pi/2$, $S_\phi^0 = Q/2$ and $S_\omega^0 = 1/4$. According to the models of Section III, this architecture is stable provided $\varepsilon \in]-1, +\infty[$, and this is confirmed by transient simulations of the system (without noise). However, this "infinite" locking range is limited by the oscillation amplitude of the resonators, which drops as $|\varepsilon|$ increases. Case ii) $\psi_{12} = 0$, $\psi_{21} = \pi$ has the same characteristics, with the only difference that $\phi^0 = -\pi/2$ (it results in fact from a simple permutation of resonators 1 and 2). Letting iii) $\psi_{21} = \psi_{12} = \pi/2$ or iv) $\psi_{21} = \psi_{12} = -\pi/2$, the same sensitivities and locking range as above are found, except $\phi^0 = 0$ in case iii) and $\phi^0 = \pi$ in case iv). In theory, the performances of these architectures are the same (see Table I). They differ in practice by the ease with which they can be implemented.

For example, in a MEMS resonator with an ideal capacitive readout [Fig. 5(a)], the output is a voltage which is proportional to the position of the resonator x, as supposed in Section II of this paper. In this context, the implementation of cases i) and ii) only requires two comparators, whereas the implementation of cases iii) and iv) also requires an element providing a $\pm\pi/2$ phase-shift, such as a differentiator or an integrator.

Conversely, if the MEMS resonator has an ideal resistive readout [Fig. 5(b)], it outputs a voltage which is proportional to the velocity of the resonator $\dot{x}$, so that cases i) and ii) now require the implementation of a $\pm\pi/2$-shifting element, whereas cases iii) and iv) only require two comparators.

Another degree of freedom for the practical implementation of the mixer is the fact that the phase-shifting elements and the comparator implementing the "sign" nonlinearity can usually be switched to some degree. For example, at the system-level, it is equivalent to:

— take the sign of the output of a resistive readout, and feed this signal to the other resonator [Fig. 5(c)].
— differentiate the signal output by a capacitive readout, take the sign of the resulting sine-wave, feed it to the other resonator [Fig. 5(d)].
— take the sign of the output of a capacitive readout, differentiate the square-wave at the comparator output, and feed this signal to the other resonator [Fig. 5(e)].

Although the generated waveforms are either a square-wave (in the first two cases) or a train of short voltage pulses (in the last case), the three approaches output a signal with $\pi/2$ phase-shift with respect to x, whose amplitude is independent from that of x. More precisely, in the first two cases, the projections of the forces on $\sin(\omega^\varepsilon t)$ and $\cos(\omega^\varepsilon t)$ can be written, as in Section III

$$f_i^\varepsilon = -\frac{4}{\pi} K' G_{ji} \sin(\phi^\varepsilon) \tag{36}$$

$$g_i^\varepsilon = \frac{4}{\pi} K' G_{ji} \cos(\phi^\varepsilon). \tag{37}$$

In the pulse-actuation case, the first harmonic component of the forces can be written

$$f_i^\varepsilon = -\frac{4}{\pi} \omega^\varepsilon \tau K' G_{ji} \sin(\phi^\varepsilon) \tag{38}$$

$$g_i^\varepsilon = \frac{4}{\pi} \omega \tau K' G_{ji} \cos(\phi^\varepsilon) \tag{39}$$

where $\tau \ll 1$ is the time-constant of the differentiator. Since $S_\omega^0 \ll S_\phi^0$, one may conclude that the generated forces have the same first-order dependence to ϕ, provided $\varepsilon \ll 1$, and that the three approaches are equivalent. However, the non-idealities of the electronics (finite bandwidth, finite input impedance) and of the MEMS devices (nonlinearities, feedthrough) must be considered for a practical application. For example, in a MEMS context, the excitation waveform is an important factor: not only does it affect the startup conditions of the MILO, because of capacitive feedthrough phenomena, but it also has an impact on the maximal oscillation amplitude of the system before resonant pull-in occurs [33]. These phenomena are not taken into account in the model developed in Section III, which should then be extended accordingly.

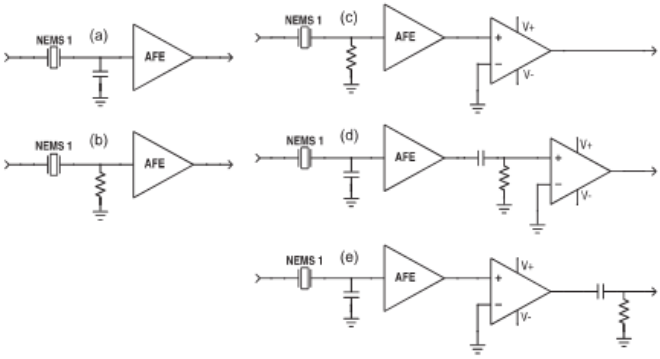

Fig. 5. Block schematics for different electronic readouts. Purely capacitive readouts (a) integrate the motional current (proportional to the resonator velocity) in the input capacitance and consequently deliver voltages proportional to the position of the resonator. Resistive readouts (b) deliver voltages proportional to the velocity of the resonator. Circuits (c) and (d) output square signals in quadrature with the position of the resonator, whereas (e) outputs a pulse-train, also in quadrature with the position.

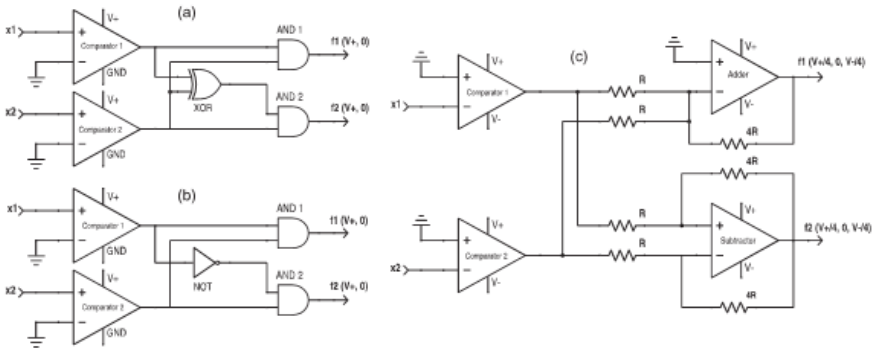

Fig. 6. Possible mixer implementations in the $\gamma = 1$ case.

B. Case $\gamma = 1$

We introduced in [7] a mixer based on the use of logic components (one XOR and two ANDs). This mixer is represented in Fig. 6(a), along with an alternative digital implementation [based on one NOT and two ANDs, Fig. 6(b)] and an alternative analog implementation based on a subtractor and an adder [Fig. 6(c)]. Associated to an ideal capacitive readout, these mixers correspond to the phase-shifts $\psi_{11} = \psi_{22} = \psi_{21} = 0$, and $\psi_{12} = \pi$. The architecture has a single stable steady-state solution with a theoretically infinite locking range, and the same sensitivity as the (simpler) ones presented in subsection A. However, S_ϕ^0 can be boosted by adding a phase-shift in the loop: it is maximal for $\psi_{11} = \psi_{22} = \psi_{21} = \pi/4$, and $\psi_{12} = 5\pi/4$, in which case $S_\phi^0 = Q$.

As shown in Table I, this gain in sensitivity comes with a reduction of the locking range, which is limited to $|\varepsilon| < \sqrt{2}/Q$. A similar case is experimentally studied in Section VI. An increase of the phase-shift from $\pi/4$ to $\pi/2$ (so that $\psi_{11} = \psi_{22} = \psi_{21} = \pi/2$, and $\psi_{12} = -\pi/2$) results in an architecture with two stable steady-state solutions, a reduced sensitivity and an increased response time compared to the $\pi/4$ case.

C. Case $\gamma < 1$

Two architectures based on LC resonators are studied in detail in [19]. At the system-level, they can be described as two identical ideal oscillators ("ideal" in the sense that $\psi_{11} = \psi_{22} = \pi/2$), that are cross-coupled with the same level of injection $\gamma < 1$. The case corresponding to $\psi_{21} = \pi/2 = -\psi_{12}$ was already addressed in subsection B, for $\gamma = 1$. When $\gamma < 1$, there are still two stable steady-state solutions, corresponding to $\phi^0 = \pm\pi/2$. The sensitivity S_ϕ^0 for both solutions is equal to $Q/2\gamma^2$ ($Q \gg 1$). However, the gain in sensitivity and resolution is also compensated by a reduction of the locking range and an increase of the response time, as shown in Table I. It should be noted that this architecture is extremely sensitive to "symmetry" errors: its characteristics in the $\gamma \ll 1$ case are guaranteed only if γ_{12} is precisely equal to γ_{21}. This motivated the authors of [19] to promote the more robust architecture of lines 8

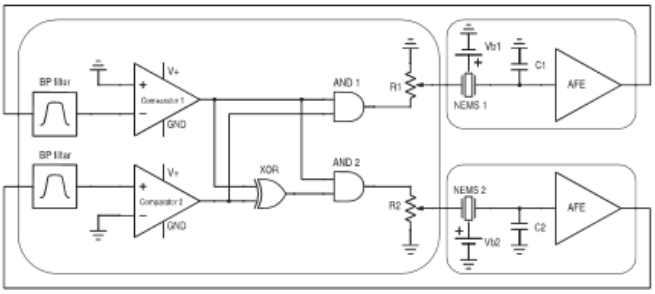

Fig. 7. Schematic of the experimental setup. The different PCBs are symbolized by the rounded rectangles.

and 9, corresponding to $\psi_{12} = \pi$, and $\psi_{21} = 0$. In this case, there exists a single stable steady-state solution with $\phi^0 = \pi/2$ and $S_\phi^0 = (1 + 1/\gamma)Q/2$. As above, the increase in sensitivity resulting from a smaller γ is compensated by the reduction of the locking range and the increase of the response time.

D. Discussion

We have defined an FOM in Section IV-D, by the light of which one may try to compare the presented architectures. Looking at Table I, one can easily reach the conclusion that architectures with $\gamma < 1$ have little interest for differential resonant sensing applications, since the gain in sensitivity and resolution made by decreasing γ is always (more than) compensated for by a reduction of the sensor bandwidth (and locking range), compared to the case $\gamma = 1$. They are also more delicate to implement, because dispersions will impact the accuracy of the coupling coefficients and may be detrimental to the nominal behavior of the system. Finally, one should keep in mind that, as mentioned in the introduction, a weak coupling at the electronic level may not be able to overcome other parasitic weak couplings (mechanical, etc.) between the two resonators. These weak couplings may be modeled as (static) perturbations of the cross-coupling gains and phase delays of the mixer, so that, in the presence of parasitic coupling, the cross-coupling gains become $G'_{ij} = G_{ij} + \delta G$. These perturbations should have little influence on the behavior of the system, provided $\delta G \ll G_{ij}$. So, in practice, γ is limited to values that are large with respect to $\delta G/G_{ii}$. The magnitude of this ratio depends on several factors, notably the physical distance between the two resonators: these should be close enough to guarantee that they operate in the same environmental conditions (for efficient temperature drift removal), and far enough so that the parasitic coupling phenomena do not become overwhelming.

It might be argued that the architectures with $\gamma = \infty$ have a theoretically infinite locking range, and that this quantity should be incorporated in the FOM. However, the locking range is limited in practice by the fact that the oscillation amplitude drops considerably for $|\varepsilon| > 1/Q$. Furthermore, closed-loop control techniques can always be used to actively compensate for mismatch ε, so that one remains at the optimal operating point of the system.

In this light, the best two choices of coefficients and phase-shifts are i) Mirzaei's architecture, with $\gamma = 1$, corresponding to line 8 of Table I, ii) the $\pi/4$-shifted digital architecture of subsection B, corresponding to line 5 of Table I. The phase-shifting elements of these architectures may be implemented in a number of ways: from passive filters, as already discussed, to (voltage-controlled) delay lines, depending on whether they are placed before or after the comparators, and on the waveform one is willing to generate. It should also be kept in mind that a good choice of architecture cannot be made without considering the specificities of the MEMS part of the system (transduction principle, existence of feedthrough, etc.)

In the next section, some experimental results are reported and compared to the theoretical results of Sections III and IV.

VI. Experimental Validation

Our experimental setup (Fig. 7) consists in three distinct PCBs:

— Two PCBs with a chip on which a MEMS resonator has been fabricated and monolithically integrated with its AMS035 electronic readout. The resonators are cantilever beams made of tungsten (Young's modulus 410 GPa, density 19 300 kg.m^{-3}) with 10 μm length, 500 nm width, 900 nm thickness, and an electrostatic actuation gap of 450 nm. The capacitive readout is described in detail in [34]. The bias voltage of each beam can be adjusted independently in order to change the electrostatic stiffness of the resonators and, consequently, tune and detune them at will (i.e., changing the bias voltage of one of the resonators modifies the mismatch ε).

— A PCB on which a discrete digital mixer is implemented with two AD8561 comparators, one 74HCT86 XOR and two 74HCT08 AND gate. A passive bandpass filter is used at the mixer input to remove the DC component and smooth the output of the MEMS readout. A variable resistor is used to adjust the actuation voltage of the MEMS beam to a level on the order of 200 mV. Note that the signal paths in this mixer are slightly different from those in Fig. 6(a) and [7]: this particular routing makes it possible to remove a parasitic spike from the actuation voltage.

The characterization of the MEMS PCBs shows that the two resonators have very linear 2nd-order responses (Fig. 8), so that the assumptions of Section II can be considered to be valid (the

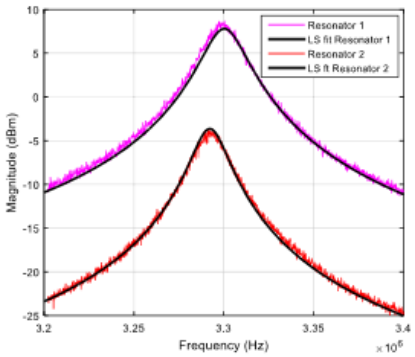

Fig. 8. Frequency responses of the CMOS-MEMS devices.

model of Appendix A predicts oscillation amplitudes on the order of 7% of the electrostatic gap at most). Their characteristics are similar, with $Q_1 \approx Q_2 \approx 170$, and a resonance frequency of 3.287 MHz when tuned at $V_{b1} = 20$ V and $V_{b2} = 39.9$ V. The limited bandwidth of the readout amplifiers introduces a parasitic delay in the responses of the resonators: their phase at resonance is $-\pi/2 + \psi_{\text{readout}}$, where $\psi_{\text{readout}} = -0.52$ rad (about $-30°$).

Regarding the mixer PCB, the bandpass filters and the finite propagation delays of the comparators and the logic gates result in a supplementary $\psi_{\text{mixer}} = -0.25$ rad phase-delay (about $-15°$) in the system.

The system may then be modelled as in Section III, with the following parameters:

$$\gamma = 1,\ Q = 170,\ \psi_{21} = \psi_{\text{mixer}} + \psi_{\text{readout}} = -0.77 \approx -\pi/4$$
$$\psi_{11} = \psi_{22} = \psi_{12} = \pi - \psi_{21} \approx \frac{3\pi}{4}$$

close to one of the "optimal" configurations mentioned in Section V (line 5 of Table I). In the absence of mismatch, the resonators should oscillate in quadrature, with $S_\phi^0 \approx Q = 170$ and $S_\omega^0 = 1/4$. Note that the generalized Adler's approach predicts an infinite locking range for this set of parameters, whereas our model predicts a theoretical locking range of $|\varepsilon| < 8.3 \times 10^{-3}$.

When the resonators are tuned and the PCBs are connected, the MILO oscillates with the resonators in quadrature, as predicted in theory. The measured oscillation frequency of the system is plotted in Fig. 9(a), versus the bias voltage of resonator 2. To determine the correspondence between the change of bias voltage δV and the relative stiffness mismatch ε, we use the fact that our model predicts that the value of S_ω^0 is exactly equal to $1/4$, independently of the values of the quality factors or of the parasitic phase delay. Thus, we infer from our measurements an empirical formula for ε

$$\varepsilon \approx -4.45 \times 10^{-3}\ \delta V. \tag{40}$$

This makes it possible to compare the experimental results to the theoretical ones [Fig. 9(b) and (c)].

First of all, the experimental locking range is found to be $\varepsilon \in]-3.56 \times 10^{-3}, 3.79 \times 10^{-3}[$, corresponding to a 12 kHz mismatch, less than predicted by the harmonic-balance model ($|\varepsilon| < 8.3 \times 10^{-3}$, or a 27 kHz mismatch) or by transient simulation of (1). This is an expected consequence of the non-idealities of the mixer: as shown in Fig. 9(c), one of the detected voltage amplitudes decreases (whereas the other, not shown, increases) as the mismatch increases. Experimentally, this results in poorer SNR and less clean zero-crossings of the corresponding comparator and partly explains the reduced locking range. Moreover, the finite propagation delays in the AND and XOR limit in practice the minimal duration of the voltage pulses delivered to the resonators.

The phase difference between the signals [Fig. 9(b)] is deduced from the duty cycle of either of the (binary) mixer outputs. A linear fit of our measurements yields $S_\phi^0 \approx 190$, which is slightly larger than the expected value. The variation of the oscillation amplitude across the experimental locking range also agrees well with the predicted behavior [Fig. 9(c)].

An underestimation of the actual quality factors of the resonators may explain the difference between theory and practice: the theoretical results corresponding to $Q = 190$ (all other parameters unchanged) are also plotted in Fig. 9 and are a better fit to the experimental results. The locking range calculated with our model for $Q = 190$ is $|\varepsilon| < 7.4 \times 10^{-3}$. Thus, an underestimation of the quality factors would also partly explain the reduced experimental locking-range. Another possible source of discrepancy is the nonlinearity of the readout electronics, which results in a slight amplitude-dependent distortion of the signals arriving to the mixer and may cause this enhancement of the sensitivity to mismatch.

VII. Conclusion

In this paper, we have revisited previous work [19] on the dynamics of injection-locked oscillators, extending it to the case of very strong coupling, in the context of MEMS differential resonant sensing applications. This let us relate the various performance parameters of any sensor application (sensitivity, resolution, etc.) to the design parameters of a generic cross-coupling scheme. We could compare the performance of MILOS to those of "classical" resonant sensors, and demonstrate the expected tradeoffs between different system parameters (such as locking range and sensitivity, or bandwidth and sensitivity). The practical implementation of architectures based on the proposed mixing scheme was also discussed, and the performance of such architectures was assessed. This modeling approach was validated with simulations and with experimental results, in the $\gamma = 1$ case. The extended demonstration of the performance of this architecture and further explanations on the use of MILOs in resonant sensing applications may be found in [35].

An important outcome of this study is that the gain in resolution made by decreasing the cross-coupling coefficient γ is always (more than) compensated by a corresponding increase of the sensor response time. Thus, for given values of the phase-shifts ψ_{ij}, choosing $\gamma = 1$ and averaging the sensor output ϕ over time yields similar or better performance than decreasing γ, with two other major benefits: i) simpler implementation (for example with combinational logic gates), ii) improved immunity to parasitic coupling phenomena.

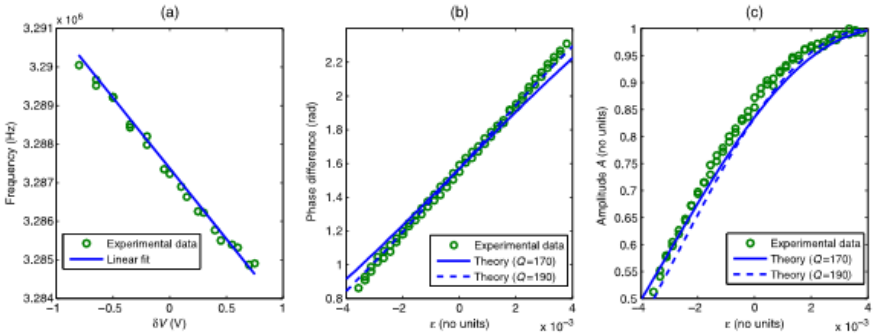

Fig. 9. Experimental results (circles) obtained by sweeping the bias voltage of one of the resonators up and down, and comparison to theory. The oscillation amplitudes (c) are normalized with respect to the maximal measured value.

Another benefit is that the locking range at $\gamma = 1$ is larger than at $\gamma < 1$. However, this point is less critical than the others, since the locking range can be increased by closed-loop control of the mismatch between the resonators (by adjusting the bias voltage of one resonator to track the resonance frequency of the other).

In this paper, we also showed that the actuation waveform has little, if any, impact on the performance of *linear* MILOs, whereas phase-shift plays an essential role. For the sake of completeness, the study of these aspects should also be carried out in a nonlinear framework: it is indeed known that the actuation waveform, the phase-shift in the feedback loop, the existence of concurrent types of nonlinearity (hardening and softening) [27]–[29], [33], [36], [37] may all play a determinant role in the oscillation characteristics of non-injection-locked nonlinear M/NEMS oscillators. However, it seems difficult to achieve a general study of such diverse and complex phenomena, and it will be probably best accomplished on a case by case basis, using the present work as a linear reference point.

Finally, the monolithic integration of the resonators and the mixer studied in the experimental section of this paper should make it possible to decrease the level of noise in the system, and to push our investigation of its behavior to the theoretical limits of its locking range. This work is currently ongoing.

Appendix A
Derivation of Non-Dimensional Beam Model

Let us consider a MEMS resonator with stiffness K, mass M, natural pulsation $\omega_0 = \sqrt{K/M}$ and quality factor Q. An electrode with surface area S_e is situated across a gap G_0 from the resonator, supposed to be very small with respect to the lateral dimensions of the electrode. A voltage $V(t) = V_b - V_{\mathrm{act}}(t)$ is applied across the gap. It exerts an electrostatic force on the resonator and sets it into motion. Another electrode, at a constant potential V_{det}, is used for detection (Fig. 10). The position of the resonator as it moves across the gap is given by $G(t) = G_0 x(t)$, so that $x = \pm 1$ means that the tip of the structure touches one of the two electrodes. The dynamics of the resonator are governed by

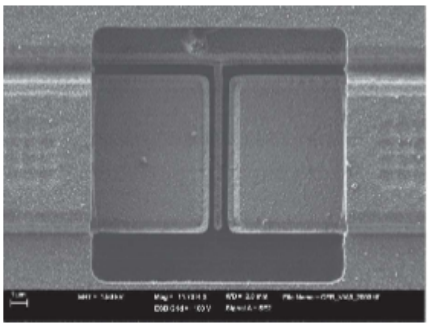

Fig. 10. Cantilever beam fabricated at UAB in the AMS035 process, similar to those used in Section VI. The beam is at potential V_b, the left electrode at V_{act}, and the right one at V_{det}.

$$\frac{d^2x}{dt^2} + \frac{\omega_0}{Q}\frac{dx}{dt} + \omega_0^2 x = \eta\left[(V_b - V_{\mathrm{act}})^2 N(x) - (V_b - V_{\mathrm{det}})^2 N(-x)\right] \quad \text{(A-1)}$$

where we define the electromechanical coefficient η as

$$\eta = \frac{\varepsilon_0 S_e}{2MG_0^3} \quad \text{(A-2)}$$

with ε_0 the permittivity of vacuum, and where $N(x)$ represents the dependence of the electrostatic force to x. This function depends on the resonator geometry (parallel-plate, CC-beam, cantilever, see [33]) and also on the effective area of the electrode (the electrode might be smaller than the resonator). With these notations, the input and output capacitance are

$$C_{\mathrm{in}} = (\varepsilon_0 S_e/G_0)\,\Gamma(x) \triangleq C_0\Gamma(x),\ C_{\mathrm{out}} = C_0\Gamma(-x) \quad \text{(A-3)}$$

where $\Gamma(x)$ is also a geometry-dependent function. For example, in the case of an initially straight cantilever beam with

Young's modulus E, density ρ, length L, width (in direction of motion) h, and thickness b, whose input/output electrodes have the same length as the beam, we find, following [33], [38]:

$$K = \frac{0.257Ebh^3}{L^3},\ M = 0.25\rho bhL$$
$$N(x) \approx 0.392\left(\frac{1+0.783x}{1-x} + (0.531+0.114x)\log(1-x)\right)$$
$$\Gamma(x) \approx 1 - 0.505x - (0.888 - 0.201x)\log(1-x). \quad \text{(A-4)}$$

When $x \ll 1$, $V_{\text{act}} \ll V_b$, and if we are close to resonance, one may linearize (A-1) and drop constant terms, leading to

$$\frac{d^2x}{dt^2} + \frac{\omega_0}{Q}\frac{dx}{dt} + \left(\omega_0^2 - 2\eta N'(0)V_b^2\right)x \approx -2\eta V_b N(0)V_{\text{act}}. \quad \text{(A-5)}$$

The non-dimensional equation governing one resonator can be obtained by letting $t = \omega_0\tau$ in (A-5), which becomes

$$\frac{d^2x}{d\tau^2} + \frac{1}{Q}\frac{dx}{d\tau} + \left(1 - \frac{2\eta N'(0)V_b^2}{\omega_0^2}\right)x \approx \frac{-2\eta V_b N(0)}{\omega_0^2}V_{\text{act}}. \quad \text{(A-6)}$$

If a capacitive readout (e.g., a charge amplifier with a feedback capacitor C_{fb}) is used to integrate the motional current, it outputs a voltage

$$V_{\text{out}} = N(0)\frac{C_0 V_b}{C_{fb}}x. \quad \text{(A-7)}$$

Appendix B
Derivation of Perturbed Model

Let us suppose (1) is slightly perturbed by exogenous additive noise sources $b_1(t)$ and $b_2(t)$

$$x_1 + \frac{\dot{x}_1}{Q_1} + \ddot{x}_1 = f_1 + b_1,\ (1+\varepsilon)x_2 + \frac{\dot{x}_2}{Q_2} + \ddot{x}_2 = f_2 + b_2\ . \quad \text{(B-1)}$$

We assume

$$x_1 = (A_1^\varepsilon + a_1(t))\sin(\omega^\varepsilon t + \theta_1(t)) \quad \text{(B-2)}$$
$$x_2 = (A_2^\varepsilon + a_2(t))\sin(\omega^\varepsilon t + \phi^\varepsilon + \theta_2(t)). \quad \text{(B-3)}$$

The velocities $\dot{x}_i$ and accelerations $\ddot{x}_i$ can be deduced from (B-2) and (B-3) by straightforward differentiation. These quantities are then replaced in (1), which is projected on $\sin(\omega^\varepsilon t + \theta_i)$ and $\cos(\omega^\varepsilon t + \theta_i)$, yielding a set of four equations

$$(A_1^\varepsilon + a_1)\left(1 - (\omega^\varepsilon + \dot{\theta}_1)^2\right) + \frac{\dot{a}_1}{Q_1} + \ddot{a}_1 = b_{\sin,1} + f_1(\phi^\varepsilon + \xi) \quad \text{(B-4)}$$
$$(A_2^\varepsilon + a_2)\left(1 + \varepsilon - (\omega^\varepsilon + \dot{\theta}_2)^2\right) + \frac{\dot{a}_2}{Q_2} + \ddot{a}_2 = b_{\sin,2} + f_2(\phi^\varepsilon + \xi) \quad \text{(B-5)}$$
$$2\dot{a}_1(\omega^\varepsilon + \dot{\theta}_1) + (A_1^\varepsilon + a_1)\ddot{\theta}_1 + \frac{A_1^\varepsilon + a_1}{Q_1}(\omega^\varepsilon + \dot{\theta}_1) = b_{\cos,1} + g_1(\phi^\varepsilon + \xi) \quad \text{(B-6)}$$
$$2\dot{a}_2(\omega^\varepsilon + \dot{\theta}_2) + (A_2^\varepsilon + a_2)\ddot{\theta}_2 + \frac{A_2^\varepsilon + a_2}{Q_2}(\omega^\varepsilon + \dot{\theta}_2) = b_{\cos,2} + g_2(\phi^\varepsilon + \xi) \quad \text{(B-7)}$$

where $\xi \triangleq \theta_2 - \theta_1$ is the phase-difference perturbation and $b_{\sin,i}$ and $b_{\cos,i}$ are the projections of perturbation $b_i(t)$ on sin and cos. Assuming $a_i \ll A_i^\varepsilon$, $\dot{\theta}_i \ll \omega^\varepsilon$ and using (3), (4), a first-order expansion of these equations gives

$$\dot{\theta}_i + \frac{1}{2Q_i g_i^\varepsilon}\left.\frac{df_i}{d\phi}\right|_{\phi^\varepsilon}\xi = \frac{1}{2Q_i g_i^\varepsilon}\left(\frac{\omega^\varepsilon f_i^\varepsilon}{Q_i g_i^\varepsilon}a_i + \frac{\dot{a}_i}{Q_i} + \ddot{a}_i - b_{\sin,i}\right) \quad \text{(B-8)}$$

$$\dot{a}_i + \frac{1}{2Q_i}a_i = \frac{1}{2\omega^\varepsilon}\left(\left.\frac{dg_i}{d\phi}\right|_{\phi^\varepsilon}\xi - \frac{g_i^\varepsilon}{\omega^\varepsilon}\dot{\theta}_i - \frac{Q_i g_i^\varepsilon}{\omega^\varepsilon}\ddot{\theta}_i + b_{\cos,i}\right). \quad \text{(B-9)}$$

The time derivatives appearing on the right-hand sides of (B-8) and (B-9) have only a very small impact on the time constants of the system, and hence on its stability. This is readily seen by applying $(d/dt) + (1/2Q_i)$ to (B-8) and using (B-9) to eliminate a_i in the resulting equation. With $Q_i = Q_j = Q$, this yields

$$\frac{1}{4\omega^{\varepsilon 2}}\dddot{\theta}_i + \frac{1}{4\omega^{\varepsilon 2}}\frac{2}{Q}\dddot{\theta}_i + \left(1 + \frac{1}{4Q\omega^{\varepsilon 2}}\left(\frac{\omega^\varepsilon f_i^\varepsilon}{g_i^\varepsilon} + \frac{1}{Q}\right)\right)\ddot{\theta}_i - \frac{1}{4Q\omega^\varepsilon g_i^\varepsilon}\left.\frac{dg_i}{d\phi}\right|_{\phi^\varepsilon}\ddot{\xi} + \frac{1}{2Q}\left(\left(1 + \frac{1}{2Q\omega^{\varepsilon 2}}\right)\dot{\theta}_i + \frac{1}{g_i^\varepsilon}\left(\left.\frac{df_i}{d\phi}\right|_{\phi^\varepsilon} - \frac{1}{2Q\omega^\varepsilon}\right)\dot{\xi}\right) \times \frac{1}{4Q^2}\left.\frac{d}{d\phi}\left(\frac{f_i}{g_i}\right)\right|_{\phi^\varepsilon}\xi = \text{s.t.} \quad \text{(B-10)}$$

where "s.t." designates source terms. Thus, accounting for the time derivatives on the right-hand sides of (B-8) and (B-9) only results in minor corrections to the second-order model obtained when neglecting them

$$\ddot{\theta}_i + \frac{1}{2Q}\left(\dot{\theta}_i + \frac{1}{g_i^\varepsilon}\left(\left.\frac{df_i}{d\phi}\right|_{\phi^\varepsilon}\right)\dot{\xi}\right) + \frac{1}{4Q^2}\left.\frac{d}{d\phi}\left(\frac{f_i}{g_i}\right)\right|_{\phi^\varepsilon}\xi = \text{s.t.} \quad \text{(B-11)}$$

One can in fact notice that the relative differences between the second- and first-order coefficients of (B-10) and (B-11) are on the order of $1/Q \ll 1$. The higher-order coefficients appearing in (B-10) can be neglected as long as "slow" variations of θ_i are considered, which is implicit in our use of the harmonic balance method. Hence, the following model may be used to study the dynamic characteristics of the MILO:

$$\dot{\theta}_i + \frac{1}{2Q_i g_i^\varepsilon}\left.\frac{df_i}{d\phi}\right|_{\phi^\varepsilon}\xi = \frac{1}{2Q_i g_i^\varepsilon}\left(\frac{\omega^\varepsilon f_i^\varepsilon}{Q_i g_i^\varepsilon}a_i - b_{\sin,i}\right) \quad \text{(B-12)}$$

$$\dot{a}_i + \frac{1}{2Q_i}a_i = \frac{1}{2\omega^\varepsilon}\left(\left.\frac{dg_i}{d\phi}\right|_{\phi^\varepsilon}\xi + b_{\cos,i}\right). \quad \text{(B-13)}$$

References

[1] M. C. Cross, A. Zumdieck, R. Lifshitz, and J. L. Rogers, "Synchronization by nonlinear frequency pulling," *Phys. Rev. Lett.*, vol. 93, 2004, Art. no. 22401.

[2] M. C. Cross, J. L. Rogers, R. Lifshitz, and A. Zumdieck, "Synchronization by reactive coupling and nonlinear frequency pulling," *Phys. Rev. E*, vol. 73, 2006, Art. no. 03625.

[3] A. B. Sabater and J. F. Rhoads, "On the dynamics of two mutually-coupled, electromagnetically-actuated microbeam oscillators," *J. Comput. Nonlinear Dyn.*, vol. 7, 2012, Art. no. 031011.

[4] D. K. Agrawal, J. Woodhouse, and A. A. Seshia, "Observation of locked phase dynamics and enhanced frequency stability in synchronized micromechanical oscillators," *Phys. Rev. Lett.*, vol. 111, 2013, Art. no. 084101.

[5] D. K. Agrawal, J. Woodhouse, and A. A. Seshia, "Synchronization in a coupled architecture of microelectromechanical oscillators," *J. Appl. Phys.*, vol. 115, 2014, Art. no. 164904.

[6] M. H. Matheny *et al.*, "Phase synchronization of two anharmonic nanomechanical oscillators," *Phys. Rev. Lett.*, vol. 112, 2014, Art. no. 014101.

[7] J. Juillard *et al.*, "A novel architecture for differential resonant sensing," *Procedia Eng.*, vol. 87, pp. 1573–1576, 2014.

[8] A. B. Sabater and J. F. Rhoads, "Dynamics of globally and dissipatively coupled resonators," *J. Vib. Acoust.*, vol. 37, 2015, Art. no. 021016.

[9] D. Antonio *et al.*, "Nonlinearity-induced synchronization enhancement in micromechanical oscillators," *Phys. Rev. Lett.*, vol. 114, 2015, Art. no. 034103.

[10] H. C. Chang, X. Cao, U. K. Mishra, and R. A. York, "Phase noise in coupled oscillators: Theory and experiment," *IEEE Trans. Microw. Theory Techn.*, vol. 45, pp. 604–615, 1997.

[11] L. Romano *et al.*, "Multiphase LC oscillators," *IEEE Trans. Circuits Syst. I, Reg. Papers*, vol. 53, pp. 1579–1588, 2006.

[12] A. Mazzanti, F. Svelto, and P. Andreani, "On the amplitude and phase errors of quadrature LC-tank CMOS oscillators," *IEEE J. Solid-State Circuits*, vol. 41, pp. 1305–1313, 2006.

[13] P. Maffezzoni, "Nonlinear phase-domain macromodeling of injection-locked frequency dividers," *IEEE Trans. Circuits Syst. I, Reg. Papers*, vol. 60, pp. 2878–2887, 2013.

[14] P. Maffezzoni and S. Levantino, "Phase noise of pulse injection-locked oscillators," *IEEE Trans. Circuits Syst. I, Reg. Papers*, vol. 61, pp. 2912–2919, 2014.

[15] J. C. Salvia *et al.*, "Real-time temperature compensation of MEMS oscillators using an integrated micro-oven and a phase-locked loop," *IEEE J. MEMS*, vol. 19, pp. 192–201, 2010.

[16] F. C. Hoppenstaedt and E. M. Izhikevich, "Synchronization of MEMS resonators and mechanical neurocomputing," *IEEE Trans. Circuits Syst. II, Analog Digit. Signal Process.*, vol. 48, pp. 133–138, 2002.

[17] M. Zhang *et al.*, "Synchronization of micromechanical oscillators using light," *Phys. Rev. Lett.*, vol. 109, 2012, Art. no. 233906.

[18] J. L. Munoz-Gamarra, N. Barniol, and J. Juillard, "Analysis of a MEMS-based ring oscillator," in *Proc. ISCAS*, 2012, pp. 2103–2106.

[19] A. Mirzaei *et al.*, "The quadrature LC oscillator: A complete portrait based on injection locking," *IEEE J. Solid-State Circuits*, vol. 42, pp. 1916–1932, 2007.

[20] A. Mirzaei and H. Darabi, "Mutual pulling between two oscillators," *IEEE J. Solid-State Circuits*, vol. 49, pp. 360–372, 2014.

[21] U. L. Rohde *et al.*, "Low noise low cost ultra wideband N-push VCO," in *IEEE Microw. Symp. Dig.*, 2005, pp. 1171–1174.

[22] U. L. Rohde and A. K. Poddar, "Technique to minimize phase noise of crystal oscillators," *Microw. J.*, vol. 56, no. 5, pp. 132–150, 2013.

[23] U. L. Rohde and A. K. Poddar, "Mode-coupled VCO replaces expensive DRO," in *Proc. IEEE Freq. Control Symp.*, 2008, pp. 296–304.

[24] A. K. Poddar and U. L. Rohde, "Evanescent-mode phase-injection mode-coupled (EMPIMC) metamaterial resonator based tunable signal sources," in *Proc. IEEE Wireless Microw. Technol. Conf.*, 2014, pp. 1–9.

[25] L. Zhang, A. K. Poddar, U. L. Rohde, and A. Daryoush, "Analytical and experimental evaluation of SSB phase noise reduction in self-injection locked oscillators using optical delay loops," *IEEE Photon. J.*, vol. 5, no. 6, pp. 1–18, 2013.

[26] L. Zhang, A. K. Poddar, U. L. Rohde, and A. Daryoush, "Comparison of optical self-phase locked loop techniques for frequency stabilization of oscillators," *IEEE Photon. J.*, vol. 6, pp. 1–16, 2014.

[27] M. H. Bao, *Micro-Mechanical Transducers: Pressure Sensors, Accelerometers and Gyroscopes*, Amsterdam, The Netherlands: Elsevier, 2000.

[28] V. Kaajakari *et al.*, "Nonlinear limits for single-crystal silicon microresonators," *IEEE J. Microelectromech. Syst.*, vol. 13, pp. 715–724, 2004.

[29] D. Agrawal, J. Woodhouse, and A. Seshia, "Modeling nonlinearities in MEMS oscillators," *IEEE Trans. Ultrason., Ferroelectr., Freq. Control*, vol. 60, pp. 1646–1659, 2013.

[30] A. Gelb and W. Van der Welde, *Multiple-Input Describing Functions and Nonlinear System Design*. New York, NY, USA: McGraw-Hill, 1968.

[31] G. A. Leonov, N. V. Kuznetsov, M. V. Yuldashev, and R. V. Yuldashev, "Hold-in, pull-in, lock-in ranges of PLL circuits: Rigorous mathematical definitions and limitations of classical theory," *IEEE Trans. Circuits Syst. I, Reg. Papers*, vol. 62, pp. 2454–2464, 2015.

[32] G. A. Leonov and N. V. Kuznetsov, "Hidden attractors in dynamical systems. From hidden oscillations in Hilbert-Kolmogorov, Aizerman, Kalman problems to hidden chaotic attractor in Chua circuits," *Int. J. Bifurcation Chaos*, vol. 62, 2013, p. 69.

[33] J. Juillard, "Analysis of resonant pull-in of micro-electromechanical oscillators," *J. Sound Vib.*, vol. 350, pp. 123–139, 2015.

[34] J. Verd, A. Uranga, J. Segura, and N. Barniol, "A 3 V CMOS-MEMS oscillator in 0.35 μm CMOS technology," in *Proc. Transducers*, 2013, pp. 806–809.

[35] P. Prache, N. Barniol, A. Uranga, and J. Juillard, "Temperature-drift rejection and sensitivity to mismatch of synchronized strongly-coupled M/NEMS resonators," in *Proc. IEEE MEMS Conf.*, 2016, p. 4.

[36] L. G. Villanueva *et al.*, "Surpassing fundamental limits of oscillators using nonlinear resonators," *Phys. Rev. Lett.*, vol. 110, 2013, Art. no. 177208.

[37] J. Juillard, G. Arndt, and E. Colinet, "Enhancing the frequency stability of a NEMS oscillator with electrostatic and mechanical nonlinearities," *Procedia Chem.*, vol. 1, pp. 1415–1418, 2009.

[38] J. Juillard, G. Arndt, and E. Colinet, "Modeling of micromachined beams subject to nonlinear restoring or damping forces," *IEEE J. Microelectromech. Syst.*, vol. 20, pp. 165–177, 2010.

Jérôme Juillard (M'07) was born in Nice, France, in 1973. He graduated from Ecole Centrale de Paris (ECP), France, in 1995, with a specialization in electronics and signal processing. After a master's degree in acoustics and signal processing at IRCAM, he received his Ph.D. degree in physical acoustics from University Paris 7, France, in 1999. In 2000, he joined Supélec (now CentraleSupélec), where he is now a full Professor. His research is conducted in the Electronic Systems team of the GEEPs laboratory. His interests are nonlinear oscillators, as well as M/NEMS modelling, design, characterization, and test.

Pierre Prache was born in 1989. He graduated from ENS Cachan in 2014, with a major in applied physics. He received one M.S. degree in high education training from ENS Cachan, France, in 2013, and a M.S. degree in nanosciences from Université Paris-Sud, France, in 2014. He is currently a Ph.D. student at Université Paris-Sud, under the joint supervision of J. Juillard and N. Barniol. His research focusses on the design and test of monolithic CMOS-MEMS injection-locked oscillators.

Núria Barniol (M'99) received her B.S. and Ph.D. degrees from the Universitat Autonoma de Barcelona (UAB), Spain, in 1987 and 1992, respectively. She has been a Professor at the UAB in the Electronics Engineering Department since 1993, becoming a full Professor in 2004. Nowadays, she is the leader of the Electronic Circuits and Systems research group of UAB. Her research interests focus upon the combination and integration of new MEMS and NEMS devices into CMOS technologies, looking for system on chips solutions in the field of RF signal processing and sensor applications.

Annex 2: Code for the characteristics of a MILO

This code is based on [130]. It aims to obtain the differential mode characteristics of a MILO (S_φ, S_ω, ε_{lock} and comparison with [121], but also the motion amplitude of both resonators versus ε) given its phase delays and quality factors.

```
function simu_DO_simple(phase_ampli,phase_mixer,Q,Qe,Reduction,Stable_only)
%Gives the characteristics of the MILO given quality factors of Q and Qe,
resonance frequencies of 1 et 1+e, the phases in the amplifier is
phase_ampli (in degrees) and the phase in the mixer is phase_mixer (in
degree)
%simu_DO_simple(71,26,90,110,0.5,'y')was used in section 3.4.1
%simu_DO_simple(65,28,120,140,0.5,'y')was used in section 3.4.2.
%For other MILOs architecture, the coupling gains can be changed (g0e, Gee,
Ge0 and G00 in the first lines)

Nfig=ceil(rand*10000);
G00=1;
g0e=1;
ge0=1;
Gee=1;
Psi00=pi-pi/180*(phase_ampli-phase_mixer);
Psi0e=pi-pi/180*(phase_ampli-phase_mixer);
Psie0=-pi/180*(phase_ampli-phase_mixer);
Psiee=pi-pi/180*(phase_ampli-phase_mixer);
[Phi0,Nsol]=find_PF(G00,g0e,ge0,Gee,Psi00,Psi0e,Psie0,Psiee,Q,Qe);

[Phi0,Nsol]=find_PF(G00,g0e,ge0,Gee,Psi00,Psi0e,Psie0,Psiee,Q,Qe);

if Nsol==0,
    disp('Pas de solution faisable (A,Ae>0) pour cette architecture')
else
    disp([num2str(Nsol),' solutions faisables (A,Ae>0) pour cette
architecture en : '])
    for k_sol=1:Nsol

[~,~,~,~,~,~,Poles,~,~,~]=simu_DO_lin_1sol(Phi0(k_sol),G00,g0e,ge0,Gee,Psi0
0,Psi0e,Psie0,Psiee,Q,Qe);
        if real(Poles)>0
            disp(['Phi = ',num2str(Phi0(k_sol)),'. Cette solution est
instable.'])
        else
            disp(['Phi = ',num2str(Phi0(k_sol)),'. Cette solution est
stable.'])
            Phi=linspace(-1.5,1.5,1001)*Reduction+Phi0(k_sol);

[Phi,e,V,Ve,A,Ae,Poles,~,Q_p,Adler]=simu_DO_lin_1sol(Phi,G00,g0e,ge0,Gee,Ps
i00,Psi0e,Psie0,Psiee,Q,Qe);

            if strcmp(Stable_only,'y')
                I=find(real(Poles)>0);

Phi(I)=NaN;V(I)=NaN;Ve(I)=NaN;A(I)=NaN;Ae(I)=NaN;Poles(I)=NaN;Q_p(I)=NaN;%A
dler(I)=NaN;
```

```
            end

            I=find(Ae<0 | A<0);

Phi(I)=NaN;V(I)=NaN;Ve(I)=NaN;A(I)=NaN;Ae(I)=NaN;Poles(I)=NaN;Q_p(I)=NaN;

            figure(Nfig)
            subplot(3,2,1)
            plot(e,Phi*180/pi,'.');hold all; axis tight
            title('\phi (°) versus \epsilon')
            grid on
            subplot(3,2,3)
            plot(e,(gradient(Phi,e)),'.');hold all; axis tight
            title('Sensibilite (rad/\epsilon) versus \epsilon')
            grid on
            subplot(3,2,5)
            plot(e,A,'+',e,Ae,'o');hold all; axis tight
            legend('A','A_e')
            title('Amplitude versus \epsilon')
            grid on
            subplot(3,2,2)
            plot(e,(V./A),'.');hold all; axis tight
            title('Pulsation (rad/s) versus \epsilon')
            grid on
            subplot(3,2,4)
            plot(e,real(Poles),'.');hold all
            plot(e,Adler,'or'); axis tight;
h=get(gca,'YLim');set(gca,'YLim',[h(1) 0])
            title('Marge stabilite versus \epsilon (Adler en rouge)')
            grid on
            subplot(3,2,6)
            plot(e,Q_p,'.');hold all; axis tight; set(gca,'YLim',[0 5])
            title('Facteur de qualité versus \epsilon')
            grid on
            figure()
            plot((V./A)/mean(V./A)-1,Phi/mean(Phi)-1)

        end
    end
end

function [Phi0,Nsol]=find_PF(G00,g0e,ge0,Gee,Psi00,Psi0e,Psie0,Psiee,Q,Qe)

%Definition of the transfer function of the mixer
fsin=@(Phi) G00*cos(Psi00)+ge0*cos(Psie0+Phi);
fsine=@(Phi) Gee*cos(Psiee)+g0e*cos(Psi0e-Phi);
fcos=@(Phi) G00*sin(Psi00)+ge0*sin(Psie0+Phi);
fcose=@(Phi) Gee*sin(Psiee)+g0e*sin(Psi0e-Phi);

%Definition of the mismatch
tocancel=@(Phi) (fsine(Phi).*fcos(Phi)./Qe-fsin(Phi).*fcose(Phi)./Q);

%Definition of the steady-state amplitudes (hypothesis omega close to 1)
A=@(Phi) Q*fcos(Phi)./(-
fsin(Phi)/2./(Q*fcos(Phi))+sqrt(1+(fsin(Phi)/2./(Q*fcos(Phi))).^2));
```

```
Ae=@(Phi) Qe*fcose(Phi)./(-
fsine(Phi)/2./(Qe*fcose(Phi))+sqrt(1+(fsine(Phi)/2./(Qe*fcose(Phi))).^2));

Phi_vec=linspace(-pi+0.01,pi+0.01,25);
J=find(diff((tocancel(Phi_vec))>0));
Phi0=[];Nsol=0;
for k=1:length(J)
    Phi_test=fzero(@(Phi) tocancel(Phi),[Phi_vec(J(k)) Phi_vec(J(k)+1)]);
    if A(Phi_test)>0.01 && Ae(Phi_test)>0.01
        Nsol=Nsol+1;Phi0=[Phi0 Phi_test];
    end
end

function
[Phi,e,V,Ve,A,Ae,Poles,Omega_p,Q_p,Adler]=simu_DO_lin_1sol(Phi,G00,g0e,ge0,
Gee,Psi00,Psi0e,Psie0,Psiee,Q,Qe)

%Definition of the mixer's transfer function
fsin=G00*cos(Psi00)+ge0*cos(Psie0+Phi);
fsine=Gee*cos(Psiee)+g0e*cos(Psi0e-Phi);
fcos=G00*sin(Psi00)+ge0*sin(Psie0+Phi);
fcose=Gee*sin(Psiee)+g0e*sin(Psi0e-Phi);
%Definition of the derivative of the mixer's transfer function
dfsin=-ge0*sin(Psie0+Phi);
dfsine=g0e*sin(Psi0e-Phi);
dfcos=ge0*cos(Psie0+Phi);
dfcose=-g0e*cos(Psi0e-Phi);

%Definition of the mismatch
e=(fsine./Qe./fcose-
fsin./Q./fcos)./(sqrt(1+(fsin/2/Q./fcos).^2)+fsin/2/Q./fcos);

%Definition of the steady-state velocity
V=Q*fcos;
Ve=Qe*fcose;
% Definition of the steady-state amplitudes (hypothesis omega close to 1)
A=V./(-fsin/2./V+sqrt(1+(fsin/2./V).^2));
Ae=Ve./(-fsine/2./Ve+sqrt(1+e+(fsine/2./Ve).^2));


Poles=zeros(size(Phi));
Omega_p=zeros(size(Phi));
Q_p=zeros(size(Phi));

for k=1:length(Phi)
    Jacob=[-1/2/Qe, 0, 1/2*dfcose(k);...
        0, -1/2/Q, 1/2*dfcos(k);...
        fsine(k)/2/Ve(k)^2*(1-
fsine(k)/2/Ve(k)/sqrt(1+e(k)+(fsine(k)/2/Ve(k))^2)),...
        -fsin(k)/2/V(k)^2*(1-fsin(k)/2/V(k)/sqrt(1+(fsin(k)/2/V(k))^2)),...
        -dfsine(k)/2/Ve(k)*(1-
fsine(k)/2/Ve(k)/sqrt(1+e(k)+(fsine(k)/2/Ve(k))^2))+dfsin(k)/2/V(k)*(1-
fsin(k)/2/V(k)/sqrt(1+(fsin(k)/2/V(k))^2))];
    E=eigs(Jacob);
    [Rmax,I]=max(real(E));
    Poles(k)=E(I);
```

```
    Omega_p(k)=abs(Poles(k));
    if Rmax<0 && Ae(k)>0 && A(k)>0 && Ve(k)>0 && V(k)>0
        if imag(Poles(k))==0
            Q_p(k)=0;
        else
            Q_p(k)=-1/2/(Rmax/Omega_p(k));
        end
    else
        Q_p(k)=NaN;
    end
end
%Adler stability margin
Adler=-1/2*((dfsine.*fcose-fsine.*dfcose)./Qe./fcose.^2-(dfsin.*fcos-
fsin.*dfcos)./Q./fcos.^2);
```

Annex 3: Periodogram and Allan deviation

This algorithm aims to plot the power spectral density of the phase difference and of the period. Its input is the waveform of V_{in1} or V_{in2} (i.e. nominally digital signals with duty cycles around 25 %).

```
m=ch3;%ch3 is the waveform of Vin1 or Vin2
m=filter(ones(50,1),50,m);%filtering to have clean transition (50 is an
arbitrary value)
seuil_montant=0.2;%threshold values (positive and negative transitions)
seuil_descendant=0.4;
Foscillo=2.5e9; ;%Scope's sampling rate
tau_vec=logspace(log10(6e-7),log10(4e-4),100);

I=find(m(1:end-1)<seuil_montant & m(2:end)>seuil_montant);%indexes of
positive transitions
J=find(m(1:end-1)>seuil_descendant & m(2:end)<seuil_descendant);%indexes of
negative transitions
Ifin=I+(seuil_montant-m(I))./(m(I+1)-m(I));%linear interpolation cleaning
Jfin=J+(seuil_descendant-m(J))./(m(J+1)-m(J));%linear interpolation
cleaning

Ifin(1)=[];
Jfin(1)=[];

if Ifin(1)>Jfin(1)
    Jfin(1)=[];
end

if length(Jfin)<length(Ifin)
Ifin=Ifin(1:length(Jfin));
elseif length(Jfin)>length(Ifin);
Jfin=Jfin(1:length(Ifin));
end

DPHASE_up=((Jfin(2:end))-(Ifin(2:end)))./diff((Ifin))/0.5*pi;%positive duty
cycle extraction
DPHASE_down=((Jfin(1:end-1))-(Ifin(2:end)))./diff((Ifin))/0.5*pi;%negative
duty cycle extraction
PHASE=cumsum((-diff(Ifin)+mean(diff(Ifin)))/mean(diff(Ifin)))*2*pi;%phase
noise extraction

OSR=mean(diff((Ifin)));
Fs=Foscillo/OSR;
freq=1/mean(diff(Ifin))*Foscillo;
figure
%PSD extraction with the periodogram routine
[p_POSDP,f_POSDP]=periodogram(1-(DPHASE_up/mean(DPHASE_up)),[],[],Fs);
[p_NEGDP,f_NEGDP]=periodogram(1-(DPHASE_down/mean(DPHASE_down)),[],[],Fs);
[p_T,f_T]=periodogram(1-diff((Ifin))/mean(diff((Ifin))),[],[],Fs);
POSDCmean=mean(DPHASE_up)/2/pi;
NEGDCmean=mean(DPHASE_down)/2/pi;
POSDP_relstd=std(1-(DPHASE_up/mean(DPHASE_up)));
NEGDP_relstd=std(1-(DPHASE_down/mean(DPHASE_down)));
```

```
Tmean=1/Fs;
T_relstd=std(1-diff((Ifin))/mean(diff((Ifin))));

%plotting
semilogx(f_POSDP,10*log10(p_POSDP),f_POSDP,10*log10(p_POSDP)-
20*log10(8*100/pi),'b',f_T,10*log10(p_T),'r',f_T,linspace(-150,-
150,length(f_T)));
legend('Pos. Rel. Ph. PSD','Rel. Period PSD')
t=title({['Pos. DC = ',num2str(POSDCmean*100),'% , Std. Rel. Pos. Ph. = ',
num2str(POSDP_relstd)];['Mean Period = ',num2str(Tmean*1e9),' ns ',', Std.
Rel. Period = ',num2str(T_relstd)]});
ylabel('Power density (dB/Hz)')
xlabel('Frequency (Hz)')
set(gca,'FontName','Times New Roman','FontSize',12,'FontWeight','normal');
set(t,'FontName','Times New Roman','FontSize',12,'FontWeight','normal');

%Allan variance then deviation extraction and plotting
AVAR_POSDP_th=zeros(1,length(tau_vec));
AVAR_T_th=zeros(1,length(tau_vec));
w_POSDP=2*pi*f_POSDP(2:end);
w_T=2*pi*f_T(2:end);
for p=1:length(tau_vec),
    tau=tau_vec(p);

AVAR_POSDP_th(p)=w_POSDP(1)/pi*sum(p_POSDP(2:end).*sin(w_POSDP*tau/2).^4./(
w_POSDP*tau/2).^2);

AVAR_T_th(p)=w_T(1)/pi*sum(p_T(2:end).*sin(w_T*tau/2).^4./(w_T*tau/2).^2);
end
ADEV_POSDP=sqrt(AVAR_POSDP_th);
ADEV_T=sqrt(AVAR_T_th);
semilogx(tau_vec,10*log10(ADEV_POSDP)-
10*log10(8*99/pi),'b',tau_vec,10*log10(ADEV_T),'r',tau_vec,10*log10(ADEV_PO
SDP))
figure
```

References

[1] A. Devices, "ADXL337 Small, Low Power, 3-Axis ±3 g (Datasheet)," 2010. [Online]. Available: http://www.analog.com/media/en/technical-documentation/data-sheets/ADXL337.pdf.

[2] A. Devices, "ADXRS290 Ultralow Noise, Dual-Axis MEMS Gyroscope (Datasheet)," 2014. [Online]. Available: http://www.analog.com/media/en/technical-documentation/data-sheets/ADXRS290.pdf.

[3] S. Microelectronics, "MEMS nano pressure sensor: 260-1260 hPa absolute digital output barometer (Datasheet)," 2015. [Online]. Available: http://www.st.com/.

[4] OMRON, "D6T MEMS Thermal Sensors (Datasheet)," [Online]. Available: https://www.omron.com/ecb/products/pdf/en-d6t.pdf.

[5] G. W. Platzman, "Tidal Evidence for Ocean Normal Modes," *Tidal Hydrodynamics,* p. 883, 1991.

[6] C. D. Murray and S. F. Dermott, Solar System Dynamics, Cambridge: University Press, 1999.

[7] W. Hollingworth et al., "The Diagnostic and Therapeutic Impact of MRI: an Observational Multi-centre Study," *Clinical Radiology,* vol. 55, no. 11, pp. 825-831, 2000.

[8] A. E. Siegman, "Laser beams and resonators: the 1960s," *IEEE Journal of Selected Topics in Quantum Electronics,* vol. 6, no. 6, pp. 1380-1388, 2000.

[9] K. Billah and R. Scanlan, "Resonance, Tacoma Narrows Bridge Failure, and Undergraduate Physics Textbooks," *Americal Journal of Physics,* vol. 59, pp. 118-124, 1991.

[10] H. M. Smith and G. B. Wellgate, "Quartz crystal clocks," *Vistas in Astronomy,* vol. 1, pp. 438-447, 1955.

[11] H. Nyquist, "Thermal Agitation of Electric Charge in Conductors," *Phys. Rev.,* vol. 32, no. 1, pp. 110-113, 1928.

[12] R. Kubo, "The fluctation-dissipation theorem," *Reports on Progress in Physics,* vol. 29, p. 255, 1966.

[13] E. P. Quevy and D. H. Bernstein, "Method for temperature compensation in MEMS resonators with isolated regions of distinct material". Patent US7639104 B1, dec. 29 2009.

[14] A. A. Seshia et al., "A vacuum packaged surface micromachined resonant accelerometer," *Journal of Microelectromechanical Systems,* vol. 11, no. 6, pp. 784-793, 2002.

[15] A. Hajjam, A. Rahafrooz, J. C. Wilson and S. Pourkamali, "Thermally actuated MEMS resonant sensors for mass measurement of micro/nanoscale aerosol particles," *2009 IEEE Sensors,* pp. 707-710, 2009.

[16] X. Du, L. Wang, A. Li, L. Wang and D. Sun, "High Accuracy Resonant Pressure Sensor With Balanced-Mass DETF Resonator and Twinborn Diaphragms," *Journal of Microelectromechanical Systems,* vol. 26, pp. 235-245, 2017.

[17] E. Rubiola, "On the measurement of frequency and of its sample variance with high-resolution counters," *Review of Scientific Instruments,* vol. 76, no. 5, 2005.

[18] J. H. Huijsing, "Signal Conditioning On The Sensor Chip," *Sensors and Actuators,* vol. 10, pp. 219-237, 1986.

[19] R. T. Howe and R. S. Muller, "Resonant-microbridge vapor sensor," *IEEE Transactions on Electron Devices,* vol. 33, pp. 499-506, 1986.

[20] G. Piazza, P. J. Stephanou and A. P. Pisano, "Piezoelectric Aluminium Nitride Vibrating Contour-Mode MEMS Resonators," *Journal of Microelectromechanical Systems,* vol. 15, pp. 1406-1418, 2006.

[21] A. Abbasalipour, M. Mahdavi, V. Kumar, S. Pourkamali, S. Darydel and M. Minary, "Nano-precision micromachined frequency output profilometer," *2016 IEEE SENSORS,* pp. 1-3, 2016.

[22] J. W. Judy and R. S. Muller, "Magnetic microactuation of torsional polysilicon structures," *Sensors and Actuators A: Physical,* vol. 53, pp. 392-397, 1996.

[23] R. Abdolvand, B. Bahreyni, J. E. Y. Lee and F. Nabki, " Micromachined Resonators: A Review," *Micromachines 2016,* vol. 7, p. 160, 2016.

[24] L. Khine, M. Palaniapan and W. K. Wong, "6Mhz Bulk-Mode Resonator with Q Values Exceeding One Million," *TRANSDUCERS 2007 - 2007 International Solid-State Sensors, Actuators and Microsystems Conference,* pp. 2445-2448, 2007.

[25] S. B. Horowitz, "A low frequency MEMS vibration sensor for low power missile health monitoring," *2013 IEEE Aerospace Conference,* pp. 1-9, 2013.

[26] J. Wang, Z. Ren and C.-T. C. Nguyen, "Self-aligned 1.14GHz vibrating radial-mode disk resonators," *Dig. of Tech Papers, the 12th Int. Conf. on Solid-state Sensors & Actuators (Transducers '03),* pp. 947-950, 2003.

[27] H. C. Nathanson, W. E. Newell, R. A. Wickstrom and J. R. Davis Jr., "The resonant gate transistor," *IEEE Transactions on Electron Devices,* vol. 14, pp. 117-133, 1967.

[28] K. E. Peterson, "Silicon as a mechanical material," *Proceedings of the IEEE,* vol. 70, no. 5, pp. 420-457, 1982.

[29] W. C. Tang, T.-C. H. Nguyen and R. T. Howe, "Laterally Driven Polysilicon Resonant Microdevices," *Sensors and Actuators,* vol. 20, pp. 25-32, 1989.

[30] G. Stemme, "Resonant silicon sensors," *Journal of Micromechanics and Microengineering,* vol. 1, p. 113, 1991.

[31] P. Hauptmann, "Resonant Sensors and Applications," *Sensors and Actuators A,* pp. 371-377, 1991.

[32] G. M. Rebeiz, RF MEMS: Theory, Design, and Technology, Wiley, 2003.

[33] O. Brand and I. Dufour, Resonant MEMS: Fundamentals, Implementation, and Application, Wiley, 2015.

[34] N. Arumugam et al., "2-die wafer-level chip scale packaging enables the smallest TCXO for mobile and wearable applications," *2015 IEEE 65th Electronic Components and Technology Conference (ECTC),* pp. 1338-1342, 2015.

[35] S. Galliou et al., "Quality Factor Measurements of Various Types of Quartz Crystal Resonators Operating Near 4 K," *IEEE Transactions on Ultrasonics, Ferroelectrics, and Frequency Control,* vol. 63, no. 7, pp. 975-980, 2016.

[36] E. Colinet, P. Andreucci, L. Duraffourg and S. Hentz, "Measuring system having electromechanical resonators method for manufacturing system and method for reading at least two electromechanical resonators". France Patent US 2014/0013848 A1, 16 Jan 2014.

[37] A. Hajjam, J. C. Wilson and S. Pourkamali, "Individual Air-Borne Particle Mass Measurement Using High-Frequency Micromechanical Resonators," *IEEE Sensors Journal,* vol. 11, no. 11, pp. 2883-2890, 2011.

[38] K. L. Ekinci, X. M. H. Huang and M. L. Roukes, "Ultrasensitive nanoelectromechanical mass detection," *Applied Physics Letters,* vol. 84, p. 4469, 2004.

[39] J. Mandle, O. Lefort and A. Migeon, "A new micromachined silicon high-accuracy pressure sensor," *Sensors and Actuators A,* vol. 46, pp. 129-132, 1995.

[40] R. G. Azevedo et al., "A SiC MEMS Resonant Strain Sensor for Harsh Environment Applications," *IEEE Sensors Journal,* vol. 7, no. 4, pp. 568-576, 2007.

[41] C. Akar and A. M. Shkel, "Experimental evaluation and comparative analysis of commercial variable-capacitance MEMS accelerometers," *Journal of Micromechanics and Microengineering,* vol. 13, no. 5, 2003.

[42] K. E. Wojciechowski, B. E. Boser and A. P. Pisano, "A MEMS resonant strain sensor with 33 nano-strain resolution in a 10 kHz bandwidth," *IEEE Sensors,* pp. 4-7, 2005.

[43] M. Li, V. T. Rouf, M. J. Thompson and D. A. Horsley, "Three-Axis Lorentz-Force Magnetic Sensor for Electronic Compass Applications," *Journal of Microelectromechanical Systems,* vol. 21, pp. 1002-1010, 2012.

[44] R. Sunier, T. Vancura, Y. Li, K. U. Kirstein, H. Baltes and O. Brand, "Resonant Magnetic Field Sensor With Frequency Output," *Journal of Microelectromechanical Systems,* vol. 15, no. 5, pp. 1098-1107, 2006.

[45] N. Dumas, L. Latorre and P. Nouet, "Development of a low-cost piezoresistive compass on CMOS," *Sensors and Actuators A: Physical,* vol. 14, pp. 302-311, 2006.

[46] C. Comi, A. Corigliano, A. Ghisi and S. Zerbini, "A resonant micro accelerometer based on electrostatic stiffness variation," *Meccanica,* vol. 48, pp. 1893-1900, 2013.

[47] X. Zou and A. A. Seshia, “A high-resolution resonant MEMS accelerometer,” *2015 Transducers - 2015 18th International Conference on Solid-State Sensors, Actuators and Microsystems (TRANSDUCERS),* pp. 1247-1250, 2015.

[48] T. L. Naing, “2.97-GHz CVD diamond ring resonator with Q >40,000,” *2012 IEEE International Frequency Control Symposium Proceedings,* pp. 1-6, 2012.

[49] M. T. Amin, “On the selection of passive elements for low phase noise LC tank VCO in 65 nm process,” *2016 3rd International Conference on Electrical Engineering and Information Communication Technology (ICEEICT),* pp. 1-5, 2016.

[50] L. X. Chuo et al., “A 915MHz asymmetric radio using Q-enhanced amplifier for a fully integrated 3×3×3mm3 wireless sensor node with 20m non-line-of-sight communication,” *2017 IEEE International Solid-State Circuits Conference (ISSCC),* pp. 132-133, 2017.

[51] C. T. C. Nguyen, “MEMS-based RF channel selection for true software-defined cognitive radio and low-power sensor communications,” *IEEE Communications Magazine,* vol. 51, pp. 110-119, 2013.

[52] P. D. Mitcheson, T. C. Green, E. M. Yeatman and A. S. Holmes, “Architectures for vibration-driven micropower generators,” *Journal of Mictroelectromechanical Systems,* vol. 13, pp. 429-440, 2004.

[53] D. Shen et al., “The design, fabrication and evaluation of a MEMS PZT cantilever with an integrated Si proof mass for vibration energy harvesting,” *Journal of Micromechanics and Microengineering,* vol. 18, p. 055017, 2008.

[54] R. Ramesham and R. Ghaffarian, “Challenges in interconnection and packaging of microelectromechanical systems (MEMS),” *2000 Proceedings. 50th Electronic Components and Technology Conference,* pp. 666-675, 2000.

[55] K. F. Harsh, B. Su, W. Zhang, V. M. Bright and Y. C. Lee, “The realization and design considerations of a flip-chip integrated MEMS tunable capacitor,” *Sensors and Actuators A: Physical,* vol. 80, no. 2, pp. 108-118, 2000.

[56] Y.-R. Jeng, S. M. Chiu, P. Y. Huang and S. H. Shyu, “Investigation of Thermosonic Wire Bonding Resistance of Gold Wire Onto Copper Pad,” *IEEE Transactions on electronics packaging manufacturing,* vol. 33, pp. 65-71, 2010.

[57] G. Arndt, System architecture and circuit design for micro and nanoresonators-based mass sensing arrays, Orsay, 2011.

[58] O. Brand and G. K. Fedder, CMOS-MEMS, Wiley, 2008.

[59] G. K. Fedder, R. T. Howe, T.-J. K. Liu and E. P. Quevy, “Technologies for Cofabricating MEMS and Electronics,” *Proceedings of the IEEE,* vol. 96, pp. 302-322, 2008.

[60] A. Uranga, J. Verd and N. Barniol, “CMOS–MEMS resonators: From devices to applications,” *Microelectronic Engineering,* vol. 132, pp. 58-73, 2015.

[61] J. L. Lopez et al., "A CMOS-MEMS RF-Tunable Bandpass Filter Basd on Two High-Q 22-MHz Polysilicon Clamped-Clamped Beam Resonators," *IEEE Electron Device Letters,* vol. 30, no. 7, pp. 718-720, 2009.

[62] J. Verd et al., "CMOS Cantilever-based Oscillator for Attogram Mass Sensing," *2007 IEEE International Symposium on Circuits and Systems,* pp. 3319-3322, 2007.

[63] M. Riverola et al., "CMOS-NEM relay based on tungsten VIA layer," *IEEE Sensors 2014 Proceedings,* pp. 162-165, 2014.

[64] AMS, "0.35um CMOS Technology Selection Guide (C35)," 2017. [Online]. Available: http://ams.com/eng/Products/Full-Service-Foundry/Process-Technology/CMOS/0.35-m-CMOS-Technology-Selection-Guide.

[65] J. Verd Martorell, Monolithic CMOS-MEMS Resonant Beams for Ultrasensitive Mass Detection, Barcelona, 2008.

[66] M. Riverola, G. Sobreviela, A. Uranga and N. Barniol, "Intrinsic feedthrough current cancellation in a seesaw CMOS-MEMS resonator for integrated oscillators," *2016 IEEE International Frequency Control Symposium (IFCS),* pp. 1-4, 2016.

[67] O. A. Bauchau and J. I. Craig, "Euler-Bernoulli beam theory," in *Structural Analysis*, Springer Netherlands, 2009, pp. 173-221.

[68] A. H. Nayfeh and D. T. Mook, Nonlinear oscillations, Blacksburg, Virginia: Wiley Classics Library Edition, 1995.

[69] J. Juillard, "Analysis of resonant pull-in of micro-electromechanical oscillators," *Journal of Sound and Vibration,* vol. 350, pp. 123-139, 2015.

[70] J. Juillard, G. Arndt and E. Colinet, "Modeling of Micromachined Beams Subject to Nonlinear Restoring or Damping Forces," *Journal of Microelectromechanical Systems,* vol. 20, no. 1, pp. 165-177, 2011.

[71] A. H. Nayfeh, M. I. Younis and E. M. Abdel-Rahman, "Reduced-Order Models for MEMS Applications," *Nonlinear Dynamics,* vol. 41, pp. 211-236, 2005.

[72] V. Kaajakari, Practical Mems: Design of Microsystems, Accelerometers, Gyroscopes, RF Mems, Optical Mems, and Microfluidic Systems, Small Gear Publishing, 2009.

[73] R. Lifshitz and M. C. Cross, Nonlinear Dynamics of Nanomechanical and Micromechanical Resonators, Wiley: Heinz Georg Schuster, 2008.

[74] M. Imboden and P. Mohanty, "Dissipation in nanoelectromechanical systems," *Physics Reports,* vol. 534, pp. 89-146, 2013.

[75] G. Sobreviela, CMOS-MEMS para aplicaciones de RF: Osciladores, Barcelona, 2016.

[76] M. Bao and H. Yang, "Squeeze film air damping in MEMS," *Sensors and Actuators A: Physical,* vol. 136, pp. 3-27, 2007.

[77] G. K. Ho, K. Sundaresan, S. Pourkamali and F. Ayazi, "Temperature compensated IBER reference oscillators," *19th IEEE International Conference on Micro ElectroMechanical Systems,* pp. 910-913, 2006.

[78] W.-M. Zhang, H. Yan, Z.-K. Peng and G. Meng, "Electrostatic pull-in instability in MEMS/NEMS: a review," *Sensors and Actuators A: Physical,* vol. 214, pp. 187-218, 2014.

[79] M.-H. Bao, Micro Mechanical Transducers, Volume 8, Elsevier, 2000.

[80] A. K. Pandey, K. P. Venkatesh and R. S. Pratap, "Effect of metal coating and residual stress on the resonant frequency of MEMS resonators," *Sadhana,* vol. 34, p. 651, 2009.

[81] L. M. Zhang, D. Uttamchandani, B. Culshaw and P. Dobson, "Measurement of Young's modulus and internal stress in silicon microresonators using a resonant frequency technique," *Measurement Science and Technology,* vol. 1, pp. 1343-1346, 1990.

[82] G. K. Fedder et al., "Laminated high-aspect-ratio microstructures in a conventional CMOS process," *Sensors and Actuators A: Physical,* vol. 57, pp. 103-110, 1996.

[83] W. Fang and J. A. Wickert, "Determining mean and gradient residual stresses in thin films using micromachined cantilevers," *Journal of Micromechanics and Microengineering,* vol. 6, pp. 301-309, 1996.

[84] "Coefficients of Linear Thermal Expansion," [Online]. Available: http://www.engineeringtoolbox.com/linear-expansion-coefficients-d_95.html.

[85] R. Lowrie and A. M. Gonas, "Dynamic Elastic Properties of Polycrystalline Tungsten, 24°–1800°C," *Journal of Applied Physics,* vol. 36, p. 2189, 2004.

[86] G. S. Pisarenko, V. A. Borisenki and Y. A. Kashtalyan, "The effect of temperature on the hardness and modulus of elasticity of tungsten and molybdenum (20–2700)," *Soviet Powder Metallurgy and Metal Ceramics,* vol. 1, pp. 371-374, 1964.

[87] S. Sung, J. G. Lee, B. Lee and T. Kang, "Design and performance test of an oscillation loop for a MEMS resonant accelerometer," *J. Micromech. Microeng.,* vol. 13, pp. 246-253, 2003.

[88] C. S. Lam, "A review of the recent development of MEMS and crystal oscillators and their impacts on the frequency control products industry," *2008 IEEE Ultrasonics Symposium,* pp. 694-704, 2008.

[89] X. Sun, R. Horowitz and K. Komvopoulos, "Stability and resolution analysis of a phase-locked loop natural frequency tracking system for MEMS fatigue testing," *ASME J. Dyn. Syst. Meas. Contr,* pp. 599-605, 2002.

[90] S. L. Lee and C. T. C. Nguyen, "Influence of automatic level control on micromechanical resonator oscillator phase noise," *IEEE International Frequency Control Symposium and PDA Exhibition Jointly with the 17th European Frequency and Time Forum, 2003. Proceedings of the 2003,* pp. 341-349, 2003.

[91] A. Brenes, J. Juillard, L. Bourgois and F. Vinci Dos Santos, "Influence of the Driving Waveform on the Open-Loop Frequency Response of MEMS Resonators With Nonlinear Actuation Schemes," *Journal of Microelectromechanical Systems,* vol. 25, pp. 812-820, 2016.

[92] K. E. Wojciechowski, B. E. Boser and A. P. Pisano, "A MEMS resonant strain sensor operated in air," *17th IEEE International Conference on Micro Electro Mechanical Systems. Maastricht MEMS 2004 Technical Digest,* pp. 841-845, 2004.

[93] C. T. C. Nguyen, "MEMS technology for timing and frequency control," *IEEE Transactions on Ultrasonics, Ferroelectrics, and Frequency Control,* pp. 251-270, 2007.

[94] G. C. Wei and M. S. C. Lu, "A CMOS MEMS capacitive resonant sensor array utilizing a PLL-based oscillator loop," *2013 Transducers & Eurosensors XXVII: The 17th International Conference on Solid-State Sensors, Actuators and Microsystems,* pp. 82-85, 2013.

[95] O. Mancini, "Frequency Electronics, Inc.," 18 March 2004. [Online]. Available: https://www.ieee.li/pdf/viewgraphs/precision_frequency_generation.pdf.

[96] TXC Corporation, "Technical Terminology: Quartz Frequency-Temperature Characteristics," [Online]. Available: http://txccrystal.com/term.html.

[97] K. A. A. Makinwa, "Smart temperature sensors in standard CMOS," *Procedia Engineering,* vol. 5, pp. 930-939, 2010.

[98] H. Lee, A. Partridge and F. Assaderaghi, "Low jitter and temperature stable MEMS oscillators," *2012 IEEE International Frequency Control Symposium Proceedings,* pp. 1-5, 2012.

[99] B. Kim et al., "Temperature Dependence of Quality Factor in MEMS Resonators," *19th IEEE International Conference on Micro Electro Mechanical Systems,* pp. 590-593, 2006.

[100] M. A. Hopcroft, Temperature-stabilized silicon resonators for frequency references, 2007.

[101] M. H. Roshan et al., "Dual-MEMS-resonator temperature-to-digital converter with 40 K resolution and FOM of 0.12pJK2," *2016 IEEE International Solid-State Circuits Conference (ISSCC),* pp. 200-201, 2016.

[102] J. C. Salvia et al., "Real-Time Temperature Compensation of MEMS Oscillators Using an Integrated Micro-Oven and a Phase-Locked Loop," *Journal of Microelectromechanical Systems,* vol. 19, no. 1, pp. 192-201, 2010.

[103] Y. Chen et al., "Ovenized dual-mode clock (ODMC) based on highly doped single crystal silicon resonators," *2016 IEEE 29th International Conference on Micro Electro Mechanical Systems (MEMS),* pp. 91-94, 2016.

[104] Y. Chen, D. D. Shin, I. B. Flader and T. W. Kenny, "Tri-mode operation of highly doped silicon resonators for temperature compensated timing references," *IEEE 30th International Conference on Micro Electro Mechanical Systems (MEMS),* pp. 1158-1161, 2017.

[105] SiTime, "Elite DualMEMS Architecture," [Online]. Available: https://www.sitime.com/technology/mems-oscillators/architecture/elite-dualmems.

[106] A. A. Trusov, S. A. Zotov, B. R. Simon and A. M. Shkel, "Silicon accelerometer with differential Frequency Modulation and continuous self-calibration," *2013 IEEE 26th International Conference on Micro Electro Mechanical Systems (MEMS),* pp. 29-32, 2013.

[107] B.-L. Lee et al., "Vacuum packaged differential resonant accelerometer using gap sensitive electrostatic stiffness changing effect," *Proceedings IEEE Thirteenth Annual International Conference on Micro Electro Mechanical Systems,* pp. 352-357, 2000.

[108] C. Cobianu and B. Serban, "All-differential resonant nanosensors apparatus and method". US Patent US 2011/0113856 A1, 19 May 2011.

[109] R. G. Azavedo, W. Huang, O. M. O'Reilly and A. P. Pisano, "Dual-mode temperature compensation for a comb-driven MEMS resonant strain gauge," *Sensors and Actuators A: Physical,* vol. 144, pp. 374-380, 2008.

[110] J. R. Vig, "Temperature-insensitive dual-mode resonant sensors - a review," *IEEE Sensors Journal,* vol. 1, pp. 62-68, 2001.

[111] M. Spletzer, A. Raman, A. Q. Wu and X. Xu, "Ultrasensitive mass sensing using mode localization in coupled microcantilevers," *Applied Physics Letters,* vol. 88, p. 254102, 2006.

[112] P. Thiruvenkatanathan, J. Yan and A. A. Seshia, "Differential Amplification of Structural Perturbations in weakly Coupled MEMS Resonators," *IEEE Transactions on Ultrasonics, Ferroelectrics and Frequency Control,* vol. 57, no. 3, pp. 690-697, 2010.

[113] C. Zhao, G. S. Wood, J. Xie, H. Chang, S. H. Pu and M. Kraft, "A Three Degree-of-Freedom Weakly Coupled Resonator Sensor With Enhanced Stiffness Sensitivity," *Journal of Microelectromechanical Systems,* vol. 25, no. 1, pp. 38-51, 2016.

[114] C. Zhao et al., "A review on coupled MEMS resonators for sensing applications utilizing mode localization," *Sensors and Actuators A: Physical,* vol. 249, pp. 93-111, 2016.

[115] C. Zhao et al., "A Comparative Study of Output Metrics for a MEMS Resonant Sensor Consisting of Three Weakly Coupled Resonators," *Journal of Microelectromechanical Systems,* vol. 25, no. 4, pp. 626-636, 2016.

[116] P. Thiruvenkatanathan, J. Yan, J. Woodhouse and A. A. Seshia, "Enhancing Parametric Sensitivity in Electrically Coupled MEMS Resonators," *Journal of Microelectromechanical Systems,* vol. 18, no. 5, pp. 1077-1086, 2009.

[117] J. Juillard, P. Prache, P. Maris Ferreira and N. Barniol, "Impact of output metric on the resolution of mode-localized MEMS resonant sensors," *2017 IEEE International Frequency Control Symposium (IFCS),* 2017.

[118] C. Zhao, G. S. Wood, S. H. Pu and M. Kraft, "A Feasibility Study for a Self-oscillating Loop for a Three Degree-of-Freedom Coupled MEMS Resonator Force Sensor," *Procedia Engineering,* vol. 120, pp. 887-891, 2015.

[119] C. Zhao, M. Pandit, B. Sun, G. Sobreviela, X. Zou and A. Seshia, "A Closed-Loop Readout Configuration for Mode-Localized Resonant MEMS Sensors," *Journal of Microelectromechanical Systems ,* vol. PP, pp. 1-3, 2017.

[120] M. Olivera and L. V. Melo, "Huygens synchronization of two clocks," *Sci. Rep.,* p. 11548, 2015.

[121] R. Adler, "A Study of Locking Phenomena in Oscillators," *Proceedings of the I.R.E. and Waves and Electrons,* pp. 351-357, 1946.

[122] A. Mazzanti, F. Svelto and P. Andreani, "On the Amplitude and Phase Errors of Quadrature LC-Tank CMOS Oscillators," *IEEE Journal of Solid-State Circuits,* vol. 41, no. 6, pp. 1305-1313, 2006.

[123] A. Mirzaei, M. E. Heidari, R. Bagheri, S. Chehrazi and A. A. Abibi, "The Quadrature LC Oscillator: A Complete Potrait Based on Injection Locking," *IEEE Journal of Solid-State Circuits,* vol. 42, no. 9, pp. 1916-1932, 2007.

[124] O. Shoshani and S. W. Shaw, "Phase Noise Reduction and Optimal Operating Conditions for a Pairs of Synchronized Oscillators," *IEEE Transactions on Circuits and Systems,* vol. 63, no. 1, pp. 1-11, 2016.

[125] M. Matheny et al., "Phase Synchronization of Two Anharmonic Nanomechanical Oscillators," *Physical Review Letters,* vol. 112(1), p. 014101(5), 2014.

[126] H. C. Chang, X. Cao and U. K. Mishra, "Phase Noise in Coupled Oscillators: Theory and Experiments," *IEEE Transactions on Microwave Theory and Techniques,* vol. 45, pp. 604-615, 1997.

[127] D. K. Agrawal, J. Woodhouse and A. A. Seshia, "Synchronisation in a coupled architecture of microelectromechanical oscillators," *Journal of Applied Physics,* vol. 115, p. 164904, 2014.

[128] R. Sotner et al., "Quadrature Oscillator Solution Suitable with Arbitrary and Electronically Adjustable Phase Shift," *2015 IEEE International Symposium on Circuits and Systems (ISCAS),* pp. 3056-3059, 2015.

[129] J. Juillard, A. Bonnoit, N. Barniol, A. Uranga and G. Vidal-Alvarez, "A Novel Architecture for Differential Resonant Sensing," *Procedia Engineering,* vol. 87, pp. 1573-1576, 2014.

[130] J. Juillard, P. Prache and N. Barniol, "Analysis of Mutually Injection-Locked Oscillators for Differential Resonant Sensing," *IEEE Transactions on Circuits and Systems I: Regular Papers,* vol. 63, pp. 1055-1066, 2016.

[131] P. Prache, A. Uranga, N. Barniol and J. Juillard, "Temperature-drift rejection and sensitivity to mismatch of synchronized strongly-coupled M/NEMS resonators," *2016 IEEE 29th International Conference on Micro Electro Mechanical Systems (MEMS),* pp. 1054-1057, 2016.

[132] J. Verd, A. Uranga, J. Segura and N. Barniol, "A 3V CMOS-MEMS oscillator in 0.35µm CMOS technology," *2013 Transducers & Eurosensors XXVII: The 17th International Conference on Solid-State Sensors, Actuators and Microsystems,* pp. 806-809, 2013.

[133] C. C. Lo, F. Chen and G. K. Fedder, "Integrated HF CMOS-MEMS square-frame resonators with on-chip electronics and electrothermal narrow gap mechanism," *The 13th International Conference on Solid-State Sensors, Actuators and Microsystems,* vol. 2, pp. 2074-2077, 2005.

[134] P. Prache, P. M. Ferreira, N. Barniol and J. Juillard, "Monolithic integration of mutually injection-locked CMOS-MEMS oscillators for differential resonant sensing applications," *2016 IEEE International Conference on Electronics, Circuits and Systems (ICECS),* pp. 756-759, 2016.

[135] K. Chain, J. H. Huang and J. Duster, "A MOSFET electron mobility model of wide temperature range (77 - 400 K) for IC simulation," *Semiconductor Science and Technology,* vol. 12, p. 355, 1997.

[136] E. Rubiola, Phase noise and frequency stability in oscillators, Cambridge: Cambridge University Press, 2008.

[137] E. Rubiola, "Phase Noise," 2005. [Online]. Available: http://www.rubiola.org/pdf-slides/2005T-ifcs-basics.pdf.

[138] E. Rubiola, "Experimental methods for the measurement of phase noise and frequency stability," 2007. [Online]. Available: http://www.rubiola.org/pdf-slides/2007T-fortef-experimental.pdf.

[139] A. N. Cleland, "Noise processes in nanomechanical resonators," *Journal of Applied Physics,* vol. 92, p. 2758, 2002.

ÉCOLE DOCTORALE
Physique et ingénierie : électrons, photons, sciences du vivant (EOBE)

Titre : Modélisation, conception et intégration de nouvelles architectures différentielles pour des capteurs M/NEMS résonants

Mots clés : M/NEMS, capteur résonant différentiel, CMOS-MEMS, oscillateur verrouillé par injection.

Résumé : Les capteurs M/NEMS résonants, grâce à leur petite taille, faible consommation, et caractère quasi-numérique (leur grandeur de sortie est une fréquence la plupart du temps), sont des outils incontournables dans les systèmes embarqués modernes, des objets connectés simples à l'industrie aérospatiale et militaire.
Cependant, ils sont soumis aux dérives environnementales, et malgré la possibilité d'en diminuer l'effet par différentes techniques de conception, parfois l'association de deux capteurs en mode différentiel est nécessaire pour assurer la fiabilité de l'information en environnement difficiles.
Dans cette thèse, une technique particulière de mesure différentielle est étudiée, qui consiste à synchroniser deux résonateurs, dont l'un est une référence et l'autre soumis à la grandeur physique à mesurer.
Placés dans une seule boucle de rétroaction, les deux résonateurs oscillent à la même fréquence, et un désaccord entre les deux, issu de la grandeur physique à mesurer entraine un déphasage. La mesure de ce déphasage est un moyen simple de remonter à l'information à mesurer, théoriquement insensible aux variations environnementales identiquement appliquées aux deux résonateurs. Cette technique bénéficie est également peu complexe au niveau de son implémentation, donc adapté à l'intégration à grande échelle.
Après avoir étudié le cadre théorique de la synchronisation de résonateurs par verrouillage par injection, on dégage des contraintes d'implémentation, qui servent de ligne directrice dans la fabrication d'un démonstrateur. On dégage également des performances théoriques, qui sont comparées aux performances du démonstrateur.

Title : Modelling, design and integration of new differential architectures for M/NEMS resonant sensors

Keywords : M/NEMS, differential resonant sensors, CMOS-MEMS, injection-locked oscillator

Abstract : M/NEMS resonant sensors, due to their small size, consumption and quasi-digital output (a frequency most of the time) are unavoidable tools for on-board systems, from smartphones to aeronautic technology.
However, they suffer from environmental drifts, and even though the effect of these drifts can be limited by the design, it is sometimes necessary to use differential architectures to properly remove the drifts from the measurements and ensure the output reliability even in harsh environments.
In this work, a special technique for differential measurement is studied, consisting in the synchronization of two resonators, one reference and one sensor. Placed in a single feedback loop, they oscillate at the same frequency and eventual phase shift when the physical quantity to be sensed is applied. This phase shift is a theoretically drift-free way to measure this physical quantity. This technique also benefits from its ease of integration, making it a good candidate for large scale integration.
After studying the theoretical framework, several design guidelines are found, which are used in the fabrication of a proof of concept. The theoretical performances are found as well, and compared to the experimental ones.

Université Paris-Saclay
Espace Technologique / Immeuble Discovery
Route de l'Orme aux Merisiers RD 128 / 91190 Saint-Aubin, France